



Mathematical Modelling of Active Nematic
Liquid Crystals in Confined Regions

Josh Walton

Department of Mathematics and Statistics
University of Strathclyde

A thesis submitted in fulfilment of the requirements
for the degree of Doctor of Philosophy

February 2020

Declaration of Authenticity and Author's Rights

This thesis is the result of the author's original research. It has been composed by the author and has not been previously submitted for examination which has led to the award of a degree.

The copyright of this thesis belongs to the author under the terms of the United Kingdom Copyright Acts as qualified by University of Strathclyde Regulation 3.50. Due acknowledgement must always be made of the use of any material contained in, or derived from, this thesis.

Chapter 3 of the thesis contains material published in an article, reference [147]; the results contained therein are the result of the author's original research in collaboration with the article's co-authors, Prof. Nigel J. Mottram and Dr Geoff McKay.

Chapter 4 of the thesis contains material which will be submitted for publication in the near future, reference [146]; the results contained therein are the result of the author's original research in collaboration with the article's co-authors, Dr Geoff McKay, Dr Michael Grinfeld and Prof. Nigel J. Mottram. The bifurcation diagrams in this chapter were produced by Dr Geoff McKay. The discussion between equations (4.3.16) and (4.3.17) on Page 100 is based on work done by Dr Michael Grinfeld and is being used as part of a present research investigation.

Signed:

Date:

Contents

Dedication	vii
Acknowledgements	viii
Abstract	ix
1 Introduction	1
1.1 An Introduction to Inactive and Active Liquid Crystalline Fluids .	1
1.2 Classification of Active Matter	5
1.2.1 Classification Based on Damping	5
1.2.2 Classification Based on Symmetries	6
1.2.3 Classification Based on Active Stresses	8
1.3 Motivation	9
1.4 Organisation of the Thesis	10
2 Continuum Theories of Inactive and Active Nematic Liquid Crystals	15
2.1 Introduction	15
2.2 Ericksen-Leslie Theory	16
2.2.1 Ericksen-Leslie Equations for an Active Nematic Liquid Crystal	22
2.2.2 Elastic Energy Density	23
2.2.3 Magnetic Energy Density	25

2.2.4	Surface Energy Density	26
2.2.5	Dissipation	27
2.2.6	Activity	29
2.2.7	Additional Active Terms	30
2.2.8	Boundary Conditions	31
2.3	Q-Tensor Theory	32
2.3.1	Dynamic Equations for Uniaxial Active Nematic Liquid Crystals With Variable Scalar Order Parameter	34
2.3.2	Elastic Energy Density	35
2.3.3	Thermotropic Energy Density	37
2.3.4	Dissipation	38
2.3.5	Activity	40
2.4	Summary	41
3	Nematic Liquid Crystal Director Structures in Rectangular Re-	
	gions	42
3.1	Introduction	42
3.2	Mathematical Model	46
3.3	Bifurcations From Undistorted States	50
3.3.1	Linearisation Around the Undistorted Solutions	50
3.3.2	Energies of Elastically Isotropic Nematics	55
3.3.3	Energies of Elastically Anisotropic Nematics	59
3.4	Modelling Defects at Weakly Anchored Corners For Large Anchor-	
	ing Strength	62
3.4.1	Outer Solution	63
3.4.2	Inner Solution	63
3.4.3	Asymptotic Matching	64
3.5	Linearisation in the Large Anchoring Strength Case	65

3.5.1	Linearisation Around the Preferred Directions	66
3.5.2	Solutions for the Director Angle	67
3.5.3	Asymptotic Approximations of the Energy	70
3.5.4	Comparison of Analytic and Numerical Energies	79
3.5.5	Comparison of Numerical Energies in the Limit of Large Anchoring Strength	84
3.6	Conclusions	88
4	Spontaneous and Pressure-Driven States in Channel Flow of Ac- tive Nematic Liquid Crystals	90
4.1	Introduction	90
4.2	Mathematical Model	92
4.3	Asymptotic Solutions and Linear Stability Analysis	96
4.3.1	Decoupling of the Ericksen-Leslie Equations	96
4.3.2	Asymptotic Solutions for Large Pressure Gradients	97
4.3.3	Asymptotic Solutions for Large Activity	98
4.3.4	Linear Stability Analysis of Bifurcations from the Trivial Solution with Zero Pressure Gradient	101
4.4	Numerical Calculations	103
4.4.1	Extensile Active Nematic Liquid Crystals with Zero Pres- sure Gradient	104
4.4.2	Extensile Active Nematic Liquid Crystals with Non-Zero Pressure Gradient	109
4.4.3	Contractile Active Nematic Liquid Crystals with Zero Pres- sure Gradient	112
4.4.4	Contractile Active Nematic Liquid Crystals with Non-Zero Pressure Gradient	114
4.5	Two-Parameter Continuation	115

4.6	Reorientation of Active Nematic Liquid Crystals Subject to an External Orienting Field	122
4.6.1	Reorientation of Contractile Active Nematic Liquid Crystals	125
4.6.2	Reorientation of Extensile Active Nematic Liquid Crystals	127
4.6.3	Kickback in Active Nematic Liquid Crystals	130
4.7	Conclusions	135
5	Active Nematic Liquid Crystals with Variable Degree of Orientation	137
5.1	Introduction	137
5.2	Mathematical Model	138
5.3	The Effect of Temperature Changes on the Bifurcation of Non-Trivial States	141
5.3.1	Linear Stability Analysis	141
5.3.2	Numerical Calculations I: Extensile Active Nematic Liquid Crystals	143
5.3.3	Numerical Calculations II: Contractile Active Nematic Liquid Crystals	150
5.4	Conclusions	158
6	Active Fluids Confined in Two-Dimensional Geometries	160
6.1	Introduction	160
6.2	A Simplified Ericksen-Leslie Model of Active Fluids	162
6.3	Flow of Active Fluids in a Wedge Geometry	163
6.3.1	Calculating the Streamfunction	166
6.3.2	Active Fluid Flows Close to Sharp Corners	170
6.3.3	Active Fluid Flows Close to Flat Plates	171
6.3.4	The Special Cases of $s = 1$ and $s = 2$ Defects	174

6.4	Director and Flow Structures of Active Nematic Liquid Crystals in Rectangular Regions	177
6.4.1	Non-Dimensionalisation	178
6.4.2	Flow Induced with Zero Ericksen Number	181
6.4.3	Flow Induced with Non-Zero Ericksen Numbers	189
6.5	Conclusions	197
7	Conclusions and Future Work	199
7.1	Summary of Work Undertaken	199
7.2	Future Work	201
A	Derivation of the Active Stress Tensor	204
B	Energies Close to the Critical Anchoring Strengths	207
C	Decoupling of the Ericksen-Leslie Equations	211
	Bibliography	214

Dedication

This thesis is dedicated to the memory of my grandfather, Stanley Purcell (1937–2012).



Acknowledgements

First and foremost, I am indebted to my supervisors Prof. Nigel J. Mottram and Dr Geoff McKay for the opportunity to continue my studies under their supervision, and for their patience and invaluable guidance over the last three and a half years – it has been a privilege to have worked with you both. I am also hugely grateful to the Department of Mathematics and Statistics at the University of Strathclyde for awarding me a scholarship funded by the Engineering and Physical Science Research Council (EPSRC), without which, this opportunity would not have been possible.

I would also like to thank both Jon Devlin and Ainsley Miller, who I have known since 2011 when we started studying our undergraduate degrees at the University of Strathclyde, and have been good friends throughout. I have benefited hugely from Jon’s knowledge of computational mathematics and Ainsley’s knowledge of Latex. I am also grateful to Dr Stephen Corson, who has been there to help me through the most challenging times of my studies.

I consider myself very fortunate to have such a supportive family, and I am incredibly grateful for all they have done for me. I won’t list every single member (as you have all contributed in some way) but a massive “thank you” must go to my parents Elisa and Michael Walton for everything they have done in helping me get to where I am today - I could not have asked for better parents!

Abstract

This thesis focusses on the application of continuum theories and modelling techniques of liquid crystalline fluids to the area of anisotropy and self-organisation derived from active agents. The research involves a continuum description of anisotropic active fluids, using adapted forms of continuum hydrodynamic theories of liquid crystals.

We first consider the director structures of inactive nematic liquid crystals confined in rectangular regions. We use a mixture of analytical and numerical calculations to examine the energies of non-trivial nematic equilibria which exchange stabilities with constant equilibria at critical anchoring strengths. For the remainder of the thesis, we consider active nematic liquid crystals in confined regions. We first use an adapted Ericksen-Leslie theory to investigate spontaneous flow transitions of active nematics, with the liquid crystal confined in a one-dimensional shallow channel. We examine how internally generated flows induced by activity are affected by externally induced flows due to, pressure gradients and external orienting fields. We then investigate a shallow channel of active nematic in terms of an adapted \mathbf{Q} -tensor theory for uniaxial nematic liquid crystals. Such a model allows for an investigation into the effects of variable ordering caused by changes in the temperature. Finally, we investigate active nematics confined in two-dimensional regions. We first consider wedge geometries containing an active nematic with a singularity at the wedge corner, deriving analytic solutions of a simplified version of the Ericksen-Leslie equations. We then employ numerical calculations to find steady solutions of the full non-linear Ericksen-Leslie equations for active nematics confined in rectangular regions.

Chapter 1

Introduction

1.1 An Introduction to Inactive and Active Liquid Crystalline Fluids

As the name suggests, liquid crystals are intermediate states of matter, with characteristic properties which are used to describe both crystalline solids and isotropic liquids. The discovery of liquid crystals is attributed to the Austrian botanist Friedrich Reinitzer [117, 118] who observed that heating a sample of cholesteryl benzoate (a solid at room temperature) led to two melting points. The first of the melting points occurred at 145.5°C and led to the formation of a cloudy liquid. Upon further heating, a second melting point occurred at 178.5°C , at which the cholesteryl benzoate turned into a transparent liquid. The cloudy liquid reported by Reinitzer is now known to be a cholesteric liquid crystal phase. The larger of the two melting points is termed as the clearing point and corresponds to the temperature at which the cholesteryl benzoate turns into an isotropic liquid. Reinitzer sent a letter to the German physicist Otto Lehmann, along with two samples of cholesteryl benzoate, in which he requested an investigation to confirm his experimental observations [70]. Examination of these samples led Lehmann to use the expression “flowing crystals” [79] to classify these samples, before eventually settling on the term “liquid crystals” in 1900. In 1907, Vorländer, a German chemist, discovered that anisotropic (either rod-

like or disc-like) molecules were essential for a given material to exhibit the two melting points described by Reinitzer [125, 145]. This discovery was of substantial importance for the theoretical modelling of liquid crystals as it enabled for a mathematical description of the molecular structure.

There are a number of possible liquid crystal phases, each with distinct structural characteristics. The classification of different phases of inactive liquid crystals was introduced by Friedel in 1922 [53], who proposed a classification scheme for liquid crystals consisting of three categories: nematic, cholesteric and smectic. The term “nematic” originates from the Greek word for thread, arising due to the existence of thread-like lines found in these materials. These lines are present due to a type of defect in nematic liquid crystals, known as disclinations. In the nematic (or achiral nematic) phase the long axes of the constituent molecules tend to align parallel to each other along a single preferred direction referred to as the anisotropic axis. The constituent molecules in a nematic liquid crystal are often rod-like or disc-like in shape. The cholesteric (or chiral nematic) liquid crystal phase is similar to the nematic phase, except that the molecular orientation shows a preferred helical configuration. This helical structure arises from the chiral properties of the constituent molecules. Smectic liquid crystals are layered structures and are, therefore, more ordered than nematics and generally occur at lower temperatures than that of the nematic phase. We will not be considering either the cholesteric or smectic liquid crystal phases in this thesis. The interested reader is referred to Oswald and Pieranski [109] for background reading on cholesteric liquid crystals, and the books of de Gennes and Prost [56] and Stewart [129] for details on the continuum theories of smectic liquid crystals.

The area of active fluids is currently a topic of significant research interest in biology, engineering, mathematics and physics. Active fluids consist of self-driven agents which can be influenced by the flow of fluid around them but, crucially, also influence the flow themselves. The active agents exhibit a continuous generation of internal energy, as in suspensions of bacteria [66, 123], swimming organisms [91] and cytoskeletal filaments such as microtubule networks [28, 135], allowing for collective orientational ordering and spontaneous flow generation [12, 41, 63, 144].

The continuous energy production leads to the active agents (the bacteria or microtubule-forming motors) exerting a stress on the background fluid, which generates a system that is always away from thermodynamic equilibrium [39, 92, 135]. By contrast, inactive (or passive) systems induce flow when the system is driven out of equilibrium by some form of external forcing, which may act on the entire system, such as pressure gradients and orienting fields, or at the boundaries (e.g., shear gradients). Once the external forcing is no longer applied, the externally induced flow begins to dissipate and eventually vanishes. Two examples of inactive systems include isotropic liquids, such as water, and standard molecular liquid crystals, the latter of which will, together with active fluids, be considered in this thesis.

Flow-generating agents are generally considered to be anisotropic and are defined by, for instance, the long axis of an active agent (e.g., the bacterium or microtubule), with the macroscopic symmetry of a liquid crystalline-like phase. The resulting states of matter are commonly referred to as active liquid crystalline fluids. The fluids combine the flow-molecular orientation coupling phenomena observed in standard molecular liquid crystals and the presence of internal energy generation that leads to a spontaneous flow. Internally driven flows in active liquid crystals can lead to interesting effects, including hydrodynamic instabilities and non-equilibrium defect configurations [29, 39, 60, 62, 92, 115, 149].

The constituent units of an active fluid span not just subcellular length scales, such as microtubules, and micron length scales, as in bacterial suspensions, but also larger length scales, from centimetres to metres, (e.g., fish). The orientational ordering of swarms of bacteria and fish are shown in Figure 1.1. In both of these active systems, the agents tend to align parallel to one another along an average preferred direction [25]. This is reminiscent of how elongated rod-like organic molecules are ordered in inactive nematic liquid crystals. The similarity between the orientational ordering of active agents in a fluid and elongated rod-like molecules in a nematic liquid crystal means that continuum hydrodynamic models of nematic liquid crystals have frequently been used in the theoretical modelling of active liquid crystalline fluids. The models are modi-

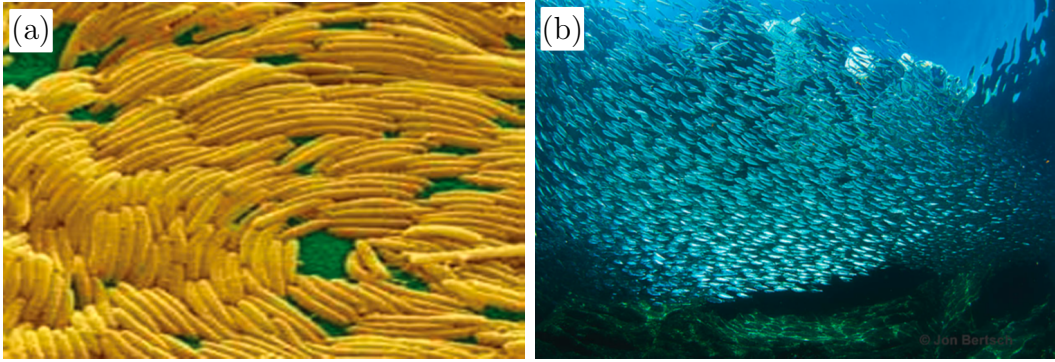


Figure 1.1: Examples of active fluid systems which exhibit liquid crystalline order, from smaller length scales such as (a) arrangements of bacteria, to larger length scales such as (b) fish. Figure adapted from [92].

fied to include non-equilibrium terms in the governing equations due to activity [41, 57, 58, 59, 61, 92, 131]. This is the approach which we will adopt throughout this thesis in order to model active nematic liquid crystals confined in one and two-dimensional geometries. Recent progress has also been made in modelling three-dimensional active systems [9, 22, 36, 122], although this is outwith the scope of the work considered here.

Another example of an active fluid system which has received significant interest both from experimentalists and theoreticians is shown in Figure 1.2, where the active system consist of a mixture of microtubule suspensions, molecular motors in the form of kinesin clusters and the non-adsorbing depleting agent polyethylene glycol (PEG). The addition of PEG induces depletion forces that results in the formation of microtubule bundles. In an aqueous suspension, the addition of a chemical fuel such as adenosine triphosphate (ATP) to the kinesin clusters leads to the conversion of the chemical energy from ATP hydrolysis into mechanical movement. This allows the molecular motors to move along the microtubules, where the ends of two kinesin clusters can cause neighbouring microtubules to cross-link as the molecular motors move along the microtubules. If a kinesin cluster assembles two microtubules with differing polarities, the movement of the motors can force the microtubules to slide relative to each other. At large concentrations of ATP, the microtubule bundles are driven by the molecular

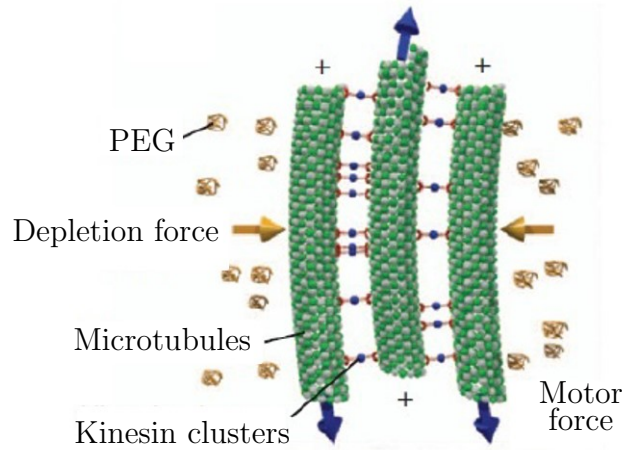


Figure 1.2: Orientational ordering in an active liquid crystalline fluid consisting of microtubules, kinesin clusters and PEG. Similar orientational ordering is exhibited by elongated rod-like molecules in inactive nematic liquid crystals. Figure adapted from [154].

motors, leading to an active nematic liquid crystalline phase with large distortions in the director field and complex flow patterns. At low concentration of ATP, the molecular motors are not sufficiently affected and there is no spontaneously induced flow.

1.2 Classification of Active Matter

1.2.1 Classification Based on Damping

Active systems can be classified according to the nature of the internal forces between the constituent active agents and the surrounding environment, or by the symmetries of the individual agents. It is possible in some active systems for hydrodynamic interactions between the constituent agents to be dominated by the movement of the agents throughout a medium or on a substrate due to frictional damping. An active system for which the viscous dissipation is dominated by friction is referred to as a “dry” active system. Examples of “dry” active systems include vibrated granular rods and flocks of birds [91, 92, 135, 138]. In such

systems, there is no conservation of momentum between the active agents and the surrounding environment. By contrast, when frictional damping is considered to be negligible compared to viscous dissipation, the active system is referred to as “wet”. Examples of “wet” active systems include cell cytoskeleton, swimming organisms, microtubule bundles and suspensions of bacteria [71, 92, 98]. Such systems must satisfy the conservation of momentum since the hydrodynamic interactions between nearby active agents and the surrounding medium, usually an incompressible viscous fluid, play a crucial role in the dynamics. The governing equations of “wet” active systems (e.g., the Navier-Stokes equations [4] and Ericksen-Leslie equations [82]) must satisfy Galilean (or inertial frame) invariance. In this thesis, we will only consider “wet” active systems.

1.2.2 Classification Based on Symmetries

Ordered liquid crystalline phases of active matter can be classified according to the symmetry of the constituent agents, as is also the case for inactive liquid crystals. Active agents such as some bacteria and fish (see Figure 1.1) have a head and a tail, and are therefore intrinsically polar. These active agents exhibit long range collective ordering and generate motion by self-propelling along their axis towards their heads, leading to the generation of an active polar liquid crystal phase. In this case the average preferred direction of the active agents can be modelled by a polarisation vector field \mathbf{p} . Alternatively, if the active agents align parallel to one another along an average preferred direction which is head-tail symmetric, then an active apolar (or nematic) phase will be generated. In such materials, the direction of spontaneously broken symmetry is modelled by a unit vector \mathbf{n} , known as the director, which is also used to describe the average preferred direction of a group of elongated rod-like molecules in an inactive nematic liquid crystal. Unlike active polar liquid crystals, the active nematic phase is therefore invariant under the transformation $\mathbf{n} \rightarrow -\mathbf{n}$. In other words, physical properties of a nematic liquid crystal cannot change under this transformation. Throughout this thesis, we will only be considering the active nematic phase,

although we briefly discuss in Chapter 2 how active polar liquid crystals can be mathematically modelled using additional non-equilibrium terms in the governing equations, as well as the activity term which we consider throughout this thesis.

As well as the average orientation, it is sometimes necessary to consider how ordered active agents are with respect to the average orientation. If we consider a ball B which contains active agents that are oriented on average in the direction of the director \mathbf{n} , a probability distribution of the orientations of the active agents in B can be constructed. As well as the director orientation, we can define a measure of the degree of local alignment to be the scalar order parameter S , which is an average of the orientation angles θ_m between the long axes and the director [103]

$$S = \langle \mathcal{P}_2(\cos \theta_m) \rangle = \left\langle \frac{3}{2} \cos^2 \theta_m - \frac{1}{2} \right\rangle, \quad (1.2.1)$$

where \mathcal{P}_2 is the second Legendre polynomial in the cosine of the angle between the molecular axis and the director. The Legendre polynomials $\mathcal{P}_n(x)$ are solutions to Legendre's differential equation [1]

$$\frac{d}{dx} \left[(1-x^2) \frac{d}{dx} \mathcal{P}_n(x) \right] + n(n-1) \mathcal{P}_n(x) = 0. \quad (1.2.2)$$

The brackets $\langle \dots \rangle$ in equation (1.2.1) denote the statistical average so that over a volume V ,

$$S = \frac{1}{2} \int (3 \cos^2 \theta_m - 1) f(\theta_m) dV, \quad (1.2.3)$$

where $f(\theta_m)$ is the probability distribution function of the angle θ_m . Due to the head-tail symmetry of apolar active agents, it follows that $f(\theta_m)$ is periodic so that $f(\theta_m + \pi) = f(\theta_m)$.

When the active agents are randomly orientated, the scalar order parameter $S = 0$, and the material is in the isotropic phase, whereas a non-zero S indicates a preferred direction. Two extremes of ordering are when the active agents are all perpendicular to the director, so that $\theta_m = \pi/2$ and $S = -1/2$, or when $\theta_m = 0$ so that the active agents align exactly parallel with the director with $S = 1$ so that the material is in a crystalline phase. Although it is possible to achieve configurations of the active agents for which $S < 0$ (i.e., $-1/2 < S < 0$),

it is more common for S to be positive in the equilibrium liquid crystal state. In general, as the temperature of the material decreases the scalar order parameter will increase, from $S = 0$ in the isotropic state, to $S = 1$ in the crystalline state.

1.2.3 Classification Based on Active Stresses

The mechanism by which momentum is transferred from the active agents into the surrounding fluid allows for the classification of two types of active nematic fluid, depending on the behaviour of the active agents relative to the surrounding fluid - the active agents can either push the fluid out or pull the fluid in along the long axis. This simple description of “pushers” and “pullers” to describe active agents is commonly replaced by the terms “extensile” and “contractile”, respectively. We will be discussing this in more detail in Chapter 2. The pushing and pulling effect of active agents is usually taken into account in continuum models of active fluids through an additional term in the stress tensor first proposed by Simha and Ramaswamy [123]. This additional term corresponds to local active stresses proportional to the degree of orientational order in which spontaneously induced non-zero distortion of the director will generate fluid flow. The form of this active stress term is given by

$$\boldsymbol{\sigma}^\zeta = \zeta (\mathbf{n} \otimes \mathbf{n}), \quad (1.2.4)$$

where the dyadic product is defined as

$$[\mathbf{n} \otimes \mathbf{n}]_{ij} = \mathbf{e}_i \cdot [(\mathbf{n} \otimes \mathbf{n})\mathbf{e}_j] = n_i n_j, \quad (1.2.5)$$

and n_i ($i = 1, 2, 3$) is the i^{th} component of the nematic director. The coefficient ζ is termed the activity strength parameter, which can be positive or negative, thereby distinguishing extensile and contractile active nematic liquid crystals. The magnitude of ζ quantifies the degree of activity, or equivalently and more specifically, the pressure the active agents exert on the background fluid. We will discuss this activity term in further detail in Chapter 2, where we introduce mathematical models of active nematic fluids based on two continuum theories of inactive nematic liquid crystals. A derivation of the active stress term (1.2.4) is

given in Appendix A, and closely follows the derivation in [123], where each individual active agent is treated as a permanent force dipole, leading to local active stresses proportional to the degree of orientational order. Alternative derivations of (2.2.30) can be found in Hatwalne *et al.* [66] and Thampi and Yeomans [135]. In this thesis we will consider both extensile and contractile active nematic liquid crystals, showing that they can be very different from each other.

1.3 Motivation

As we have already mentioned, a striking phenomenon of active nematic liquid crystals is spontaneous flow generation. This behaviour was predicted theoretically using continuum models of active fluids [41, 93, 144, 151, 153], which demonstrated that the active nematic fluid undergoes a spontaneous flow transition from a uniform director configuration to a non-trivial structure when the activity strength magnitude exceeds a critical threshold value. This transition is similar to a classic electric/magnetic field-induced Fredericksz transition in inactive nematic liquid crystals [52, 54, 112]. When an electric/magnetic field is applied to a sample of nematic liquid crystal in a direction perpendicular to an initially uniform director orientation throughout the sample, there exists a critical field strength at which the orientation of the liquid crystal begins to change, i.e., the Fredericksz threshold. Beyond this critical threshold value, a non-trivial director configuration that minimises the free energy exists in which the director aligns closer to the field as the magnitude of the field strength increases. One of the ideas we will be exploring in this thesis is how similarities can be drawn between spontaneous flow transitions and Fredericksz transitions.

Another interesting phenomenon of active fluids which we will examine in this thesis and that has been extensively studied theoretically is the existence of topological defects [58, 59, 111, 131]. These are discontinuities in the director orientation and also exist in inactive nematics. Defects can be generated in liquid crystals by, for example, incompatible boundary conditions for the director orientation at orthogonal boundaries [86, 107]. In active liquid crystalline fluids,

defect configurations can occur spontaneously in the bulk and can be continuously regenerated due to irregular flow patterns, also known as active turbulence [38, 57, 92]. Defects can occur as points, lines or sheets, and can be observed in experimental samples of inactive nematics due to their optical pattern between cross polarisers. Sheet defects occur on surfaces and are unstable [56] but point or line defects are commonly found experimentally [85]. Point defects are isolated points where the director orientation is undefined whereas line defects are lines along which the director orientation is discontinuous, and are often termed disclination lines. Each of these defects can be described in terms of their “strength” s , or winding number, which represents the number of complete rotations of the director on a closed circuit containing the defect. Examples of the director field surrounding defects for a mixture of half-integer and integer strengths are shown in Figure 1.3. In this thesis we concentrate only on axial disclinations, such as those shown in Figure 1.3, where the director rotation occurs about the axis of the disclination. Figure 1.4 shows examples of active turbulence in active systems, where higher levels of activity lead to high elastic energy densities, which in turn lead to hydrodynamic instabilities. These hydrodynamic instabilities lead to a continuous cycle of creation and annihilation of defect pairs in active systems [58, 135]. Figure 1.5 shows the presence of internally generated defects with strengths $s = \pm 1/2$ in an active nematic liquid crystal consisting of microtubule suspensions. The observation of these defects were based on (a) experiments and (b) computer simulations. These computer simulations were carried out using a continuum theory approach based on liquid crystalline hydrodynamics and show remarkably good agreement with the experiments, thereby suggesting that the theoretical approach which we consider in this thesis is a reasonable one.

1.4 Organisation of the Thesis

In this thesis, we present a range of theoretical studies examining the confinement of inactive nematic and active nematic liquid crystals. For the most part, we employ an adapted form of the Ericksen-Leslie dynamic theory of nematic liquid

crystals [80, 81]. We also make use of a continuum theory which describes nematic liquid crystals with variable scalar order parameter [48, 127].

The thesis is structured as follows. In Chapter 2 we review the Ericksen-Leslie and scalar order parameter theories of liquid crystals mentioned above. In order to model a system which is out of equilibrium, we adapt these two theories by including additional terms in the governing equations for a standard inactive nematic liquid crystal. In Chapter 3, we consider a static inactive nematic liquid crystal confined to a rectangular region, subject to weak anchoring boundary conditions. For very weak surface anchoring, we find non-trivial solutions that emerge from two possible trivial states at critical anchoring strength values which depend on the aspect ratio of the region. We then examine the system in the limit of large anchoring strength, using a mixture of analytic and numerical calculations. In this limit, we find there are similarities in the results with previous experimental and theoretical investigations of similar systems.

Chapter 4 presents an investigation of spontaneous flow transitions that occur in active nematic liquid crystals. We employ an adapted Ericksen-Leslie theory and assume the active nematic is confined to be a thin film bounded by solid surfaces. We show that non-trivial solutions exist at critical activity values which depend on geometric and liquid crystal material parameters. Unlike a classic external field-induced Freedericksz transition, we show that there are non-trivial solutions which are not connected to a trivial state. We then consider how the flows created by activity can be designed using similar methodologies to those commonly used in the design of liquid crystal display devices, such as pressure gradients and external orienting fields. In Chapter 5, we consider the same geometrical set-up as in Chapter 4, except the model includes a variable degree of orientation. We demonstrate that the model considered in this chapter simplifies to that considered in Chapter 4 in the special case of uniform ordering. The effect of changes in the system temperature is also examined.

Finally, Chapter 6 combines the ideas from the previous chapters in order to investigate the flow of active fluids confined in two-dimensional geometries. Throughout this chapter, we employ the adapted Ericksen-Leslie theory also used

in Chapter 4. We first present an analytic study of the flow close to a sharp corner of a wedge geometry which contains a discontinuity in the director structure. We then present a numerical investigation of the director orientation and flow of an active nematic liquid crystal confined within rectangular regions, with a particular focus on the generation of flow due to distortion in the director close to the corners and sides of the region. Finally, in Chapter 7 we draw conclusions and discuss possible future areas of research.

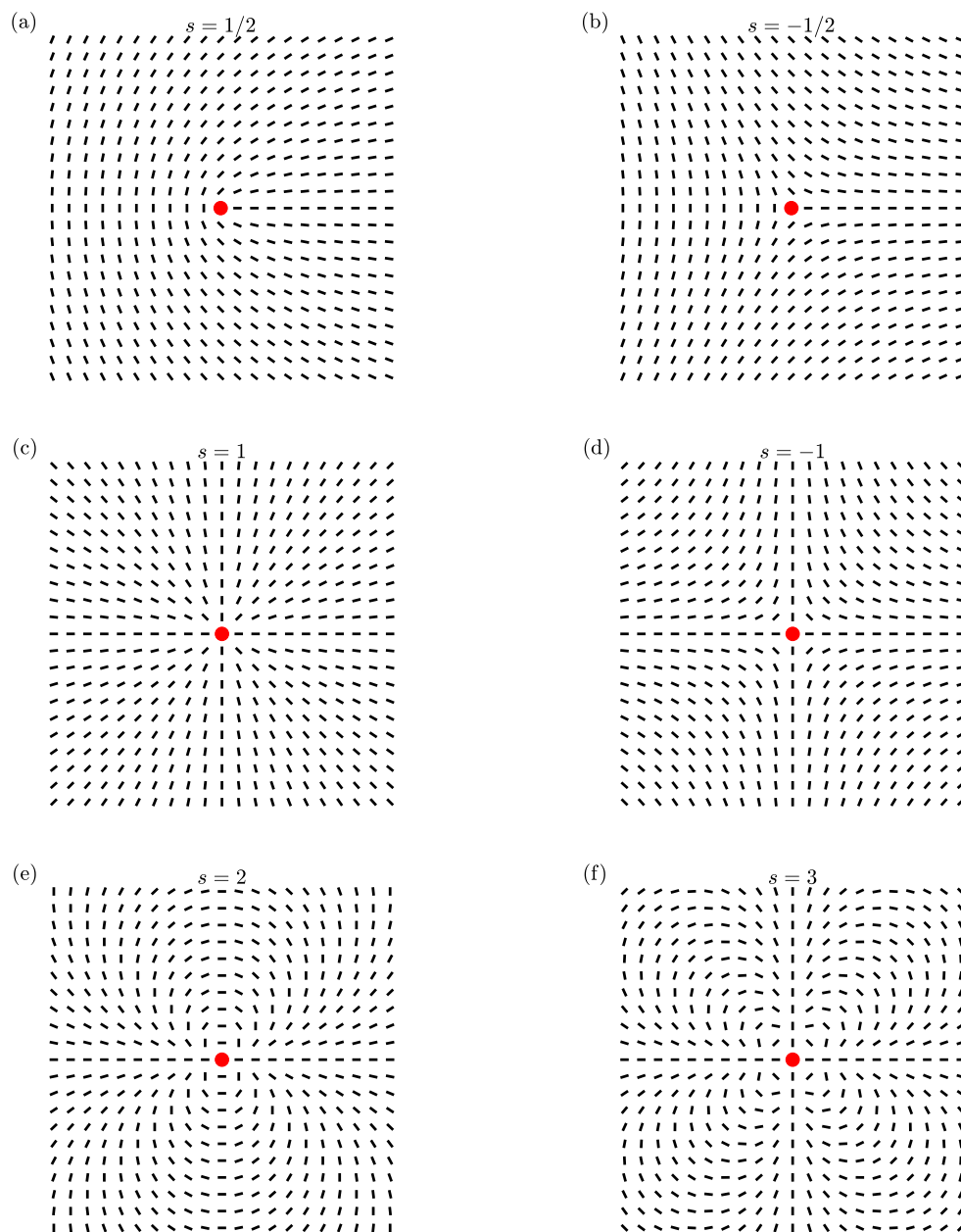


Figure 1.3: Local behaviour of the director about line disclinations of strength (a) $s = 1/2$, (b) $s = -1/2$, (c) $s = 1$, (d) $s = -1$, (e) $s = 2$ and (f) $s = 3$. Each of these line disclinations are located perpendicular to the page and pass through the points indicated by the red markers.

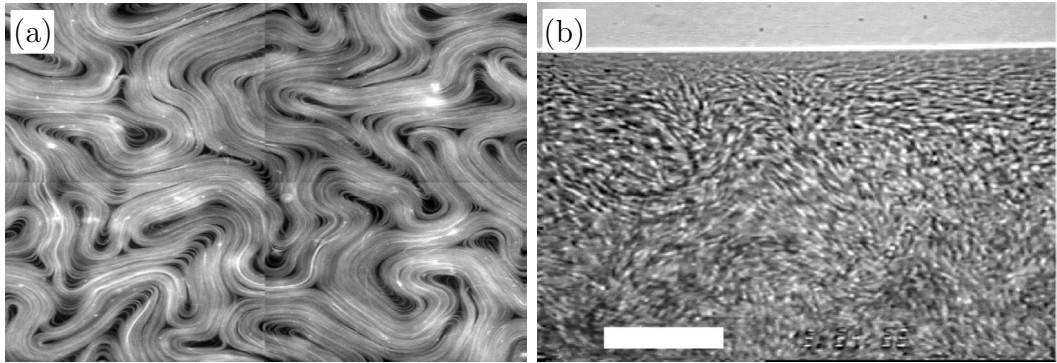


Figure 1.4: Active turbulence in (a) a microtubule bundle and kinesin suspension and (b) a suspension of bacteria. Figures (a) and (b) adapted from [57] and [92], respectively.

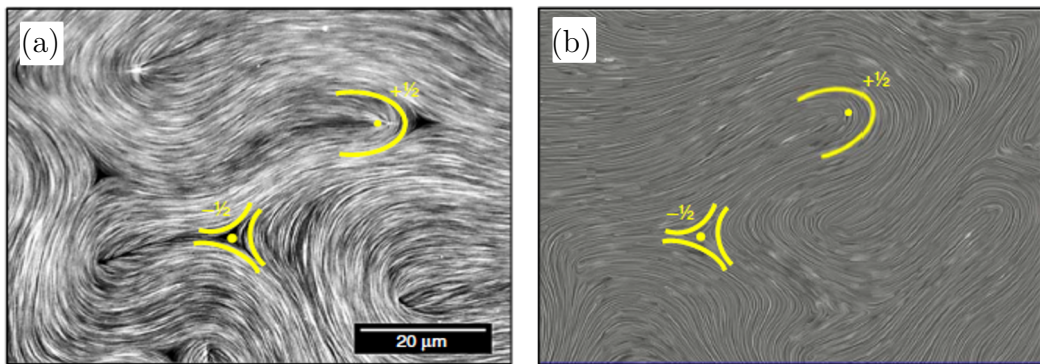


Figure 1.5: The presence of defects of strengths $s = \pm 1/2$ in an active liquid crystal consisting of microtubules and kinesin clusters. These defects were observed from (a) experiments and (b) computer simulations. Figures (a) and (b) adapted from [37].

Chapter 2

Continuum Theories of Inactive and Active Nematic Liquid Crystals

2.1 Introduction

As we discussed in Chapter 1, the similarity between the orientational ordering of active agents in a fluid and elongated rod-like molecules in a nematic liquid crystal means that continuum hydrodynamic models of nematic liquid crystals have frequently been used in the theoretical modelling of active liquid crystalline fluids with nematic ordering. One commonly adopted approach used in order to model the active nematic liquid crystal phase is to take these continuum hydrodynamic models and include extra terms in the governing equations which generate a system which is always out of thermodynamic equilibrium. This is the only approach we will consider in this thesis, where we refer to such additional terms as active terms. Throughout this thesis, we make use of adapted forms of two continuum theories of nematic liquid crystals, namely, the Ericksen-Leslie theory and the \mathbf{Q} -tensor theory. The models of active nematic liquid crystals we consider involve additional terms in the governing equations which are formulated either in terms of a director field or an alignment tensor (i.e., a \mathbf{Q} -tensor field). In

both cases, a spontaneously induced non-zero distortion will generate fluid flow. It is worth mentioning that there are other approaches to modelling active liquid crystals. An entirely different approach has been considered by Brand *et al.* [14] and Pleiner *et al.* [113, 114], where activity is introduced through a finite relative velocity between the active and passive parts of the system, and the constitutive equations of an active liquid crystal are derived using symmetry and linear irreversible thermodynamics. The same arguments are also used by the same authors in the derivation of an alternative set of hydrodynamic equations of inactive liquid crystals (see [13] and Chapter 2 of [16]). There have also been recent extensions in the modelling of other phases of active liquid crystal, including active cholesteric liquid crystals [7, 88, 95, 148] and active smectic liquid crystals [50, 119], although we do not consider either of these phases in this thesis. In this chapter, we provide an overview of adapted forms of the Ericksen-Leslie and \mathbf{Q} -tensor theories, which will include active terms in the governing equations.

2.2 Ericksen-Leslie Theory

The earliest attempt at a theory which describes the dynamics of nematic liquid crystals was undertaken in 1931 by Anzelius [3]. However, his theory was deficient as the necessary concepts in continuum mechanics had not been established. The first widely accepted dynamic theory of nematic liquid crystals was formulated in 1961 by Ericksen [44] using conservation laws from continuum mechanics and a generalisation of the static theory for nematic liquid crystals [45]. Ericksen's dynamic theory was completed in 1968 by Leslie [81], who derived suitable constitutive equations, and hence proposed a complete set of equations for the various dynamic effects in nematic liquid crystals. This followed after Leslie derived constitutive equations for general anisotropic fluids in 1966 [80], which were previously considered in 1960 by Ericksen [43]. This theoretical description of nematic liquid crystal dynamics is referred to as the Ericksen-Leslie theory. The resulting non-linear equations couple the fluid flow to the director orientation. Alternative formulations of the Ericksen-Leslie theory have been published since

its establishment. For example, Leslie [82] published an alternative derivation of the Ericksen-Leslie theory in 1992, which led to a simpler presentation of the original results derived by Ericksen [44] and Leslie [80]. A full derivation of the Ericksen-Leslie theory can be found in Leslie [81, 83] and Stewart [129].

In the following subsections, we will require a mathematical description of the evolution of the nematic director \mathbf{n} . Ericksen [47] presented a formulation of the governing equations of motion for a nematic liquid crystal in which the director is expressed as a function of two angles θ_1 and θ_2 ,

$$\mathbf{n} = \mathbf{n}(\theta_1, \theta_2), \quad \mathbf{n} \cdot \mathbf{n} = 1. \quad (2.2.1)$$

In this thesis, we will consider only a nematic director of the form

$$\mathbf{n} = (\cos \theta_1 \cos \theta_2, \cos \theta_1 \sin \theta_2, \sin \theta_1), \quad (2.2.2)$$

where for each problem we will define the two angles.

The starting point for the derivation of the Ericksen-Leslie equations is to consider the conservation laws for mass, linear momentum and angular momentum for a volume V of nematic liquid crystal bounded by a surface A . These conservation laws are, respectively,

$$\frac{D}{Dt} \int_V \rho dV = 0, \quad (2.2.3)$$

$$\frac{D}{Dt} \int_V \rho \mathbf{v} dV = \int_V \rho \mathbf{F} dV + \int_A \boldsymbol{\sigma} dA, \quad (2.2.4)$$

$$\frac{D}{Dt} \int_V \rho (\mathbf{x} \times \mathbf{v}) dV = \int_V \rho (\mathbf{x} \times \mathbf{F} + \mathbf{K}) dV + \int_A (\mathbf{x} \times \boldsymbol{\sigma} + \mathbf{l}) dA, \quad (2.2.5)$$

where ρ is the fluid density, \mathbf{x} is the position vector, \mathbf{v} is the velocity vector, \mathbf{F} is the external body force per unit mass, $\boldsymbol{\sigma}$ is the surface force per unit area, \mathbf{K} is the external body moment per unit mass, \mathbf{l} is the surface moment per unit area (also known as the couple stress vector), and D/Dt denotes the usual material time derivative

$$\frac{D}{Dt} = \frac{\partial}{\partial t} + \mathbf{v} \cdot \nabla. \quad (2.2.6)$$

If ν_j is the j^{th} coordinate of the unit outward normal to the surface A , then the components of the surface force σ_i and surface moment l_i can be written in terms

of the components of the stress tensor σ_{ij} and couple stress tensor l_{ij} , respectively, through the relations

$$\sigma_i = \sigma_{ij}\nu_j, \quad l_i = l_{ij}\nu_j. \quad (2.2.7)$$

If the sample is assumed to be of arbitrary volume V and incompressible (i.e., the fluid density ρ is constant), then the three conservation laws can be reduced to the point forms

$$\frac{\partial v_i}{\partial x_i} = 0, \quad (2.2.8)$$

$$\rho \frac{Dv_i}{Dt} - \rho F_i - \frac{\partial \sigma_{ij}}{\partial x_j} = 0, \quad (2.2.9)$$

$$\rho K_i + \epsilon_{ijk}\sigma_{kj} + \frac{\partial l_{ij}}{\partial x_j} = 0, \quad (2.2.10)$$

where ϵ_{ijk} is defined as the Levi-Civita symbol, also known as the alternator [129]. It proves convenient to introduce the symmetric rate of strain tensor \mathbf{A} and the anti-symmetric vorticity tensor \mathbf{W} which, in component form, are given by

$$A_{ij} = \frac{1}{2} \left(\frac{\partial v_i}{\partial x_j} + \frac{\partial v_j}{\partial x_i} \right), \quad W_{ij} = \frac{1}{2} \left(\frac{\partial v_i}{\partial x_j} - \frac{\partial v_j}{\partial x_i} \right), \quad (2.2.11)$$

respectively. Following Leslie [82], a vector \mathbf{N} is introduced and defined in component form by

$$N_i = \frac{Dn_i}{Dt} - W_{ij}n_j. \quad (2.2.12)$$

In the terminology used by Truesdell and Noll [139], \mathbf{N} is the co-rotational time flux of the director and measures the rotation of the director relative to the surrounding fluid.

In order to determine the constitutive equations for σ_{ij} and l_{ij} , Leslie [82] introduced a rate of work hypothesis. This hypothesis assumes that the rate at which forces and moments do work on a volume of nematic liquid crystal will be absorbed into changes in the nematic energy density w_F or the kinetic energy, or will be lost by means of dissipation. The principle of work proposed by Leslie is

$$\begin{aligned} \int_V \rho(\mathbf{F} \cdot \mathbf{v} + \mathbf{K} \cdot \mathbf{w}) dV &= \frac{D}{Dt} \int_V \left(\frac{1}{2} \rho \mathbf{v} \cdot \mathbf{v} + w_F \right) dV \\ &+ \int_V \Delta dV - \int_A (\boldsymbol{\sigma} \cdot \mathbf{v} + \mathbf{l} \cdot \mathbf{w}) dA, \end{aligned} \quad (2.2.13)$$

where \mathbf{w} is the local angular velocity of the nematic director, Δ is the rate of dissipation per unit volume, which is assumed to be positive semi-definite for inactive nematics, and w_F is the bulk energy density which, in this thesis, is considered to be the sum of the elastic energy density, w_{elastic} , and the energy density due to an externally applied orienting field, w_{field} . We will review one example of an external orienting field later in this chapter, namely, a magnetic field, with magnetic energy density w_{magnetic} . In addition, a surface energy density w_S can be specified so that the total free energy W can be defined as

$$W = \int_V w_F dV + \int_A w_S dA. \quad (2.2.14)$$

With the aid of the relations in (2.2.7) and simplification through (2.2.9) and (2.2.10), the rate of work hypothesis can be expressed in point form as

$$\sigma_{ij} \frac{\partial v_i}{\partial x_j} + l_{ij} \frac{\partial w_i}{\partial x_j} - w_i \epsilon_{ijk} \sigma_{kj} = \frac{Dw_F}{Dt} + \Delta. \quad (2.2.15)$$

Detailed calculations (see Stewart [129]) show that the components of the stress and couple stress tensors proposed by Leslie [82] are given by

$$\sigma_{ij} = -p\delta_{ij} - \frac{\partial w_F}{\partial(\partial_j n_p)} \frac{\partial n_p}{\partial x_i} + \tilde{\sigma}_{ij}, \quad (2.2.16)$$

$$l_{ij} = \epsilon_{ipq} n_p \frac{\partial w_F}{\partial(\partial_j n_q)} + \tilde{l}_{ij}, \quad (2.2.17)$$

where p is a pressure resulting from the enforced incompressibility, δ_{ij} is the Kronecker delta [129], $\partial_j n_p \equiv \partial n_p / \partial x_j$, and $\tilde{\sigma}_{ij}$ and \tilde{l}_{ij} are dynamic contributions to the components of the stress tensor and couple stress tensor, respectively. Further calculations shows that the expressions in (2.2.16) and (2.2.17) reduce the rate of work hypothesis to the following result for Δ :

$$\tilde{\sigma}_{ij} \frac{\partial v_i}{\partial x_j} + \tilde{l}_{ij} \frac{\partial w_i}{\partial x_j} - w_i \epsilon_{ijk} \tilde{\sigma}_{kj} = \Delta. \quad (2.2.18)$$

In the Ericksen-Leslie theory, it is assumed that the dynamic contributions to the stress and couple stress depend on the director orientation n_i , the velocity gradients $\partial_j v_i$ and the local angular velocity of the director w_i at any material point and at any instant. Since \tilde{l}_{ij} is assumed not to depend upon the gradients of the local angular velocity of the director $\partial_j w_i$, it follows from the assumption

that Δ is positive semi-definite that $\tilde{l}_{ij} = 0$ because the gradients of the angular velocity, which may be of arbitrary sign, appear in (2.2.18) linearly with \tilde{l}_{ij} . Therefore, (2.2.18) simplifies to

$$\tilde{\sigma}_{ij} \frac{\partial v_i}{\partial x_j} - w_i \epsilon_{ijk} \tilde{\sigma}_{kj} = \Delta. \quad (2.2.19)$$

It can be assumed that the dynamic stress tensor $\tilde{\boldsymbol{\sigma}}$ depends on the co-rotational flux \mathbf{N} instead of the local angular velocity of the director \mathbf{w} [129]. This means that $\tilde{\boldsymbol{\sigma}}$ is assumed to be a function of \mathbf{n} , \mathbf{A} and \mathbf{N} , all of which can easily be shown to be frame-indifferent. The simplest form of $\tilde{\boldsymbol{\sigma}}$ was constructed based on the experiments of Miesowicz [96] and Zwetkoff [160], which suggested that $\tilde{\boldsymbol{\sigma}}$ depends on \mathbf{A} and \mathbf{N} linearly. Detailed calculations (see Stewart [129]) reveal that the components of the dynamic stress tensor $\tilde{\sigma}_{ij}$ can be written as

$$\begin{aligned} \tilde{\sigma}_{ij} = & \alpha_1 n_k A_{kp} n_p n_i n_j + \alpha_2 N_i n_j + \alpha_3 n_i N_j + \alpha_4 A_{ij} \\ & + \alpha_5 n_j A_{ik} n_k + \alpha_6 n_i A_{jk} n_k. \end{aligned} \quad (2.2.20)$$

The coefficients α_i , $i \in \{1, \dots, 6\}$ are known as the Leslie viscous coefficients and will be discussed later in this chapter. From equation (2.2.20), and noting that $\epsilon_{ijk} n_k n_j = 0$ and $\epsilon_{ijk} A_{kj} = 0$ (since both $n_k n_j$ and A_{kj} are symmetric tensors), it follows that $\epsilon_{ijk} \tilde{\sigma}_{kj}$ can be expressed as

$$\begin{aligned} \epsilon_{ijk} \tilde{\sigma}_{kj} &= \epsilon_{ijk} (\alpha_2 N_k n_j + \alpha_3 n_k N_j + \alpha_5 n_j A_{kp} n_p + \alpha_6 n_k A_{jp} n_p) \\ &= \epsilon_{ijk} n_j \tilde{g}_k. \end{aligned} \quad (2.2.21)$$

The vector \tilde{g}_i can be expressed in terms of the viscosities γ_1 and γ_2 such that

$$\tilde{g}_i = -\gamma_1 N_i - \gamma_2 A_{ip} n_p, \quad (2.2.22)$$

$$\gamma_1 = \alpha_3 - \alpha_2, \quad (2.2.23)$$

$$\gamma_2 = \alpha_6 - \alpha_5. \quad (2.2.24)$$

It is possible to write $\tilde{\boldsymbol{\sigma}}$ in terms of Δ as follows. First, the local angular velocity of the liquid crystal director \mathbf{w} can be expressed in terms of two angular velocities: a regional angular velocity $\hat{\mathbf{w}} = (\nabla \times \mathbf{v})/2$, which measures the average rotation of the liquid crystal over a neighbourhood of the material element, and a

relative angular velocity $\boldsymbol{\omega}$ which measures the difference between \mathbf{w} and $\widehat{\mathbf{w}}$ [129]. Therefore, the relation between these three angular velocities is $\boldsymbol{\omega} = \mathbf{w} - \widehat{\mathbf{w}}$. The definitions of the co-rotational time flux (2.2.12) and material time derivative of the director $D\mathbf{n}/Dt$ can be re-written as $\mathbf{N} = \boldsymbol{\omega} \times \mathbf{n}$ and $D\mathbf{n}/Dt = \mathbf{w} \times \mathbf{n}$, respectively. From these definitions and equation (2.2.21), it can be shown that the left hand side of (2.2.19) is given by

$$\tilde{\sigma}_{ij} \frac{\partial v_i}{\partial x_j} - w_i \epsilon_{ijk} \tilde{\sigma}_{kj} = \tilde{\sigma}_{ij} A_{ij} - N_i \tilde{g}_i = \Delta. \quad (2.2.25)$$

From (2.2.20) and (2.2.22), the expression for Δ is given by

$$\begin{aligned} \Delta = & \alpha_1 (n_i A_{ij} n_j)^2 + (\alpha_2 + \alpha_3 + \gamma_2) N_i A_{ij} n_j \\ & + \alpha_4 A_{ij} A_{ij} + (\alpha_5 + \alpha_6) n_i A_{ij} A_{jk} n_k + \gamma_1 N_i N_i. \end{aligned} \quad (2.2.26)$$

The components of \tilde{g}_i and $\tilde{\sigma}_{ij}$ can be obtained from (2.2.26) via [83]

$$\tilde{g}_i = -\frac{1}{2} \frac{\partial \Delta}{\partial \dot{n}_i}, \quad \tilde{\sigma}_{ij} = \frac{1}{2} \frac{\partial \Delta}{\partial (\partial_j v_i)}. \quad (2.2.27)$$

The superposed dot in (2.2.27) is used as a shorthand representation of the material time derivative (2.2.6). It is common to write $\Delta(A_{ij}, N_i, n_i)$ in terms of a (Rayleigh) dissipation function \mathcal{D} which depends the velocity gradient $\partial_j v_i$ and the angles θ_α ($\alpha = 1, 2$) using [83, 129]

$$\Delta(A_{ij}, N_i, n_i) = 2\mathcal{D}\left(\frac{\partial v_i}{\partial x_j}, \theta_\alpha, \theta_\alpha\right). \quad (2.2.28)$$

In the Ericksen-Leslie theory, the dissipation function is given by

$$\begin{aligned} \mathcal{D} = & \frac{1}{2} \left(\alpha_1 (n_i A_{ij} n_j)^2 + (\alpha_2 + \alpha_3 + \gamma_2) N_i A_{ij} n_j + \alpha_4 A_{ij} A_{ij} \right. \\ & \left. + (\alpha_5 + \alpha_6) n_i A_{ij} A_{jk} n_k + \gamma_1 N_i N_i \right). \end{aligned} \quad (2.2.29)$$

In order to account for effects due to activity in liquid crystals, we include additional terms in the Ericksen-Leslie equations. One possible form of an activity term which has frequently been used in the theoretical modelling of active nematic liquid crystals was first introduced by Simha and Ramaswamy [123], and is given by equation (1.2.4), restated here in component form,

$$\sigma_{ij}^\zeta = \zeta n_i n_j. \quad (2.2.30)$$

A stress term of the same form as (2.2.30) was considered as part of the continuum theory for anisotropic fluids in 1960 by Ericksen [43] and in 1966 by Leslie [80]. In 1968, Leslie [81] used the Clausius-Duhem inequality to deduce that in order for liquid crystals to satisfy the thermodynamic argument that dissipation must be positive semi-definite, the coefficient of $n_i n_j$ must equal zero. In this thesis, we adapt the Ericksen-Leslie equations by including (2.2.30) as a source of stress due to activity.

2.2.1 Ericksen-Leslie Equations for an Active Nematic Liquid Crystal

We now provide a summary of the Ericksen-Leslie equations for an active nematic liquid crystal. The equations considered here are an adapted version of those derived by Leslie [82, 83] for an inactive nematic liquid crystal. The conservation of mass is

$$\frac{\partial v_i}{\partial x_j} = 0. \quad (2.2.31)$$

The balance of angular momentum is governed by the two equations

$$\frac{\partial}{\partial x_i} \left(\frac{\partial w_F}{\partial (\partial_i \theta_\alpha)} \right) - \frac{\partial w_F}{\partial \theta_\alpha} - \frac{\partial \mathcal{D}}{\partial \dot{\theta}_\alpha} = 0 \quad (\alpha = 1, 2). \quad (2.2.32)$$

Finally, the balance of linear momentum with the additional active stress term (2.2.30) is given by

$$\rho \frac{Dv_i}{Dt} = \frac{\partial}{\partial x_j} \left(\frac{\partial \mathcal{D}}{\partial (\partial_j v_i)} + \zeta n_i n_j \right) - \frac{\partial \mathcal{D}}{\partial \dot{\theta}_\alpha} \frac{\partial \theta_\alpha}{\partial x_i} - \frac{\partial \tilde{p}}{\partial x_i} \quad (i = 1, 2, 3), \quad (2.2.33)$$

where \tilde{p} is a modified pressure, defined in terms of the isotropic pressure p and bulk energy density w_F by

$$\tilde{p} = p + w_F. \quad (2.2.34)$$

In order to construct the Ericksen-Leslie equations (2.2.31)–(2.2.33), only the bulk energy density w_F , dissipation function \mathcal{D} and activity strength ζ of the liquid crystal are needed. When the activity strength $\zeta = 0$ in equation (2.2.33), we revert back to the classic Ericksen-Leslie equations for an inactive nematic.

The Ericksen-Leslie equations govern the dynamic behaviour of the nematic liquid crystal but can also be used in the static case. In a static situation, there is no dissipation function or activity and so the Ericksen-Leslie equations reduce to the equations

$$\frac{\partial}{\partial x_i} \left(\frac{\partial w_F}{\partial (\partial_i \theta_\alpha)} \right) - \frac{\partial w_F}{\partial \theta_\alpha} = 0, \quad (2.2.35)$$

which are the Euler-Lagrange equations for minimisation of the bulk energy density w_F with respect to the angles θ_α .

2.2.2 Elastic Energy Density

The free energy W given by (2.2.14) is composed of energy densities in the bulk due to elasticity and external orienting fields (e.g., magnetic field) and a surface energy density. We now discuss each of these energy densities, beginning with the elastic energy density. One of the characteristic features of a nematic liquid crystal is the ability to maintain permanently an internal elasticity due to persistent elastic distortions of the director structure, a property not found in isotropic fluids. Such distortions are usually modelled through an elastic energy density w_{elastic} of the form

$$w_{\text{elastic}} = w_{\text{elastic}}(\mathbf{n}, \nabla \mathbf{n}), \quad (2.2.36)$$

often taken to be quadratic in \mathbf{n} and the gradients of \mathbf{n} , assuming that higher order terms are small in comparison. An elastic energy density of the form given by (2.2.36) originates with the work of Oseen [108] and Zocher [159] in the 1930s, later constructed by Frank [51] in 1958 and is now commonly called the Frank-Oseen elastic energy density. For any relaxed and unforced orientation of the director, $w_{\text{elastic}} = 0$. Any other state or configuration of the nematic liquid crystal yields an elastic energy density which is greater than or equal to that of the relaxed orientation so that

$$w_{\text{elastic}}(\mathbf{n}, \nabla \mathbf{n}) \geq 0. \quad (2.2.37)$$

Given the lack of polarity in nematic liquid crystals, it is required that w_{elastic} remains unchanged under the transformation $\mathbf{n} \rightarrow -\mathbf{n}$, that is,

$$w_{\text{elastic}}(\mathbf{n}, \nabla \mathbf{n}) = w_{\text{elastic}}(-\mathbf{n}, -\nabla \mathbf{n}). \quad (2.2.38)$$

The elastic energy density must also be the same when described in any two reference frames, that is, it must be frame-indifferent. Consequently,

$$w_{\text{elastic}}(\mathbf{n}, \nabla \mathbf{n}) = w_{\text{elastic}}(\mathbf{B}\mathbf{n}, \mathbf{B}\nabla \mathbf{n}\mathbf{B}^T), \quad (2.2.39)$$

where \mathbf{B} is an orthogonal matrix (i.e., $\mathbf{B}\mathbf{B}^T = \mathbf{I}$) and \mathbf{I} is the identity tensor. Using these constraints the Frank-Oseen elastic energy density for nematic liquid crystals can be expressed as (see Stewart [129] for a derivation)

$$\begin{aligned} w_{\text{elastic}} = & \frac{1}{2}K_1(\nabla \cdot \mathbf{n})^2 + \frac{1}{2}K_2(\mathbf{n} \cdot \nabla \times \mathbf{n})^2 + \frac{1}{2}K_3(\mathbf{n} \times \nabla \times \mathbf{n})^2 \\ & + \frac{1}{2}(K_2 + K_4) (\text{tr}((\nabla \mathbf{n})^2) - (\nabla \cdot \mathbf{n})^2), \end{aligned} \quad (2.2.40)$$

where K_1 , K_2 and K_3 are the Frank elastic constants associated with splay, twist and bend distortions of the nematic director, respectively. These elastic constants are typically of the order 10^{-12} N to 10^{-11} N. The combination $K_2 + K_4$ in the elastic energy density (2.2.40) is known as the saddle-splay constant. The associated saddle-splay term can be written in the alternative form

$$\text{tr}((\nabla \mathbf{n})^2) - (\nabla \cdot \mathbf{n})^2 = \nabla \cdot ((\mathbf{n} \cdot \nabla)\mathbf{n} - (\nabla \cdot \mathbf{n})\mathbf{n}), \quad (2.2.41)$$

and is frequently omitted when modelling nematic liquid crystals since, being a divergence term, it may be expressed as a surface energy using the divergence theorem so that it does not contribute to the bulk equilibrium equations. Such a term is known as a null Lagrangian and is examined in greater detail by Virga [142] with an alternative derivation considered by Clark [23]. As part of the hydrostatic theory of inactive nematic liquid crystals, Ericksen [46] derived a set of inequalities that the Frank elastic constants must satisfy in order for the elastic energy density to be positive semi-definite. These are known as the Ericksen inequalities and are given by

$$\begin{aligned} K_1 \geq 0, \quad K_2 \geq 0, \quad K_3 \geq 0, \\ K_2 \geq |K_4|, \quad 2K_1 \geq K_2 + K_4 \geq 0. \end{aligned} \quad (2.2.42)$$

It is sometimes useful to make use of a simplification known as “the one-constant approximation” [20, 129] in which the elastic constants for splay, twist and bend are all equal and with K_4 set equal to zero, that is, $K \equiv K_1 = K_2 = K_3$, $K_4 = 0$. This approximation is particularly useful if analytic progress is to be made, as the elastic energy density (2.2.40) can sometimes lead to a complicated set of equations which can only be solved numerically. With this approximation, the elastic energy density (2.2.40) simplifies to

$$w_{\text{elastic}}(\mathbf{n}, \nabla \mathbf{n}) = \frac{K}{2} \|\nabla \mathbf{n}\|^2 = \frac{K}{2} \left(\text{tr}[(\nabla \mathbf{n})^T (\nabla \mathbf{n})] \right). \quad (2.2.43)$$

2.2.3 Magnetic Energy Density

The application of a magnetic field \mathbf{H} across a sample of liquid crystal induces a magnetisation \mathbf{M} in the liquid crystal due to the magnetic dipole moments imposed upon the molecular alignment by the magnetic field. Assuming a linear dependence upon the field and taking into account nematic symmetries, when \mathbf{H} makes an angle with the director \mathbf{n} the magnetisation is given by

$$\mathbf{M} = \chi_{m_\perp} \mathbf{H} + (\chi_{m_\parallel} - \chi_{m_\perp})(\mathbf{n} \cdot \mathbf{H})\mathbf{n}, \quad (2.2.44)$$

where the coefficients χ_{m_\parallel} and χ_{m_\perp} denote the magnetic susceptibilities parallel and perpendicular to the director, respectively. In most nematic liquid crystals, both of the magnetic susceptibilities are negative dimensionless parameters. The magnetic induction \mathbf{B} is related to the magnetic field and magnetisation by

$$\mathbf{B} = \mu_0(\mathbf{H} + \mathbf{M}), \quad (2.2.45)$$

where $\mu_0 = 4\pi \times 10^{-7} \text{ Hm}^{-1}$ is the permeability of free space. Substituting (2.2.44) into (2.2.45) shows that the director dependent relation between the magnetic induction and magnetic field is

$$\mathbf{B} = \mu_0(1 + \chi_{m_\perp})\mathbf{H} + \mu_0\Delta\chi(\mathbf{n} \cdot \mathbf{H})\mathbf{n}, \quad (2.2.46)$$

where $\Delta\chi = \chi_{m_\parallel} - \chi_{m_\perp}$ is defined as the magnetic anisotropy. This is a dimensionless quantity whose sign influences the preferred orientation of the molecules with

respect to the magnetic field. Specifically, when $\Delta\chi < 0$, the molecules prefer to align perpendicular to the magnetic field, whilst with $\Delta\chi > 0$, the molecules prefer to align parallel to the magnetic field. In most nematic liquid crystals, $\Delta\chi$ is a small and positive parameter, and of order 10^{-6} when described in SI units.

The magnetic energy density w_{magnetic} is calculated via

$$\begin{aligned} w_{\text{magnetic}} &= - \int \mathbf{B} \cdot d\mathbf{H} \\ &= - \int (\mu_0(1 + \chi_{\text{m}\perp})\mathbf{H} + \mu_0\Delta\chi(\mathbf{n} \cdot \mathbf{H})\mathbf{n}) \cdot d\mathbf{H} \\ &= -\frac{1}{2} (\mu_0(1 + \chi_{\text{m}\perp})H^2 + \mu_0\Delta\chi(\mathbf{n} \cdot \mathbf{H})^2). \end{aligned} \quad (2.2.47)$$

Part of the magnetic energy density in (2.2.47) is independent of the orientation of the director, so a more frequently adopted form of the magnetic energy density used in calculations is

$$w_{\text{magnetic}} = -\frac{1}{2}\mu_0\Delta\chi(\mathbf{n} \cdot \mathbf{H})^2. \quad (2.2.48)$$

In general, the magnetic induction \mathbf{B} and magnetic field \mathbf{H} must satisfy the Maxwell equations

$$\nabla \cdot \mathbf{B} = 0, \quad \nabla \times \mathbf{H} = \mathbf{0}. \quad (2.2.49)$$

It is known from experiments that in equilibrium situations, magnetic fields are virtually unaffected by the presence of the liquid crystal since $\Delta\chi$ is small, which leads to

$$\nabla \cdot \mathbf{H} = 0, \quad \nabla \times \mathbf{H} = \mathbf{0}, \quad (2.2.50)$$

and, therefore, \mathbf{H} is constant. We will make use of this approximation in order to examine the reorientation of an active nematic liquid crystal subject to a spatially uniform orienting field. For a discussion on electric fields, we refer the interested reader to Stewart [129].

2.2.4 Surface Energy Density

The influence of a solid boundary on the molecular alignment of a liquid crystal is often characterised through the specification of a surface energy density, w_S .

This surface energy density, often termed weak anchoring energy, is a function of the macroscopic variables, such as the director \mathbf{n} , as well as parameters that measure the strength of interaction between the molecular orientation and the boundary. One of the first models of weak anchoring was proposed by Rapini and Papoular [116], who introduced a weak anchoring surface energy density of the form

$$w_S = \frac{\omega}{2}(\mathbf{n} \cdot \boldsymbol{\nu})^2, \quad (2.2.51)$$

where ω is a constant anchoring strength and $\boldsymbol{\nu}$ is the unit outward normal to the surface. For $\omega > 0$, the weak anchoring energy will prefer a director orientation perpendicular to the unit outward normal, indicating that a homogeneous alignment tangential to the surface will be favoured. When $\omega < 0$, w_S will induce a director alignment parallel to the unit outward normal and the preferred director orientation will be homeotropic (i.e., perpendicular to the boundary surface).

Another possible form of surface anchoring is infinite anchoring. This occurs when the director orientation is fixed at a boundary due to suitable treatment of the boundary [86]. Two examples of infinite anchoring are planar and homeotropic anchoring, where the director has, respectively, a fixed orientation in one direction in the plane of the surface or perpendicular to it. Unlike weak anchoring, infinite anchoring does not require any additional terms in the free energy. In this thesis, we will consider weak surface anchoring with $\omega > 0$, as well as infinite planar anchoring of the director at surface boundaries.

2.2.5 Dissipation

We now discuss the physical interpretation of the viscous coefficients in the dissipation function (2.2.29). In Newtonian isotropic fluids only one viscosity coefficient is present in the stress tensor and is defined in terms of the relationship between stress and shear rate. However, in nematic liquid crystals, there are six Leslie viscosity coefficients, although only five of them are independent since the sixth Leslie viscous coefficient, α_6 , can be written in terms of three Leslie viscosities, that is, $\alpha_6 = \alpha_5 + \alpha_2 + \alpha_3$, as proposed by Parodi [110] via an Onsager relation.

The Leslie viscous coefficients are quite difficult to describe physically, but certain linear combinations of them can be identified experimentally via measurements of the type first proposed by Miesowicz [96, 97]. The measured viscosities are known as the Miesowicz viscosities, which, in terms of the Leslie viscous coefficients are

$$\eta_1 = (\alpha_3 + \alpha_4 + \alpha_6)/2 = (\alpha_2 + 2\alpha_3 + \alpha_4 + \alpha_5)/2, \quad (2.2.52)$$

$$\eta_2 = (\alpha_4 + \alpha_5 - \alpha_2)/2, \quad (2.2.53)$$

$$\eta_3 = \alpha_4/2, \quad (2.2.54)$$

$$\gamma_1 = \alpha_3 - \alpha_2, \quad (2.2.55)$$

$$\gamma_2 = \alpha_6 - \alpha_5 = \alpha_3 + \alpha_2, \quad (2.2.56)$$

$$\eta_{12} = \alpha_1. \quad (2.2.57)$$

The first three of the Miesowicz viscosities can be measured from a simple shear experiment by considering the orientation of the director \mathbf{n} with respect to the velocity \mathbf{v} and the velocity gradient: η_1 when \mathbf{n} is aligned parallel to \mathbf{v} ; η_2 when \mathbf{n} is aligned in the velocity gradient direction; and η_3 when \mathbf{n} is perpendicular to both \mathbf{v} and the velocity gradient direction. The fourth viscosity, γ_1 , is known as the rotational viscosity and determines the relaxation of the director through rotation. The viscosity η_{12} can be measured experimentally when the director is not aligned with an axis [101] and finally, the viscosity γ_2 is commonly referred to as the torsion viscosity and satisfies the relation $\gamma_2 = \eta_1 - \eta_2$. The expressions for the Leslie viscous coefficients in terms of the Miesowicz viscosities are

$$\alpha_1 = \eta_{12}, \quad (2.2.58)$$

$$\alpha_2 = (\eta_1 - \eta_2 - \gamma_1)/2 = (\gamma_2 - \gamma_1)/2, \quad (2.2.59)$$

$$\alpha_3 = (\eta_1 - \eta_2 + \gamma_1)/2 = (\gamma_2 + \gamma_1)/2, \quad (2.2.60)$$

$$\alpha_4 = 2\eta_3, \quad (2.2.61)$$

$$\alpha_5 = (\eta_1 + 3\eta_2 - 4\eta_3 - \gamma_1)/2, \quad (2.2.62)$$

$$\alpha_6 = (3\eta_1 + \eta_2 - 4\eta_3 - \gamma_1)/2. \quad (2.2.63)$$

The signs of the Leslie viscous coefficients α_2 and α_3 are important in understanding the response of the director to a shear. Nematic liquid crystals are

called flow-aligning when $\alpha_2\alpha_3 > 0$ and non-flow aligning, or tumbling, when $\alpha_2\alpha_3 < 0$. In flow-aligning liquid crystals, the velocity gradient aligns the director due to director-shear stress interaction at an angle called the flow-alignment or Leslie angle. The requirement that the dissipation function is positive semi-definite leads to a set of inequalities that the nematic viscosities must satisfy. These inequalities were originally derived by Leslie [80] as part of his continuum theory for anisotropic fluids and are given by

$$\gamma_1 = \alpha_3 - \alpha_2 \geq 0, \quad (2.2.64)$$

$$\alpha_4 \geq 0, \quad (2.2.65)$$

$$2\alpha_4 + \alpha_5 + \alpha_6 \geq 0, \quad (2.2.66)$$

$$2\alpha_1 + 3\alpha_4 + 2\alpha_5 + 2\alpha_6 \geq 0, \quad (2.2.67)$$

$$4\gamma_1(2\alpha_4 + \alpha_5 + \alpha_6) \geq (\gamma_2 + \alpha_3 + \alpha_2)^2. \quad (2.2.68)$$

Details on the derivation of these inequalities are also outlined by Leslie [83] and Stewart [129].

2.2.6 Activity

The influence of activity of the liquid crystal is determined by the magnitude and sign of the activity strength coefficient ζ in the active stress term (2.2.30). The magnitude of ζ quantifies the amount of stress that the active agents exert on the background fluid. The sign of ζ distinguishes how the active agents behave relative to the surrounding fluid, with the agents either pushing the fluid out or pulling the fluid in along the long axis. As discussed in Chapter 1, this simple description of “pushers” and “pullers” to describe active agents is commonly replaced by the terms “extensile” and “contractile”, respectively. A schematic illustration of these two contrasting behaviours for active agents is shown in Figure 2.1. In this description, extensile active nematic liquid crystals are identified by an activity strength parameter $\zeta < 0$, and for contractile nematic liquid crystals $\zeta > 0$, as adopted in, for example, [60, 63, 151, 153]. Note that the opposite sign of the activity parameter has been assumed in a number of publications, with a

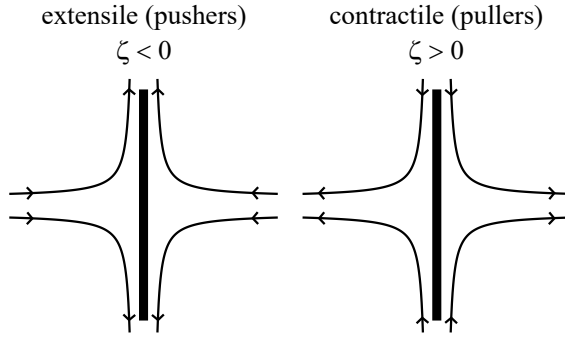


Figure 2.1: A schematic illustration of the flow of extensile and contractile active agents, with arrows indicating the direction of the flow around the long axes of the active agent, indicated by the central thick solid line.

corresponding negative active stress term in (2.2.30) [41, 72, 135, 144]. The form of the active stress term means that distortion in the director can generate a flow within an active system. At first glance, this seems to suggest that there is a similarity in the behaviour between these two active agents. However, as we will see over the course of this thesis, extensile and contractile active nematics can have completely different behaviours in terms of their orientation and flow.

2.2.7 Additional Active Terms

The inclusion of the active stress term (2.2.30) in the Ericksen-Leslie equations is just one of many ways that can be adopted to model active liquid crystals. Another example is an additional term in the stress tensor which models the frictional effect due to the relative motion of the active agents [41, 151, 152, 153],

$$\boldsymbol{\sigma}^\beta = \beta(\nabla \mathbf{n} + (\nabla \mathbf{n})^T), \quad (2.2.69)$$

where β in the above citations is referred to as an “active viscosity”, despite having dimensions of surface tension, and can be positive or negative. This term is derived using an analogy to the viscous stress in isotropic fluids when gradients in the director field is recognised as being analogous to the velocity gradients for the active particles. Another possible model of activity is an additional term which accounts for self-advection in active liquid crystals by adapting the definition of

the material time derivative of the director [12, 41, 136, 137],

$$\frac{\partial \mathbf{n}}{\partial t} + (\mathbf{v} \cdot \nabla) \mathbf{n} \rightarrow \frac{\partial \mathbf{n}}{\partial t} + [(\mathbf{v} + \Omega \mathbf{n}) \cdot \nabla] \mathbf{n}, \quad (2.2.70)$$

where Ω is the swimming speed relative to the bulk fluid, which, like the coefficient β , can also be positive or negative. Such a term is incorporated due to the tendency of some active agents to swim along the direction of their orientation. Neither the active stress term (2.2.69) or the self-propelling speed term (2.2.70) satisfy the symmetry between \mathbf{n} and $-\mathbf{n}$, and so cannot be used to model the flows of apolar active nematic liquid crystals. They can, however, be used in the mathematical modelling of active polar liquid crystals where the nematic director \mathbf{n} is replaced by a polar vector field \mathbf{p} for which \mathbf{p} and $-\mathbf{p}$ are no longer indistinguishable. As we will only be considering apolar active nematic liquid crystals, it follows that the two active terms considered in this subsection are beyond the scope of the work presented in this thesis.

2.2.8 Boundary Conditions

We conclude our review of the Ericksen-Leslie theory with a summary of different possible boundary conditions for the velocity and director. The classical no-slip and no-penetration boundary conditions are usually considered for the velocity, that is, $\mathbf{v} = \mathbf{0}$ on the boundaries. This is the only boundary condition for the velocity we consider in this thesis, although other examples for active liquid crystals are considered in [144]. We consider two possible boundary conditions for the director alignment in this thesis - infinite anchoring and weak surface anchoring. The former is modelled by a Dirichlet boundary condition in which the director orientation is fixed to a substrate. The equilibrium boundary conditions for weak anchoring are derived from calculus of variations and are given by [68]

$$\nu_i \frac{\partial w_F}{\partial (\partial_i \theta_\alpha)} + \frac{\partial w_S}{\partial \theta_\alpha} = 0. \quad (2.2.71)$$

Dynamic versions of the boundary conditions (2.2.71) include a surface viscosity for the motion of the director near a solid boundary [69], although these are not considered in this thesis.

2.3 Q-Tensor Theory

Despite being the first widely accepted dynamic theory of nematic liquid crystals, the Ericksen-Leslie theory does have limitations. One such difficulty occurs when modelling liquid crystals which contain defects. The Frank-Oseen version of the elastic energy density leads to unphysical results for the free energy when modelling liquid crystals which contain defects. Specifically, the free energy can be shown to diverge logarithmically around defects [56]. As we have already discussed in Chapter 1, defects are important not just in inactive liquid crystals, but also in active liquid crystalline systems. It follows, therefore, that if we want to examine active liquid crystals containing defects using a continuum theory approach, then we first need to introduce a continuum theory of liquid crystals which can be used for modelling defects. One such continuum theory of liquid crystals is the **Q**-tensor theory. In this section, we first introduce some of the basic properties of the **Q**-tensor, before then examining an adapted version of the dynamic equations which will be used in this thesis for modelling active nematic liquid crystals.

A **Q**-tensor is defined as the traceless part of the second moment of the probability distribution function discussed in Chapter 1, and contains information about the average molecular axes orientations as well as the ordering about these axes. The **Q**-tensor is, therefore, a second rank symmetric traceless 3×3 matrix. It can be written in terms of three eigenvalues S_i ($i = 1, 2, 3$) satisfying $S_1 + S_2 + S_3 = 0$, and an orthonormal basis of three perpendicular eigenvectors (i.e., nematic directors \mathbf{n}_i),

$$\mathbf{Q} = S_1(\mathbf{n}_1 \otimes \mathbf{n}_1) + S_2(\mathbf{n}_2 \otimes \mathbf{n}_2) + S_3(\mathbf{n}_3 \otimes \mathbf{n}_3). \quad (2.3.1)$$

The eigenvalues of physical **Q**-tensors are subject to the inequalities $-1/3 < S_i < 2/3$ [90, 105]. Since each of the eigenvectors \mathbf{n}_i are unit vectors, it follows that the condition

$$\mathbf{n}_1 \otimes \mathbf{n}_1 + \mathbf{n}_2 \otimes \mathbf{n}_2 + \mathbf{n}_3 \otimes \mathbf{n}_3 = \mathbf{I}, \quad (2.3.2)$$

must also be satisfied. The representation of the **Q**-tensor given by (2.3.1) al-

lows for the categorisation of three different configurations, depending on the eigenvalues. One possible configuration is the isotropic phase for which the three eigenvalues S_i are equal to zero and there is no orientational ordering, therefore $\mathbf{Q}=\mathbf{0}$. When two of the eigenvalues are equal, then the material is in the uniaxial nematic phase. For example, if we assume that $S_2 = S_3 = -S/3$, so that $S_1 = 2S/3$, then (2.3.1) simplifies to

$$\mathbf{Q} = S \left(\mathbf{n} \otimes \mathbf{n} - \frac{1}{3} \mathbf{I} \right). \quad (2.3.3)$$

where we have set $\mathbf{n}_1 = \mathbf{n}$ in (2.3.3). Equation (2.3.3) is the standard form of a second-rank tensor of a uniaxial nematic liquid crystal [105, 127], where S is a scalar order parameter. As mentioned in Chapter 1, S determines the degree of orientation. The third possible configuration occurs when the three eigenvalues of \mathbf{Q} are all distinct, which corresponds to biaxial ordering in the nematic phase. We will not consider biaxial ordering in this thesis and refer the interested reader to references [84, 103, 128].

By use of (2.3.3), a continuum theory for uniaxial nematic liquid crystals with variable degree of order is obtained naturally as a special case of a theory for the full second-rank alignment tensor [128]. In this thesis, we treat the director \mathbf{n} and scalar order parameter S as two independent variables instead of a single alignment tensor \mathbf{Q} , as done in Sonnet and Virga [127]. In this way we can relate the results for the \mathbf{Q} -tensor model of active nematic liquid crystals to those in the adapted Ericksen-Leslie model. In this type of model of liquid crystals, defects can be modelled by assuming that $S = 0$ where \mathbf{n} is undefined. Since the scalar order parameter S is permitted to vanish at the defects, the free energy remains finite. This model was proposed by Ericksen in 1991 [48] as part of his continuum theory for nematic liquid crystals with variable degree of orientation in order to overcome the infinite energies that can occur when modelling defects with the Frank–Oseen version of the elastic energy density.

2.3.1 Dynamic Equations for Uniaxial Active Nematic Liquid Crystals With Variable Scalar Order Parameter

The derivation of the dynamic equations for a uniaxial nematic liquid crystal with variable degree of orientation can be found in Sonnet and Virga [127]. Using a similar approach to that used for the Ericksen-Leslie theory, we adapt these equations by including an additional term in the stress tensor to account for the activity of the fluid. This additional active term is now also expressed in terms a scalar order parameter as well as the nematic director [18, 72, 136],

$$\boldsymbol{\sigma}^\mu = \mu S(\mathbf{n} \otimes \mathbf{n}), \quad (2.3.4)$$

where μ is a spatially homogeneous activity strength parameter. The system of equations in the theory proposed by Sonnet and Virga consists of the incompressibility condition and three coupled partial differential equations for the flow velocity, the director orientation and the scalar order parameter:

$$\nabla \cdot \mathbf{v} = 0, \quad (2.3.5)$$

$$\rho \frac{D\mathbf{v}}{Dt} - \nabla \cdot \boldsymbol{\sigma} = \mathbf{0}, \quad (2.3.6)$$

$$\frac{\partial w}{\partial \mathbf{n}} - \nabla \cdot \left(\frac{\partial w}{\partial \nabla \mathbf{n}} \right) + \frac{\partial \mathcal{D}}{\partial \mathbf{N}} + \delta \mathbf{n} = \mathbf{0}, \quad (2.3.7)$$

$$\frac{\partial w}{\partial S} - \nabla \cdot \left(\frac{\partial w}{\partial \nabla S} \right) + \frac{\partial \mathcal{D}}{\partial \dot{S}} = 0. \quad (2.3.8)$$

In equations (2.3.5)–(2.3.8), ρ is the fluid density, \mathcal{D} is the dissipation function, w is the total bulk energy density, which we consider as composed of elastic and thermotropic energy densities, δ is a Lagrange multiplier included to ensure that \mathbf{n} is a unit vector and, finally, $\boldsymbol{\sigma}$ is the stress tensor, which is composed of the usual inactive terms (i.e., a hydrostatic pressure, elastic stresses and a viscous stress), as well as the active stress (2.3.4), so that

$$\boldsymbol{\sigma} = -p\mathbf{I} - (\nabla \mathbf{n})^T \frac{\partial w}{\partial \nabla \mathbf{n}} - \nabla S \otimes \frac{\partial w}{\partial \nabla S} + \frac{\partial \mathcal{D}}{\partial \nabla \mathbf{v}} + \mu S(\mathbf{n} \otimes \mathbf{n}). \quad (2.3.9)$$

In the following subsections, we will discuss the energy densities, dissipation function and activity for this theory of liquid crystals.

2.3.2 Elastic Energy Density

An elastic energy is induced by distortion of the \mathbf{Q} -tensor in space. Similar to the Frank-Oseen description in terms of a nematic director, any spatial gradients in \mathbf{Q} will lead to an increase in the elastic energy. The general form of the elastic energy for a uniaxial nematic liquid crystal often used in \mathbf{Q} -tensor theory [103] is given by

$$w_F = \frac{L_1}{2} \left(\frac{\partial Q_{ij}}{\partial x_k} \right)^2 + \frac{L_2}{2} \frac{\partial Q_{ij}}{\partial x_j} \frac{\partial Q_{ik}}{\partial x_k} + \frac{L_3}{2} \frac{\partial Q_{ik}}{\partial x_j} \frac{\partial Q_{ij}}{\partial x_k} + \frac{L_4}{2} Q_{lk} \frac{\partial Q_{ij}}{\partial x_l} \frac{\partial Q_{ij}}{\partial x_k}, \quad (2.3.10)$$

where L_i ($i = 1, 2, 3, 4$) are elastic coefficients assumed to be spatially homogeneous and temperature independent parameters. The first three terms are quadratic in S , whilst the final term is cubic in S . This is only one of seven possible terms which is cubic in the scalar order parameter and as we will see, is included to allow K_1 to be different to K_3 . In order to compare with the classical Frank-Oseen elastic energy density we may consider the situation when the scalar order parameter, S , in (2.3.3) is constant. Substitution of (2.3.3) into (2.3.10) means that the elastic energy density can be expressed in terms of the director \mathbf{n} and scalar order parameter S as [105]

$$\begin{aligned} w_F = & L_1 S^2 \left[\text{tr}((\nabla \mathbf{n})^2) + (\mathbf{n} \cdot \nabla \times \mathbf{n})^2 + (\mathbf{n} \times \nabla \times \mathbf{n})^2 \right] \\ & + \frac{1}{2} L_2 S^2 \left[(\nabla \cdot \mathbf{n})^2 + (\mathbf{n} \times \nabla \times \mathbf{n})^2 \right] \\ & + \frac{1}{2} L_3 S^2 \left[(\mathbf{n} \times \nabla \times \mathbf{n})^2 + \text{tr}((\nabla \mathbf{n})^2) \right] \\ & + \frac{1}{3} L_4 S^3 \left[2(\mathbf{n} \times \nabla \times \mathbf{n})^2 - \text{tr}((\nabla \mathbf{n})^2) - (\mathbf{n} \cdot \nabla \times \mathbf{n})^2 \right]. \end{aligned} \quad (2.3.11)$$

When we have a variable scalar order parameter, then the elastic energy density becomes a function $w_F = w_F(\mathbf{n}, \nabla \mathbf{n}, S, \nabla S)$, that is, (2.3.11) would include terms due to gradients in S . If we compare (2.3.11) with the elastic energy density in the Ericksen-Leslie theory (2.2.40), we see the same terms due to distortion in the director. In the Ericksen-Leslie theory, the elastic coefficients K_i in the Frank-Oseen elastic energy density (2.2.40) are constant parameters, measured at a single value of temperature and therefore, do not vary spatially. In reality, each of the elastic coefficients is a scalar order parameter dependent function, which

can vary for different degrees of orientation. A comparison of the coefficients means that each of the Frank elastic coefficients can be expressed as functions of the spatially homogeneous elastic coefficients L_i and the scalar order parameter S . The calculations which determine expressions for each K_i in terms of L_i and S are not reproduced here but can be found in [105] where it is shown that the S -dependent Frank elastic coefficients $K_i(S)$ are

$$K_1(S) = (2L_1 + L_2 + L_3)S^2 - \frac{2}{3}L_4S^3, \quad (2.3.12)$$

$$K_2(S) = 2L_1S^2 - \frac{2}{3}L_4S^3, \quad (2.3.13)$$

$$K_3(S) = (2L_1 + L_2 + L_3)S^2 + \frac{4}{3}L_4S^3, \quad (2.3.14)$$

$$K_4(S) = L_3S^2. \quad (2.3.15)$$

These expressions have also been derived by Ball [6]. As mentioned earlier, the final term in the elastic energy density (2.3.11) is one of seven possible terms that are linear in \mathbf{Q} and quadratic in $\nabla\mathbf{Q}$ and as mentioned earlier, allows for the S -dependent splay and bend elastic coefficients to be differentiated, as these two are the same up to order S^2 . The remaining six terms can be found in Ericksen [48], where it is asserted that these seven terms are connected by a linear relation. The values of each L_i can therefore be determined by considering experimental measurements of the Frank elastic constants and scalar order parameter at a particular temperature. At the chosen temperature, the uniaxial scalar order parameter takes a constant value which we define by $S = \bar{S}$, with experimentally measured Frank elastic coefficients \bar{K}_i . The relations (2.3.12)–(2.3.15) can then be rearranged to calculate each L_i in terms of \bar{K}_i and \bar{S} ,

$$L_1 = \frac{\bar{K}_3 - \bar{K}_1 + 3\bar{K}_2}{6\bar{S}^2}, \quad (2.3.16)$$

$$L_2 = \frac{\bar{K}_1 - \bar{K}_2 - \bar{K}_4}{\bar{S}^2}, \quad (2.3.17)$$

$$L_3 = \frac{\bar{K}_4}{\bar{S}^2}, \quad (2.3.18)$$

$$L_4 = \frac{\bar{K}_3 - \bar{K}_1}{2\bar{S}^3}. \quad (2.3.19)$$

2.3.3 Thermotropic Energy Density

In the Ericksen-Leslie theory, it is assumed that the material is deep in the nematic phase, and so potential phase transitions such as the nematic to isotropic phase transition are not considered. Such transitions are connected with changes in the ordering of a system induced by varying the temperature. In order to account for possible phase transitions in liquid crystals, an additional contribution to the free energy density is necessary. In the \mathbf{Q} -tensor theory, phase transitions are introduced via a thermotropic energy density, w_T , which determines the preferred state of the material at a particular temperature. At high temperatures this potential function should have a minimum energy in the isotropic state. As the temperature reduces, the nematic state will eventually become the energetically preferred state. One form of w_T that is commonly adopted is given by

$$w_T = a \text{tr}(\mathbf{Q}^2) + \frac{2b}{3} \text{tr}(\mathbf{Q}^3) + \frac{c}{2} (\text{tr}(\mathbf{Q}^2))^2, \quad (2.3.20)$$

where a is a temperature dependent coefficient, $a = \alpha(T - T^*) \equiv \alpha\Delta T$, with $\alpha > 0$ and T^* defined as the temperature at which the isotropic state becomes unstable [103]. In contrast to a , the coefficients b and c are commonly assumed to be independent of temperature with $b < 0$ and $c > 0$. Each of the coefficients a , b and c is typically of order 10^6 Nm^{-2} [103]. For uniaxial nematic liquid crystals, (2.3.20) becomes

$$w_T = \frac{2a}{3} S^2 + \frac{4b}{27} S^3 + \frac{2c}{9} S^4. \quad (2.3.21)$$

Minimisation of the thermotropic energy density (2.3.21) leads to equilibrium values of the scalar order parameter S in terms of the coefficients a , b and c , which are then subsequently used to determine the critical temperatures at which phase transitions occur and stability conditions for each phase (see Mottram and Newton [103]). The thermotropic energy density (2.3.20) is constructed using a Taylor series expansion of a potential function close to the point $\mathbf{Q} = \mathbf{0}$, meaning that \mathbf{Q} -tensor theory is only really valid close to the nematic-isotropic transition temperature, where $\mathbf{Q} \approx \mathbf{0}$. It is for this reason that higher order powers of \mathbf{Q} are not considered in in (2.3.20).

2.3.4 Dissipation

The dynamic behaviour of uniaxial nematic liquid crystals in the \mathbf{Q} -tensor theory is derived from a dissipation principle in which the change in internal energy within the system is balanced by the dissipation. Sonnet and Virga [128] use symmetry arguments to construct the appropriate dissipation function for a nematic liquid crystal with variable degree of orientation. The dissipation function for a uniaxial nematic liquid crystal is

$$\begin{aligned} \mathcal{D} = & \frac{1}{2}\xi_1\text{tr}(\overset{\circ}{\mathbf{Q}}^2) + \xi_2\text{tr}(\mathbf{A}\overset{\circ}{\mathbf{Q}}) + \xi_3\text{tr}(\mathbf{A}\overset{\circ}{\mathbf{Q}}\mathbf{Q}) + \frac{1}{2}\xi_4\text{tr}(\mathbf{A}^2\mathbf{Q}) \\ & + \frac{1}{2}\xi_5\text{tr}(\mathbf{A}^2\mathbf{Q}^2) + \frac{1}{2}\xi_6(\text{tr}(\mathbf{A}\mathbf{Q}))^2 + \frac{1}{2}\xi_7\text{tr}(\mathbf{A}^2)\text{tr}(\mathbf{Q}^2) + \frac{1}{2}\xi_8\text{tr}(\mathbf{A}^2), \end{aligned} \quad (2.3.22)$$

where the ξ_i 's are spatially homogeneous viscosity coefficients, $\overset{\circ}{\mathbf{Q}} = \dot{\mathbf{Q}} - \mathbf{W}\mathbf{Q} + \mathbf{Q}\mathbf{W}$ is the co-rotational derivative of the \mathbf{Q} -tensor and $\dot{\mathbf{Q}}$ is the material time derivative of \mathbf{Q} . As pointed out by Sonnet and Virga [126, 128], in order to compare (2.3.22) with the dissipation function in the Ericksen-Leslie theory, the viscosities ξ_3 , ξ_5 and ξ_7 can be neglected from (2.3.22) as they only contribute corrections of order S^2 in \mathcal{D} . As in Subsection 2.3.2, in order to compare to the classic Ericksen-Leslie theory, we consider the case in which the scalar order parameter is constant. When the viscosities ξ_3 , ξ_5 and ξ_7 are set equal to zero and S is constant, (2.3.22) can be rewritten in the familiar form of the dissipation function used in the Ericksen-Leslie theory and, therefore, [126, 127],

$$\begin{aligned} \mathcal{D} = & \xi_1 S^2 \mathbf{N}^2 + 2\xi_2 S (\mathbf{N} \cdot \mathbf{A}\mathbf{n}) + \frac{1}{2}\xi_4 S (\mathbf{A}\mathbf{n})^2 + \frac{1}{2}\xi_6 S^2 (\mathbf{n} \cdot \mathbf{A}\mathbf{n})^2 \\ & + \frac{1}{2} \left(\xi_8 - \frac{1}{3}\xi_4 S \right) \text{tr}(\mathbf{A}^2). \end{aligned} \quad (2.3.23)$$

The coefficient of each term in the dissipation function (2.3.23) can be compared with that in the Ericksen-Leslie theory in order to determine how the Miesowicz viscosities depend on the scalar order parameter S , as well as the constant

parameters ξ_i . We find that the S -dependent Miesowicz viscosities are

$$\eta_1(S) = \frac{1}{2}\xi_1 S^2 + \xi_2 S + \frac{1}{12}\xi_4 S + \frac{1}{2}\xi_8, \quad (2.3.24)$$

$$\eta_2(S) = \frac{1}{2}\xi_1 S^2 - \xi_2 S + \frac{1}{12}\xi_4 S + \frac{1}{2}\xi_8, \quad (2.3.25)$$

$$\eta_3(S) = \frac{1}{2}\xi_8 - \frac{1}{6}\xi_4 S, \quad (2.3.26)$$

$$\gamma_1(S) = 2\xi_1 S^2, \quad (2.3.27)$$

$$\gamma_2(S) = 2\xi_2 S, \quad (2.3.28)$$

$$\eta_{12}(S) = \xi_6 S^2. \quad (2.3.29)$$

The viscous coefficients ξ_i can be determined by an experimental measurement of the S -dependent nematic viscosities $\eta_i(S)$, $\gamma_i(S)$ and the scalar order parameter S . We define these experimentally measured parameters by $\bar{\eta}_i$, $\bar{\gamma}_i$ and \bar{S} . The relations (2.3.24)–(2.3.29) can then be rearranged to calculate ξ_i ,

$$\xi_1 = \frac{\bar{\gamma}_1}{2\bar{S}^2}, \quad (2.3.30)$$

$$\xi_2 = \frac{\bar{\gamma}_2}{2\bar{S}}, \quad (2.3.31)$$

$$\xi_4 = \frac{2\bar{\eta}_1 + 2\bar{\eta}_2 - 4\bar{\eta}_3 - \bar{\gamma}_1}{\bar{S}}, \quad (2.3.32)$$

$$\xi_6 = \frac{\bar{\eta}_{12}}{\bar{S}^2}, \quad (2.3.33)$$

$$\xi_8 = \frac{2(\bar{\eta}_1 + \bar{\eta}_2 + \bar{\eta}_3) - \bar{\gamma}_1}{3}. \quad (2.3.34)$$

For the sake of completeness, we also provide the expressions for the S -dependent Leslie viscous coefficients $\alpha_i(S)$ in terms of the homogeneous coefficients ξ_i and scalar order parameter S ,

$$\alpha_1(S) = \xi_6 S^2, \quad (2.3.35)$$

$$\alpha_2(S) = \xi_2 S - \xi_1 S^2, \quad (2.3.36)$$

$$\alpha_3(S) = \xi_2 S + \xi_1 S^2, \quad (2.3.37)$$

$$\alpha_4(S) = \xi_8 - \frac{1}{3}\xi_4 S, \quad (2.3.38)$$

$$\alpha_5(S) = \frac{1}{2}\xi_4 S - \xi_2 S, \quad (2.3.39)$$

$$\alpha_6(S) = \frac{1}{2}\xi_4 S + \xi_2 S. \quad (2.3.40)$$

In terms of the experimentally measured Leslie coefficients parameters $\bar{\alpha}_i$ and scalar order parameter \bar{S} , the coefficients ξ_i are given by

$$\xi_1 = \frac{\bar{\alpha}_3 - \bar{\alpha}_2}{2\bar{S}^2}, \quad (2.3.41)$$

$$\xi_2 = \frac{\bar{\alpha}_3 + \bar{\alpha}_2}{2\bar{S}}, \quad (2.3.42)$$

$$\xi_4 = \frac{\bar{\alpha}_6 + \bar{\alpha}_5}{\bar{S}}, \quad (2.3.43)$$

$$\xi_6 = \frac{\bar{\alpha}_1}{\bar{S}^2}, \quad (2.3.44)$$

$$\xi_8 = \frac{\bar{\alpha}_6 + \bar{\alpha}_5 + 3\bar{\alpha}_4}{3}. \quad (2.3.45)$$

When we have a variable scalar order parameter, the dissipation function (2.3.23) is extended to include additional terms due to changes in S . The form of the dissipation which includes changes in S has been constructed by Ericksen [48], as well as Sonnet and Virga [127],

$$\begin{aligned} \mathcal{D} = \frac{1}{2} \left(\gamma_1(S)\mathbf{N}^2 + 2\gamma_2(S)\mathbf{N} \cdot \mathbf{An} + \alpha_4(S)\text{tr}(\mathbf{A}^2) + (\alpha_5(S) + \alpha_6(S))(\mathbf{An})^2 \right. \\ \left. + \alpha_1(S)(\mathbf{n} \cdot \mathbf{An})^2 + \beta_2(S)\dot{S}^2 \right) + \beta_1(S)\dot{S}\mathbf{n} \cdot \mathbf{An}, \end{aligned} \quad (2.3.46)$$

where $\beta_1(S)$ and $\beta_2(S)$ are additional scalar order parameter dependent viscosities that are included due to dynamic changes in the scalar order parameter. Since S is a scalar, its material time derivative \dot{S} is frame-indifferent. Equation (2.3.46) represents a function which is quadratic in \mathbf{A} , \mathbf{N} and \dot{S} , and is the same as that given by (2.3.22) when the coefficients ξ_3, ξ_5 and ξ_7 in (2.3.22) are set equal to zero. When the scalar order parameter is constant (i.e., $\dot{S} = 0$ and $\nabla S = \mathbf{0}$), and from the Parodi relation (2.2.56), it is clear that (2.3.46) simplifies to exactly the same dissipation function used in the adapted Ericksen-Leslie theory (2.2.29).

2.3.5 Activity

For this model of uniaxial active nematic liquid crystals, the influence of activity is governed by the active stress tensor (2.3.4), where μ is a spatially homogeneous activity strength parameter. Following the same approach used for the elastic energy density and dissipation function, we can compare (2.3.4) with the

corresponding active stress tensor used in the adapted Ericksen-Leslie theory (i.e., equation (2.2.30)) in order to determine how ζ depends on S and μ . Comparing (2.2.30) and (2.3.4) reveals that the S -dependent activity strength $\zeta(S)$ is defined in terms of the homogenous activity strength μ as

$$\zeta(S) = \mu S. \quad (2.3.47)$$

We can then determine μ by experimental measurement of $\zeta(S)$ and S . These experimental values are defined by $\bar{\zeta}$ and \bar{S} , where we find that

$$\mu = \frac{\bar{\zeta}}{\bar{S}}. \quad (2.3.48)$$

We will only consider positive scalar order parameter values so that the sign of the spatially homogenous activity strength parameter μ and the corresponding type of active agent in this \mathbf{Q} -tensor model is consistent with that in the Ericksen-Leslie model. That is, $\mu < 0$ corresponds to extensile active agents, whereas contractile active agents are characterised by activity strength $\mu > 0$.

2.4 Summary

In this chapter, we have introduced adapted versions of continuum theories of nematic liquid crystals which will be employed throughout this thesis to model the active nematic phase. In Chapter 3, we use the equilibrium Euler-Lagrange equations to investigate static director structures of inactive nematic liquid crystals confined in rectangular regions. In Chapter 4, we employ the adapted Ericksen-Leslie theory to model an active nematic liquid crystal confined in a shallow channel. In Chapter 5, the \mathbf{Q} -tensor model of active nematic liquid crystal will be used to examine a uniaxial active nematic confined in the same shallow channel as in Chapter 4. Finally, we use the adapted Ericksen-Leslie theory in Chapter 6 in order to model active nematic liquid crystals confined in two-dimensional geometries.

Chapter 3

Nematic Liquid Crystal Director Structures in Rectangular Regions

3.1 Introduction

Interest in the confinement of liquid crystals between solid boundaries originally came about through necessity, since viewing a liquid crystal under a microscope was only possible if the material was held in place by at least one solid boundary. Later it became clear that the competition between the orientational influence of a solid boundary and the role of internal effects (such as elasticity) or external effects (e.g., an applied electric field) could lead to interesting behaviour of both scientific and technological interest. In fact, in liquid crystal display devices, the bounding surface plays a crucial role in the optical switching [150]. Here we consider an inactive nematic in a confined region as the precursor to a study of a confined active nematic.

Confinement of a liquid crystal in shallow rectangular wells has been studied by a number of authors in recent years because it offers the possibility of multiple stable director configurations [155]. The relative stability of these different director structures and the mechanisms through which the system switches

between different states is of particular interest if low-power electro-optic devices are to be developed [8]. This was the motivation behind the work of Tsakonas *et al.* [140], where a device consisting of an array of shallow rectangular wells was considered experimentally and theoretically. In their theoretical work, where the director was assumed to stay within a single plane, a two-dimensional analysis was effective in modelling director configurations observed experimentally. The \mathbf{Q} -tensor modelling of [140] imposed infinite planar anchoring of the nematic director on the boundaries of the wells (where the preferred director orientation is tangential to the boundaries) and predicted multistable configurations of the director exhibiting defects at the corners of the wells. Their work has subsequently led a number of researchers to consider similar geometries of confined nematics. Luo *et al.* [87] extend the analysis of [140] to incorporate surface energies and a degree of weak anchoring, still within the context of \mathbf{Q} -tensor, or Landau-de Gennes, theory. They also propose a dynamic model for switching between equilibrium director states based on dielectric effects. Kusumaatmaja and Majumdar [77] model the same device as [87] with a surface energy potential, computing minimum energy pathways between the stable equilibria for variable surface anchoring strength. Landau-de Gennes theory is also employed by Kralj and Majumdar [74], Canevari *et al.* [17] and Slavinec *et al.* [124] in studies which allowed for biaxial order reconstruction. Other work modelling confined liquid crystal systems include using Monte Carlo techniques [21, 55], while Davidson and Mottram [34] derive the director orientation in a variety of geometries via conformal mappings. Studies of confined regions have not been restricted to planar (or near-planar) surface anchoring. For example, Zheng and Hu [157, 158] examine models for polydimethylsiloxane micro-channels where the liquid crystal molecules exhibit homeotropic ordering on boundary surfaces, so that the preferred director orientation is perpendicular to the boundaries.

In recent work on nematics in a rectangular geometry, Lewis *et al.* [86] examined a director model of equilibria in a well when the liquid crystal is subject to fixed planar alignment on the four sides. Their theoretical model recovered the director structures found experimentally and theoretically in [140], where the

infinite anchoring boundary conditions considered in [86] forced the liquid crystal to adopt diagonal or rotated director structures in the bulk of the cell, as shown in Figure 3.1 for a square well. The notation used in [86] to describe each nematic state is D for the diagonal state and $U_{1,2}$ for the two rotated states where the director rotates by π radians across the well in the horizontal (U_1) and vertical (U_2) directions. The director angle θ measures the rotation of the director with respect to the positive, horizontal direction. For this case of infinite anchoring, each state is characterised by the choice of director angle on the four boundaries σ_i ($i = 1, 2, 3, 4$), as indicated in Figure 3.1. The approach of Lewis *et al.* [86] was to introduce four fixed boundary director angles, the values of which, for each of the states in Figure 3.1, are shown in Table 3.1.

However, in this situation difficulties arise because of incompatible director angles on adjacent boundaries, leading to defects at each corner for which a director-based model breaks down as the free energy diverges logarithmically around such points [56]. By making use of the one-constant approximation for the elastic constants, energy minimisation leads to a requirement that the director angle θ satisfies Laplace's equation in the domain $\Gamma = \{(x, y) \in [0, 1] \times [0, \lambda]\}$, where λ is the aspect ratio. This equation was solved subject to the Dirichlet boundary conditions $\theta = \Theta_i$, ($i = 1, 2, 3, 4$) on each boundary, using the method of separation of variables. The solution for the director angle, which we denote by θ_{Lewis} , is expressed as a Fourier series in terms of a function $\Phi(X, Y, \Lambda)$ and the angles Θ_i ,

$$\begin{aligned} \theta_{\text{Lewis}}(x, y, \lambda) = & \Theta_1 \Phi\left(\frac{y}{\lambda}, \frac{1-x}{\lambda}, \frac{1}{\lambda}\right) + \Theta_2 \Phi\left(\frac{y}{\lambda}, \frac{x}{\lambda}, \frac{1}{\lambda}\right) \\ & + \Theta_3 \Phi(x, \lambda - y, \lambda) + \Theta_4 \Phi(x, y, \lambda), \end{aligned} \quad (3.1.1)$$

where

$$\begin{aligned} \Phi(X, Y, \Lambda) = & \sum_{n=0}^{\infty} \frac{4 \sin((2n+1)\pi X)}{(2n+1)\pi} \left[\cosh((2n+1)\pi Y) \right. \\ & \left. - \coth((2n+1)\pi \Lambda) \sinh((2n+1)\pi Y) \right]. \end{aligned} \quad (3.1.2)$$

As mentioned above, the Dirichlet boundary conditions mean that solution (3.1.1) is not valid at the corners and leads to unphysical results for the energy. There-

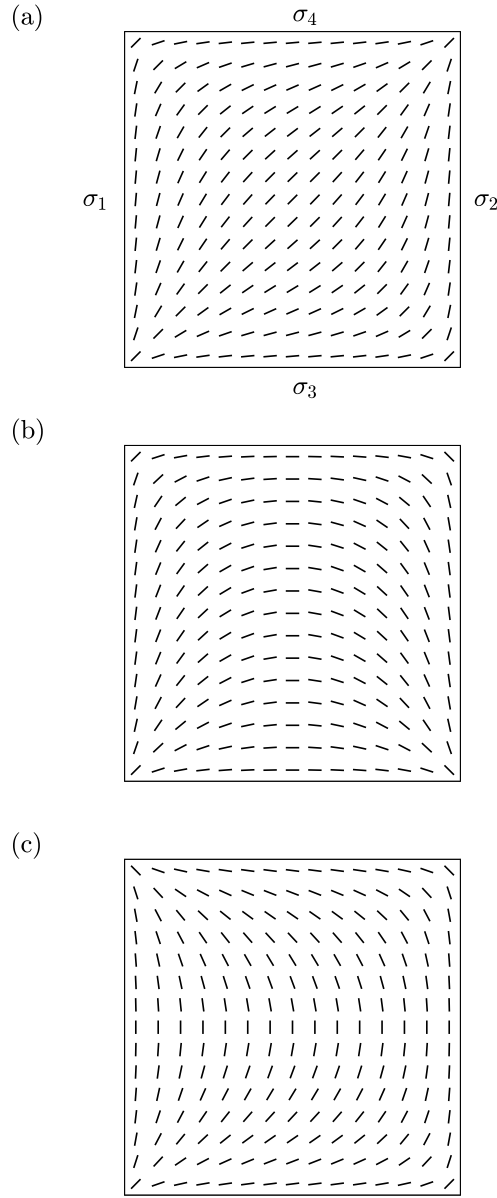


Figure 3.1: (a) The diagonal (D) state, (b) the rotated (U_1) state and (c) the rotated (U_2) state in a square well.

fore, in order to calculate the energy of the system, Lewis *et al.* [86] remove a small disc of radius ϵ around each defect, thought of as a model of a defect core region. An asymptotic analysis of the regularised free energy per unit depth, W_ϵ , then leads to an energy expansion in terms of the defect core radius,

$$W_\epsilon \sim 2\pi \ln \left(\frac{1}{\epsilon} \right) + \tilde{W}(\theta) + O(\epsilon^2), \quad (3.1.3)$$

where $\tilde{W}(\theta)$ changes depending on the equilibrium state under consideration. We

Boundary director angle	D state	U ₁ state	U ₂ state
$\theta = \Theta_1$	$\pi/2$	$\pi/2$	$\pi/2$
$\theta = \Theta_2$	$\pi/2$	$-\pi/2$	$\pi/2$
$\theta = \Theta_3$	0	0	0
$\theta = \Theta_4$	0	0	π

Table 3.1: The infinite anchoring angles Θ_i for each of the states in Figure 3.1.

have mentioned this problem in detail here because we adopt a somewhat similar approach in Section 3.5. In this chapter, we consider a shallow rectangular well of nematic liquid crystal, but instead of imposing infinite planar anchoring on the boundaries of the well, we introduce weak planar anchoring through a Rapini-Papoular surface energy. This approach allows us to carry out an analysis of the director configuration equilibria in the well without the need to exclude point defects at the corners of the rectangle, in other words, avoiding the problems faced in [86]. We are able to derive analytic expressions for the director alignment angle, written as an infinite series involving roots of a transcendental equation, finding a critical anchoring strength at which a uniform director configuration exchanges stability with a distorted structure. Using the analytic form for the director orientation, we are then able to examine the asymptotic behaviour of our system both close to the critical anchoring strength and in the limit of infinite anchoring. The latter analysis allows a comparison with the results of previous work in this area. We also show that the asymptotic expansions agree very well with numerical calculations.

3.2 Mathematical Model

We consider a static inactive nematic liquid crystal confined in a rectangular well of depth μd , side lengths d and λd , so that the aspect ratio in the xy -plane is λ (see Figure 3.2). We will assume that the depth of the well is considerably smaller than the other two lengths, so that $\mu \ll 1$ and $\mu \ll \lambda$, and that planar degenerate anchoring on the faces $z = 0$ and $z = \mu d$ forces the director to remain

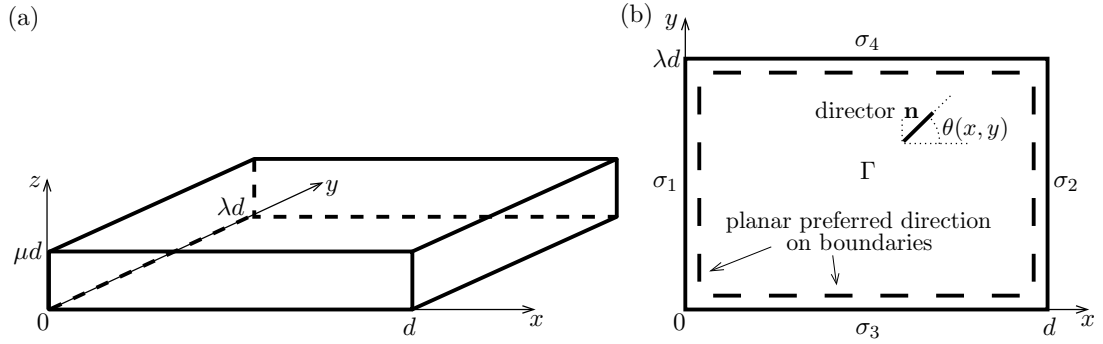


Figure 3.2: (a) Sketch of the rectangular well geometry containing the nematic liquid crystal; (b) cross-sectional area Γ of the rectangular well. The director \mathbf{n} is described in terms of the angle $\theta(x, y)$. Each bounding surface σ_i ($i = 1$ to 4) prefers planar director alignment.

in the xy -plane. These conditions lead us to assume that the director lies in the xy -plane throughout the well and we may simplify the mathematical model to consider only the director configuration in the cross-sectional area of the well, specified as $\Gamma = \{(x, y) \in [0, d] \times [0, \lambda d]\}$. Since the nematic director is assumed to lie in the xy -plane, we set the angles $\theta_1 = 0$ and $\theta_2 = \theta(x, y)$ in (2.2.2) so that

$$\mathbf{n} = (\cos \theta(x, y), \sin \theta(x, y), 0), \quad (3.2.1)$$

where $\theta(x, y)$ is the director angle measured relative to the positive x -direction. The director configuration $\theta(x, y)$ can be determined by a minimisation of the total free energy of the system, a sum of the bulk elastic energy and the surface energies at each boundary. The elastic energy density is derived by substituting (3.2.1) into (2.2.40), giving

$$w_F = \frac{1}{4} \left((K_3 - K_1) ((\theta_x^2 - \theta_y^2) \cos(2\theta) + 2\theta_x \theta_y \sin(2\theta)) + (K_1 + K_3)(\theta_x^2 + \theta_y^2) \right), \quad (3.2.2)$$

where we adopt the notation that θ_x represents the first partial derivative of θ with respect to x , etc. The four boundaries of region Γ are denoted by σ_i ($i = 1$ to 4) as indicated in Figure 3.2. Each boundary has associated with it an easy, or preferred, direction whereby the director tries to align parallel to the boundary

surface (i.e., planar alignment). We introduce weak anchoring by employing the Rapini-Papoular form for the surface energy density w_{σ_i} given by (2.2.51) on each surface σ_i . Although it is possible to proceed with the general situation in which the anchoring strengths on each side of the region are all different (i.e., ω_i for $i = 1, 2, 3, 4$), the analysis is cumbersome and little is gained in terms of general insights into this problem. Therefore, we restrict our attention to a uniform anchoring strength $\omega > 0$ to ensure planar alignment. We can now express the total energy of the system as

$$W = \mu d \left(\frac{1}{4} \int_0^{\lambda d} \int_0^d \left((K_3 - K_1) ((\theta_x^2 - \theta_y^2) \cos(2\theta) + 2\theta_x \theta_y \sin(2\theta)) \right. \right. \\ \left. \left. + (K_1 + K_3)(\theta_x^2 + \theta_y^2) \right) dx dy + \sum_{i=1}^4 \frac{\omega}{2} \int_{\sigma_i} (\mathbf{n} \cdot \boldsymbol{\nu})^2 d\sigma_i \right), \quad (3.2.3)$$

where $d\sigma_i$ represents integration along the surface in the positive direction of the corresponding Cartesian coordinate. We introduce dimensionless Cartesian coordinates $(\bar{x}, \bar{y}) = (x/d, y/d)$ so that the cross-sectional region is now $\bar{\Gamma} = \{(\bar{x}, \bar{y}) \in [0, 1] \times [0, \lambda]\}$ with boundary surfaces $\bar{\sigma}_i$. We need only consider the case $\lambda \geq 1$ since the transformation $\lambda \rightarrow 1/\lambda$ with $(\bar{x}; \bar{y}) \rightarrow (\bar{y}; \bar{x})$ will provide solutions for the case $\lambda < 1$.

With the non-dimensionalisation above, we obtain the dimensionless free energy

$$\bar{W} = \frac{2W}{\mu d K_1} = \frac{1}{2} \int_0^\lambda \int_0^1 \left((k - 1) ((\theta_{\bar{x}}^2 - \theta_{\bar{y}}^2) \cos(2\theta) + 2\theta_{\bar{x}} \theta_{\bar{y}} \sin(2\theta)) \right. \\ \left. + (1 + k)(\theta_{\bar{x}}^2 + \theta_{\bar{y}}^2) \right) d\bar{x} d\bar{y} + \sum_{i=1}^4 \tau \int_{\bar{\sigma}_i} (\mathbf{n} \cdot \boldsymbol{\nu})^2 d\bar{\sigma}_i, \quad (3.2.4)$$

where the parameter $\tau = \omega d/K_1$ represents dimensionless anchoring strength or, equivalently, the ratio of the surface extrapolation length K_1/ω and the well dimension d . The dimensionless constant $k = K_3/K_1$ measures elastic anisotropy in the liquid crystal.

Our aim is now to minimise the dimensionless energy \bar{W} in equation (3.2.4) with respect to the possible director angle configurations $\theta(\bar{x}, \bar{y})$ for a given an-

choring parameter τ , elastic constant ratio k and aspect ratio λ . By a standard application of the calculus of variations, the Euler-Lagrange equation (2.2.35) derived from (3.2.4) is

$$0 = (k + 1)(\theta_{\bar{x}\bar{x}} + \theta_{\bar{y}\bar{y}}) + (k - 1)((\theta_{\bar{x}\bar{x}} + 2\theta_{\bar{x}}\theta_{\bar{y}} - \theta_{\bar{y}\bar{y}}) \cos(2\theta) + (\theta_{\bar{y}}^2 + 2\theta_{\bar{x}\bar{y}} - \theta_{\bar{x}}^2) \sin(2\theta)), \quad (\bar{x}, \bar{y}) \in (0, 1) \times (0, \lambda). \quad (3.2.5)$$

The boundary conditions due to weak anchoring at each boundary are obtained via a balance of couples which relate the bulk energy density and surface energy density [129]. From equation (2.2.71), the boundary conditions are

$$\begin{aligned} \bar{\sigma}_1 : \quad & (1 + k)\theta_{\bar{x}} + \tau \sin(2\theta) + (k - 1)(\theta_{\bar{x}} \cos(2\theta) + \theta_{\bar{y}} \sin(2\theta)) = 0, \\ \bar{\sigma}_2 : \quad & (1 + k)\theta_{\bar{x}} - \tau \sin(2\theta) + (k - 1)(\theta_{\bar{x}} \cos(2\theta) + \theta_{\bar{y}} \sin(2\theta)) = 0, \\ \bar{\sigma}_3 : \quad & (1 + k)\theta_{\bar{y}} - \tau \sin(2\theta) - (k - 1)(\theta_{\bar{y}} \cos(2\theta) - \theta_{\bar{x}} \sin(2\theta)) = 0, \\ \bar{\sigma}_4 : \quad & (1 + k)\theta_{\bar{y}} + \tau \sin(2\theta) - (k - 1)(\theta_{\bar{y}} \cos(2\theta) - \theta_{\bar{x}} \sin(2\theta)) = 0. \end{aligned} \quad (3.2.6)$$

Equations (3.2.5) and (3.2.6) are solved by the trivial solutions $\theta(\bar{x}, \bar{y}) = 0$ and $\theta(\bar{x}, \bar{y}) = \pi/2$ (or the equivalent solutions $\theta(\bar{x}, \bar{y}) = n\pi$ and $\theta(\bar{x}, \bar{y}) = (n + 1/2)\pi$ for $n \in \mathbb{Z}$), and in the next section we will first consider solutions that bifurcate from these undistorted states as the anchoring parameter τ increases. We will also consider the asymptotic limit for large anchoring parameter, i.e., $\tau \rightarrow \infty$, which approximates the infinite anchoring limit considered by Lewis *et al.* [86].

In contrast to the work of Lewis *et al.* [86], the approach considered here leads to no director discontinuities and there is no need to remove corner regions to regularise the energy. Indeed, at each corner the boundary conditions (3.2.6) for two adjacent walls do not conflict and can be satisfied independently. While it is relatively straightforward to implement a numerical scheme to solve (3.2.5) and (3.2.6), the non-linear nature of our system makes any type of analysis difficult. However, in the following sections we will also show how linearisation can lead to very effective results in certain limits of the anchoring strength. In the sections that follow, we omit the $\bar{\cdot}$ from all dimensionless quantities (specifically, \bar{x} , \bar{y} , $\bar{\Gamma}$, $\bar{\sigma}_i$, \bar{W}) with the understanding that, henceforth, in this chapter, all quantities are dimensionless.

3.3 Bifurcations From Undistorted States

3.3.1 Linearisation Around the Undistorted Solutions

As mentioned in Section 3.2, regardless of the anchoring parameter τ , elastic constant ratio k and aspect ratio λ , equations (3.2.5) and (3.2.6) are solved by the trivial solutions $\theta(x, y) = 0$ and $\theta(x, y) = \pi/2$. Using (3.2.4), we see that these two constant equilibria correspond to total energies of $W_0 = 2\lambda\tau$ and $W_{\pi/2} = 2\tau$, respectively, so that when $\lambda = 1$ the undistorted states have equal energies, and $\lambda \lesssim 1$ correspond to $W_0 \lesssim W_{\pi/2}$.

Linearising equation (3.2.5) about $\theta = 0$, we obtain

$$k\theta_{xx} + \theta_{yy} = 0, \quad (x, y) \in (0, 1) \times (0, \lambda), \quad (3.3.1)$$

which we solve subject to corresponding linearised boundary conditions on each boundary

$$\begin{aligned} \sigma_1 : \quad k\theta_x + \tau\theta &= 0, & \sigma_3 : \quad \theta_y - \tau\theta &= 0, \\ \sigma_2 : \quad k\theta_x - \tau\theta &= 0, & \sigma_4 : \quad \theta_y + \tau\theta &= 0. \end{aligned} \quad (3.3.2)$$

A relatively straightforward application of separation of variables leads to the non-trivial solution of (3.3.1) subject to (3.3.2), namely,

$$\theta(x, y) = A_0 \left(\cosh\left(\frac{px}{\sqrt{k}}\right) - \frac{\tau}{p\sqrt{k}} \sinh\left(\frac{px}{\sqrt{k}}\right) \right) \left(\cos(py) + \frac{\tau}{p} \sin(py) \right), \quad (3.3.3)$$

for a constant $A_0 \neq 0$, and where the mode number p and anchoring strength τ must satisfy the simultaneous equations

$$(\tau^2 + kp^2) \sinh\left(\frac{p}{\sqrt{k}}\right) - 2p\tau\sqrt{k} \cosh\left(\frac{p}{\sqrt{k}}\right) = 0, \quad (3.3.4)$$

$$(\tau^2 - p^2) \sin(p\lambda) + 2p\tau \cos(p\lambda) = 0. \quad (3.3.5)$$

Equation (3.3.4) yields two expressions for τ in terms of p and k , namely,

$$\tau_{\pm}^0 = p\sqrt{k} \left(\coth\left(\frac{p}{\sqrt{k}}\right) \pm \operatorname{csch}\left(\frac{p}{\sqrt{k}}\right) \right), \quad (3.3.6)$$

which, upon substitution into (3.3.4), lead to two corresponding transcendental

equations for p ,

$$f_{\pm}(p; \lambda) := 2\sqrt{k} \sinh\left(\frac{p}{\sqrt{k}}\right) + \left((k-1) \cosh\left(\frac{p}{\sqrt{k}}\right) \pm (1+k)\right) \tan(p\lambda) = 0. \quad (3.3.7)$$

The solutions of the transcendental equations (3.3.7) form an infinite set of values, corresponding to mode numbers p_i ($i = 1, 2, \dots$). Each mode has associated with it a corresponding value τ given by (3.3.6). As we will see later, these values of τ are critical anchoring strengths at which each mode appears in the system in order to reduce the free energy. Corresponding to each mode number p_i is an amplitude $A_{0,i}$ so that the general solution of (3.3.1) and (3.3.2) is then

$$\theta(x, y) = \sum_{i=1}^{\infty} A_{0,i} \left[\cosh\left(\frac{p_i x}{\sqrt{k}}\right) - \left(\coth\left(\frac{p_i}{\sqrt{k}}\right) \pm \operatorname{csch}\left(\frac{p_i}{\sqrt{k}}\right) \right) \sinh\left(\frac{p_i x}{\sqrt{k}}\right) \right] \\ \times \left[\cos(p_i y) + \left(\coth\left(\frac{p_i}{\sqrt{k}}\right) \pm \operatorname{csch}\left(\frac{p_i}{\sqrt{k}}\right) \right) \sin(p_i y) \right]. \quad (3.3.8)$$

For the linearisation about $\theta = \pi/2$, we adopt a similar approach, expressing the general solution in terms of amplitudes $A_{\pi/2,i}$ and mode numbers q_i as

$$\theta(x, y) = \frac{\pi}{2} - \sum_{i=1}^{\infty} A_{\pi/2,i} \left[\cos(q_i x) + \left(\coth\left(\frac{q_i \lambda}{\sqrt{k}}\right) \pm \operatorname{csch}\left(\frac{q_i \lambda}{\sqrt{k}}\right) \right) \sin(q_i x) \right] \\ \times \left[\cosh\left(\frac{q_i y}{\sqrt{k}}\right) - \left(\coth\left(\frac{q_i \lambda}{\sqrt{k}}\right) \pm \operatorname{csch}\left(\frac{q_i \lambda}{\sqrt{k}}\right) \right) \sinh\left(\frac{q_i y}{\sqrt{k}}\right) \right]. \quad (3.3.9)$$

The critical values of the anchoring strengths $\tau_{\pm}^{\pi/2}$ are calculated from

$$\tau_{\pm}^{\pi/2} = q\sqrt{k} \left(\coth\left(\frac{q\lambda}{\sqrt{k}}\right) \pm \operatorname{csch}\left(\frac{q\lambda}{\sqrt{k}}\right) \right), \quad (3.3.10)$$

where the solutions for the mode numbers q satisfy the corresponding transcendental equations

$$g_{\pm}(q; \lambda) := 2\sqrt{k} \sinh\left(\frac{q\lambda}{\sqrt{k}}\right) + \left((k-1) \cosh\left(\frac{q\lambda}{\sqrt{k}}\right) \pm (1+k)\right) \tan(q) = 0. \quad (3.3.11)$$

It is worth noting that, depending on the choice of \pm in equations (3.3.7) and (3.3.8), we can combine each x -dependent term in (3.3.8) into the form $\cosh(p_i(x - 1/2))$ or $\sinh(p_i(x - 1/2))$. In other words, one solution for $\theta(x, y)$ in (3.3.8) will

be symmetric with respect to $x = 1/2$ and the other anti-symmetric. (Symmetry about $x = 1/2$ is equivalent to $\theta(x, y) = \theta(1 - x, y)$ and anti-symmetry is $\theta(x, y) = -\theta(1 - x, y)$.) The same can be said of equations (3.3.9) and (3.3.11) with solutions symmetric or anti-symmetric with respect to $y = \lambda/2$ through a combination of hyperbolic terms involving q_i .

In order to calculate the critical anchoring strengths τ_{\pm}^0 and $\tau_{\pm}^{\pi/2}$, we first solve equations (3.3.7) and (3.3.11) to find the critical mode numbers p_i and q_i , before substituting into (3.3.6) and (3.3.10), respectively. In the calculations that follow, our analysis focusses on the four first modes found from $f_+(p; \lambda) = 0$, $f_-(p; \lambda) = 0$, $g_+(q; \lambda) = 0$ and $g_-(q; \lambda) = 0$. The p and q values which satisfy these four equations have been obtained numerically in MATLAB [94]. This will generate four symmetry breaking states, two of which originate from $f_{\pm}(p; \lambda) = 0$ with the remaining two coming from $g_{\pm}(q; \lambda) = 0$.

As an example, we plot the four director structures in Figure 3.3 for an aspect ratio of $\lambda = 1.5$, anchoring strengths τ_{\pm}^0 and $\tau_{\pm}^{\pi/2}$, amplitudes $A_0 = A_{\pi/2} = 0.5$ and elastic constant ratio $k = 1$. For three of the states (D, U_1 and U_2), we have used the same notation as [86], indicating the Diagonal or U-shaped nature of the distortion. We denote the fourth state by DD to recognise that it is, essentially, a double D state with symmetric diagonal distortions in $0 < y < \lambda/2$ and $\lambda/2 < y < \lambda$. We are able to classify the four different branches, and associate them with solutions in [86] because the states exhibit particular (anti)-symmetries with respect to $x = 1/2$ and/or $y = \lambda/2$. For example, in the D state, $\theta(x, y) = \theta(1 - x, \lambda - y)$. There are actually two versions of each of the four non-trivial states that come out of our analysis, where the mirror images of the director profiles in Figure 3.3 are also possible nematic states. The first modes of $f_+(p; \lambda) = 0$ and $g_+(q; \lambda) = 0$, respectively, give rise to the U_1 and U_2 states. In the case of $f_-(p; \lambda) = 0$ and $g_-(q; \lambda) = 0$, the first modes generate the DD and D states, respectively.

In Figure 3.4(a), we plot the two values of p and two values of q mentioned above when $k = 1$ as the aspect ratio λ varies. These p and q values are then used to calculate the corresponding critical anchoring strengths plotted in Figure

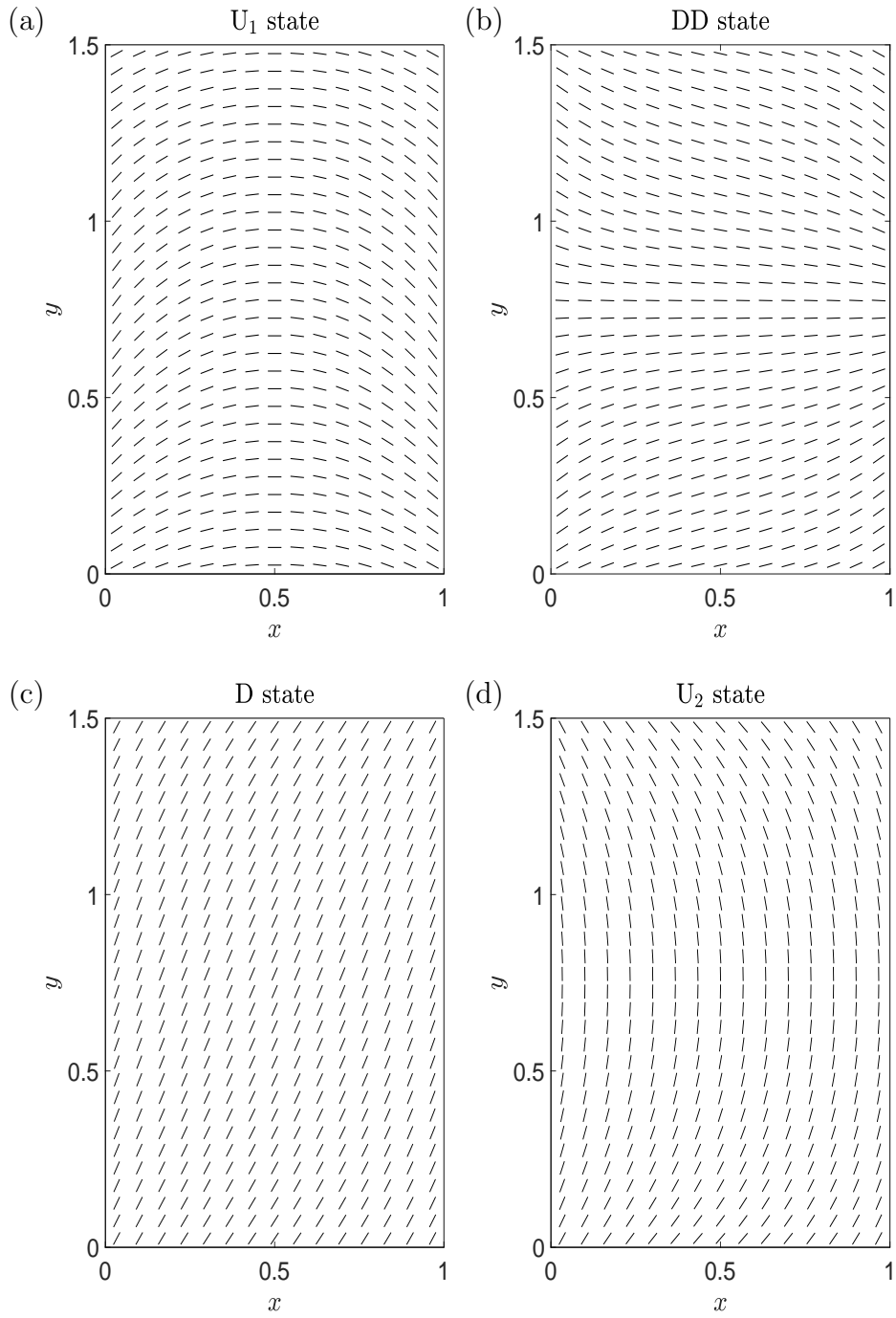


Figure 3.3: The four director structures bifurcating from the trivial solutions $\theta = 0$ ((a) U_1 and (b) DD states) and $\theta = \pi/2$ ((c) D and (d) U_2 states) for an aspect ratio $\lambda = 1.5$, anchoring strengths τ_{\pm}^0 and $\tau_{\pm}^{\pi/2}$, and elastic constant ratio $k = 1$.

3.4(b). These four lowest critical values of τ correspond to the four director distortion modes, described by the appropriate solutions (3.3.8) and (3.3.9). Figure 3.4(b) indicates that for the two states which bifurcate from the $\theta = \pi/2$ trivial solution (the D and U_2 states, shown by the dotted and dot-dashed curves respectively), it is always the D state that bifurcates at the lower critical τ value. In fact, it is simple to show analytically that the first non-zero solution to $g_+(q; \lambda) = 0$ tends to $q = \pi/2$ from above as $\lambda \rightarrow \infty$, and the first non-zero solution to $g_-(q; \lambda) = 0$ tends to $q = \pi/2$ from below as $\lambda \rightarrow \infty$. The asymptotic behaviour for the corresponding critical values of the anchoring parameter is then $\tau \rightarrow \pi/2^+$ for the U_2 state and $\tau \rightarrow \pi/2^-$ for the D state since, for $q \in \mathbb{Z}^+$,

$$\lim_{\lambda \rightarrow \infty} (\coth(q\lambda) \pm \operatorname{csch}(q\lambda)) = 1. \quad (3.3.12)$$

For the two states bifurcating from the $\theta = 0$ trivial solution (the DD and U_1 states, shown by the solid and dashed curves respectively), the situation is slightly more complicated. While the solutions of $f_{\pm}(p; \lambda) = 0$ both tend to $p = 0$ from above as $\lambda \rightarrow \infty$, the critical value of the anchoring parameter behaves as $\tau \rightarrow 2^+$ for the U_1 state and $\tau \rightarrow 0^+$ for the DD state. The values of the critical anchoring parameters at $\lambda = 1$ are found from equation (3.3.7) to be $\tau_+^0 \approx 2.55$ for the U_1 state and $\tau_-^0 \approx 4.61$ for the DD state. There is, therefore, a critical value of λ , which we denote by λ_c , at which the critical values of τ for the U_1 and DD states cross, as can be seen in Figure 3.4(b). This value is found numerically to be $\lambda_c \approx 1.75$ corresponding to $\tau_c \approx 2.24$.

Figure 3.4(c) shows the smallest positive solutions of equations (3.3.7) and (3.3.11) when the elastic anisotropy is reduced to $k = 0.5$. The corresponding critical anchoring strengths are shown in Figure 3.4(d), where we observe that reducing the elastic constant ratio has resulted in a change in the critical aspect ratio at which the U_1 and DD states exchange bifurcation ordering. Specifically, when $k = 0.5$, the U_1 state bifurcates from the zero state before the DD state until a critical aspect ratio value of $\lambda_c \approx 2.32$, at which $\tau_c \approx 1.107$. There is no crossover in the bifurcation ordering of the D and U_2 states, which was also the case when $k = 1$. For each symmetry breaking solution, we are able to deduce

from the numerical calculations that reducing k has led to a decrease in the critical anchoring strength at which all four states emerge from the trivial states.

Figure 3.4(e) shows the smallest positive solutions of equations (3.3.7) and (3.3.11) when the elastic anisotropy is increased to $k = 2$, with the corresponding values of the critical anchoring strengths shown in Figure 3.4(f). We see that, for the same aspect ratio, $k > 1$ causes an increase in the critical anchoring strengths for each state compared to the special case of $k = 1$. When $k = 2$, the DD state will be the first state to bifurcate from $\theta = 0$ for aspect ratios $\lambda \geq 1.33$. The critical value of the anchoring strength at which the U_1 and DD states exchange bifurcation ordering is approximately $\tau_c \approx 4.525$. By contrast, the critical anchoring strengths of the D state remain less than those for the U_2 state. Therefore, the role of the elastic constant ratio k is to enhance ($k < 1$) or delay ($k > 1$) the transition due to weak anchoring that we observed for an elastically isotropic nematic liquid crystal.

Figure 3.5 shows the variation of the smallest positive solutions of equations (3.3.7) and (3.3.11) with the elastic constant ratio k at aspect ratio (a) $\lambda = 1.5$, (c) $\lambda = 2$, and (e) $\lambda = 3$. The critical anchoring strengths for each of the four states when $\lambda = 1.5$ are shown in Figure 3.5(b), where we find that the bifurcation ordering of the U_1 and DD states change at elastic constant ratio $k \approx 1.48$. By increasing the aspect ratio to $\lambda = 2$, Figure 3.5(d) shows that the change in the bifurcation ordering of the U_1 and DD states occurs at $k \approx 0.72$. In Figure 3.5(f), we plot the critical anchoring strengths when $\lambda = 3$, which shows that the DD state will bifurcate from the trivial state $\theta = 0$ before the U_1 state for all elastic constant ratios $0.5 \leq k \leq 2$. For all values of λ and k considered, the U_2 state will always bifurcate from the trivial state $\theta = \pi/2$ at a larger critical anchoring strength than that of the D state.

3.3.2 Energies of Elastically Isotropic Nematics

The presence of trigonometric terms in the energy (3.2.4) makes it exceptionally difficult, if not impossible, to undertake an analytic investigation of the energy

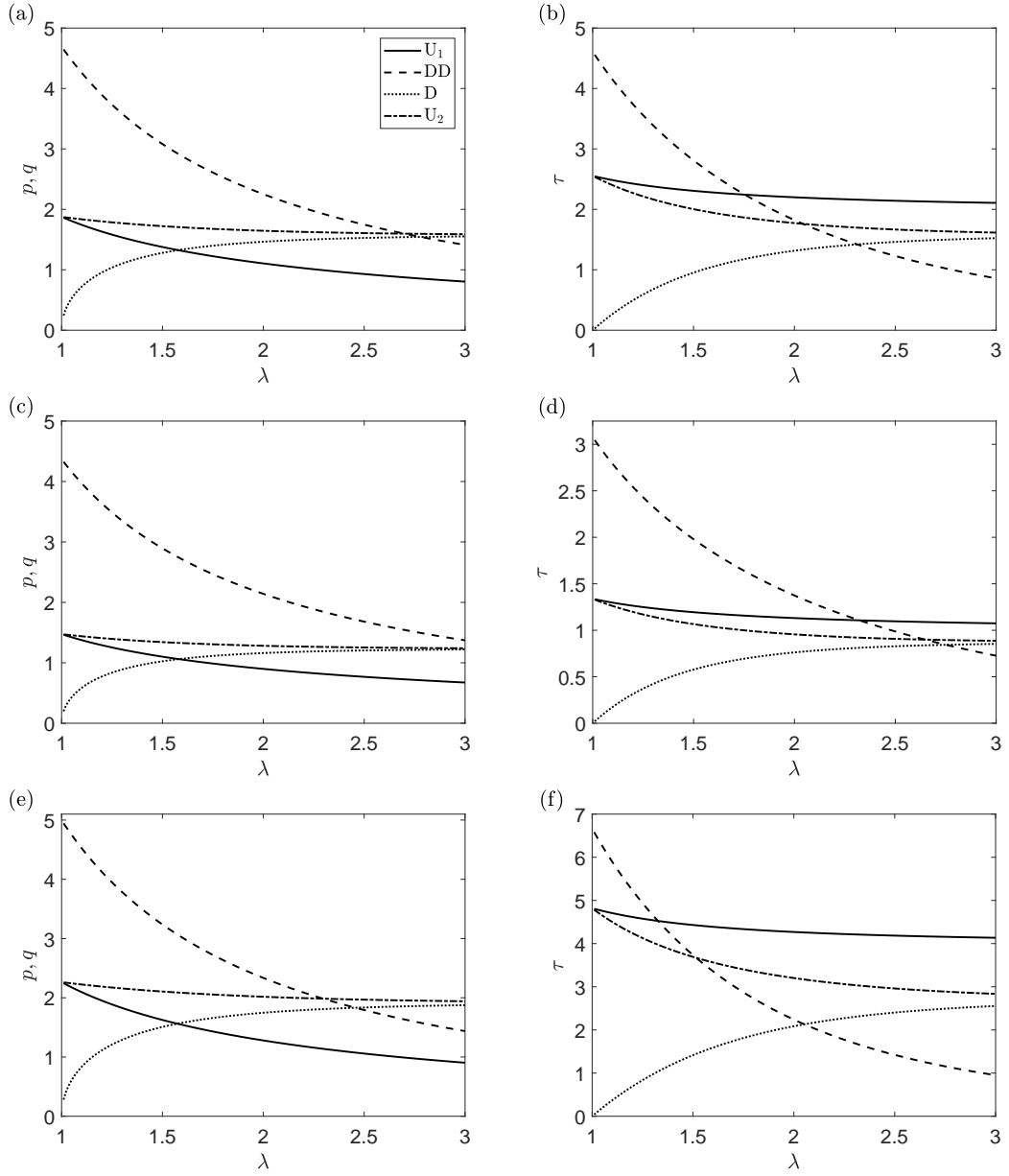


Figure 3.4: Smallest positive wavenumbers of the functions $f_{\pm}(p; \lambda)$ (labelled DD and U_1) and $g_{\pm}(q; \lambda)$ (labelled D and U_2) for varying aspect ratio λ when (a) $k = 1$, (c) $k = 0.5$ and (e) $k = 2$. The critical anchoring strengths as a function of λ when (b) $k = 1$, (d) $k = 0.5$ and (f) $k = 2$.

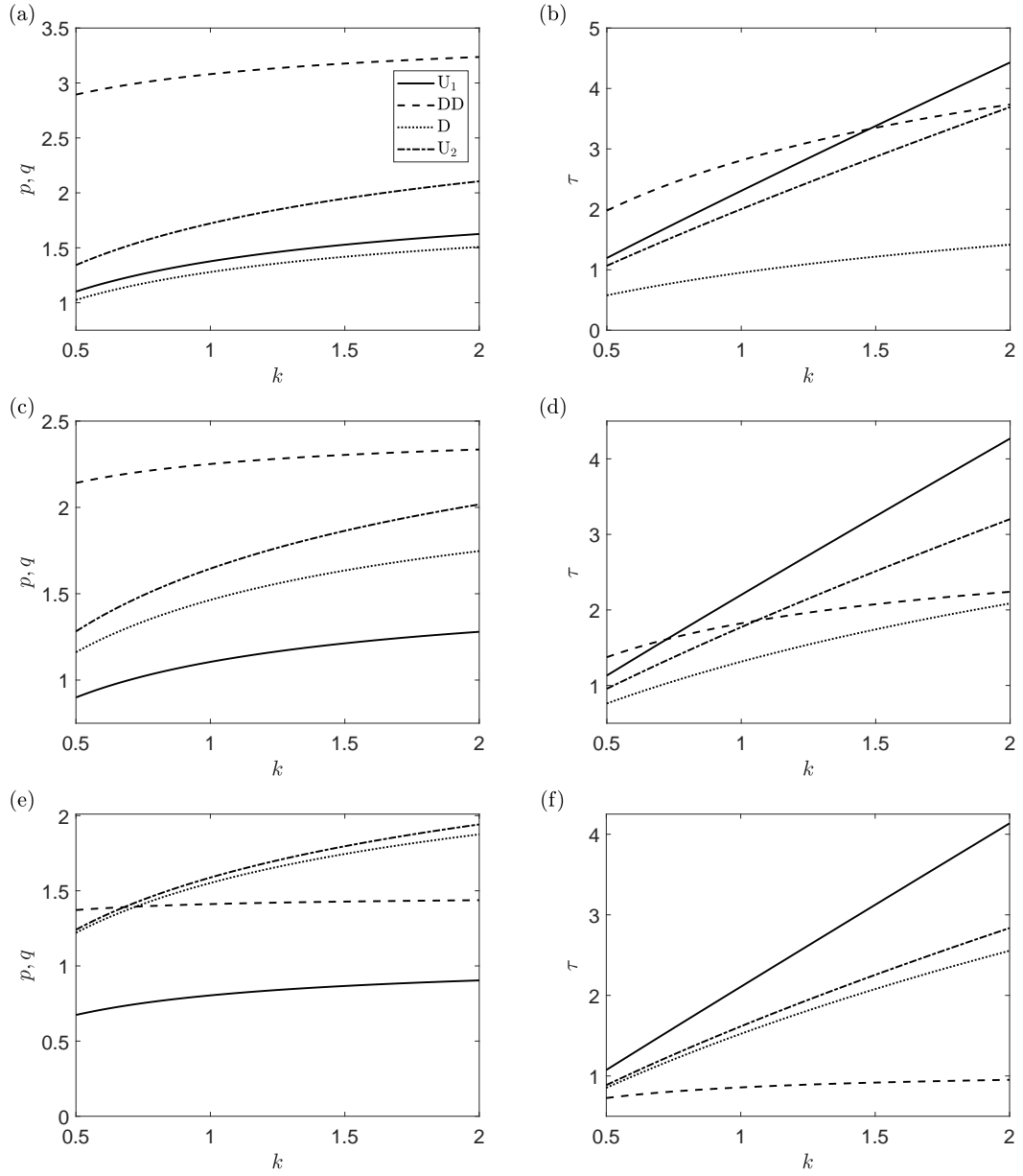


Figure 3.5: Smallest positive wavenumbers of the functions $f_{\pm}(p; \lambda)$ (labelled DD and U_1) and $g_{\pm}(q; \lambda)$ (labelled D and U_2) for varying elastic constant ratio k when (a) $\lambda = 1.5$, (c) $\lambda = 2$ and (e) $\lambda = 3$. The critical anchoring strengths as a function of k when (b) $\lambda = 1.5$, (d) $\lambda = 2$ and (f) $\lambda = 3$.

associated with the director profiles (3.3.8) and (3.3.9). The trigonometric terms in the bulk energy density all include a factor of $(k - 1)$, and so in order to make progress, we focus on the special case of $k = 1$. Trigonometric terms also occur in (3.2.4) through the surface energies. We therefore approximate the non-linear Rapini-Papoular energies as Taylor polynomials to fourth order in θ around the two trivial states. This now allows us to evaluate the energy for any positive anchoring strength τ . In the calculations that follow, we restrict our analysis to the first modes of the director profiles (3.3.8) and (3.3.9), therefore our calculations will be valid only close to the respective bifurcation points.

Substituting the first modes of the director profiles (3.3.8) and (3.3.9) into (3.2.4) and integrating, we find

$$W \approx 2\lambda\tau + a_2(\tau)A_{0,1}^2 + a_4(\tau)A_{0,1}^4, \quad (3.3.13)$$

for θ close to 0, and

$$W \approx 2\tau + b_2(\tau)A_{\pi/2,1}^2 + b_4(\tau)A_{\pi/2,1}^4, \quad (3.3.14)$$

for θ close to $\pi/2$. The coefficients $a_2(\tau)$, $a_4(\tau)$, $b_2(\tau)$ and $b_4(\tau)$ are derived analytically and presented in Appendix B. We now need to determine the critical values of the amplitudes $A_{0,1}$ and $A_{\pi/2,1}$ associated with the first mode. We do so by minimising the energies (3.3.13) and (3.3.14) with respect to the amplitudes. The resultant cubic polynomials lead to non-trivial critical amplitudes

$$A_{0,1} = \pm \sqrt{-\frac{a_2(\tau)}{2a_4(\tau)}}, \quad A_{\pi/2,1} = \pm \sqrt{-\frac{b_2(\tau)}{2b_4(\tau)}}, \quad (3.3.15)$$

although $A_{0,1} = A_{\pi/2,1} = 0$ are also possible amplitudes from the energy minimisation and reproduce the energies of the two trivial states. Replacing $A_{0,1}$ in (3.3.13) and $A_{\pi/2,1}$ in (3.3.14) by the non-trivial critical amplitudes (3.3.15), we now have

$$W \approx 2\lambda\tau - \frac{a_2^2(\tau)}{4a_4(\tau)}, \quad (3.3.16)$$

for θ close to 0, and

$$W \approx 2\tau - \frac{b_2^2(\tau)}{4b_4(\tau)}, \quad (3.3.17)$$

for θ close to $\pi/2$. We can now compare the energies (3.3.16) and (3.3.17) with those calculated numerically for the full non-linear system when $k = 1$. The order of the bifurcations is illustrated in Figure 3.6. Since there are no linear terms in A_0 and $A_{\pi/2}$ present in the energies (3.3.16) and (3.3.17), and all of the symmetry breaking states we consider exist at anchoring strengths greater than and equal to their critical threshold values, each of these bifurcations is a supercritical pitchfork bifurcation. As mentioned previously, there are two forms of the non-trivial states in Figure 3.3 as their mirror images are also possibilities. Energetically, however, the states are equivalent to their mirror images, therefore we do not observe typical pitchfork shaped bifurcation curves.

In Figure 3.6 we have considered equilibrium states obtained both numerically from equations (3.2.5) and (3.2.6) (solid curves, calculated using the finite-element package COMSOL [26]) and analytically using the perturbation approach around each of the bifurcation points (dashed curves). Figure 3.6 shows W_0 and $W_{\pi/2}$, the energies for the trivial solutions, and energies for the bifurcating states when $\lambda = 1.5 < \lambda_c$ (Figures 3.6 (a) and (c)) and $\lambda = 3 > \lambda_c$ (Figures 3.6 (b) and (d)). We see that, as expected, for $\lambda < \lambda_c$ the U_1 state bifurcates at a lower value of τ than the DD state while, for $\lambda > \lambda_c$ the ordering exchanges and the DD state bifurcates at a lower value of τ . For bifurcations from the trivial state $\theta = \pi/2$, however, the D state always bifurcates at a lower value of anchoring parameter τ . As would be expected with a perturbation method, the analytic energy calculation agrees exactly with the numerics only at the bifurcation points, though close to the respective bifurcation points we still see a level of agreement between the two approaches.

3.3.3 Energies of Elastically Anisotropic Nematics

Since the energies of the base states are proportional to the anchoring strength, it follows from previous calculations that for the same aspect ratio λ , the four non-trivial states will bifurcate at a lower energy than (3.3.16) and (3.3.17) for elastic constant ratios $k < 1$ and a higher energy than (3.3.16) and (3.3.17) when

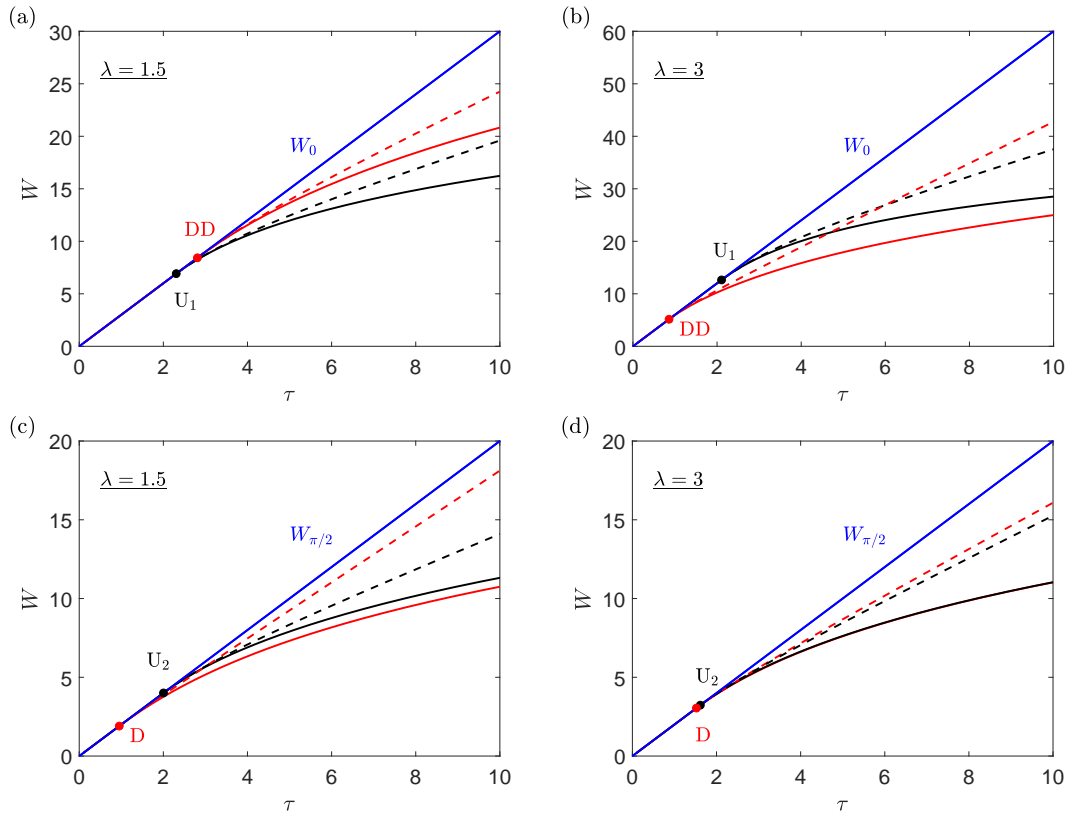


Figure 3.6: Total free energy W including elastic and surface contributions as a function of anchoring parameter τ close to the bifurcation points, calculated numerically (solid curves) and analytically (dashed curves) when $k = 1$. Also shown are the energies W_0 and $W_{\pi/2}$ for the trivial states. Bifurcations from $\theta = 0$ for (a) $\lambda = 1.5$ and (b) $\lambda = 3$ show that the order of the U_1 and DD bifurcations exchanges as λ increases. Bifurcations from the $\theta = \pi/2$ for (c) $\lambda = 1.5$ and (d) $\lambda = 3$. In this case, the D state bifurcation always occurs at a lower value of τ . In (d), the D and U_2 numerical branches are very close.

$k > 1$. We now consider the energies of the four non-trivial nematic equilibria for elastic constant ratio $k \neq 1$. Figures 3.7(a) and (c) show the energies as a function of the anchoring strength for the nematic equilibria which bifurcate from the trivial states $\theta = 0$ and $\theta = \pi/2$, respectively. These energies have been calculated numerically at aspect ratio $\lambda = 1.5$ and elastic constant ratio $k = 0.5$. This shows that the U_1 state bifurcates from $\theta = 0$ at a lower anchoring strength than the DD state, with the U_2 state emerging from $\theta = \pi/2$ at a larger anchoring

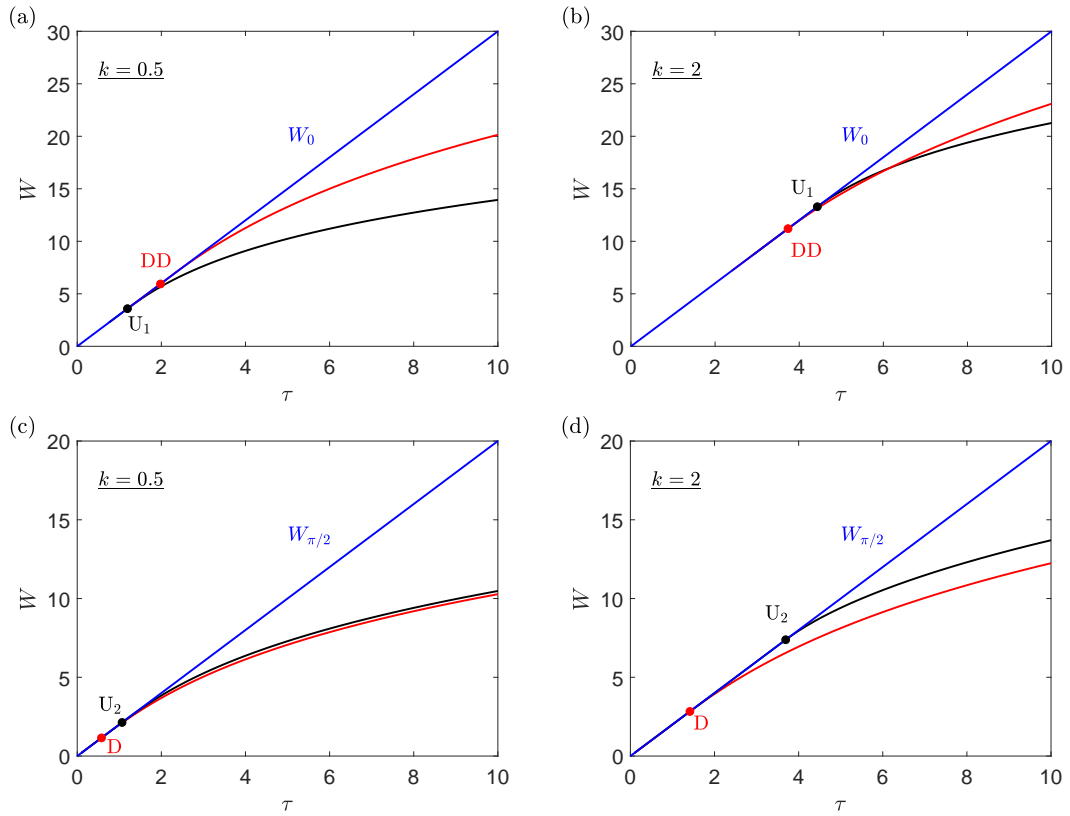


Figure 3.7: Total free energy W including elastic and surface contributions as a function of anchoring parameter τ close to the bifurcation points, calculated numerically at elastic constant ratios $k = 0.5$ and $k = 2$ and aspect ratio $\lambda = 1.5$. Also shown are the energies W_0 and $W_{\pi/2}$ for the trivial states. Bifurcations from $\theta = 0$ for (a) $k = 0.5$ and (b) $k = 2$ show that the order of the U_1 and DD bifurcations exchanges as k increases. Bifurcations from the $\theta = \pi/2$ for (c) $k = 0.5$ and (d) $k = 2$. In this case, the D state bifurcation always occurs at a lower value of τ . In (c), the D and U_2 numerical branches are very close.

strength than the D state. The energies when $k = 2$ are shown in Figures 3.7(b) and (d). We can see that the increase in k leads to a change in the bifurcation ordering of the U_1 and DD states, although the energy of the DD state is larger than that of the U_1 state at higher anchoring strengths. The difference in critical anchoring strengths between the D and U_2 states increases for larger k . As was the case in Figure 3.6, we have also included the energies W_0 and $W_{\pi/2}$.

3.4 Modelling Defects at Weakly Anchored Corners For Large Anchoring Strength

Competing surface orientation angles, when the anchoring is infinite, can lead to the formation of defects at the four corner points, as was the case in the model considered in [86]. As we mentioned before, the analytic solution for the director angle derived in [86] is not valid at the corners of the region due to the presence of defects. In this section, we show that when the elastic constant ratio $k = 1$, an approximate analytic solution for the director orientation which satisfies the non-linear Robin boundary conditions (3.2.6) can be derived using the method of matched asymptotic expansions. This process involves obtaining several different approximate solutions of Laplace's equation, each of which are valid for part of the range of the independent variables x and y . The various solutions are then combined to generate a single approximate solution that is valid for all values of x and y . As we will see, this approach allows for an analytic solution for the equilibrium director orientation to be derived which is valid in the bulk and close to the corners of the region.

We divide the rectangular region into two subdomains, the first of which consists of the director orientation in the bulk of the well (i.e., away from the corners). The asymptotic series solution for the director orientation in this subdomain is referred to as the outer solution [10, 106] and is valid for $x, y = O(1)$. This solution for the director orientation in the bulk will not be accurate close to the corners as the outer solution does not satisfy the Robin boundary conditions. However, close to the corners, the corresponding solutions at each corner, known as the inner solutions [10, 106], do satisfy the boundary conditions and can be constructed analytically. An approximate solution for the director orientation, valid for the whole domain is then obtained by combining the outer and inner solutions via a process called "matching".

3.4.1 Outer Solution

We begin by solving (3.2.5) in the bulk of the region and define this solution by θ_{Outer} (i.e., the outer solution), where $x, y = O(1)$ and $\tau \gg 1$. Setting $\tau = 1/\epsilon$, where ϵ is a small parameter such that $0 < \epsilon \ll 1$, we seek an asymptotic series solution of (3.2.5) of the form

$$\theta_{\text{Outer}} = \theta_0 + \epsilon\theta_1 + \epsilon^2\theta_2 + O(\epsilon^3). \quad (3.4.1)$$

At $O(1)$, the asymptotic solution (3.4.1) simplifies the boundary conditions (3.2.6) to $\sin(2\theta_0) = 0$, which has solutions $\theta_0 = n\pi/2$ for $n \in \mathbb{Z}$. The solution of equation (3.2.5) with Dirichlet boundary conditions on the boundaries is exactly the same obtained by Lewis *et al.* [86]. At leading order, the solution in the outer region is therefore

$$\theta_{\text{Outer}} = \theta_{\text{Lewis}} + O(\epsilon), \quad (3.4.2)$$

where θ_{Lewis} is given by (3.1.1) and is expressed in terms of the planar angles Θ_i , ($i = 1, \dots, 4$), which are defined in Table 3.1.

3.4.2 Inner Solution

As mentioned previously, the series solution (3.1.1) is not valid close to the corners. We now consider an asymptotic series solution for the director orientation close to the corners, θ_{Inner} , (i.e., the inner solution). For brevity, we only examine the director orientation solution which is valid close to the corner $(0, 0)$, where the solutions close to the remaining corners can be obtained by a translation and rotation of the solution close to $(0, 0)$. In this subdomain, we solve (3.2.5), subject to the local boundary conditions

$$2\theta_x + \frac{1}{\epsilon} \sin(2\theta) = 0 \quad \text{on} \quad x = 0, \quad (3.4.3)$$

$$2\theta_y - \frac{1}{\epsilon} \sin(2\theta) = 0 \quad \text{on} \quad y = 0. \quad (3.4.4)$$

In the inner region, x, y and ϵ are all very small and comparable in size. We introduce two new $O(1)$ length scales X and Y by setting $x = X\epsilon$ and $y = Y\epsilon$,

with $\tau = 1/\epsilon$, and seek an asymptotic series solution for (3.2.5) of the form

$$\theta_{\text{Inner}} = \theta_0 + \epsilon\theta_1 + \epsilon^2\theta_2 + O(\epsilon^3). \quad (3.4.5)$$

At leading order, we solve (3.2.5) with the boundary conditions

$$2\theta_X + \sin(2\theta) = 0 \quad \text{on} \quad X = 0, \quad (3.4.6)$$

$$2\theta_Y - \sin(2\theta) = 0 \quad \text{on} \quad Y = 0. \quad (3.4.7)$$

The inner solution of (3.2.5) is given by [73]

$$\theta_{\text{Inner}}(X, Y) = s_1 \tan^{-1} \left(\frac{Y - Y_0}{X - X_0} \right), \quad (3.4.8)$$

where s_1 is a coefficient which will induce a different director structure close to the corners, depending on the solution under consideration (i.e., D, U_1 or U_2), and X_0, Y_0 are the “shifts” in the x and y coordinates, respectively. In the model considered in [86], there are defects of strength ± 1 at the corners and so we consider values of s_1 such that $s_1 = \pm 1$. The boundary conditions (3.4.6) and (3.4.7) reveal that $X_0 = -1$ and $Y_0 = -1$. The solution in the inner region can then be expressed in terms of x and y such that

$$\theta_{\text{Inner}}(x, y) = s_1 \tan^{-1} \left(\frac{y + \epsilon}{x + \epsilon} \right). \quad (3.4.9)$$

The solution (3.4.9) is clearly singular at $(x, y) = -(1/\tau, 1/\tau)$. However, since $\tau > 0$, this singularity lies outside the region and so there are no internal defects. We can think of this solution as generating a “virtual” defect in the system and, for sufficiently large τ , it leads to a director structure close to the corner $(0, 0)$ which is identical to that when there is a defect on the corners of the region. For smaller values of τ , the “virtual” defect will move further away from the corner. In total, there are four separate inner solutions, one for each corner. These four solutions come together when we construct the composite solution in the next subsection.

3.4.3 Asymptotic Matching

To obtain the final, matched composite solution, valid on the whole domain, we combine the inner and outer solutions and subtract the values where the outer

and inner solutions overlap [10, 106]. In this case, the outer and inner solutions overlap in the limit $\lim_{X, Y \rightarrow \infty} \theta_{\text{Inner}}$, or equivalently, $\lim_{\epsilon \rightarrow 0} \theta_{\text{Inner}}$. The final approximate solution to this problem in terms of the anchoring strength τ is therefore

$$\begin{aligned}
\theta(x, y) &\approx \theta_{\text{Outer}} + \theta_{\text{Inner}} - \lim_{\epsilon \rightarrow 0} \theta_{\text{Inner}} \\
&= \theta_{\text{Lewis}} + s_1 \tan^{-1} \left(\frac{\tau y + 1}{\tau x + 1} \right) - s_2 \tan^{-1} \left(\frac{\tau y + 1}{\tau(x-1) - 1} \right) \\
&\quad + s_3 \tan^{-1} \left(\frac{\tau(y-\lambda) - 1}{\tau(x-1) - 1} \right) - s_4 \tan^{-1} \left(\frac{\tau(y-\lambda) - 1}{\tau x + 1} \right) \\
&\quad - s_1 \tan^{-1} \left(\frac{y}{x} \right) + s_2 \tan^{-1} \left(\frac{y}{x-1} \right) \\
&\quad - s_3 \tan^{-1} \left(\frac{y-\lambda}{x-1} \right) + s_4 \tan^{-1} \left(\frac{y-\lambda}{x} \right). \tag{3.4.10}
\end{aligned}$$

Despite having found an approximate analytic solution for the full non-linear problem, computing the energy analytically using solution (3.4.10) is not possible. Another difficulty is the change in the value of the director angle along the vertical boundaries in the DD state, which is not accounted for in the solution (3.4.10). The outer and inner solutions would have to include an additional two contributions, one for each of the vertical walls, as well as the solutions in the inner regions at $(0, \lambda/2)$ and $(1, \lambda/2)$ in order to generate the solution for the DD state. It therefore follows that if we are to gain any analytic insight into the energies of the nematic equilibria found in Section 3.3 in the limit of infinite anchoring, we require an alternative approach to that considered in this section.

3.5 Linearisation in the Large Anchoring Strength Case

In this section, we will consider the asymptotic limit for large anchoring parameter, i.e., $\tau \rightarrow \infty$ using a different approach to that considered in the previous section. As mentioned previously, due to the discontinuities in the director angle θ at the four corners for the model with infinite anchoring at the boundaries presented in [86], which can be thought of as line defects along the z -direction, the free energy diverges logarithmically around these points [73]. A large anchor-

ing strength τ in energy (3.2.4) corresponds to, for example, a well dimension d that is much larger than the surface extrapolation length K/ω , where K is the isotropic elastic constant. In this case, the director is anchored relatively strongly at each well boundary and we may assume that on σ_i , away from the corners, the director angle θ is close to the constant angle the director takes in the infinite anchoring limit. The infinite anchoring angles Θ_i for the D, U₁, U₂ were shown in Table 3.1, whereas those for the DD state are shown in Table 3.2.

3.5.1 Linearisation Around the Preferred Directions

By linearising the boundary conditions (3.2.6) around the preferred directions Θ_i , we are able to derive analytic solutions for the director angle profiles associated with the four non-trivial diagonal and U-shaped nematic equilibria. As was the case in Section 3.3, we can only make analytic progress with the energies if we assume that the nematic liquid crystal is elastically isotropic. Therefore for the remainder of this chapter, we make the system more analytically tractable by assuming that $k = 1$. As we saw in Section 3.4, it is possible to derive an analytic solution for the director angle which satisfies the non-linear boundary conditions (3.2.6) when $k = 1$ using the method of matched asymptotic expansions. However, it is impossible to calculate the energy analytically from this solution. The linearisation approach adopted here allows for the derivation of asymptotic approximations for the energy in the limit of large anchoring strength. Linearising the boundary conditions (3.2.6) about $\theta = \Theta_i$ leads to

$$\boldsymbol{\nu} \cdot \nabla \theta + \tau(\theta - \Theta_i) = 0 \quad \text{on } \sigma_i \quad (i = 1, 2, 3, 4), \quad (3.5.1)$$

or equivalently,

$$\begin{aligned} \sigma_1 : \quad \theta_x - \tau(\theta - \Theta_1) &= 0, & \sigma_3 : \quad \theta_y - \tau(\theta - \Theta_3) &= 0, \\ \sigma_2 : \quad \theta_x + \tau(\theta - \Theta_2) &= 0, & \sigma_4 : \quad \theta_y + \tau(\theta - \Theta_4) &= 0, \end{aligned} \quad (3.5.2)$$

where $\nabla \theta = (\theta_x, \theta_y)$. We can associate these linearised boundary conditions with quadratic forms of the surface energy densities in (2.2.51) via

$$(\mathbf{n} \cdot \boldsymbol{\nu})^2 \approx (\theta - \Theta_i)^2 \quad (i = 1, 2, 3, 4), \quad (3.5.3)$$

Boundary director angle	DD state
$\theta = \Theta_1$	$\pm\pi/2$ for $y \lesseqgtr \lambda/2$
$\theta = \Theta_2$	$\pm\pi/2$ for $y \lesseqgtr \lambda/2$
$\theta = \Theta_3$	0
$\theta = \Theta_4$	0

Table 3.2: The infinite anchoring angles Θ_i for the DD state found in Section 3.3.

up to an additive constant that will play no role in the minimisation of the total energy. This linear approximation of the non-linear boundary conditions will be valid everywhere except at the corners of the region, and also, at the points $(0, \lambda/2)$ and $(1, \lambda/2)$ for the DD state.

3.5.2 Solutions for the Director Angle

The assumption of isotropic elasticity reduces the equilibrium equation for the director angle (3.2.5) to Laplace's equation, which can be solved in region Γ subject to boundary conditions (3.5.2) by separation of variables. Since the system is now linear, we need only derive the solution in the case when three of the four preferred directions $\Theta_i = 0$, then employ the principle of superposition together with appropriate rescaling and rotation. One complication in our analysis is the presence of Robin boundary conditions (3.5.2) which we will show lead to eigenvalues that are solutions of a transcendental equation. Another difficulty is the piecewise nature of the boundary conditions (3.5.2) for the DD state. In the analysis that follows, we adopt one approach to derive the director angle solutions for the D, U_1 and U_2 states, with a separate method considered for the DD state.

A standard application of separation of variables is therefore used to find the solution of Laplace's equation in region Γ subject to Robin boundary conditions (3.5.2). The series solutions for the D, U_1 , and U_2 states can then be expressed

in the form

$$\begin{aligned} \theta(x, y) = \sum_{\substack{j=1 \\ j \text{ odd}}}^{\infty} \left[\Theta_1 \Phi_j \left(\frac{y}{\lambda}, \frac{1-x}{\lambda}, \frac{1}{\lambda}, \lambda\tau \right) + \Theta_2 \Phi_j \left(\frac{y}{\lambda}, \frac{x}{\lambda}, \frac{1}{\lambda}, \lambda\tau \right) \right. \\ \left. + \Theta_3 \Phi_j(x, \lambda - y, \lambda, \tau) + \Theta_4 \Phi_j(x, y, \lambda, \tau) \right]. \end{aligned} \quad (3.5.4)$$

In their most general forms, for odd and even j , $\Phi_j(U, V, \Lambda, T) = M_j \times N_j$ ($j = 1, 2, 3, \dots$), where

$$M_j(U, T) = \frac{\sqrt{2}[P_j \cos(P_j U) + T \sin(P_j U)]}{\sqrt{P_j^2 + T^2 + 2T}}, \quad (3.5.5)$$

are orthonormal with respect to $U \in (0, 1)$ and

$$\begin{aligned} N_j(V, \Lambda, T) \\ = \frac{\sqrt{2}T^2[(P_j^2 + T^2) \cos(P_j) + P_j^2 - T^2][P_j \cosh(P_j V) + T \sinh(P_j V)]}{P_j(P_j^2 - T^2)\sqrt{P_j^2 + T^2 + 2T}[(P_j^2 + T^2) \sinh(P_j \Lambda) + 2P_j T \cosh(P_j \Lambda)]}. \end{aligned}$$

The eigenvalues $P_j(T)$ are the positive solutions of the transcendental equation

$$(P_j^2 - T^2) \tan(P_j) - 2TP_j = 0 \quad (j = 1, 2, 3, \dots). \quad (3.5.6)$$

For large T (representing an anchoring parameter), we can simplify and solve (3.5.6) to find

$$P_j = j\pi \left(1 - \frac{2}{T} \right) + O\left(\frac{1}{T^2} \right) \quad (j = 1, 2, 3, \dots). \quad (3.5.7)$$

Therefore, P_j must lie in the second quadrant for j odd and the fourth quadrant for j even, both corresponding to $\tan(P_j) < 0$. Restating (3.5.6) in terms of T (> 0), we find that

$$T = (-1)^{j+1} P_j [\tan(P_j/2)]^{(-1)^{j+1}} \quad (j = 1, 2, 3, \dots). \quad (3.5.8)$$

However, upon substitution of (3.5.8) into (3.5.6), we find that $N_j(V, \Lambda, T) = 0$ for j even, hence the reason j is restricted to odd, positive integers in (3.5.4). Therefore, the only contributions to the solution for $\theta(x, y)$ come from eigenvalues $P_j(T)$ lying in the second quadrant satisfying the transcendental equation

$$T - P_j \tan(P_j/2) = 0, \quad P_j \in (j\pi - \pi/2, j\pi) \quad (j = 1, 3, 5, \dots). \quad (3.5.9)$$

Furthermore, if we also replace T in Φ_j with $P_j \tan(P_j/2)$ (odd $j \geq 1$), we eventually obtain the simplified form for Φ_j ,

$$\begin{aligned} \Phi_j(U, V, \Lambda, T) = & \frac{2[\cosh(P_j V) \cos(P_j/2) + \sinh(P_j V) \sin(P_j/2)]}{\cosh(P_j \Lambda) \sin(P_j) + \sinh(P_j \Lambda)} \\ & \times \frac{\cos(P_j(U - 1/2))[1 - \cos(P_j)]}{\sin(P_j) + P_j}. \end{aligned} \quad (3.5.10)$$

This expression is then used to construct the solution $\theta(x, y)$ for the D, U_1 , and U_2 states. We see immediately from equation (3.5.10) that Φ_j is symmetric with respect to $U = 1/2$ through a single U -dependent term, $\cos(P_j(U - 1/2))$. This will lead to symmetry in the x or y direction for each particular state, depending on the combination of terms in solution (3.5.4) and the appropriate Θ_i ($i = 1, 2, 3, 4$). It is less obvious from the nature of the V -dependent term in Φ_j , but when combined with the different choices of Θ_i in equation (3.5.4), symmetry or anti-symmetry is also introduced for the other x or y coordinate through the addition of the hyperbolic terms.

The DD solution can also be found by separation of variables, although the derivation is slightly different due to the piecewise nature of boundary condition (3.5.2). By recognising that the DD state is characterised by a symmetry about $x = 1/2$ and an anti-symmetry about $y = \lambda/2$, we seek a series solution for the director angle of the form

$$\theta(x, y) = \sum_{j=1}^{\infty} A_j \cosh\left(\frac{Q_j(2x-1)}{\lambda}\right) \sin\left(\frac{Q_j(2y-\lambda)}{\lambda}\right), \quad (3.5.11)$$

with eigenvalues Q_j and the unknown coefficients A_j to be determined. Following some relatively straightforward calculations, we obtain the following series solution for the director angle $\theta(x, y)$ of the DD state:

$$\begin{aligned} \theta(x, y) = & \sum_{j=1}^{\infty} \frac{\pi \cos(Q_j)(\cos(Q_j) - 1)}{[\cos(Q_j) \sin(Q_j) - Q_j][\sinh(Q_j/\lambda) \sin(Q_j) - \cosh(Q_j/\lambda) \cos(Q_j)]} \\ & \times \cosh\left(\frac{Q_j(2x-1)}{\lambda}\right) \sin\left(\frac{Q_j(2y-\lambda)}{\lambda}\right), \end{aligned} \quad (3.5.12)$$

where the eigenvalues Q_j are the positive solutions which satisfy the transcendental equation

$$\lambda \tau \tan(Q_j) + 2Q_j = 0. \quad (3.5.13)$$

Figure 3.8 shows the director configuration using the series solutions $\theta(x, y)$ in (3.5.4) and (3.5.12) for aspect ratio $\lambda = 1.5$ and anchoring strength $\tau = 100$, with the infinite series truncated to a maximum $j = 20$. This truncation limit for j was chosen so that the solutions (3.5.4) and (3.5.12) had an average relative error of less than 1% compared to the numerical solution of the equivalent full non-linear system. Comparing the director profiles in Figure 3.8 with those in Figure 3.3, we see that a relatively large anchoring strength forces the liquid crystal in the bulk to adopt director structures very similar to those found in Lewis *et al.* [86] using infinite anchoring boundary conditions. Our solutions differ from those in [86] at the corners, where, as mentioned previously, the series solution for the director angle (3.1.1) is not valid.

To illustrate the behaviour at the corners, we plot the director angle at the corner $(1, \lambda)$ for various anchoring strengths for both the U_1 and U_2 states when the aspect ratio $\lambda = 1.5$ in Figure 3.9. The solid curves are the values obtained by solving (3.2.5) subject to the non-linear boundary conditions (3.2.6) in COMSOL, while the dashed curves are obtained by solving the linearised system in COMSOL. This approach proved to be far more efficient compared to using the series solution (3.5.4), where many more modes were required than that used in Figure 3.8 in order to get a good approximation for $\theta(x, y)$ at the corners. There is clearly a discrepancy between the linear and non-linear results when τ is far from the large anchoring strength limit. However, the difference between the two approaches reduces as τ increases, with the two results indistinguishable at large τ , highlighting the effectiveness of our linearisation approach.

3.5.3 Asymptotic Approximations of the Energy

Having found the equilibrium solutions (3.5.4) and (3.5.12), we can calculate the total free energy W in (3.2.4) associated with the director structure, albeit using the quadratic forms of the surface energy densities (3.5.3). Although W is now quadratic in $\theta(x, y)$, through both the elastic and surface energy terms, it is possible to simplify the expression using Green's First Identity [130] and the

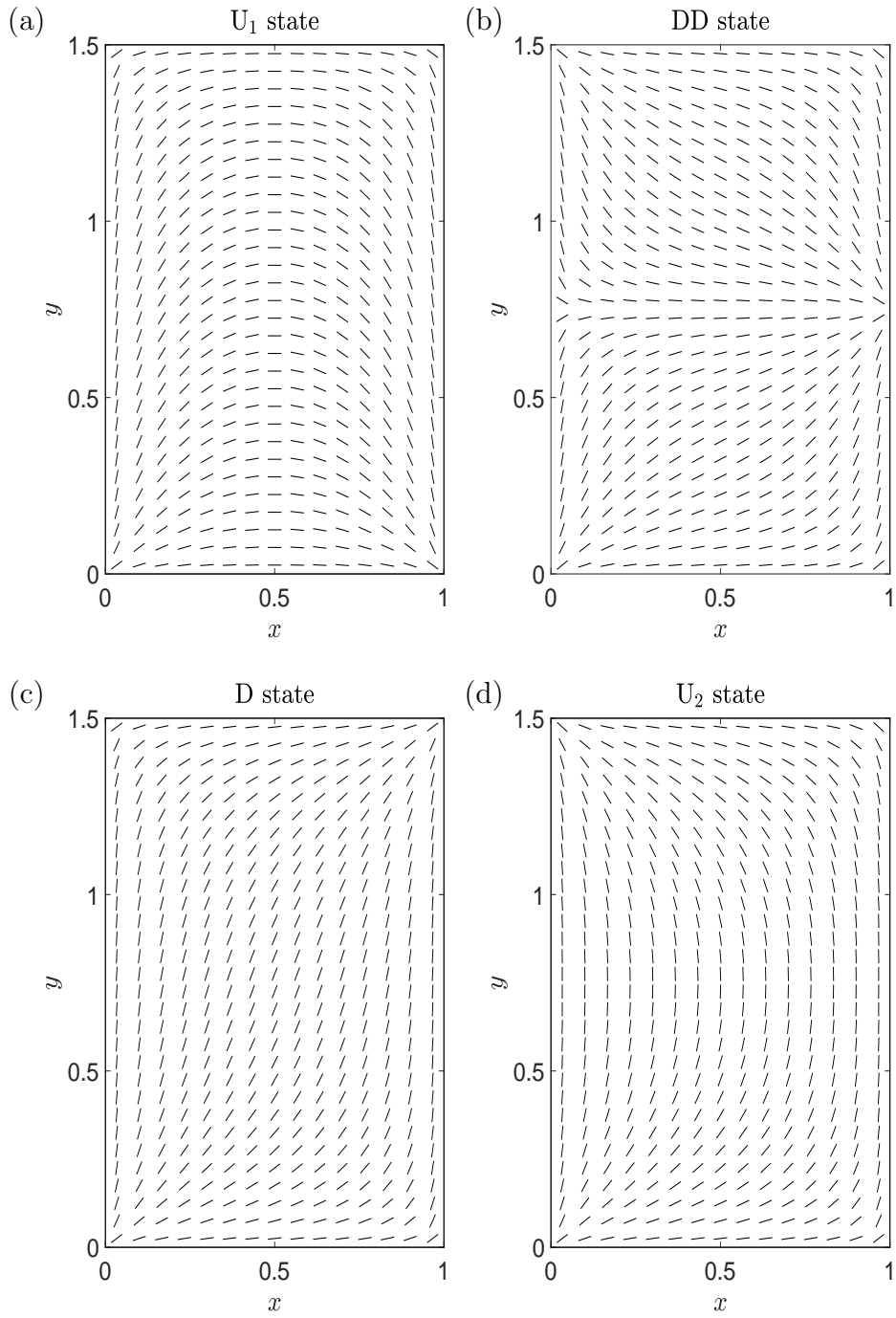


Figure 3.8: Director configuration for the series solutions (3.5.4) and (3.5.12) truncated to 20 terms in the expansions. The four profiles correspond to the four sets of preferred directions in Table 3.2 for the different bifurcation states. Aspect ratio $\lambda = 1.5$ and anchoring strength $\tau = 100$.

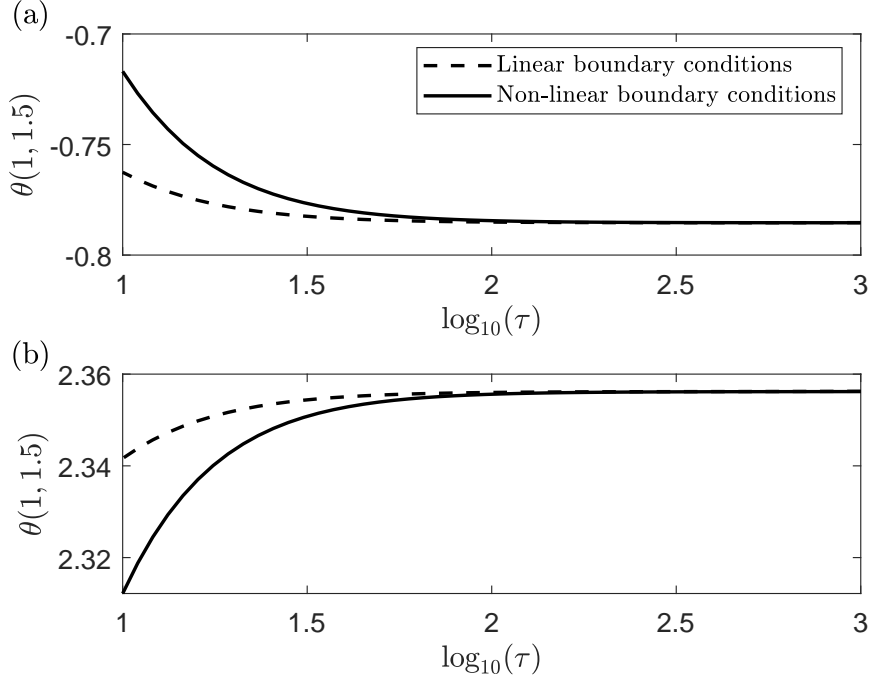


Figure 3.9: Variation of the director angle with the anchoring strength at the corner $(1, 1.5)$ for the nematic states (a) U_1 and (b) U_2 when the aspect ratio $\lambda = 1.5$. The dashed curves are obtained using (3.5.4) for the linear boundary conditions, whereas the solid curves are calculated numerically for the system subject to non-linear boundary conditions.

boundary condition (3.5.2):

$$\begin{aligned}
W &\approx \int_0^\lambda \int_0^1 (\theta_x^2 + \theta_y^2) dx dy + \sum_{j=1}^4 \tau \int_{\sigma_j} (\theta - \Theta_j)^2 d\sigma_j \\
&= \sum_{j=1}^4 \int_{\sigma_j} \theta(\boldsymbol{\nu} \cdot \nabla \theta) + \tau(\theta - \Theta_j)^2 d\sigma_j \\
&= \sum_{j=1}^4 \int_{\sigma_j} -\tau\theta(\theta - \Theta_j) + \tau(\theta - \Theta_j)^2 d\sigma_j \\
&= \sum_{j=1}^4 \tau\Theta_j \int_{\sigma_j} (\Theta_j - \theta) d\sigma_j.
\end{aligned} \tag{3.5.14}$$

The free energy can now be calculated using the series solutions (3.5.4) and (3.5.12), and integrated along the four boundaries. As was the case in deriving the series solutions for the director angle, we adopt one approach to calculate

the asymptotic energies of the D, U_1 and U_2 states, and consider an alternative method for the DD state energy.

We first consider the energy of the D state, which is calculated to be

$$W_D \approx \frac{\lambda\tau\pi^2}{2} + \sum_{\substack{j=1 \\ j \text{ odd}}}^{\infty} \mathcal{E}_j(1 + \mathcal{F}_j), \quad (3.5.15)$$

where

$$\mathcal{E}_j = \frac{-4\pi^2\lambda^4\tau^4}{P_j^2(\lambda\tau + P_j)(\lambda^2\tau^2 + P_j^2 + 2\lambda\tau)}, \quad (3.5.16)$$

$$\mathcal{F}_j = \frac{P_j[(\lambda\tau + P_j)\operatorname{sech}(P_j/\lambda) + (\lambda\tau - P_j)(\tanh(P_j/\lambda) - 1)]}{(\lambda^2\tau^2 + P_j^2)\tanh(P_j/\lambda) + 2P_j\lambda\tau}, \quad (3.5.17)$$

and the positive eigenvalues P_j (odd $j \geq 1$) satisfy the transcendental equation

$$\lambda\tau - P_j \tan(P_j/2) = 0, \quad P_j \in (j\pi - \pi/2, j\pi). \quad (3.5.18)$$

In order to derive a compact expression for the W_D energy, we first consider the term (3.5.16). Given that we consider large anchoring strengths, we can simplify and solve the transcendental equation (3.5.18) to obtain

$$P_j = j\pi \left(1 - \frac{2}{\lambda\tau}\right) + O\left(\frac{1}{\tau^2}\right) \quad (j = 1, 3, 5, \dots). \quad (3.5.19)$$

This allows us to approximate \mathcal{E}_j as

$$\mathcal{E}_j \approx \frac{-4\lambda^9\tau^9}{(\lambda\tau - 2)^2 j^2 (j\pi(\lambda\tau - 2) + \lambda^2\tau^2) (j^2\pi^2(\lambda\tau - 2)^2 + \lambda^3\tau^3(\lambda\tau + 2))}. \quad (3.5.20)$$

It is possible to express the sum of this approximation for \mathcal{E}_j by expanding the partial fractions in \mathcal{E}_j in terms of j and using the identity

$$\Psi(z) = -\gamma + \sum_{n=0}^{\infty} \left(\frac{1}{n+1} - \frac{1}{n+z} \right), \quad (z \neq 0, -1, -2, \dots), \quad (3.5.21)$$

where $\Psi(z)$ is the digamma function [1] and $\gamma \approx 0.57721$ is the Euler-Mascheroni constant. We define $\mathcal{E}_{\text{sum}}(\lambda, \tau)$ as the sum of the rational approximation for \mathcal{E}_j

over odd j from $j = 1$ to ∞ . Following this approach, we obtain

$$\begin{aligned}
\mathcal{E}_{\text{sum}}(\lambda, \tau) &\approx \sum_{\substack{j=1 \\ j \text{ odd}}}^{\infty} \frac{-4\lambda^9\tau^9}{(\lambda\tau - 2)^2 j^2 (j\pi(\lambda\tau - 2) + \lambda^2\tau^2) (j^2(\lambda\tau - 2)^2 + \lambda^3\tau^3(\lambda\tau + 2))} \\
&= \frac{\pi\lambda^2\tau^2}{2(\lambda^2\tau^2 - 4)} \left\{ \frac{\lambda\tau(\sqrt{\lambda\tau + 2} + i\sqrt{\lambda\tau})}{(\lambda\tau + 1)\sqrt{\lambda\tau + 2}} \Psi\left(\frac{1}{2} - \frac{i\lambda\tau\sqrt{\lambda\tau(\lambda\tau + 2)}}{2\pi(\lambda\tau - 2)}\right) \right. \\
&\quad + \frac{\lambda\tau(\sqrt{\lambda\tau + 2} - i\sqrt{\lambda\tau})}{(\lambda\tau + 1)\sqrt{\lambda\tau + 2}} \Psi\left(\frac{1}{2} + \frac{i\lambda\tau\sqrt{\lambda\tau(\lambda\tau + 2)}}{2\pi(\lambda\tau - 2)}\right) + 8\ln(2) \\
&\quad \left. + 4\gamma - \frac{\pi\tau^2\lambda^2}{\lambda\tau - 2} + \frac{2(\lambda\tau + 2)}{\lambda\tau + 1} \Psi\left(\frac{1}{2} + \frac{\lambda^2\tau^2}{2\pi(\lambda\tau - 2)}\right) \right\}. \quad (3.5.22)
\end{aligned}$$

Hence, we may now write W_D as

$$W_D \approx \frac{\lambda\tau\pi^2}{2} + \mathcal{E}_{\text{sum}}(\lambda, \tau) + \sum_{\substack{j=1 \\ j \text{ odd}}}^{\infty} \mathcal{E}_j \mathcal{F}_j. \quad (3.5.23)$$

Asymptotic expansions for $\mathcal{E}_{\text{sum}}(\lambda, \tau)$ and $\mathcal{E}_j \mathcal{F}_j$ are then possible as $\tau \rightarrow \infty$,

$$\mathcal{E}_{\text{sum}}(\lambda, \tau) \approx 2\pi \left[\ln(\tau) + \ln\left(\frac{2\lambda}{\pi}\right) - \frac{\pi\lambda\tau}{4} - \frac{\pi}{4} + \gamma \right], \quad (3.5.24)$$

$$\sum_{\substack{j=1 \\ j \text{ odd}}}^{\infty} \mathcal{E}_j \mathcal{F}_j \approx 2\pi \left[s_1\left(\frac{1}{\lambda}\right) - s_2\left(\frac{1}{\lambda}\right) \right], \quad (3.5.25)$$

where the imaginary parts of $\mathcal{E}_{\text{sum}}(\lambda, \tau)$ disappear and, following the same notation adopted in Lewis *et al.* [86], we have introduced the functions

$$s_1(\Lambda) = 2 \sum_{\substack{j=1 \\ j \text{ odd}}}^{\infty} \frac{\coth(j\pi\Lambda) - 1}{j}, \quad s_2(\Lambda) = 2 \sum_{\substack{j=1 \\ j \text{ odd}}}^{\infty} \frac{\text{csch}(j\pi\Lambda)}{j}. \quad (3.5.26)$$

Hence, the final asymptotic expansion for W_D in the limit as $\tau \rightarrow \infty$ is

$$W_D = 2\pi \left[\ln(\tau) + \ln\left(\frac{2\lambda}{\pi}\right) - \frac{\pi}{4} + \gamma + s_1\left(\frac{1}{\lambda}\right) - s_2\left(\frac{1}{\lambda}\right) \right] + O\left(\frac{\ln(\tau)}{\tau}\right). \quad (3.5.27)$$

Following similar analyses, we can derive the asymptotic expansions of the energies for the U_1 and U_2 states,

$$W_{U_1} = 2\pi \left[\ln(\tau) + \ln\left(\frac{2\lambda}{\pi}\right) - \frac{\pi}{4} + \gamma + s_1\left(\frac{1}{\lambda}\right) + s_2\left(\frac{1}{\lambda}\right) \right] + O\left(\frac{\ln(\tau)}{\tau}\right), \quad (3.5.28)$$

$$W_{U_2} = 2\pi \left[\ln(\tau) + \ln\left(\frac{2}{\pi}\right) - \frac{\pi}{4} + \gamma + s_1(\lambda) + s_2(\lambda) \right] + O\left(\frac{\ln(\tau)}{\tau}\right). \quad (3.5.29)$$

Although their analysis of the energy in a rectangular well employed a different approach, Lewis *et al.* [86] derived asymptotic energies for the different states that are similar to our expressions in a number terms (for example, those involving $\ln(\tau)$, $\ln(2\lambda/\pi)$ and the $s_1(\cdot)$, $s_2(\cdot)$ functions), but we have additional terms at $O(1)$ which are missing from [86]. Presumably this is due to the need in [86] to remove parts of the region (at the corners) to produce an analytically tractable problem.

It is more difficult to obtain the asymptotic approximation of the energy for the DD state compared to the other three states. In [147], we assume that in the limit of strong anchoring, the asymptotic energy for the DD state is twice the energy of the D state with the aspect ratio λ replaced by $\lambda/2$. Here, we consider an alternative approach using the series solution (3.5.12). First, we substitute (3.5.12) into (3.5.14) to obtain

$$W_{\text{DD}} \approx \frac{\pi^2 \lambda \tau}{2} + \sum_{j=1}^{\infty} (w_j + w_j^{\text{trig}} + w_j^{\text{hyp}}), \quad (3.5.30)$$

where

$$w_j = -\frac{2\pi^2 \lambda^2 \tau^2 (\lambda^2 \tau^2 + 2Q_j^2)}{Q_j^2 (\lambda^2 \tau^2 + 4Q_j^2 + 2\lambda\tau)(\lambda\tau + 2Q_j)}, \quad (3.5.31)$$

$$w_j^{\text{trig}} = \frac{2\pi^2 \lambda^2 \tau^2 (\lambda^2 \tau^2 + 4Q_j^2) \cos(Q_j)}{Q_j^2 (\lambda^2 \tau^2 + 4Q_j^2 + 2\lambda\tau)(\lambda\tau + 2Q_j)}, \quad (3.5.32)$$

$$w_j^{\text{hyp}} = \frac{4\pi^2 \lambda^2 \tau^2 (1 - \tanh(Q_j/\lambda)) + \lambda^2 \tau^2 (\cos(Q_j) - 1) + 2Q_j^2 (2 \cos(Q_j) - 1)}{Q_j (\lambda^2 \tau^2 + 4Q_j^2 + 2\lambda\tau)(\lambda\tau + 2Q_j)(\lambda\tau + 2Q_j \tanh(Q_j/\lambda))}. \quad (3.5.33)$$

As with the D state, we are able to simplify and solve the transcendental equation (3.5.13) for large anchoring strengths,

$$Q_j = j\pi \left(1 - \frac{2}{\lambda\tau}\right) + O\left(\frac{1}{\tau^2}\right), \quad (3.5.34)$$

where $j \in \mathbb{Z}^+$. We now examine the asymptotic behaviours for each of the individual contributions to the energy (3.5.31)–(3.5.33) in the limit of large anchoring strength. We first consider the contribution given by (3.5.34). If we substitute (3.5.34) into (3.5.31) and compute the sum over $j \in \mathbb{Z}^+$, we obtain an expression

in terms of the digamma function, namely,

$$\begin{aligned}
\sum_{j=1}^{\infty} w_j &= \frac{\pi(\lambda\tau)^2(i\sqrt{\lambda\tau} + \sqrt{\lambda\tau + 2})}{2(\lambda\tau + 1)(\lambda\tau + 2)^{3/2}} \Psi\left(1 - \frac{i(\lambda\tau)^{3/2}\sqrt{\lambda\tau + 2}}{2\pi(\lambda\tau - 2)}\right) \\
&\quad - \frac{\pi(\lambda\tau)^2(i\sqrt{\lambda\tau} - \sqrt{\lambda\tau + 2})}{2(\lambda\tau + 1)(\lambda\tau + 2)^{3/2}} \Psi\left(1 + \frac{i(\lambda\tau)^{3/2}\sqrt{\lambda\tau + 2}}{2\pi(\lambda\tau - 2)}\right) \\
&\quad + \frac{3\pi(\lambda\tau)^2}{(\lambda\tau - 2)(\lambda\tau + 1)} \Psi\left(1 + \frac{(\lambda\tau)^2}{2\pi(\lambda\tau - 2)}\right) \\
&\quad - \frac{\pi(\lambda\tau)^2(\pi(\lambda\tau)^2 - 12\gamma(\lambda\tau - 2))}{3(\lambda\tau - 2)^2(\lambda\tau + 2)}. \tag{3.5.35}
\end{aligned}$$

The asymptotic expansion of (3.5.35) in the limit $\tau \rightarrow \infty$ yields

$$\sum_{j=1}^{\infty} w_j \approx 4\pi \left[\ln(\tau) + \ln\left(\frac{\lambda}{2\pi}\right) + \gamma - \frac{\pi}{24} - \frac{\pi\lambda\tau}{12} \right]. \tag{3.5.36}$$

Following a similar asymptotic approximation, we also find that

$$\sum_{\substack{j=1 \\ j \text{ odd}}}^{\infty} w_j^{\text{hyp}} \approx 4\pi \left[s_1\left(\frac{2}{\lambda}\right) - s_2\left(\frac{2}{\lambda}\right) \right], \tag{3.5.37}$$

restricted to odd j because the sum of w_j^{hyp} over even j is zero. For the w_j^{trig} term in (3.5.32), we use partial fractions to rewrite w_j^{trig} as

$$w_j^{\text{trig}} = \frac{2\pi^2\lambda^2\tau^2 \cos(Q_j)}{(\lambda\tau + 2)Q_j^2} - \frac{4\lambda\tau\pi^2 \cos(Q_j)}{(\lambda\tau + 2)Q_j} + f(Q_j), \tag{3.5.38}$$

where

$$f(Q_j) = \frac{8\lambda\tau\pi^2(\lambda^2\tau^2 + 4Q_j^2 + 4\lambda\tau) \cos(Q_j)}{(\lambda^2\tau^2 + 4Q_j^2 + 2\lambda\tau)(\lambda\tau + 2Q_j)(\lambda\tau + 2)}. \tag{3.5.39}$$

The first two terms in (3.5.38) have analytic expressions for their respective sums over $j \in \mathbb{Z}$, but the term involving $f(Q_j)$ does not. Restricting our attention to the first two terms, we can show that in the limit $\tau \rightarrow \infty$,

$$\sum_{j=1}^{\infty} \frac{2\pi^2\lambda^2\tau^2 \cos(Q_j)}{(\lambda\tau + 2)Q_j^2} = 4\pi \ln(2) + O\left(\frac{1}{\tau^2}\right), \tag{3.5.40}$$

$$\sum_{j=1}^{\infty} \frac{-4\lambda\tau\pi^2 \cos(Q_j)}{(\lambda\tau + 2)Q_j} = -4\pi \left[\frac{\pi\lambda\tau}{24} + \frac{\pi}{12} \right] + O\left(\frac{1}{\tau}\right). \tag{3.5.41}$$

Despite not being able to find an analytic expression to describe the asymptotic behaviour of $f(Q_j)$, we can examine it in the limit of large anchoring strength

if we assume that $\cos(Q_j) \approx (-1)^j$. This is, in fact, the leading behaviour of $\cos(Q_j)$ in the limit $\tau \rightarrow \infty$. In making this assumption, we find that

$$\sum_{j=1}^{\infty} \frac{(-1)^j f(Q_j)}{\cos(Q_j)} = -\frac{4\pi^2}{\lambda\tau} + O\left(\frac{\ln(\tau)}{\tau^2}\right). \quad (3.5.42)$$

In the limit of $\tau \rightarrow \infty$, (3.5.42) tends to zero, and therefore does not contribute to the total sum. Combining the contributions (3.5.36), (3.5.37), (3.5.40) and (3.5.41), we obtain the asymptotic approximation of the DD state energy

$$W_{\text{DD}} = 4\pi \left[\ln(\tau) + \ln\left(\frac{\lambda}{\pi}\right) + \gamma - \frac{\pi}{8} + s_1\left(\frac{2}{\lambda}\right) - s_2\left(\frac{2}{\lambda}\right) \right] + O\left(\frac{\ln(\tau)}{\tau}\right). \quad (3.5.43)$$

There is no asymptotic energy for the DD state in [86] with which we can compare our asymptotic result. Although Lewis *et al.* [86] mention that the functions $s_1(\cdot)$, $s_2(\cdot)$ are both convergent, they do not calculate formulae for the values. The sum $s_2(\lambda)$ is expressed analytically in Bruckman [15] as

$$s_2(\lambda) = -\frac{1}{4} \ln(1-m), \quad 0 < m < 1, \quad (3.5.44)$$

where the elliptic parameter m is implicitly defined in terms of λ by $\lambda = K(1-m)/K(m)$, where

$$K(m) = \int_0^{\frac{\pi}{2}} \frac{d\theta}{\sqrt{1-m\sin^2(\theta)}} \quad (3.5.45)$$

is the complete elliptic integral of the first kind and $K(1-m)$ is the complementary elliptic integral of first kind. In order to derive a similar result for the sum $s_1(\lambda)$, we first introduce the elliptic nome $q(m)$,

$$q(m) = \exp\left(-\frac{\pi K(1-m)}{K(m)}\right) \equiv \exp(-\pi\lambda). \quad (3.5.46)$$

In terms of $q(m)$, the sum $s_1(\lambda)$ can be expressed in the form

$$s_1(\lambda) = 2 \sum_{j=1}^{\infty} [\ln(1+(q(m))^{2j}) - \ln(1-(q(m))^{2j})]. \quad (3.5.47)$$

The two infinite series in (3.5.47) have exact analytic expressions which, when combined, lead to the analytic result

$$s_1(\lambda) = -\frac{1}{4} \ln(1-m) - \ln\left(\frac{2K(m)}{\pi}\right). \quad (3.5.48)$$

Similarly, we find that the analytic expressions for the sums $s_1(1/\lambda)$ and $s_2(1/\lambda)$ are

$$s_1\left(\frac{1}{\lambda}\right) = -\frac{1}{4}\ln(m) - \ln\left(\frac{2K(1-m)}{\pi}\right), \quad (3.5.49)$$

$$s_2\left(\frac{1}{\lambda}\right) = -\frac{1}{4}\ln(m). \quad (3.5.50)$$

Hence, the asymptotic energies for each state now reduce to

$$W_D \approx 2\pi \left[\ln(\tau) - \frac{\pi}{4} + \gamma - \ln(K(m)) \right], \quad (3.5.51)$$

$$W_{U_1} \approx W_D - \pi \ln(m), \quad (3.5.52)$$

$$W_{U_2} \approx W_D - \pi \ln(1-m), \quad (3.5.53)$$

$$W_{DD} \approx 2W_D \left(\frac{\lambda}{2}\right) + \frac{\pi^2}{2}. \quad (3.5.54)$$

The differences between the approximate energies in equations (3.5.51)–(3.5.54) and the numerically calculated energies for the full non-linear problem using Rapini–Papoular boundary conditions (3.2.6) are shown in Figure 3.10, where $\Delta W = W_{\text{numerical}} - W_{\text{asymptotic}}$. In the limit of large anchoring strength, these differences are the errors due to the linear approximation of the boundary conditions close to the corners of the region. It is at the corners of the region, as well as the midpoints of the two sidewalls $x = 0$ and $x = 1$ for the DD state, where the linearisation breaks down due to non-linear effects and leads to an offset between the asymptotic and numerical results. However, comparison of energies (3.5.51)–(3.5.54) with numerical calculations for the non-linear system, restricting attention to large values of τ , indicates that this error is neither a function of λ nor τ . This suggests that, in the leading order, $O(\ln(\tau))$, and first order, $O(1)$, terms, these errors need only be obtained numerically once, and are the same for all instances of a nematic confined in a rectangular region being independent of any geometric or material properties. It should be noted that the parameter independence of these constants, ϵ_{DU} and ϵ_{DD} in the expressions below, is obtained numerically and we have not proved the result analytically. However, after extensive calculations for a wide range of physically relevant parameters, we can have a high level of confidence in this assertion. The asymptotic results for

the four full non-linear energies are then

$$W_D = 2\pi \left[\ln(\tau) + \ln\left(\frac{2\lambda}{\pi}\right) - \frac{\pi}{4} + \gamma + s_1\left(\frac{1}{\lambda}\right) - s_2\left(\frac{1}{\lambda}\right) + \epsilon_{DU} \right] + O\left(\frac{\ln(\tau)}{\tau}\right), \quad (3.5.55)$$

$$W_{U_1} = 2\pi \left[\ln(\tau) + \ln\left(\frac{2\lambda}{\pi}\right) - \frac{\pi}{4} + \gamma + s_1\left(\frac{1}{\lambda}\right) + s_2\left(\frac{1}{\lambda}\right) + \epsilon_{DU} \right] + O\left(\frac{\ln(\tau)}{\tau}\right), \quad (3.5.56)$$

$$W_{U_2} = 2\pi \left[\ln(\tau) + \ln\left(\frac{2}{\pi}\right) - \frac{\pi}{4} + \gamma + s_1(\lambda) + s_2(\lambda) + \epsilon_{DU} \right] + O\left(\frac{\ln(\tau)}{\tau}\right), \quad (3.5.57)$$

$$W_{DD} = 4\pi \left[\ln(\tau) + \ln\left(\frac{\lambda}{\pi}\right) - \frac{\pi}{8} + \gamma + s_1\left(\frac{2}{\lambda}\right) - s_2\left(\frac{2}{\lambda}\right) + \epsilon_{DD} \right] + O\left(\frac{\ln(\tau)}{\tau}\right), \quad (3.5.58)$$

where $\epsilon_{DU} \simeq -0.068$ and $\epsilon_{DD} \simeq -0.169$. From equations (3.5.56)–(3.5.57), we see that the expressions for W_{U_1} and W_{U_2} coincide for the special case of a square domain, i.e., $\lambda = 1$, for which $m = 1/2$. This is to be expected from the symmetry of a square nematic well. When λ is small, for which m is close to 1, it follows from equations (3.5.51) and (3.5.52) that the asymptotic behaviour of W_D is very similar to that of W_{U_1} . The same can be said of W_D and W_{U_2} when λ is large, corresponding to m close to zero. We can find similar relationships between W_{DD} and W_{U_1} or W_{U_2} , except that the constant error $\epsilon_{DU} \neq \epsilon_{DD}$ due to the presence of high distortion regions at the midpoints of the sidewalls $x = 0$ and $x = 1$. The asymptotic expansions for the U_1 and U_2 states differ from the D state through the logarithmic terms in (3.5.52) and (3.5.53), respectively. Therefore, since $m \in (0, 1)$, it follows that, in the limit $\tau \rightarrow \infty$, W_D is the state with lowest energy.

3.5.4 Comparison of Analytic and Numerical Energies

We can now compare various aspects of the approximate asymptotic expansions in equations (3.5.55)–(3.5.58) to the energies derived from the numerical solution

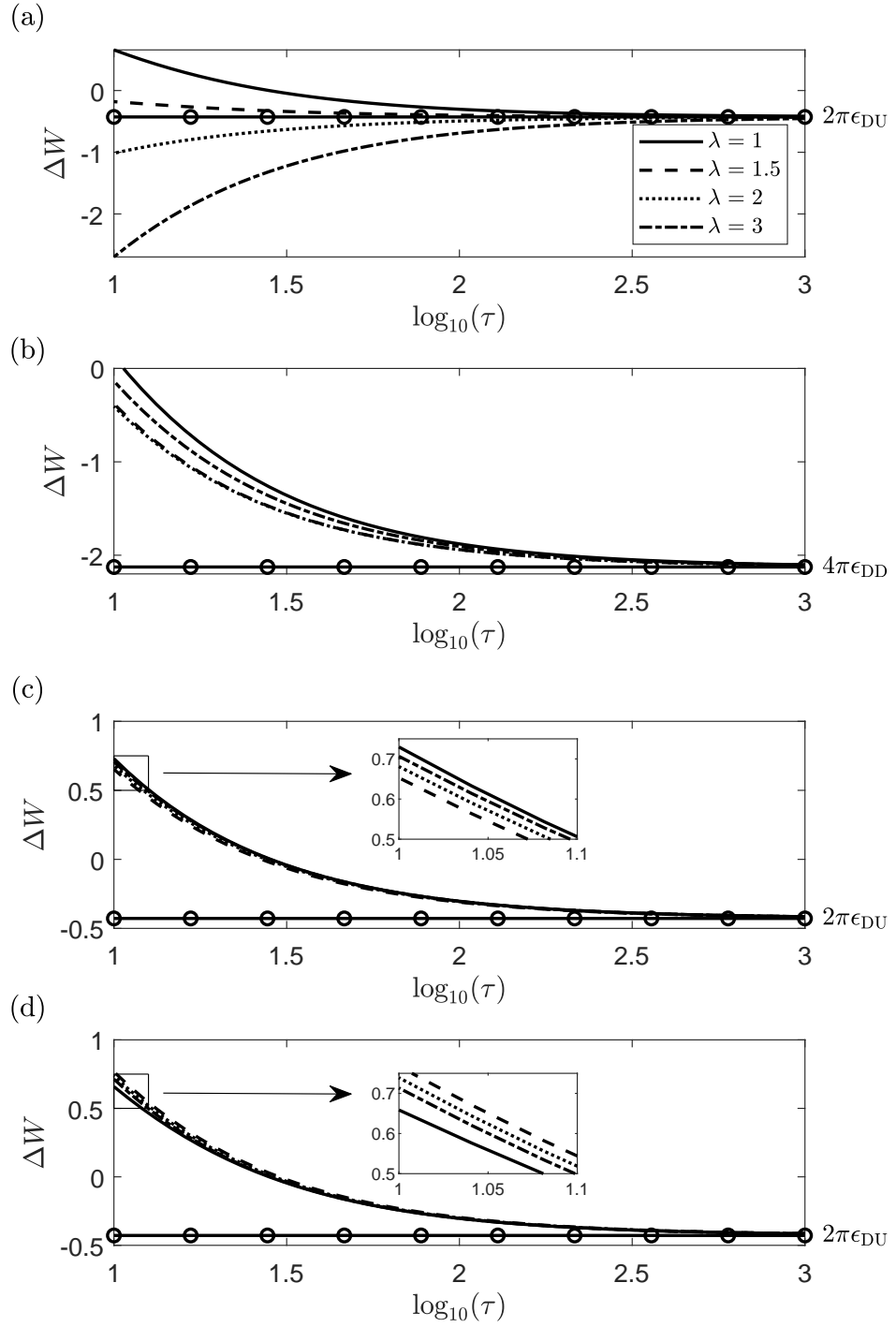


Figure 3.10: The energy differences ΔW for the (a) U_1 , (b) DD, (c) D and (d) U_2 states as the anchoring strength varies. Each curve corresponds to the energy difference at a different aspect ratio. The solid lines with markers are the errors due to the linear approximation of the boundary conditions.

of the full non-linear problem. Unlike the previous section, we consider a range of anchoring strengths, including those close to the critical bifurcation values derived in the analysis of very weak anchoring. We solve the full non-linear system using COMSOL with a non-uniform mesh, refined at the corners and sides of the region, such that further refinement does not alter the numerical energy calculation by more than 1%.

In Figure 3.11 we plot the four asymptotic energy expansions from equations (3.5.55)–(3.5.58), up to $O(\tau^{-1} \ln(\tau))$, against λ for $\tau = 10$ and $\tau = 100$ (dashed curves). In addition, we also plot the numerical energies for the non-linear system (solid curves). As expected, there is a significant difference between the asymptotic forms and numerical results for a relatively small value of $\tau = 10$, whereas for a large value $\tau = 100$, the leading terms in the asymptotic results show good accuracy over a range of aspect ratios λ .

Figure 3.12 combines our previous analytic results for bifurcations from the trivial states and strong anchoring, and compares them to the energies obtained numerically (solid curves) for $\lambda = 1.5$. The solutions in equations (3.3.8) and (3.3.9) provide approximate energies for the weakly anchored system close to the bifurcations from the trivial states (small τ , dash-dot curves), while the asymptotic behaviour as $\tau \rightarrow \infty$ is given by the leading terms in equations (3.5.55)–(3.5.58) (large τ , dashed curves). The asymptotic energies for all four nematic equilibria have been calculated for anchoring strengths $\tau \geq 10$. The energies of the trivial states, W_0 and $W_{\pi/2}$, are also indicated. Note that it is difficult to distinguish the graphs of the U_2 and D states in Figure 3.12(b), as was suggested by the forms of the asymptotic expansions in equations (3.5.55) and (3.5.57). The analytic approximate energies agree very well with the equivalent numerical graphs at anchoring strengths that are close to the bifurcation from the trivial states and also at large values of τ , with less than 1% discrepancy for $\tau \gtrsim 10^2$.

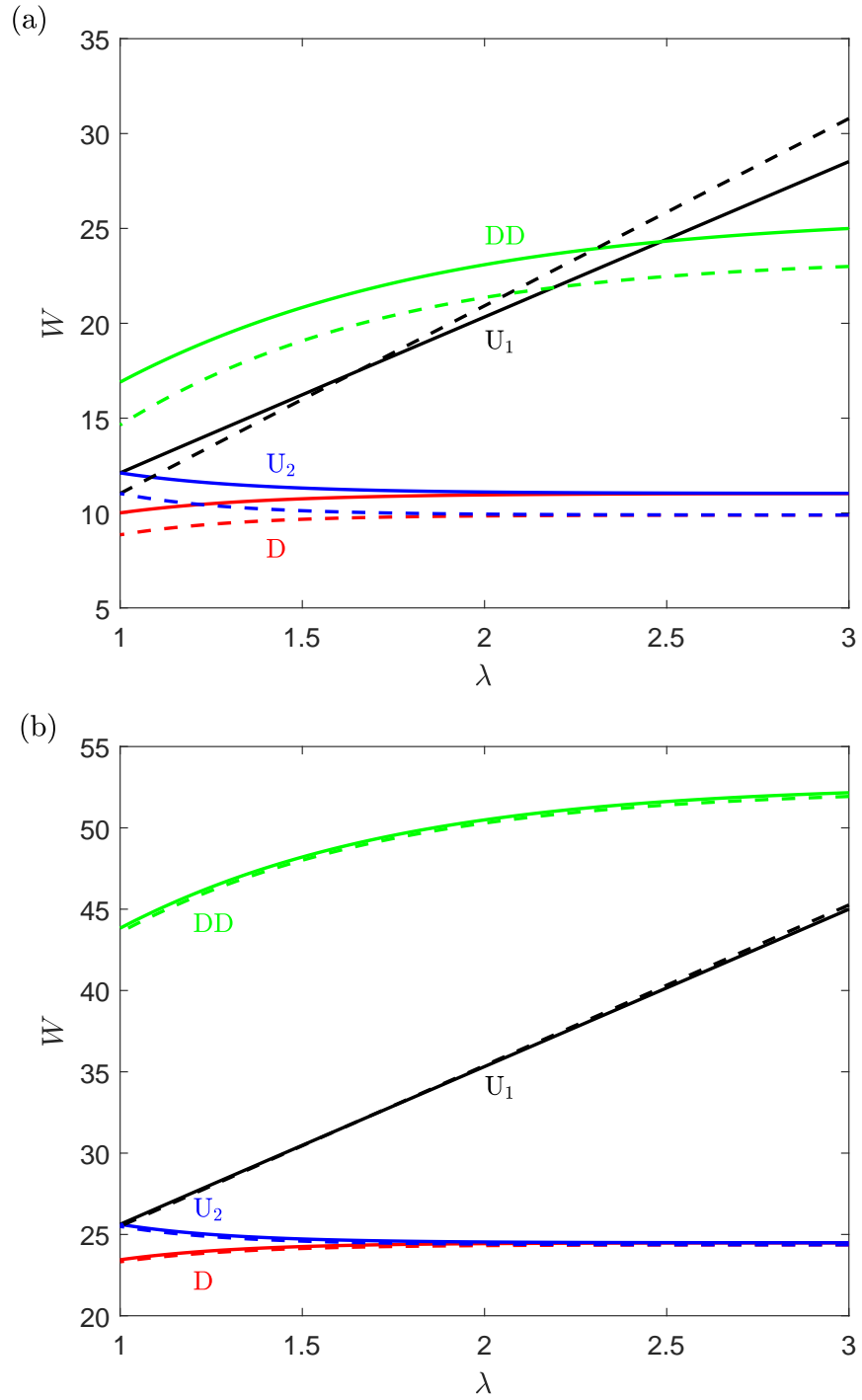


Figure 3.11: Comparison of the leading terms in the asymptotic energy expansions in equations (3.5.55)–(3.5.58) (dashed curves) with numerical calculations (solid curves) for (a) $\tau = 10$ and (b) $\tau = 100$.

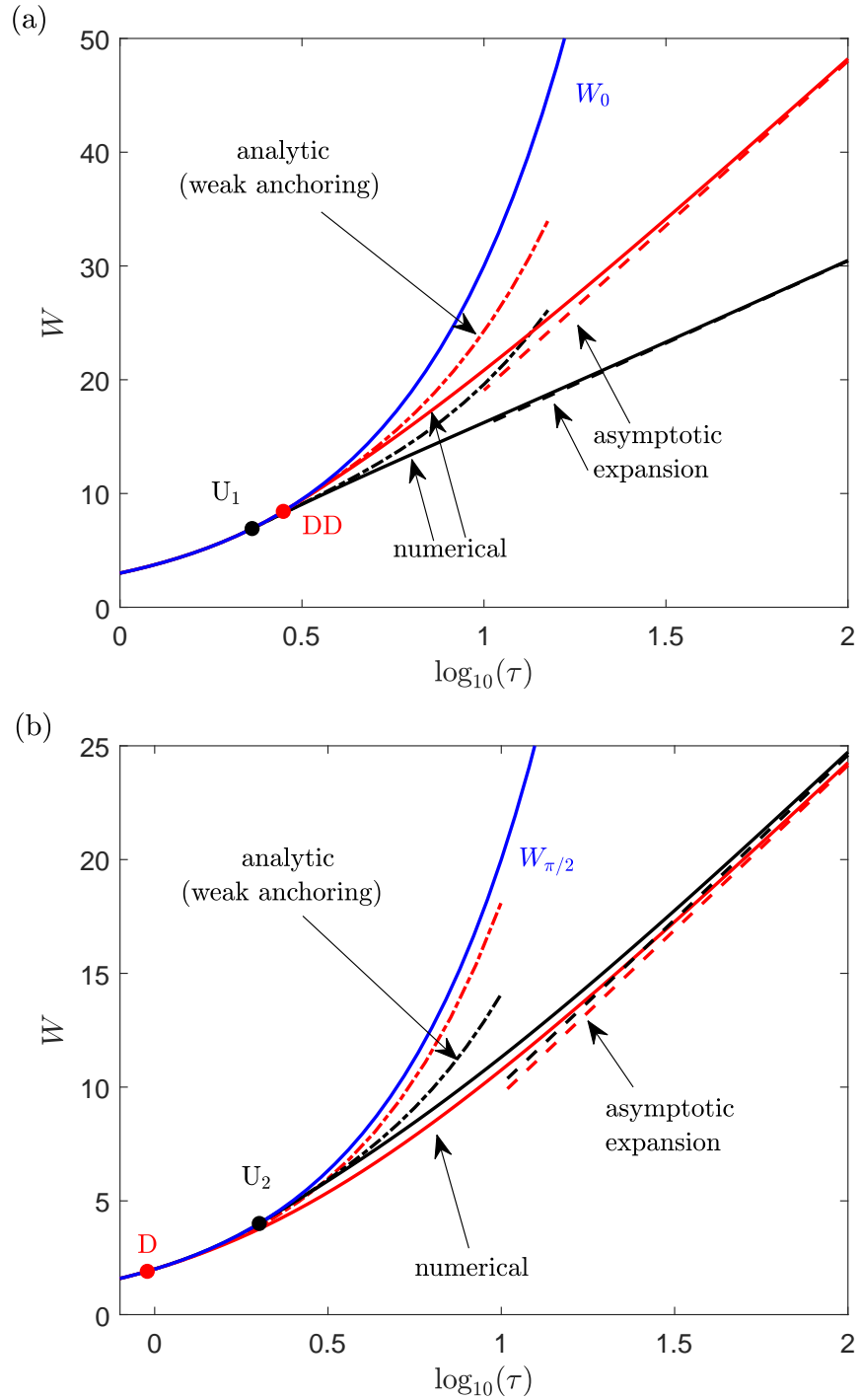


Figure 3.12: Comparison of the numerically obtained energies (solid curves) with the approximate analytic forms derived from (a) equation (3.3.8) and (b) equation (3.3.9), close to the bifurcation from the trivial states (a) $\theta = 0$ and (b) $\theta = \pi/2$ (dash-dot), and for the leading terms in the high τ asymptotic expansion (dashed curves) as a function of τ for $\lambda = 1.5$. To illustrate, the analytic (weak anchoring energy) curves are drawn for (a) $\tau \leq 15$ and (b) $\tau \leq 10$ as appropriate.

3.5.5 Comparison of Numerical Energies in the Limit of Large Anchoring Strength

To conclude this section, we now show how the energies calculated numerically using the non-linear and linear boundary conditions compare in the limit of large anchoring strength. Our calculations in the previous subsection suggest that the differences between the asymptotic and numerical energies for each state is independent of the aspect ratio λ and anchoring strength parameter τ in the large anchoring strength limit. These differences arise due to the linear approximation of the boundary conditions close to the corners of the region, as well as close to the points $(0, \lambda/2)$ and $(1, \lambda/2)$ for the DD state. The parameter independence of the constants ϵ_{DU} and ϵ_{DD} in the limit of strong anchoring is easier to deduce when we calculate the differences in the numerical energies obtained from the non-linear and linear boundary conditions, as shown in Figure 3.13, where the energy difference is given by $\Delta W = W_{\text{non-linear}} - W_{\text{linear}}$.

In Figure 3.14, we show the numerical energies for each of the states against the aspect ratio λ calculated from the linearised system (dashed curves) and the non-linear system (solid curves) at anchoring strengths (a) $\tau = 10$ and (b) $\tau = 100$. As was also the case when the full numerical and asymptotic energies were compared in Chapter 3, we find that there is a significant difference between the two energies for a weaker level of anchoring strength of $\tau = 10$. By contrast, for a larger anchoring strength of $\tau = 100$, there is better agreement between the two energies. At higher anchoring strength, the difference between the two energies are the errors calculated in Figure 3.13.

Figure 3.15 shows the bifurcations of each of the non-trivial states from the corresponding trivial states, with the non-linear energies (solid curves) compared to the energies calculated numerically from the linearised system (dashed curves) in the limit of strong anchoring for $\lambda = 1.5$. The energies of the trivial states have also been included. As the anchoring strength further increases, we again find that there is very good agreement between the two sets of numerical energies.

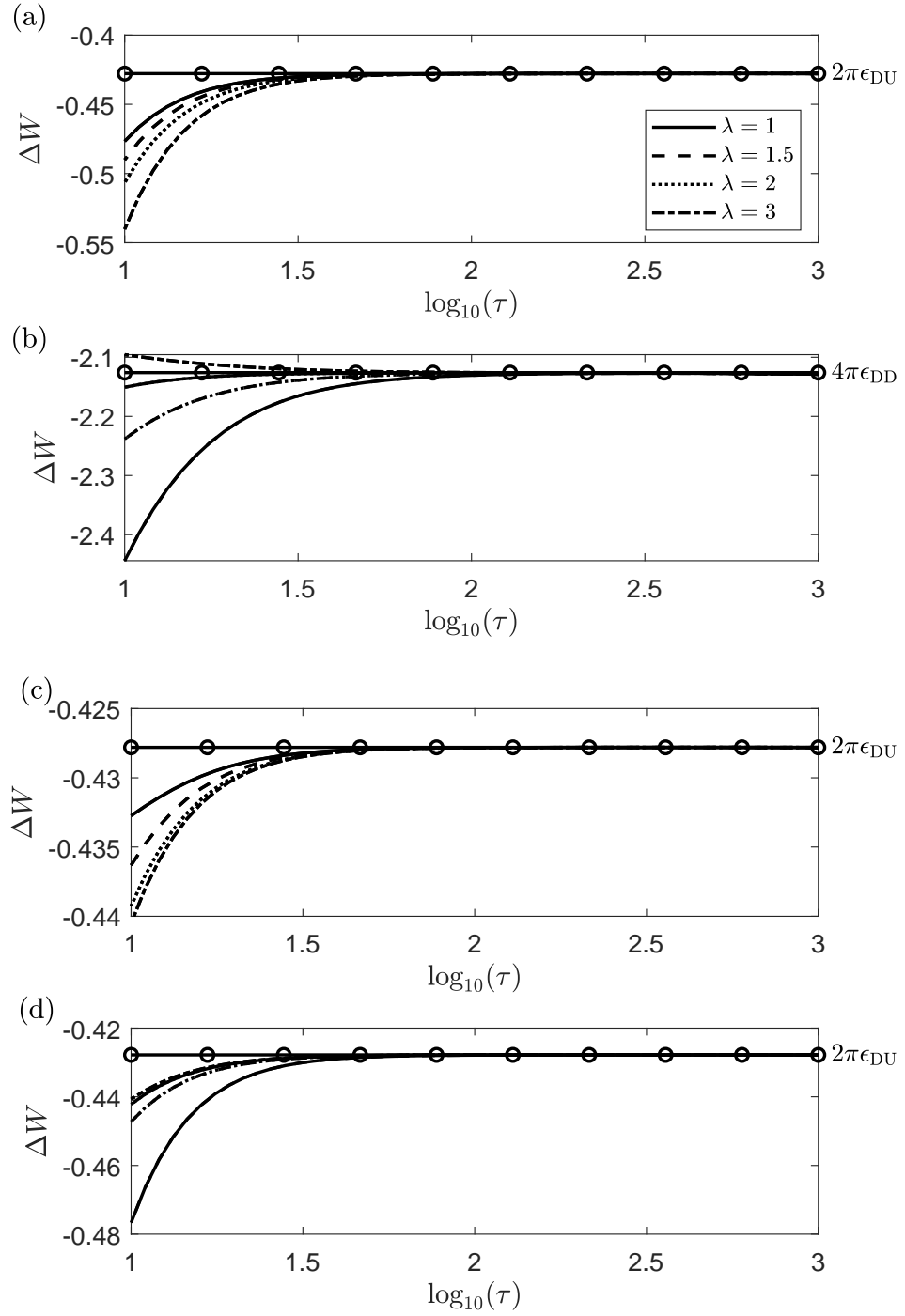


Figure 3.13: The differences between the numerical energies calculated from the non-linear and linear boundary conditions for the (a) U_1 , (b) DD, (c) D and (d) U_2 states as the anchoring strength varies. Each curve corresponds to the energy difference at a different aspect ratio. The solid lines with markers are the errors due to the linear approximation of the boundary conditions.

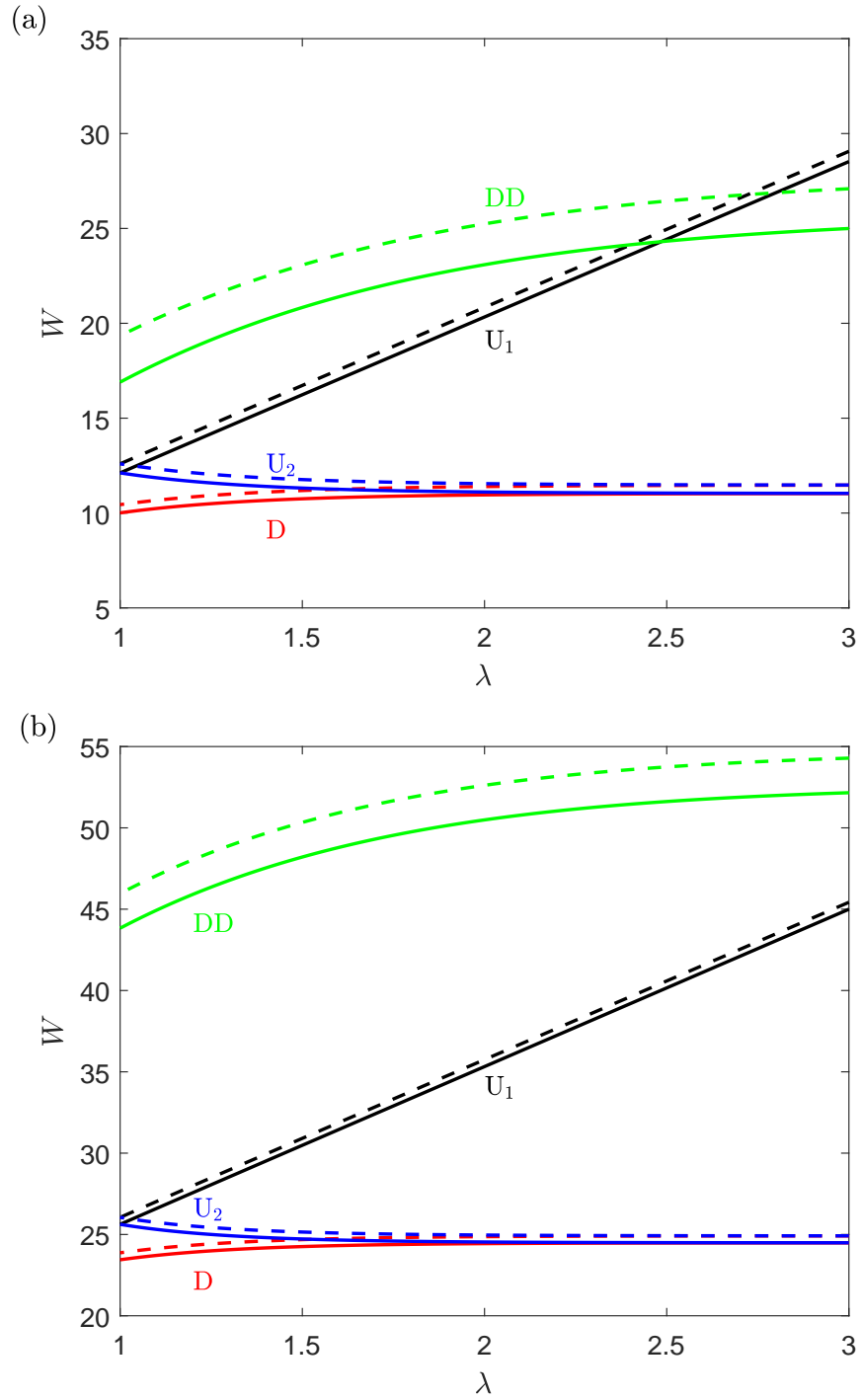


Figure 3.14: Comparison of the numerical energies calculated from the non-linear system (solid curves) with the linearised system (dashed curves) for (a) $\tau = 10$ and (b) $\tau = 100$.

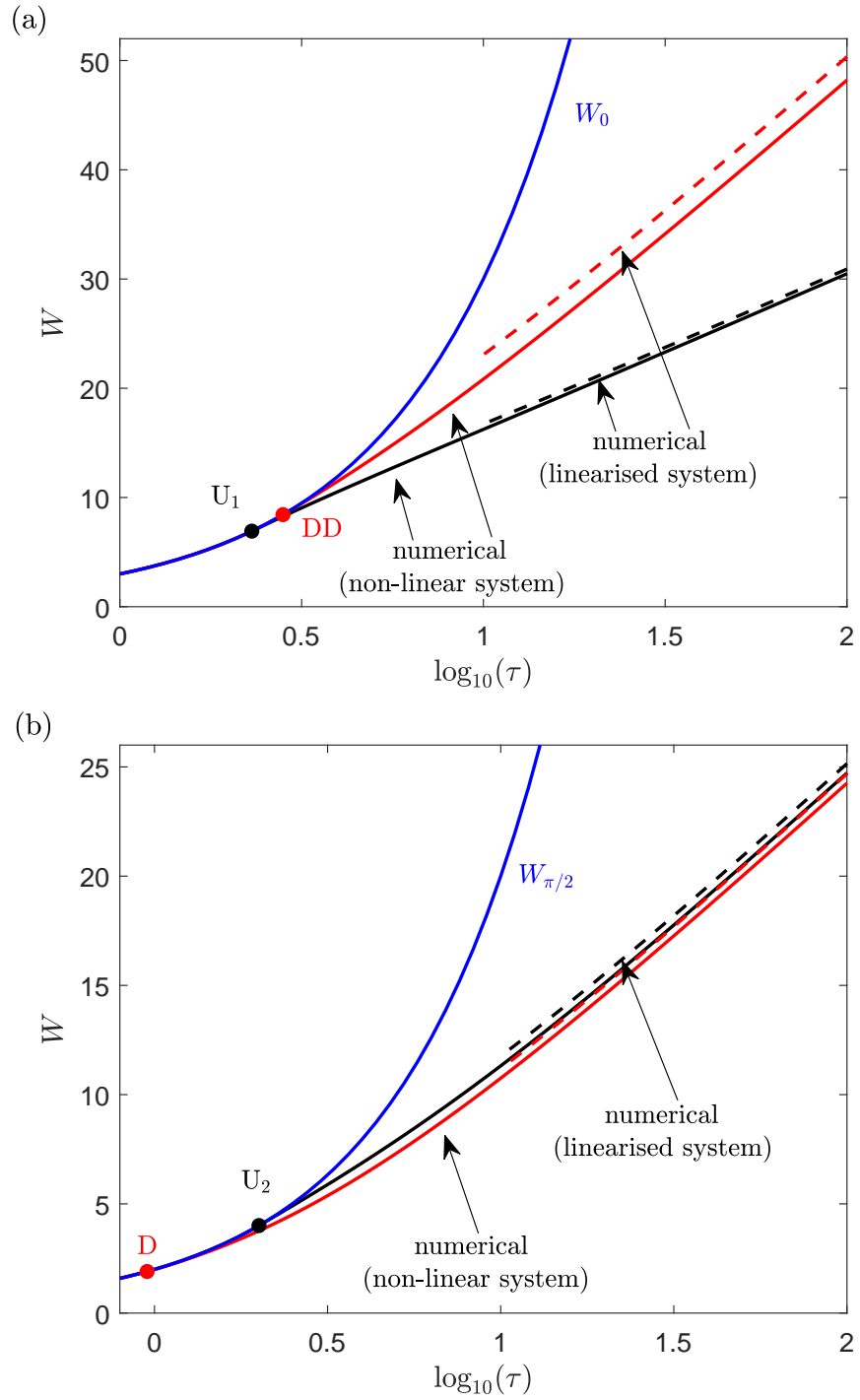


Figure 3.15: Comparison of the numerical energies obtained from the non-linear system (solid curves) with the energies calculated by integrating the linearised system numerically (dashed curves) as a function of τ for $\lambda = 1.5$. In both (a) and (b), the dashed curves have been produced for anchoring strengths $\tau \geq 10$.

3.6 Conclusions

In this chapter we have considered the director configuration of a nematic liquid crystal confined in a rectangular region with finite anchoring. The use of a standard weak anchoring energy (the Rapini-Papoular surface energy) meant we were able to find approximate analytic solutions for the nematic director angle configuration and calculate the corresponding energies, without the need to extract the core of defects at the corner points.

We first examined the system when the anchoring strengths were very close to the bifurcation from a trivial state (i.e., close to the point at which the distorted state comes into existence). We were able to derive analytic solutions for the nematic director angle in terms of an infinite series of modes, involving roots of a transcendental equation. The analytic forms of the director configuration were then used to calculate critical anchoring strengths at which uniform and distorted director structures exchanged stability. We showed that for the special case of isotropic elasticity, close to the transition from uniform to distorted states, the approximate analytic energy expansions agree very well with the corresponding numerical calculations of the full model. We then examined the effect of anisotropic elasticity on the bifurcation ordering, which showed that changes in the value of the elastic constant ratio had an impact on the critical values of the anchoring strength at which different non-trivial states bifurcate from the trivial states.

Next, we considered the limit of large anchoring strength, or alternatively, the weak elasticity limit, for an elastically isotropic nematic liquid crystal. Using the method of matched asymptotic expansions, an analytic solution for the director angle which satisfies the non-linear boundary conditions when $k = 1$ was derived. However, it was impossible to calculate the energy analytically from this director angle solution and so an alternative approach was required in order to derive analytic results for the energies of each non-trivial nematic equilibria. By linearising the system around the preferred directions along each boundary, we were able to derive asymptotic expansions for the energy of each state, all of

which agreed very well with the corresponding numerical calculations. It is worth mentioning that relaxation of the one-constant approximation for the Frank elastic constants in the limit of infinite anchoring did not lead to a significant change in the behaviour of the system. Previous work in similar systems [85] suggests that elastic anisotropy does not significantly affect the stability of states so that the qualitative behaviour would remain the same.

Given typical values of the Frank elastic constants $K_1, K_3 \approx 10^{-11}$ N and anchoring strength $\omega \approx 10^{-4}$ Nm⁻¹ [129], the high- τ energy expressions in equations (3.5.55)–(3.5.58) will be good approximations for wells of side length $d \gtrsim 10$ μ m, so that $\tau = \omega d/K_1 \gtrsim 100$. For larger anchoring strengths of $\omega \approx 10^{-3}$ Nm⁻¹, the energy expressions are accurate for a wider range of well dimensions, with $d \gtrsim 1$ μ m. Since the accuracy of most common forms of construction of such wells (i.e., photolithography) is around the length-scale of microns, it is clear that the asymptotic energies are most likely to be valid for all but the weakest of anchoring strengths. However, in this high- τ limit we have shown that it will always be the D state that is the global energy minimiser. Therefore, if bistability is required, with the possibility of switching between stable states, it may be useful to consider anchoring strengths closer to those which occur at the critical anchoring parameters for bifurcation from trivial states. It is at these anchoring strengths that it will be easiest to switch between states since the energy barriers are smaller.

Chapter 4

Spontaneous and Pressure-Driven States in Channel Flow of Active Nematic Liquid Crystals

4.1 Introduction

In the work of Voituriez *et al.* [144], it was predicted that an active polar liquid crystal will spontaneously induce a flow at a critical value of activity. The model considered in [144] was based on generalised hydrodynamics equations derived for active gels [75, 76]. As mentioned in Chapter 1, the transition, from undistorted to distorted director configurations in active liquid crystals, is similar to a classic electric/magnetic field-induced Freedericksz transition in inactive nematic liquid crystals, where now if the magnitude of the activity parameter exceeds a critical value of activity, non-trivial director structures emerge from an undistorted, no-flow solution. In the model considered in [144], the active polar liquid crystal was confined to a one-dimensional geometry and was subject to a range of boundary conditions for the velocity on the boundaries. By contrast, the polar director field was subject to Dirichlet boundary conditions only, with the director fixed

parallel to the boundaries.

The results of [144] were significant in the development of future investigations into spontaneous flow generation in active liquid crystals. Edwards and Yeomans [41] derived similar results to those in [144] for an apolar active nematic liquid crystal, with the nematic director subject to Neumann boundary conditions and the flow subject to no-slip boundary conditions. The effect of an externally imposed shear on the non-trivial states found in [41] was also considered. Turzi [141] subsequently showed that when an active nematic is confined in a one-dimensional channel, the interaction between nematic ordering and activity could either lead to spontaneous flows, or self-organisation of the active agents into sub-channels flowing in opposite directions. Marenduzzo *et al.* [93] used hybrid lattice Boltzmann simulations to model spontaneous flows of active nematic liquid crystals confined in both one-dimensional and two-dimensional geometries using \mathbf{Q} -tensor theory. Their one-dimensional model considered both splay-bend Freedericksz and hybrid aligned nematic (HAN) cells, which generated spontaneous “boundary layer”-type flows between the boundaries, as well as spontaneous flow-aligning states which are similar to those observed in Poiseuille flow of inactive nematic liquid crystals [5, 31, 32]. Pressure driven flows of active liquid crystals using \mathbf{Q} -tensor theory were recently considered by Thampi *et al.* [133], who observed that an active nematic liquid crystal responds like an inactive nematic liquid crystal when subject to sufficiently large pressure gradients, with the externally driven flow dominating the internal motion of the active agents.

By including symmetry breaking terms in the equations for active fluids, Cortese *et al.* [28] used numerical calculations and non-linear theoretical analysis to show that active polar liquid crystals not only undergo a transition to spontaneous flow above a critical threshold activity value, but they also exhibit a spontaneous asymmetry. Similar symmetry breaking effects have been observed in the model considered by Yang and Wang [153] for channel flows of active polar liquid crystals and by Bonelli *et al.* [12] for an active polar fluid confined in a square well.

In this chapter, we use the Ericksen-Leslie model of active nematics in-

troduced in Chapter 2 to re-examine a similar active nematic system to that considered in [93], finding new states, and explaining the large activity asymptotics of previously discovered states, i.e., in [93]. Through a decoupling of the Ericksen-Leslie equations, we are able to indicate a link between spontaneous flow transitions in active nematics and Freedericksz transitions in inactive nematics. We also show how the stability of particular equilibria, in particular those of a certain symmetry, can be promoted through an applied pressure gradient. Finally, we examine the reorientation of active nematic liquid crystals subject to an external orienting field with the director fixed at the boundaries at non-zero pretilt angles to ensure switching once the field is applied.

4.2 Mathematical Model

We consider an active nematic liquid crystal, confined between two parallel plates at $z = 0$ and $z = d$, and subject to a pressure gradient parallel to the x -direction (see Figure 4.1). The nematic director \mathbf{n} is constrained to lie in the (x, z) plane. We therefore set the angles $\theta_1 = \theta(z, t)$ and $\theta_2 = 0$ in (2.2.2) so that

$$\mathbf{n} = (\cos \theta(z, t), 0, \sin \theta(z, t)), \quad (4.2.1)$$

where $\theta(z, t)$ is the director angle measured with respect to the x -direction. We assume that surface treatment of the plates anchors the director such that it is forced to lie in the x -direction at $z = 0$ and $z = d$, i.e., infinite planar anchoring. The velocity of the fluid, $v(z, t)$, is assumed to be in the x -direction and satisfies the no-slip condition at the plates. The assumptions of a director confined to the (x, z) plane and rectilinear flow are related and depend on the nematic being flow-aligning and strongly anchored in the x -direction at the boundaries. For such liquid crystals, rectilinear flow promotes alignment within the shear plane, at the Leslie angle to the flow direction, as mentioned in Chapter 2, while rotation within the plane, together with the presence of the solid boundaries, restricts the flow to a single direction. In such a system, director instabilities out of the shear plane will only occur if the nematic is tumbling, [67]. We will also assume that fluid inertia is negligible, an approximation that is valid when the Reynolds number

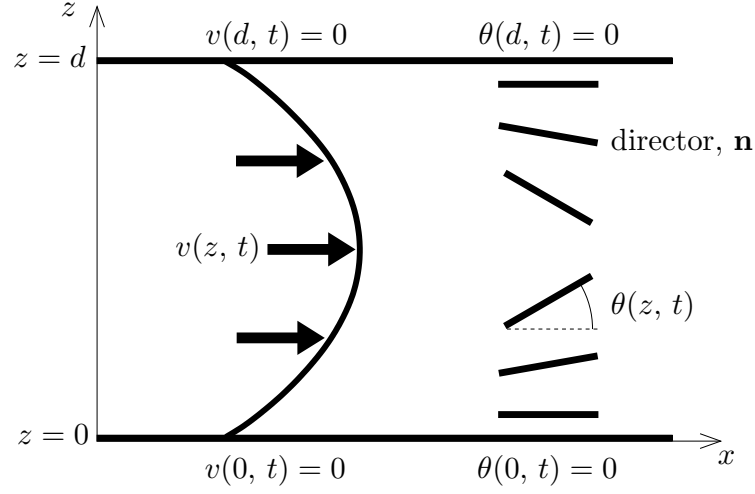


Figure 4.1: An active nematic liquid crystal in a channel between two solid plates, at $z = 0$ and $z = d$, with flow parallel to the x -direction. The director is constrained to lie in the (x, z) plane and is infinitely anchored in the x -direction on the plates. The flow velocity satisfies the no-slip condition on both plates.

is small or, equivalently in this situation, when the timescale of changes in the velocity are much smaller than the timescale of director rotation [30, 104].

The dynamics of the director angle and fluid velocity are governed by the adapted Ericksen-Leslie equations (2.2.32) and (2.2.33). In this chapter, we adopt the same subscript notation for partial derivatives used in Chapter 3. The elastic energy density (2.2.40) is given by

$$w_F = \frac{1}{2} (K_1 \cos^2 \theta + K_3 \sin^2 \theta) \theta_z^2. \quad (4.2.2)$$

The dissipation function (2.2.29) is found to be

$$\mathcal{D} = \frac{1}{2} g(\theta) v_z^2 + m(\theta) v_z \theta_t + \frac{1}{2} \gamma_1 \theta_t^2, \quad (4.2.3)$$

where the viscosity terms $m(\theta)$ and $g(\theta)$ in terms of the Miesowicz viscosities (2.2.52)–(2.2.57) are given by

$$m(\theta) = \frac{1}{2} (\gamma_1 + \gamma_2 \cos(2\theta)), \quad (4.2.4)$$

$$g(\theta) = \frac{1}{2} (\eta_1 \cos^2 \theta + \eta_2 \sin^2 \theta + \eta_{12} \sin^2 \theta \cos^2 \theta). \quad (4.2.5)$$

The viscosity term $m(\theta)$ governs the rotation and stretching of the liquid crystal, while $g(\theta)$ is an effective shear viscosity of the liquid crystal. Substituting the elastic energy density and dissipation function into the Ericksen-Leslie equations (2.2.32) and (2.2.33) leads to

$$\gamma_1 \theta_t = (K_1 \cos^2 \theta + K_3 \sin^2 \theta) \theta_{zz} + (K_3 - K_1) \sin \theta \cos \theta (\theta_z)^2 - m(\theta) v_z, \quad (4.2.6)$$

for the balance of angular momentum, and

$$0 = (g(\theta) v_z + m(\theta) \theta_t + \zeta \sin \theta \cos \theta)_z - \tilde{p}_x, \quad (4.2.7)$$

$$0 = -\tilde{p}_y, \quad (4.2.8)$$

$$0 = (\zeta \sin(2\theta) - m(\theta) v_z - \gamma_1 \theta_t) \theta_z - \tilde{p}_z, \quad (4.2.9)$$

for the balance of linear momentum. From equation (4.2.8) we can deduce that $\tilde{p} = \tilde{p}(x, z, t)$. Assuming there is a pressure difference ΔP in the x -direction between $x = 0$ and $x = L$, where L is a length in the x -direction, the modified pressure $\tilde{p}(x, z, t)$ is subject to the boundary conditions

$$\tilde{p}(x = 0, z, t) = 0, \quad \tilde{p}(x = L, z, t) = \Delta P. \quad (4.2.10)$$

Integrating equation (4.2.7) with respect to x leads to

$$\tilde{p}(x, z, t) = x(g(\theta) v_z + m(\theta) \theta_t + \zeta \sin \theta \cos \theta)_z + G(z, t) \equiv x F_z + G(z, t), \quad (4.2.11)$$

where $G(z, t)$ is an integration function of z and t . Differentiating (4.2.11) with respect to z gives, with equation (4.2.9),

$$\tilde{p}_z = x F_{zz} + G_z = (\zeta \sin(2\theta) - m(\theta) v_z - \gamma_1 \theta_t) \theta_z. \quad (4.2.12)$$

Since equation (4.2.12) is true for all x , it follows that $F_{zz} = 0$, which further means that $F_z = C(t)$, where $C(t)$ is a function of time. We can then integrate (4.2.12) with respect to z and substitute the resultant definition for $G(z, t)$ into (4.2.11) to determine \tilde{p} , which leads to

$$\tilde{p}(x, z, t) = x C(t) + D(t) + \int_0^z (\zeta \sin(2\theta) - m(\theta) v_z - \gamma_1 \theta_t) \theta_z dz, \quad (4.2.13)$$

where $D(t)$ is another function of time. Using the boundary conditions (4.2.10) and assuming that ΔP is independent of time, we find that the modified pressure \tilde{p} only depends on x , and is given by

$$\tilde{p} = \frac{\Delta P}{L}x. \quad (4.2.14)$$

We now have a non-linear system comprising two coupled partial differential equations,

$$\gamma_1 \theta_t = (K_1 \cos^2 \theta + K_3 \sin^2 \theta) \theta_{zz} + (K_3 - K_1) \sin \theta \cos \theta (\theta_z)^2 - m(\theta) v_z, \quad (4.2.15)$$

$$0 = (g(\theta) v_z + m(\theta) \theta_t + \zeta \sin \theta \cos \theta)_z - p_x, \quad (4.2.16)$$

where, by use of the definition (2.2.34), $p_x \equiv \tilde{p}_x = \Delta P/L$. Throughout this chapter, the imposed pressure gradient p_x is independent of time. The infinite planar anchoring and no-slip assumptions on the boundary plates mean that equations (4.2.15) and (4.2.16) will be solved subject to the boundary conditions

$$\theta(0, t) = \theta(d, t) = 0, \quad (4.2.17)$$

$$v(0, t) = v(d, t) = 0. \quad (4.2.18)$$

At this stage it is worth considering the possible symmetries of solutions of equations (4.2.15) and (4.2.16), with boundary conditions (4.2.17) and (4.2.18). The transformation $\theta(z, t) \rightarrow -\theta(d - z, t)$ together with $v(z, t) \rightarrow v(d - z, t)$ leave equations (4.2.15) and (4.2.16) unchanged for any value of the pressure gradient p_x , so we expect to obtain solutions for the director angle which are anti-symmetric together with velocity solutions that are symmetric, about the channel midpoint $z = d/2$. For the opposite symmetries, $\theta(z, t) \rightarrow \theta(d - z, t)$ and $v(z, t) \rightarrow -v(d - z, t)$, equations (4.2.15) and (4.2.16) are unchanged only if $p_x = 0$. We therefore expect to find symmetric director and anti-symmetric velocity solutions only for zero pressure gradient. In addition to symmetry/anti-symmetry about the channel midpoint, we notice that the governing equations are also unchanged under the transformation $\theta(z, t) \rightarrow -\theta(z, t)$, $v(z, t) \rightarrow -v(z, t)$ and $p_x \rightarrow -p_x$. Therefore, changing the sign of the pressure gradient will simply result in a change of sign of both the director angle and velocity.

4.3 Asymptotic Solutions and Linear Stability Analysis

In this section we show that by decoupling the Ericksen-Leslie equations (4.2.15) and (4.2.16) using the same approach considered in Mottram *et al.* [104], we can determine equilibrium director orientations in the asymptotic limits of large pressure gradients and activity strengths. For large magnitudes of activity strengths, we derive an analytic expression for a critical activity at which the active fluid will spontaneously transition from the no-flow state to a flowing state.

4.3.1 Decoupling of the Ericksen-Leslie Equations

The calculations used to decouple equations (4.2.15) and (4.2.16) are outlined in Appendix C, which lead to a single, non-local dynamic equation for the director angle, namely

$$\begin{aligned} \left(\gamma_1 - \frac{m^2(\theta)}{g(\theta)} \right) \theta_t &= (K_1 \cos^2 \theta + K_3 \sin^2 \theta) \theta_{zz} + (K_3 - K_1) \sin \theta \cos \theta (\theta_z)^2 \\ &\quad - \frac{m(\theta)}{g(\theta)} \left[\frac{\bar{\mathcal{A}}}{\bar{\mathcal{B}}} - \zeta \left(\sin \theta \cos \theta - \bar{\mathcal{C}} - \frac{\bar{\mathcal{D}}}{\bar{\mathcal{B}}} \right) + p_x \left(z - \bar{\mathcal{F}} - \frac{\bar{\mathcal{G}}}{\bar{\mathcal{B}}} \right) \right]. \end{aligned} \quad (4.3.1)$$

The velocity is then a function of the director orientation, namely

$$v(z, t) = \int_0^z \frac{1}{g(\theta)} \left[\bar{\mathcal{E}} - m(\theta) \theta_t - \zeta (\sin \theta \cos \theta - \bar{\mathcal{C}}) + p_x (z - \bar{\mathcal{F}}) \right] dz, \quad (4.3.2)$$

where

$$\bar{\mathcal{A}} = \int_0^d \frac{m(\theta) [(K_1 \cos^2 \theta + K_3 \sin^2 \theta) \theta_{zz} + (K_3 - K_1) \sin \theta \cos \theta (\theta_z)^2]}{\gamma_1 g(\theta) - m^2(\theta)} dz, \quad (4.3.3)$$

$$\bar{\mathcal{B}} = \int_0^d \frac{\gamma_1}{\gamma_1 g(\theta) - m^2(\theta)} dz, \quad \bar{\mathcal{C}} = \int_0^d \frac{\sin \theta \cos \theta}{g(\theta)} dz / \int_0^d \frac{1}{g(\theta)} dz, \quad (4.3.4)$$

$$\bar{\mathcal{D}} = \int_0^d \frac{m^2(\theta) (\sin \theta \cos \theta - \bar{\mathcal{C}})}{g(\theta) (\gamma_1 g(\theta) - m^2(\theta))} dz, \quad \bar{\mathcal{E}} = \int_0^d \frac{m(\theta)}{g(\theta)} \theta_t dz / \int_0^d \frac{1}{g(\theta)} dz, \quad (4.3.5)$$

$$\bar{\mathcal{F}} = \int_0^d \frac{z}{g(\theta)} dz / \int_0^d \frac{1}{g(\theta)} dz, \quad \bar{\mathcal{G}} = \int_0^d \frac{m^2(\theta) (z - \bar{\mathcal{F}})}{g(\theta) (\gamma_1 g(\theta) - m^2(\theta))} dz. \quad (4.3.6)$$

In equation (4.3.1) we see that, as a result of the decoupling, the effective rotational viscosity, the coefficient of θ_t , has been modified and is now director-dependent through the viscosity terms $m(\theta)$, $g(\theta)$. The modified rotational viscosity is less than γ_1 , so that, in this geometry, the influence of flow allows faster rotation of the director. The first two terms on the right-hand side of equation (4.3.1) are due to elasticity in the liquid crystal and are unchanged compared to the original angular momentum equation (4.2.15). The third and fourth terms on the right hand side of equation (4.3.1) are non-local contributions due to director-flow coupling. The activity parameter ζ enters equation (4.3.1) only through the fourth term whose form, $\sin \theta \cos \theta$, is similar to a magnetic or electric field term in the classic problem of director reorientation during a Fredericksz transition [129], albeit rescaled by the director dependent factor $m(\theta)/g(\theta)$ and normalised by the non-local term $\bar{\mathcal{C}} + \bar{\mathcal{D}}/\bar{\mathcal{B}}$.

4.3.2 Asymptotic Solutions for Large Pressure Gradients

Non-trivial analytic solutions to the non-linear, non-local partial differential equation in (4.3.1) are not possible. However, we can still establish information about the system, and further progress can be made using certain simplifying assumptions. We first consider two important asymptotic limits for the behaviour of the director in the bulk of the channel: the situation when the magnitude of the applied pressure gradient is large; and when the magnitude of the activity parameter is large. In the case of large values of $|p_x|$, the dynamics of the director in the bulk of the channel, away from any boundary or internal reorientation layers, where elastic effects can be ignored so that $\theta = \theta(t)$, are governed by the equation

$$\left(\gamma_1 - \frac{m^2(\theta)}{g(\theta)}\right)\theta_t = -\frac{p_x m(\theta)}{g(\theta)}\left(z - \bar{\mathcal{F}} - \frac{\bar{\mathcal{G}}}{\bar{\mathcal{B}}}\right). \quad (4.3.7)$$

The only equilibrium solutions of (4.3.7), so that $\theta_t = 0$, will be those θ values that satisfy $m(\theta) = 0$. Such solutions only exist in flow-aligning nematics and are $\theta = n\pi \pm \theta_L$, where $n \in \mathbb{Z}$ and

$$\theta_L = \pm \tan^{-1}\left(\sqrt{\frac{\gamma_2 + \gamma_1}{\gamma_2 - \gamma_1}}\right), \quad (4.3.8)$$

is the Leslie angle [129]. For these constant director angle solutions the velocity is then the classic Poiseuille parabolic profile,

$$v(z) = \frac{p_x}{2g(\theta_L)} z(z - d). \quad (4.3.9)$$

This is to be expected when an externally driven flow, and corresponding flow-alignment of the director, dominate over activity-induced alignment.

4.3.3 Asymptotic Solutions for Large Activity

The situation for highly active systems, where $|\zeta|$ is large, is more complicated. In this case we would expect the dynamics in the bulk of the channel, where spatial gradients are negligible and $\theta = \theta(t)$, to be governed by the equation

$$\left(\gamma_1 - \frac{m^2(\theta)}{g(\theta)} \right) \theta_t = \frac{\zeta m(\theta)}{g(\theta)} \left(\sin \theta \cos \theta - \bar{\mathcal{C}} - \frac{\bar{\mathcal{D}}}{\mathcal{B}} \right). \quad (4.3.10)$$

We can now consider two possible symmetries of the director profile within the channel. If θ is anti-symmetric with respect to the centre of the channel, then the integrals $\bar{\mathcal{C}}$ and $\bar{\mathcal{D}}$ in equations (4.3.4) and (4.3.5) are both zero. Therefore, in the bulk of the channel, away from boundary and internal reorientation layers where director distortions are relatively large, anti-symmetric equilibria solutions for the director angle must satisfy $m(\theta) \sin \theta \cos \theta = 0$, leading to the possibilities $\theta = \pm\theta_L, 0$ or $\pi/2$ rad (plus all π rotations of the director).

For symmetric director profiles $\bar{\mathcal{C}} \neq 0$. If we were to consider the local behaviour in the bulk of the channel, where the director angle does not vary spatially, then we would see from equations (4.3.4) and (4.3.5) that $\bar{\mathcal{C}} = \sin \theta \cos \theta$ and $\bar{\mathcal{D}} = 0$. The right-hand side of equation (4.3.10) would then be zero for *all* values of θ . Rather than all director angles in the bulk of the channel being equilibria, as this result would suggest, it is necessary to consider the non-local behaviour in the system. In this case the bulk director angle at large $|\zeta|$ can only be determined through a consideration of spatial gradient and non-local effects. In order to make progress we consider a set of simplifying assumptions. We first use the relatively standard one-constant approximation, equating the elastic splay and bend constants, $K_1 = K_3 = K$, which simplifies the elastic terms

in equation (4.3.1). Secondly, we will use two assumptions about the nematic viscosities, namely $\eta_1 = \eta_2$ and $\eta_{12} = 0$. Physically, these assumptions are an approximation of “isotropic orientational viscosity”, in a similar way to the one-constant approximation being an assumption of isotropic elasticity. They mean that the effective viscosity of the liquid crystal is constant for all values of θ , such that $g(\theta) = \eta_1$. Since the Parodi relationship [110] insists that $\gamma_2 = \eta_1 - \eta_2$, the assumption of isotropic viscosity also leads to $\gamma_2 = 0$ and, hence, that $m(\theta) = \gamma_1/2 > 0$. These assumptions on the viscosities mean that, for the following analysis, we are considering non-flow aligning nematics, we later see in Section 4.4 that a very similar numerical solution is found for a flow-aligning nematic. Although the assumptions on the nematic viscosities considered for this piece of analysis are quite restrictive, further analysis has now been conducted that allows us to consider the bulk equilibrium director angle for a flow-aligning active nematic liquid crystal (see Walton *et al.* [146]).

Applying the various assumptions mentioned above to the integrals in equations (4.3.3)–(4.3.6), we can now obtain a simplified governing equation for the dynamics of the director angle in the limit of large activity,

$$\gamma_1 \left(1 - \frac{\gamma_1}{4\eta_1}\right) \theta_t = K \left(\theta_{zz} - \frac{\gamma_1}{4\eta_1 d} \int_0^d \theta_{zz} dz \right) + \frac{\zeta \gamma_1}{2\eta_1} \left(\sin \theta \cos \theta - \frac{1}{d} \int_0^d \sin \theta \cos \theta dz \right). \quad (4.3.11)$$

Introducing dimensionless time, τ , and coordinate ξ , through the scalings $t = (\gamma_1 d^2 / K)(1 - \gamma_1 / (4\eta_1))\tau$ and $z = d\xi$, we can rewrite equation (4.3.11) as

$$\theta_\tau = \theta_{\xi\xi} - \beta_1 \int_0^1 \theta_{\xi\xi} d\xi + \beta_2 \left(\sin \theta \cos \theta - \int_0^1 \sin \theta \cos \theta d\xi \right), \quad (4.3.12)$$

where $\beta_1 = \gamma_1 / (4\eta_1)$ and $\beta_2 = \zeta \gamma_1 d^2 / (2K\eta_1)$. When we consider steady state solutions of equation (4.3.12), so that $\theta_\tau = 0$, integration of the equation between $\xi = 0$ to $\xi = 1$ shows that $\int_0^1 \theta_{\xi\xi} d\xi = 0$. Therefore, for steady state solutions, equation (4.3.12) becomes

$$0 = \theta_{\xi\xi} + \beta_2 \left(\sin \theta \cos \theta - \int_0^1 \sin \theta \cos \theta d\xi \right), \quad (4.3.13)$$

which will be solved subject to the boundary conditions $\theta(0) = \theta(1) = 0$. Standard analysis of the stability of solutions to equation (4.3.13) shows that it is only for contractile active nematics, for which $\beta_2 > 0$, that non-trivial solutions will exist. This means that for large magnitude activity parameter values we would only expect stable bulk director angle orientations for which $m(\theta) \neq 0$ if $\zeta > 0$.

We now seek the positive solution to equation (4.3.13) for θ in the limit as $\beta_2 \rightarrow \infty$. As we will see from the numerical solutions in Section 4.4, in this limit the director angle tends towards a fixed value $\theta \rightarrow \theta^*$, almost everywhere in the channel and, therefore,

$$\int_0^1 \sin \theta \cos \theta \, d\xi \rightarrow \sin \theta^* \cos \theta^* = I. \quad (4.3.14)$$

To find θ^* we first consider the related local problem

$$0 = \theta_{\xi\xi} + \beta_2 (\sin \theta \cos \theta - I), \quad (4.3.15)$$

where I is a constant. Equation (4.3.15) is of Hamiltonian form, with Hamiltonian

$$H(\theta, \theta_\xi) = \frac{1}{2}\theta_\xi^2 - \frac{\beta_2}{4} (\cos(2\theta) + 4I\theta). \quad (4.3.16)$$

For any particular value of I it can be shown that there are solutions to equation (4.3.15) provided β_2 is larger than a minimum value, i.e., $\beta_2 > \beta_2^{\min}(I)$ (see Schaaf [121]). Furthermore, when $\beta_2 = \beta_2^{\min}(I)$ the solution to equation (4.3.15) satisfies the level curve of the Hamiltonian $H(\theta, \theta_\xi) = H(0, 0) = -\beta_2/4$, and, importantly, is also the steady state solution to the non-local problem in equation (4.3.13). Through solving the local problem in equation (4.3.15) directly, we find that the function $\beta_2^{\min}(I)$ is monotonic increasing with $\beta_2^{\min} \rightarrow \infty$ as $I \rightarrow I^*$. In this limit ($\theta \rightarrow \infty$, $I \rightarrow I^*$, $\beta_2^{\min} \rightarrow \infty$) we therefore have $\theta_\xi \rightarrow 0$ and so θ^* must satisfy $H(\theta^*, 0) = H(0, 0)$, or equivalently

$$-\frac{1}{4} (\cos(2\theta^*) + 4I^*\theta^*) = -\frac{1}{4}. \quad (4.3.17)$$

Given the definition of I^* , namely $I^* = \sin \theta^* \cos \theta^*$, equation (4.3.17) is equivalent to $\tan \theta^* = 2\theta^*$. This equation may be solved numerically to give $\theta^* \approx 1.1656$ rad. This is the predicted director angle in the bulk of the region, away from any

boundary or reorientation regions, for symmetric θ solutions in the limit of large positive (contractile) activity parameter. Although we have made assumptions of isotropic elasticity and viscosity to derive this result, we will see in Section 4.4 that the value of the preferred angle for more realistic parameters is very close to the value given by equation (4.3.17). Furthermore, we find that the value of θ^* obtained by solving (4.3.15) numerically at large positive β_2 is in very good agreement with the value calculated from the asymptotic approach.

Therefore, in the large activity parameter limit, we expect to find solutions for which the director angle in the bulk of the channel may take values $\theta = \pm\theta_L, 0, \pi/2$ or $\theta^* \approx 1.1656$ rad, and all π rotations of these angles. While the first four values may be anticipated due to the presence of flow-alignment or the activity term being similar to an electric field-like reorientation torque of the form $\sin\theta \cos\theta$, the final value θ^* is unexpected and occurs only because of non-local effects derived from contractile activity-induced flow and director distortion in boundary layers.

4.3.4 Linear Stability Analysis of Bifurcations from the Trivial Solution with Zero Pressure Gradient

In the special case where there is no applied pressure gradient, $p_x = 0$, equation (4.3.1), subject to the strong anchoring boundary conditions in (4.2.17), is satisfied by the trivial solution $\theta \equiv 0$, leading to no flow, $v \equiv 0$, through equation (4.3.2). However, the presence of the activity term in equation (4.3.1) introduces the possibility that $\theta \equiv 0$ may become unstable, in a manner analogous to the effect of a magnetic or electric field in a Freedericksz transition. In a similar way to the work of Voituriez *et al.* [144] and Edwards and Yeomans [41], we examine this instability by linearising (4.3.1) around $\theta \equiv 0$ to produce the governing equation

$$\eta_{\text{splay}}\theta_t = K_1\theta_{zz} - \frac{K_1(\gamma_1 + \gamma_2)^2}{4\gamma_1\eta_1 d} \int_0^d \theta_{zz} dz + \frac{\zeta(\gamma_1 + \gamma_2)}{2\eta_1} \left[\theta - \frac{1}{d} \int_0^d \theta dz \right], \quad (4.3.18)$$

where $\eta_{\text{splay}} = \gamma_1 - (\gamma_1 + \gamma_2)^2 / (4\eta_1) > 0$ is the effective viscosity that is also found in the analogous Freedericksz transition [129].

We now consider two sets of potential instability modes, for which the director angle is either anti-symmetric or symmetric with respect to the centre of the channel. The anti-symmetric modes are of the form

$$\theta_o(z, t) = \pm\Theta \sin\left(\frac{2n\pi z}{d}\right) \exp(\sigma t), \quad (n \in \mathbb{N}), \quad (4.3.19)$$

where Θ is the mode amplitude, n is the mode number, σ is the mode growth rate and the subscript in θ_o indicates that this mode is an odd function with respect to the channel centre. It is apparent from equation (4.3.2) that these anti-symmetric director profiles will lead to symmetric velocity profiles. Substituting (4.3.19) into (4.3.18) we find an expression for the growth rate σ in terms of the nematic parameters for any given mode number n ,

$$\sigma = \frac{(\gamma_1 + \gamma_2)(\zeta - n^2\zeta_c)}{2\eta_1\eta_{\text{splay}}}, \quad (4.3.20)$$

where the critical activity for the $n = 1$ fundamental mode, ζ_c , is given by

$$\zeta_c = \frac{8\pi^2 K_1 \eta_1}{(\gamma_1 + \gamma_2)d^2}. \quad (4.3.21)$$

Arguments based on the boundedness of the elastic energy and positivity of the dissipation [129] show that, with the exception of $\gamma_1 + \gamma_2$, all the parameters in the definition of ζ_c are positive. When the viscosity $\gamma_1 + \gamma_2$ is negative, which is often the case when the active agent is rod-like, we find that $\zeta_c < 0$ and the n^{th} mode becomes unstable when $\zeta < n^2\zeta_c < 0$ for $n = 1, 2, \dots$. Therefore, for rod-like active agents the trivial state ($\theta \equiv 0, v \equiv 0$) is unstable to anti-symmetric perturbations only for extensile activity. Conversely, when $\gamma_1 + \gamma_2 > 0$, often a feature of disc-like active agents, $\zeta_c > 0$ and the n^{th} mode becomes unstable when $\zeta > n^2\zeta_c > 0$. So, for disc-like active agents the trivial state is unstable to anti-symmetric perturbations only for contractile activity.

The symmetric modes can be written as, following Pieranski *et al.* [112],

$$\theta_e(z, t) = \pm\Theta \left[\cos\left(\frac{2q_n(z - d/2)}{d}\right) - \cos q_n \right] \exp(\sigma t), \quad (4.3.22)$$

for mode number q_n ($n \in \mathbb{N}$), and where the subscript in θ_e indicates the mode is even with respect to the channel centre. Equation (4.3.2) shows that these symmetric director profiles will lead to anti-symmetric velocity profiles. From (4.3.1) we find that non-trivial states, such that $\Theta \neq 0$, are possible if both

$$\zeta = \frac{q_n^2}{\pi^2} \zeta_c \left(1 + \frac{\eta_{\text{splay}}}{\gamma_1} \frac{\tan q_n}{q_n - \tan q_n} \right), \quad (4.3.23)$$

$$\text{and} \quad \sigma = \frac{(\gamma_1 + \gamma_2)}{2\gamma_1\eta_1} \frac{q_n^2}{\pi^2} \zeta_c \left(\frac{\tan q_n}{q_n - \tan q_n} \right) \quad (4.3.24)$$

are satisfied simultaneously. The marginal stability curve, $\sigma = 0$, provides critical mode numbers $q_n = n\pi$ ($n \in \mathbb{N}$), corresponding to the critical activity $\zeta = n^2\zeta_c$ for the n^{th} mode, exactly the same value as the anti-symmetric director case. Therefore, when there is no applied pressure gradient, we have two symmetry breaking modes that lead to bifurcations from the trivial solution branch ($\theta \equiv 0, v \equiv 0$) at each value of the critical activity $\zeta = n^2\zeta_c$ ($n \in \mathbb{N}$). As we will see in the next section, these are pitchfork bifurcations although only one of them results in the formation of stable non-trivial solutions. We also show that due to the symmetry of a pressure gradient-induced flow, only one of these bifurcations is perturbed to produce a preferred state and a classic perturbed pitchfork bifurcation structure when the active nematic is subject to a pressure gradient.

4.4 Numerical Calculations

In order to examine the role of activity more fully, we now consider numerical steady state solutions $(\theta(z), v(z))$ of the full equations (4.2.15) and (4.2.16). In order to obtain numerical solutions, and continue along solution branches, we have employed both the finite-element package COMSOL, and the MATLAB-based bifurcation analysis package MATCONT [35]. The material parameters, i.e., elastic constants and viscosities, of active nematics have not yet been fully characterised and therefore we use the material parameters measured for the liquid crystal 5CB [129] and a channel width of $d = 10\mu\text{m}$. We will examine extensile and contractile active nematics separately, discussing the simpler case of zero pressure gradient before considering the effects of an applied pressure

gradient. In Section 4.5 we will summarise the behaviour of the system for extensile and contractile active nematics for various activity strengths and pressure gradients.

4.4.1 Extensile Active Nematic Liquid Crystals with Zero Pressure Gradient

In the previous section we saw that for zero pressure gradient the trivial state ($\theta \equiv 0, v \equiv 0$) is a solution for all values of the activity parameter, and that non-trivial states bifurcate from the trivial state at critical activities $\zeta = n^2\zeta_c$ ($n \in \mathbb{N}$), with ζ_c given by equation (4.3.21). For the material parameters of the liquid crystal 5CB, the first critical activity ($n = 1$ mode) is $\zeta = \zeta_c = -13.87$ Pa and the Leslie angle is $\theta_L \approx 0.2$ rad.

Setting $p_x = 0$, we find numerical solutions for the steady state director angle and corresponding velocity. Three types of solutions are shown in Figure 4.2. The equilibria are plotted for activities greater in magnitude than the critical value for the trivial branch, $\zeta_c = -13.87$ Pa, and confirm that a symmetric director angle is accompanied by an anti-symmetric velocity, and vice versa. The director angle solutions in Figures 4.2(a, c) are the anti-symmetric and symmetric modes bifurcating from the trivial state suggested by equations (4.3.19) and (4.3.22), respectively, as well as the trivial state itself. The equilibria in Figure 4.2(e) correspond to symmetric director angle profiles which do not bifurcate from the trivial branch and are associated with large elastic energies due to their spatial gradients. Note that, although not shown in Figure 4.2 but as suggested at the end of Section 4.2, negative versions of all the solutions in Figure 4.2 also exist due to the symmetry $\theta(z) \rightarrow -\theta(z), v(z) \rightarrow -v(z)$ when $p_x = 0$. The modes in Figures 4.2(a, b) and (c, d) are all to be expected, with director distortion being linked to activity-induced flow, and have been found previously in, for example, Marenduzzo *et al.* [93]. In Figures 4.2(a, c) we see that for large activities (in magnitude), the director aligns in the bulk of the channel, i.e., away from boundary and internal reorientation regions, at $\pm\theta_L \approx \pm 0.2$ rad, which was

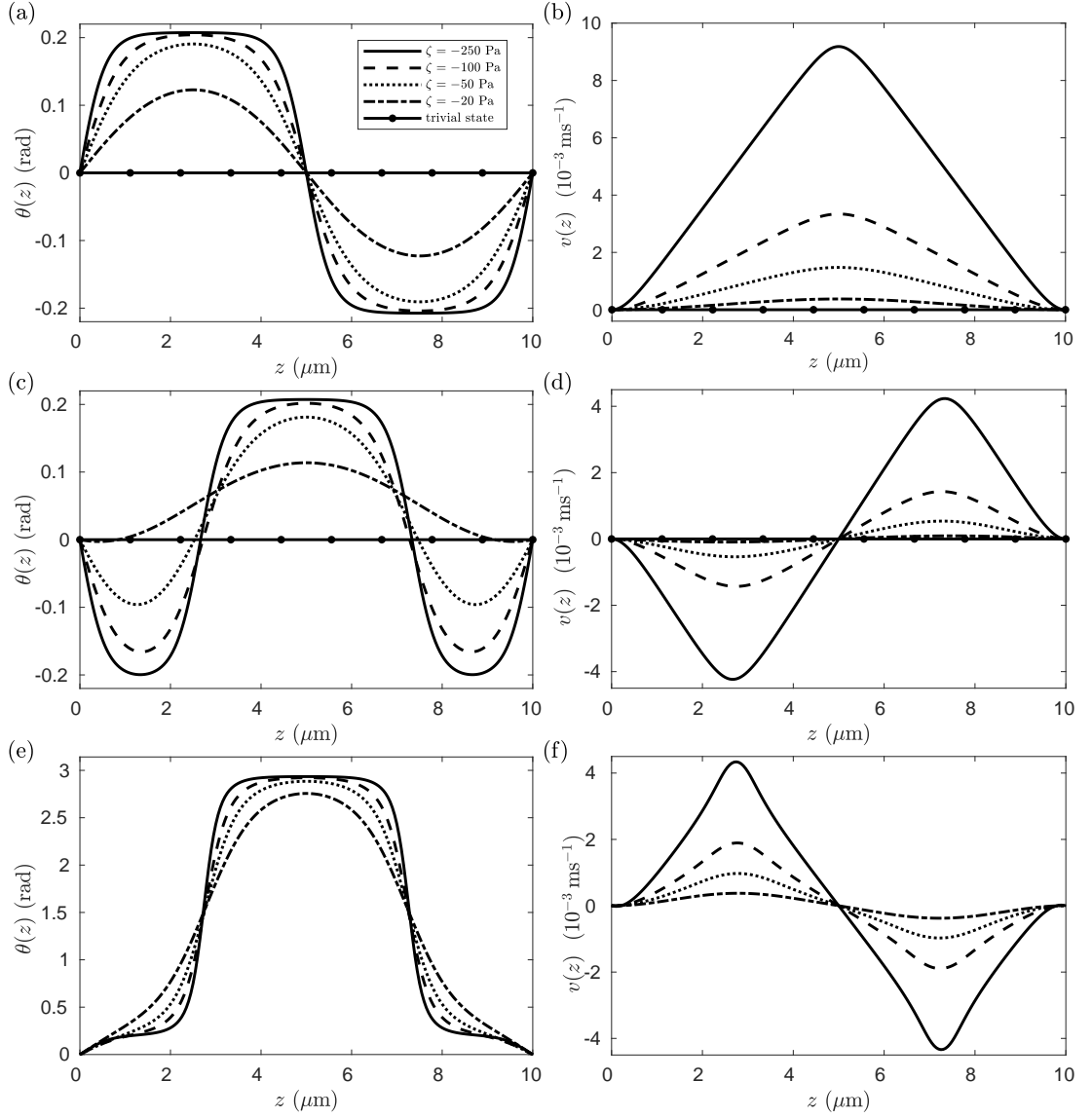


Figure 4.2: (a), (c), (e) Director angle $\theta(z)$ and (b), (d), (f) velocity $v(z)$ equilibrium profiles for activity parameter values $\zeta = -20, -50, -100, -250$ Pa and pressure gradient $p_x = 0$. The solutions in (a)-(d) bifurcate from the trivial state, which is also shown.

predicted as one possibility in Section 4.3. The mode in Figure 4.2(e, f) is less well studied, perhaps because the solution branch is not connected to the trivial state and contains high gradients in θ (note the different scale of the vertical axis in Figure 4.2(e) compared to Figures 4.2(a, c)). For all solutions in Figure 4.2, the director angle exhibits flow alignment to θ_L in regions of positive shear, $v_z > 0$, and flow alignment to $-\theta_L$ or $\pi - \theta_L$ in regions of negative shear, $v_z < 0$. As

predicted in Subsection 4.3.3, there will be higher order mode ($n > 1$) solutions at higher magnitude values of the activity parameter, similar to Figure 4.2(a) and Figure 4.2(c) but in which the director angle alternates between θ_L and $-\theta_L$ an increasing number of times. We also predict that there will be equivalent higher order mode solutions that are not connected to the trivial solution branch, similar to Figure 4.2(e) but with the director angle alternating between $(n\pi + \theta_L)$ and $(m\pi - \theta_L)$, for $n, m \in \mathbb{Z}$. However, all these higher order modes will involve large elastic distortions and may be unstable or metastable.

In order to investigate how the equilibrium solutions in Figure 4.2 change as the activity parameter changes, in Figure 4.3 we have plotted solution branches for the trivial solution and all three non-trivial modes shown in Figure 4.2. In plotting these branches we use two measures of the director angle solution in order to characterise the symmetry of $\theta(z)$ and allow comparison to the modes found in Subsection 4.3.4, namely

$$\phi_o = \frac{\langle \theta(z) \bar{\theta}_o(z) \rangle}{\langle \bar{\theta}_o^2(z) \rangle}, \quad \phi_e = \frac{\langle \theta(z) \bar{\theta}_e(z) \rangle}{\langle \bar{\theta}_e^2(z) \rangle}, \quad (4.4.1)$$

where $\langle \cdot \rangle$ represents integration across the channel from $z = 0$ to d , and $\bar{\theta}_o$ and $\bar{\theta}_e$ are normalised forms of the first modes in equations (4.3.19) and (4.3.22),

$$\bar{\theta}_o(z) = \sin\left(\frac{2\pi z}{d}\right), \quad \bar{\theta}_e(z) = \frac{1}{2} \left(\cos\left(\frac{2\pi(z - d/2)}{d}\right) + 1 \right). \quad (4.4.2)$$

For a solution $\theta(z)$ that is anti-symmetric about the centre of the channel we will therefore have $\phi_o \neq 0$ and $\phi_e = 0$, while for $\theta(z)$ that is symmetric, $\phi_o = 0$ and $\phi_e \neq 0$. To help focus on the different types of mode, the equilibria branches in Figure 4.3 have also been projected onto the shaded horizontal and vertical planes. In order to examine the detail close to the bifurcations from the trivial branch, in Figure 4.4 we reproduce the plots of Figure 4.3 in the vicinity of the plane $\phi_e = 0$, so that the branches associated with the states in Figure 4.2(e) are excluded. Figures 4.3 and 4.4 also indicate the stability of the equilibria branches. Using the continuation package MATCONT, the eigenvalues of the Jacobian of the discretised numerical system of equations are calculated for each equilibrium solution as activity varies. Solution branches for which all eigenvalues

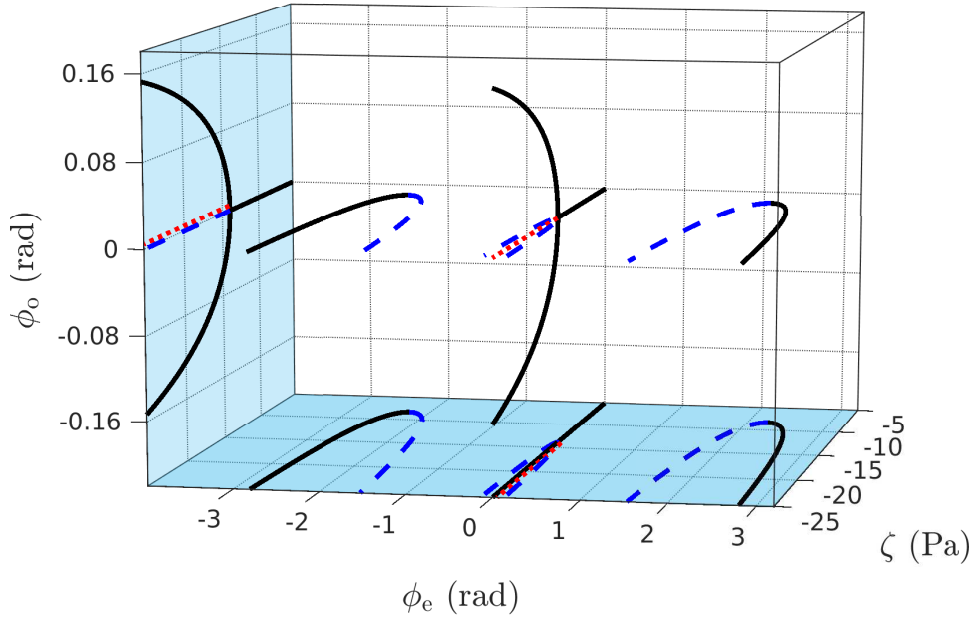


Figure 4.3: Bifurcation diagram for negative activity parameter values and zero pressure gradient, $p_x = 0$, using the measures for $\theta(z)$ solutions given in (4.4.1). Stable equilibria solution branches are indicated by solid curves and unstable equilibria solution branches are indicated by either dashed (one positive eigenvalue) or dotted (two positive eigenvalues) curves.

are negative, and thus the system is stable, are indicated by a solid curve. If exactly one eigenvalue is positive, the branch is presented as a dashed curve, while a dotted curve corresponds to two positive eigenvalues. For any branch with a positive eigenvalue the solution is unstable.

In Figure 4.4, as predicted by the analysis in Subsection 4.3.3, at the critical activity $\zeta_c = -13.87$ Pa, two coincident pitchfork bifurcations occur producing four solution branches. On two of these branches $\phi_e = 0$ (solid curve), corresponding to the positive and negative versions of the anti-symmetric $\theta(z)$ solutions shown in Figure 4.2(a). These solutions are stable to all perturbations. The other two branches $\phi_o = 0$ (dashed curve), corresponding to the positive and negative versions of the symmetric $\theta(z)$ solutions in Figure 4.2(c). These solutions are unstable but, importantly, only to anti-symmetric $\theta(z)$ perturbations - the solutions are stable to any perturbation that retains the symmetry of the director

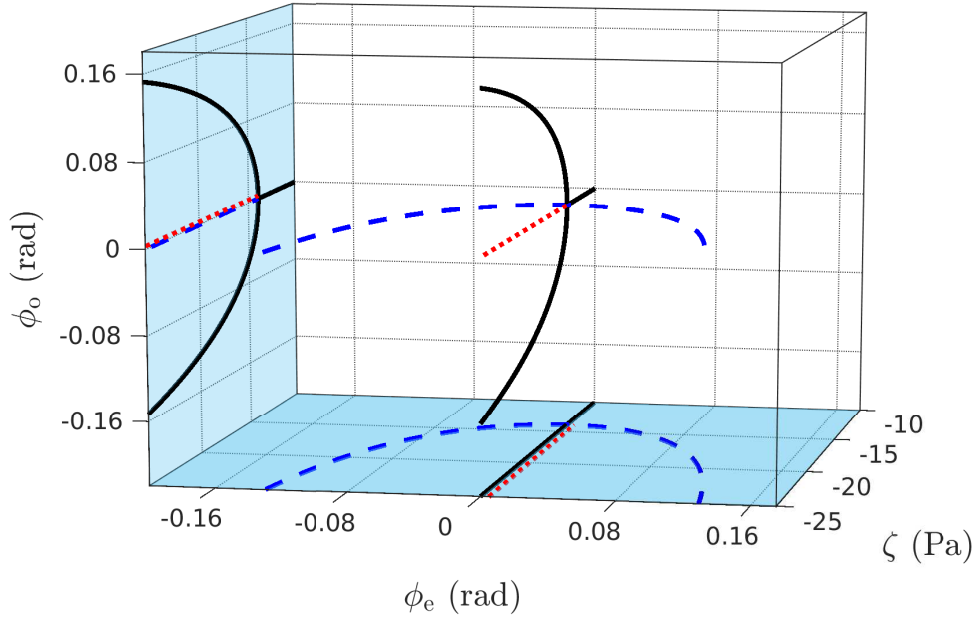


Figure 4.4: Bifurcation diagram for negative activity parameter values and zero pressure gradient, focussing on the bifurcations from the trivial state in the vicinity of $\phi_e = 0$. Stable equilibria solution branches are indicated by solid curves and unstable equilibria branches are indicated by either dashed (one positive eigenvalue) or dotted (two positive eigenvalues) curves.

angle (and the corresponding anti-symmetry of the velocity). In Figure 4.4 we have highlighted only the first mode bifurcations, i.e., $n = 1$ in equations (4.3.19) and (4.3.22), although there are similar pitchfork bifurcations at each critical activity parameter value $\zeta = n^2\zeta_c$. The symmetric $\theta(z)$ solutions in Figure 4.2(e) lie on the non-trivial, stable branch in the $\phi_o = 0$ plane in Figure 4.3 that is disconnected from the trivial state branch. For the post-bifurcation trivial state (the dotted curves in Figures 4.3 and 4.4), the solutions are unstable to both symmetric and antisymmetric perturbations, as are higher mode bifurcations from the unstable trivial branch.

4.4.2 Extensile Active Nematic Liquid Crystals with Non-Zero Pressure Gradient

The introduction of a non-zero pressure gradient alters the $\theta(z)$ and $v(z)$ profiles along with the associated bifurcation structures. At this point our primary focus is the trivial state and its bifurcations and so Figure 4.5 shows the effect of varying the pressure gradient on the equilibrium solutions seen previously in Figures 4.2(a)–(d), and for a particular value of the activity parameter, $\zeta = -20$ Pa. In an inactive Newtonian fluid, the addition of a negative pressure gradient, $p_x < 0$, would lead to a parabolic velocity profile with a maximum velocity in the centre of the channel, similar to the flow shown in Figure 4.2(b). For an active nematic, such a pressure gradient therefore reinforces the positive flow velocity associated with an anti-symmetric director angle solution, thus enhancing the alignment with the Leslie angle and increasing the magnitude of the shear gradients near the boundaries, as seen in the curves for $p_x < 0$ in Figures 4.5(a) and (b). The addition of a positive pressure gradient, $p_x > 0$, would, in a Newtonian fluid, lead to a parabolic velocity profile with a minimum velocity in the centre of the channel which will be in opposition to the activity-induced flow shown in Figure 4.2(b). Such a pressure gradient therefore acts to negate the positive flow velocity associated with an anti-symmetric director angle solution, thus reducing the alignment with the Leslie angle and decreasing the magnitude of the shear gradients near the boundaries, as seen in the curves for $p_x > 0$ in Figures 4.5(a) and (b). Further increases in the positive pressure gradient lead to reverse flow near the channel boundaries and, at sufficiently high p_x values, force the active nematic to flow in the negative x -direction throughout the channel. For both $p_x < 0$ and $p_x > 0$, the pressure gradient-induced and activity-induced velocity profiles share the same symmetry about the centre of the channel, and therefore the spatial symmetry of the final state is unaffected.

The equivalent opposite anti-symmetric solutions (the negative of the solutions in Figure 4.5(a)) are not presented in Figures 4.5(a) and (b). However, as mentioned in Section 4.2, the governing equations (4.2.15) and (4.2.16) are

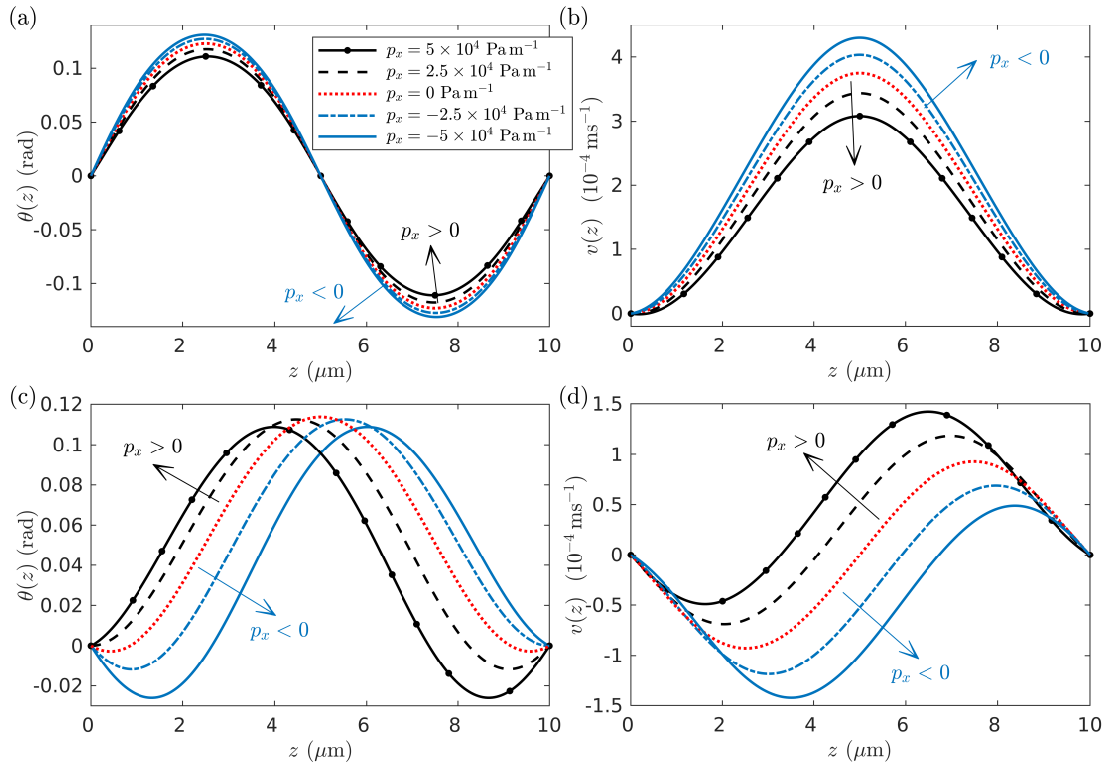


Figure 4.5: (a),(c) Director angle $\theta(z)$ and (b),(d) velocity $v(z)$ equilibrium profiles for activity $\zeta = -20$ Pa and pressure gradients $p_x = -5, -2.5, 0, 2.5, 5 \times 10^4 \text{ Pa m}^{-1}$.

unchanged under the transformation $\theta \rightarrow -\theta$, $v \rightarrow -v$, $p_x \rightarrow -p_x$ so that the equivalent opposite sign of pressure gradient will have the similar effect on the negative velocity solution. We can therefore see that for a fixed pressure gradient (i.e., $p_x = -2.5 \times 10^4 \text{ Pa m}^{-1}$ as in Figure 4.6) will enhance one version of the anti-symmetric $\theta(z)$ solution (that shown in Figure 4.5(a)) while the opposite anti-symmetric $\theta(z)$ solution will be diminished. This effect can be seen in the breaking of the $\phi_o \rightarrow -\phi_o$ symmetry of the bifurcation diagram resulting in a perturbed pitchfork bifurcation structure for the stable branches in the $\phi_e = 0$ plane, as shown in Figure 4.6.

For symmetric director angle profiles, both for the $\theta(z)$ shown in Figure 4.2(c), and the equivalent opposite state $-\theta(z)$, the introduction of a pressure gradient will increase the velocity in one half of the channel while decreasing it in the other. Consequently, both positive and negative pressure gradients will induce

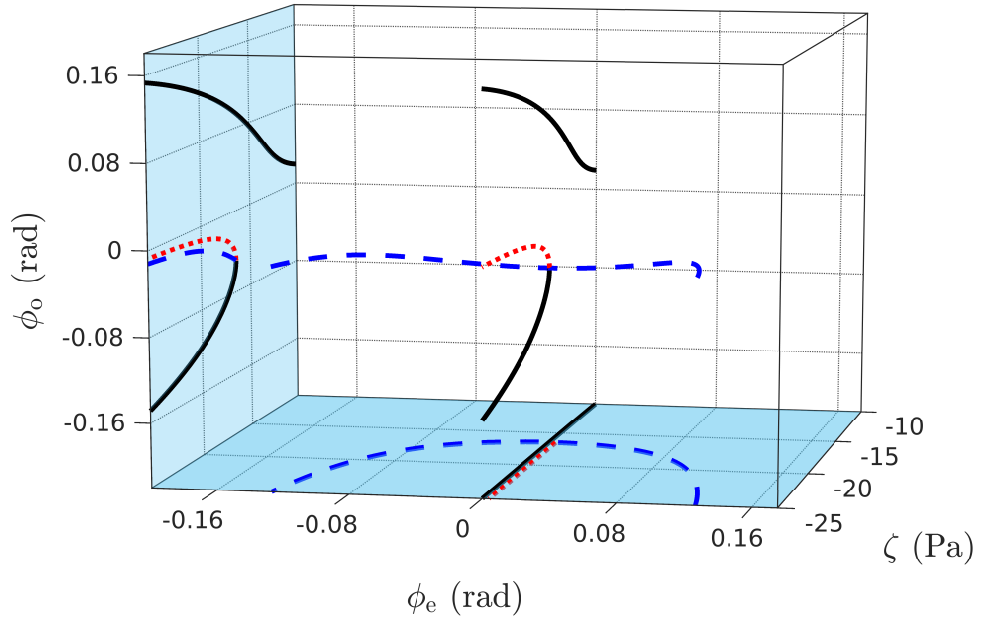


Figure 4.6: Bifurcation diagram for negative activity parameter values and pressure gradient $p_x = -2.5 \times 10^4 \text{ Pa m}^{-1}$, focussing on the effect of the pressure gradient on the bifurcations from the trivial state. Stable equilibria solution branches are indicated by solid curves and unstable equilibria branches are indicated by either dashed (one positive eigenvalue) or dotted (two positive eigenvalues) curves.

a flow that will lead to an asymmetry with respect to the centre of the channel, as shown in Figures 4.5(c) and (d). As a result, the equilibrium branches move out of the plane $\phi_o = 0$, as shown by the dashed curve in Figure 4.6. However, even when a pressure gradient is applied the $\theta(z)$ solution shown in Figure 4.2(c), and the equivalent opposite state $-\theta(z)$ retain a symmetry with each other, namely $\theta(z) = -\theta(d - z)$. Therefore, although the symmetry of the individual states is broken, the bifurcation diagram in Figure 4.6 retains the $\phi_e \rightarrow -\phi_e$ symmetry that was found in the case of zero pressure gradient.

4.4.3 Contractile Active Nematic Liquid Crystals with Zero Pressure Gradient

We now turn our attention to contractile agents, for which $\zeta > 0$, and, at least initially, the case when there is no applied pressure gradient, $p_x = 0$. From the linear analysis in Section 4.3.4 we know that, for the rod-like active agents we consider here, the trivial state is stable for all $\zeta > 0$. While there are no bifurcations from the trivial state branch, other solutions of equations (4.2.15) and (4.2.16) do exist. Figure 4.7 shows solutions obtained numerically for activity parameter values $\zeta = 5, 10, 50, 250$ Pa. As with the extensile active agents, we find symmetric or anti-symmetric director angle configurations, paired with velocities of the opposite symmetry. The solutions for contractile active nematics are characterised by director angle configurations that exhibit large gradients close to the boundaries or the centre of the channel (Figure 4.7(a, c), respectively) that are associated with localised “jets” in the velocity (Figure 4.7(b, d)) which increase in magnitude and become increasingly sharp as the activity increases. From Figures 4.7(a) and (c) we see that, for high values of activity parameter, our solutions match the predicted behaviour from Subsection 4.3.2, namely that the director angle may take the value $\theta = \pi/2$ or $\theta = \theta^* \approx 1.1656$ rad in the bulk of the channel. While Subsection 4.3.2 used an assumption of isotropic viscosity and considered a non-flow aligning nematic to obtain the value for θ^* , and here we have obtained solutions numerically using the anisotropic viscosity values of the liquid crystal 5CB, we see that our numerically calculated value $\theta \approx 1.199$ rad is very similar to the value determined analytically. As in the extensile case, the symmetry $\theta(z) \rightarrow -\theta(z)$, $v(z) \rightarrow -v(z)$ means that there are opposite signed states possible, as well as those in Figure 4.7. The solutions in Figure 4.7(a, b) have, we believe, been observed previously, in the paper of Marenduzzo *et al.* [93] although for lower values of the activity so that the asymptotic value θ^* was less readily observable. The bifurcation diagram for contractile active nematics is shown in Figure 4.8, where we see that the non-trivial branches annihilate at fold (or saddle-node) bifurcations. When we include the trivial state, there are

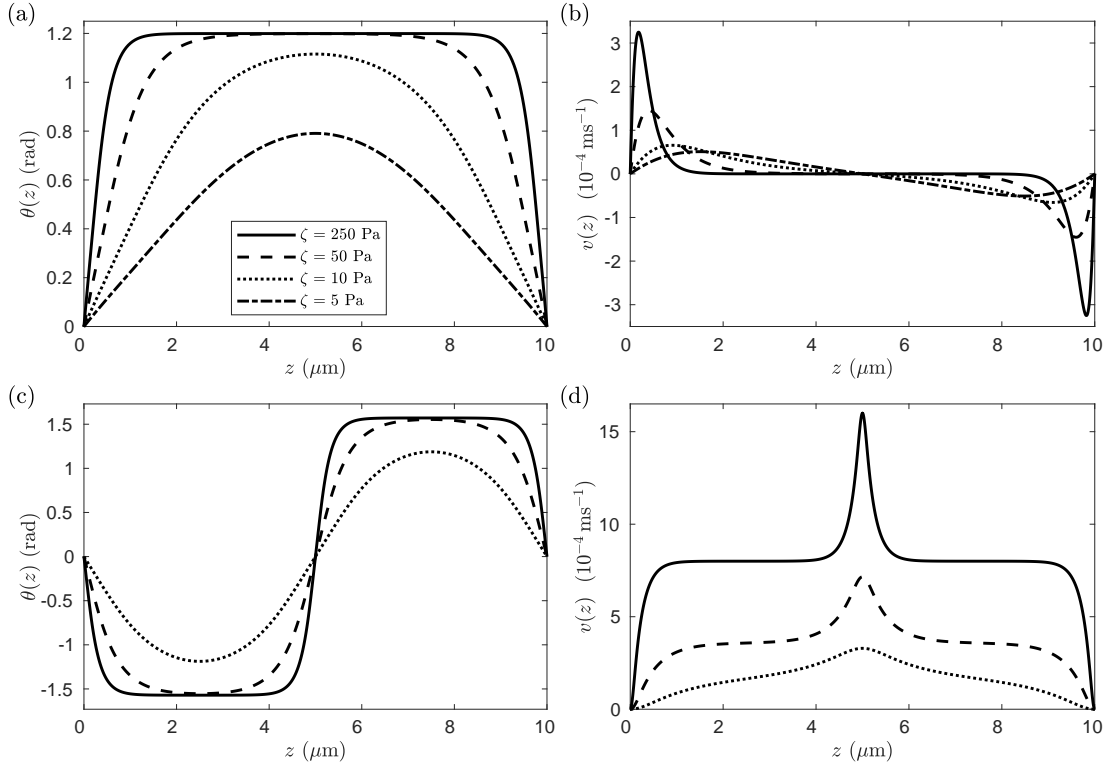


Figure 4.7: (a), (c) Director angle $\theta(z)$ and (b), (d) velocity $v(z)$ equilibrium profiles for activity parameter values $\zeta = 5, 10, 50, 250$ Pa.

up to nine possible equilibria for each activity parameter. In Figure 4.8 we have only shown solutions on two of the eight non-trivial solution branches, the two solutions (up to sign reversal) that are either stable, in the case of the symmetric director profile for Figure 4.8(a, b), or only unstable up to a single perturbation mode, in the case of the anti-symmetric director profile for Figure 4.8(c, d). These solutions can be thought of as the “most stable” for each particular symmetry.

The stable symmetric director solution branches, corresponding to Figure 4.7(a) and the equivalent solution of opposite sign, are the non-trivial solid curves in the plane $\phi_o = 0$ in Figure 4.8. The unstable antisymmetric director solution branches, corresponding to Figure 4.7(c) and the equivalent solution of opposite sign, are the the dashed curves in the plane $\phi_e = 0$ in Figure 4.8 and are stable to antisymmetric director angle perturbations but stable to symmetric director angle perturbations. Note that, in general, the fold bifurcations for the symmetric and antisymmetric director angles do not occur at the same critical

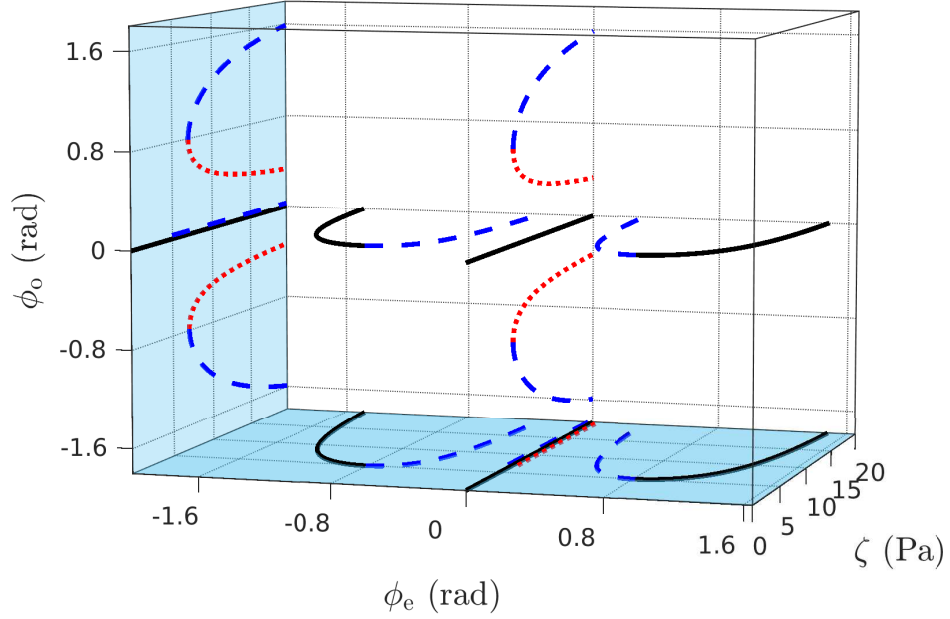


Figure 4.8: Bifurcation diagram for positive activity parameter values and zero pressure gradient, $p_x = 0$, using the measures for $\theta(z)$ solutions given in (4.4.1). Stable equilibria solution branches are indicated by solid curves and unstable equilibria branches are indicated by either dashed (one positive eigenvalue) or dotted (two positive eigenvalues) curves.

activities. For instance, in Figure 4.8 the solutions shown in Figure 4.7(a, b) exist for $\zeta \gtrsim 4.93$ Pa and the solutions in Figure 4.7(c, d) exist for $\zeta \gtrsim 7.03$ Pa.

4.4.4 Contractile Active Nematic Liquid Crystals with Non-Zero Pressure Gradient

When a pressure gradient is introduced, the solutions in Figure 4.7 adapt in a similar way to the extensile case, as seen in Figure 4.9. For equilibria with antisymmetric velocity profiles (e.g., Figure 4.7(a, b)), the introduction of a pressure gradient leads to asymmetry in both the director angle and velocity (Figure 4.9(a, b)). The positive and negative solution branches in the plane $\phi_o = 0$ in Figure 4.8 both adapt in the same way and are promoted to occur at lower values of the activity parameter. For a negative pressure gradient, equilibria for which

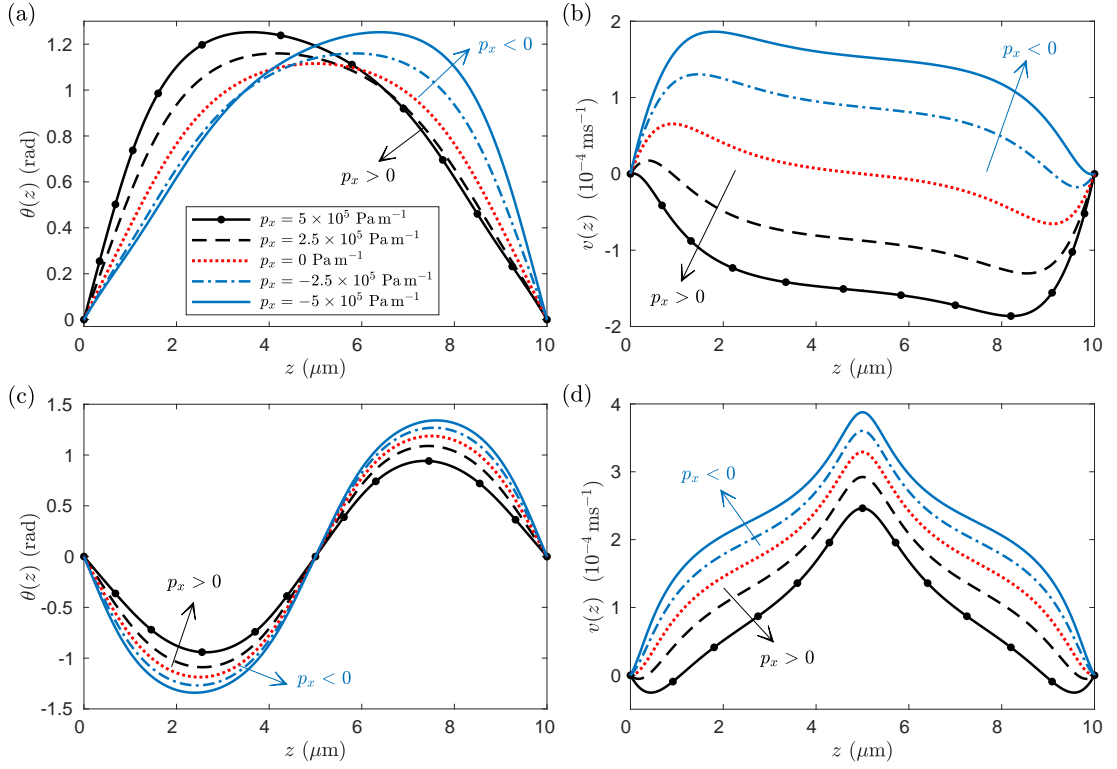


Figure 4.9: (a), (c) Director angle $\theta(z)$ and (b), (d) velocity $v(z)$ equilibrium profiles for activity $\zeta = 10 \text{ Pa}$ and pressure gradients $p_x = -5, -2.5, 0, 2.5, 5 \times 10^5 \text{ Pa m}^{-1}$.

the velocity is symmetric and positive (Figure 4.7(c, d)) will be enhanced and occur at smaller values of activity. Conversely, the pressure gradient-induced flow will retard negative velocity solutions meaning they can occur only for larger activities. This breaking of the $\phi_o \rightarrow -\phi_o$ symmetry is observed in the plane $\phi_e = 0$ in Figure 4.10.

4.5 Two-Parameter Continuation

We can summarise the effect of varying the activity parameter and applied pressure gradient on the various equilibria, for both extensile and contractile active nematics, by considering the bifurcation set in (ζ, p_x) space, i.e., the location of fold and pitchfork bifurcations.

There are seven possible critical bifurcation points: the single fold/pitchfork

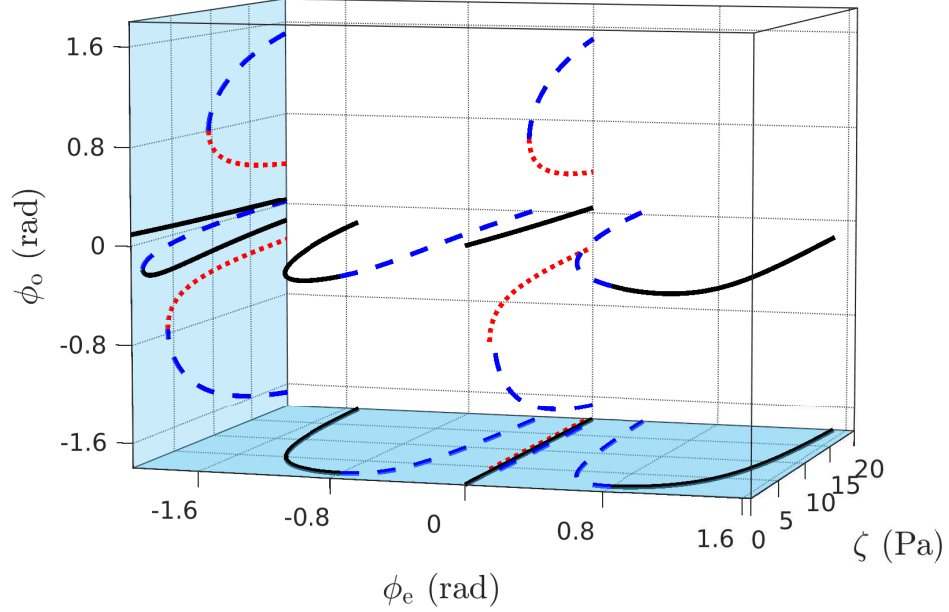


Figure 4.10: Bifurcation diagram for positive activity parameter values and pressure gradient $p_x = -10^5 \text{ Pa m}^{-1}$, using the measures for $\theta(z)$ solutions given in (4.4.1). Stable equilibria solution branches are indicated by solid curves and unstable equilibria solution branches are indicated by either dashed (one positive eigenvalue) or dotted (two positive eigenvalues) curves.

point in Figure 4.6 associated with the branches of positive and negative versions of the solutions shown in Figure 4.5; the two fold points shown in Figure 4.3 associated with the positive and negative solution branches of solutions shown in Figure 4.2(e, f); and the four fold points shown in Figure 4.10 associated with the positive and negative solution branches of solutions shown in Figure 4.9. However, for clarity we do not plot the locations of the two fold points of the branches of unstable solutions in the $\phi_e = 0$ plane in Figure 4.10 because, being unstable, these solutions are unlikely to be observed in reality. Of the remaining five critical points, the two pairs of fold points occur at the same value of the activity parameter and so the locations of the critical points will lead to only three loci in (ζ, p_x) space. We plot these three loci in Figure 4.11.

Curve (A) in Figure 4.11(a) indicates the location of the fold bifurcations where the four solution branches meet in Figure 4.6 for $p_x \neq 0$ (or the pitchfork

bifurcation point in Figure 4.3 when $p_x = 0$). The fold bifurcation points in the plane $\phi_o = 0$ in Figure 4.3 for $p_x = 0$ correspond to symmetric director angle profiles. The position of these bifurcation points as p_x varies, coinciding with the director angle losing symmetry, is represented by curve (B). Similarly, curve (C) corresponds to the fold bifurcation points lying in the plane $\phi_o = 0$ in Figure 4.8. In the region between curves (B) and (C), the only stable equilibria will therefore be on the continuous, stable branch of the perturbed pitchfork bifurcation seen in Figures 4.6 and 4.10. This region in (ζ, p_x) space is characterised by solutions of relatively low director distortion and velocity, for which the activity parameter is too small in magnitude to dominate either the elastic or the pressure gradient effects. In fact, when the pressure gradient is absent, the solutions revert to the trivial case ($\theta \equiv 0, v \equiv 0$). Therefore, in Figure 4.11 we denote the low distortion regime as the “trivial state”, though it is generally more accurate to describe it as the *perturbed* trivial state. For (ζ, p_x) to the left of curve (A) there are four stable equilibria, characterised by anti-symmetric flow-alignment close to $\pm\theta_L$ rad and asymmetric flow-alignment close to $\pm(\pi - \theta_L)$ rad. (The asymmetry is the result of a pressure gradient on a symmetric director angle structure similar to the behaviour in Figures 4.5(c) and 4.9(a).) Between curves (A) and (B) for extensile active nematics, and to the right of (C) for a contractile agent, there are two stable, asymmetric director angle solutions as well as the trivial state. These correspond, respectively, to alignment close to $\pm(\pi - \theta_L)$ rad in much of the channel for extensile activity or at the angle approximated by $\pm\theta^*$ as found in Subsection 4.3.3 for contractile activity. The process of transition between these states in the connected region surrounding the shaded area between curves (B) and (C) is now investigated.

The extent of region between (B) and (C), where the perturbed trivial state is the only equilibrium, decreases as the magnitude of the pressure gradient increases, with the two curves meeting at approximately $\zeta = -2.05$ Pa. Figure 4.11(b) focusses on the region close to this activity parameter for $p_x < 0$ highlighted by the grey box in Figure 4.11(a) and demonstrates a swallowtail catastrophe [156]. Curves (B) and (C) are symmetric with respect to the pres-

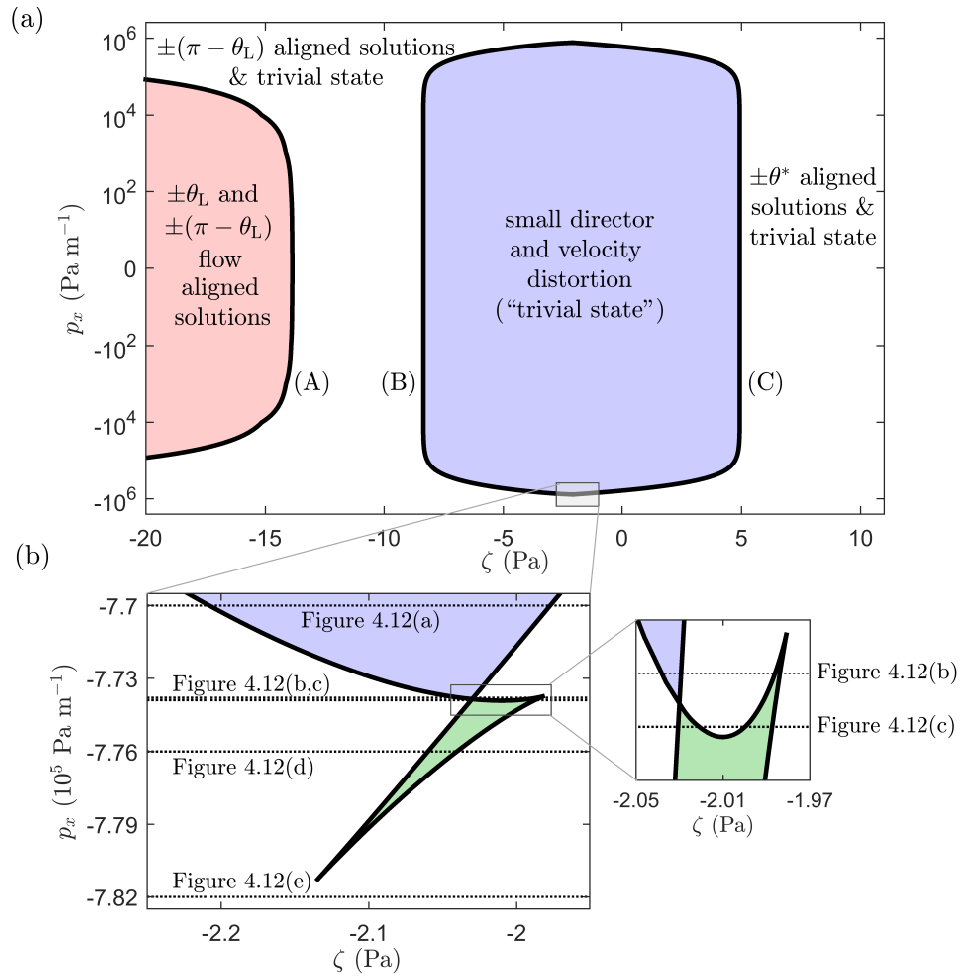


Figure 4.11: (a) Location of pitchfork and fold bifurcation points for solution branches exhibiting stable equilibria. (b) An expanded view in the grey boxed area in (a), close to $\zeta = -2.1$ Pa.

sure gradient, so a similar swallowtail feature occurs for $p_x > 0$. The process is expanded upon in Figure 4.12, where we show bifurcation plots in the (ζ, ϕ_e) plane as $|p_x|$ increases. The ϕ_o measure for equilibria $\theta(z)$ will be non-zero for these solutions, but the transition can be illustrated by restricting attention to ϕ_e . The horizontal dotted lines in Figure 4.11(b) correspond to the pressure gradients used in Figure 4.12. The perturbed trivial branch is not shown in Figure 4.12, but it does also exist for this range of pressure gradients and activities.

For $p_x = -7.7 \times 10^5 \text{ Pa m}^{-1}$ in Figure 4.12(a), there is a small interval of activity over which the trivial state is the only equilibrium, between the left-

hand fold point (curve (B) in Figure 4.11) and the right-hand fold (curve (C) in Figure 4.11). In Figure 4.12(b), the right-hand fold has transformed at a cusp catastrophe and this branch now has three fold points associated with it. In Figure 4.12(b) there is still an interval of activities close to $\zeta = -2.03$ Pa where only the trivial state exists. However, there is also a very narrow range of activities close to $\zeta = -1.99$ Pa where extra states exist. Once $p_x = -7.739 \times 10^5$ Pa m⁻¹ in Figure 4.12(c), the range of activity for these extra states has widened. Also, there are no longer any activities for which the trivial state is the unique equilibrium. Between Figure 4.12(c) and Figure 4.12(d) the two uppermost fold points have merged creating a continuous stable branch of solutions in Figure 4.12(d), when $p_x = -7.76 \times 10^5$ Pa m⁻¹, with two unstable branches now linked through two fold points and a stable branch. Finally, for large enough $|p_x|$ in Figure 4.12(e), the two fold points have annihilated leaving individual continuous stable and unstable branches. It is the formation of this continuous stable branch that allows the transition between solutions with director alignment close to $\pm(\pi - \theta_L)$ rad, for extensile activity, to solutions with director alignment close to $\pm\theta^*$ for contractile activity.

In Figures 4.13 and 4.14, we consider this transition between $\pm(\pi - \theta_L)$ rad, and $\pm\theta^*$ alignments for a value of $|p_x|$ greater than the value considered in Figure 4.12(e). Clearly pressure gradient-induced flow dominates for small activity parameter values ζ . However, activity still dominates the pressure gradient effects for sufficiently large magnitude ζ values. Figure 4.13 shows the measure ϕ_e as the activity strength values with the pressure gradient fixed at $p_x = -10^6$ Pa m⁻¹. This choice of pressure gradient leads to a continuous stable equilibrium branch in which there is an equilibria transition from $(\pi - \theta_L)$ solutions to θ^* solutions as the activity strength increases. Figure 4.14(a) shows the transformation from a solution in which there is alignment with $(\pi - \theta_L)$ rad (e.g., $\zeta = -200$ Pa, to a solution in which there is alignment with θ^* rad (e.g., $\zeta = 200$ Pa). The corresponding flow profiles are plotted in Figure 4.14(b, c), It is worth noting that the special case $\zeta = 0$ Pa in Figure 4.14 does not represent classic Poiseuille flow for an inactive nematic with a parabolic velocity profile. Poiseuille flow would

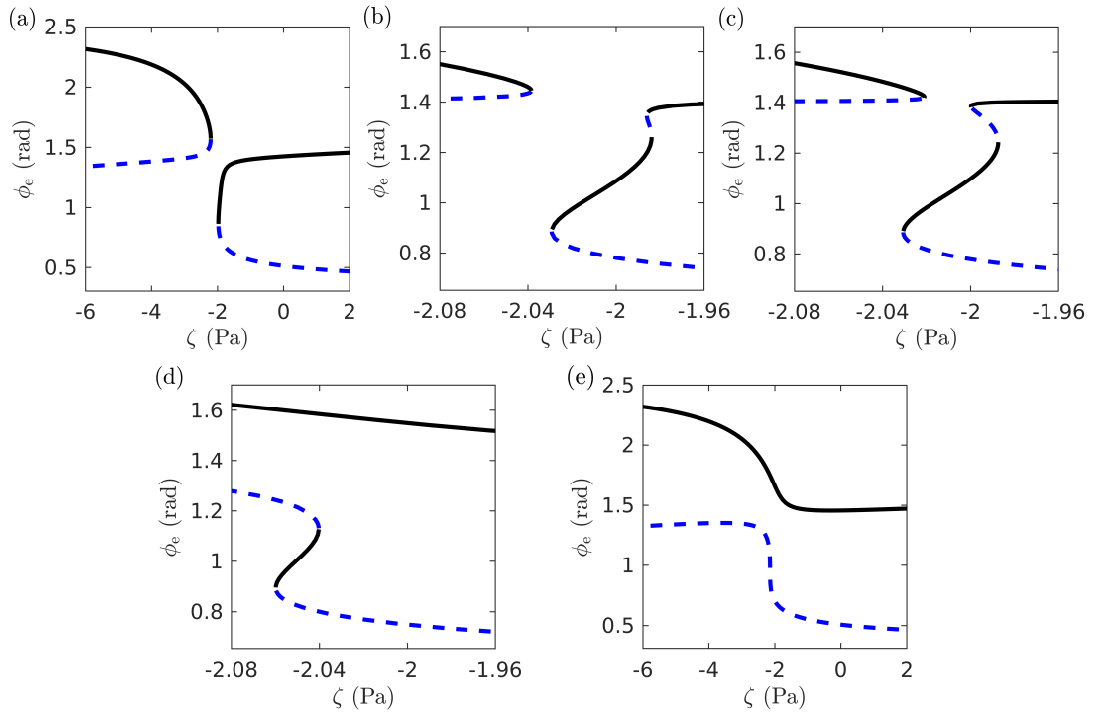


Figure 4.12: Bifurcation diagrams for pressure gradients, p_x , equal to (a) -7.7 , (b) -7.738 , (c) -7.739 , (d) -7.76 , and (e) $-7.82 \times 10^5 \text{ Pa m}^{-1}$, using the measure ϕ_e for $\theta(z)$. The five pressure gradients correspond those indicated in Figure 4.11(b). Solid curves are stable equilibria solution branches, while unstable equilibria solution branches with one positive eigenvalue are dashed curves.

be the result of applying a pressure gradient to the trivial state in the absence of activity, leading to a symmetric velocity and an anti-symmetric director angle solution which vanishes in the centre of the channel. The states examined in Figures 4.13 and 4.14 are inherently asymmetric with the director angles non-zero except at the boundaries.

In Figure 4.11 we have therefore summarised the areas in (ζ, p_x) space for which the most important solutions exist. However, as mentioned previously, there are many more possible solutions at higher magnitude activity parameter values but which are unstable to either symmetric or anti-symmetric director angle perturbations, and contain regions of high elastic energy.

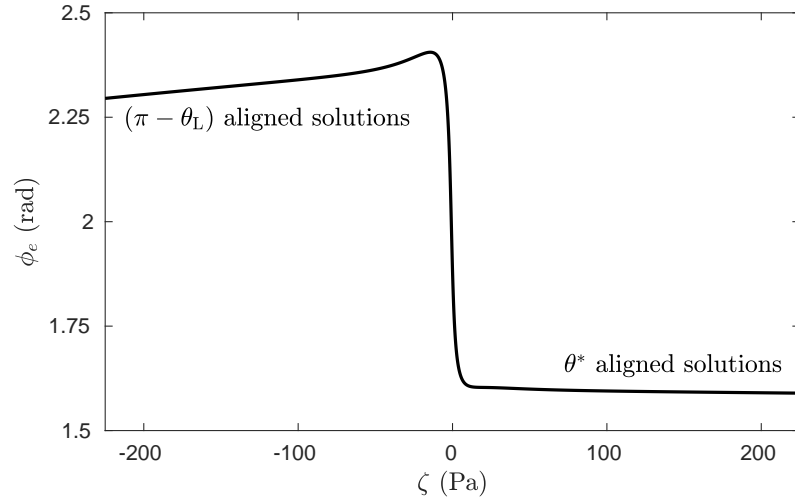


Figure 4.13: Stable equilibrium branch for pressure gradient $p_x = -10^6 \text{ Pa m}^{-1}$, using the measure ϕ_e for $\theta(z)$. As the activity parameter ζ increases, the equilibria transition from $(\pi - \theta_L)$ solutions to θ^* solutions.

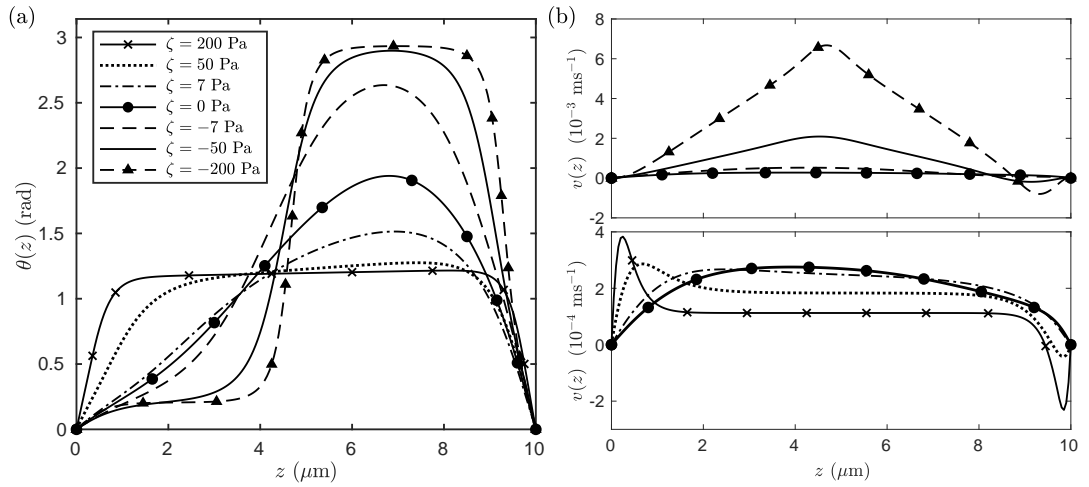


Figure 4.14: The director angle transition from $(\pi - \theta_L)$ solutions to θ^* solutions, with associated velocity profiles, along the solution branch in Figure 4.13 as the activity parameter increases: (a) Director angle $\theta(z)$ and (b) velocity $v(z)$ equilibrium profiles for pressure gradient $p_x = -10^6 \text{ Pa m}^{-1}$ and a range of activity parameter values between $\zeta = -200$ and 200 Pa . The velocity solution for $\zeta = 0 \text{ Pa}$ is shown in both plots in (b).

4.6 Reorientation of Active Nematic Liquid Crystals Subject to an External Orienting Field

In the work of Pieranski *et al.* [112] on the dynamics of the Freedericksz transition in nematic liquid crystals, it was shown that the reorientation of the director due to an externally applied field can induce fluid flow. The enhanced flow that is caused by molecular rearrangement during the switch-on of an external orienting field is known as backflow [129]. When the field is switched off, the director can either begin to relax back to its pre-switched configuration, or alternatively, the fluid can move one way before reversing direction, and then eventually dissipate, with the director decaying back to the pre-switched orientation. This initial movement of the fluid upon removal of an applied field often coincides with the director orientation overshooting past its switched-on configuration. This increase in the director is known as kickback and occurs due to the coupling between the backflow and director orientation [129]. The dynamics of the Freedericksz transition was considered recently by Mottram *et al.* [104] for an inactive nematic liquid crystal confined between two parallel electrodes and subject to a spatially varying electric field across the layer. The model considered in [104] showed, through a decoupling of the non-linear Ericksen-Leslie equations that kickback can be avoided for an appropriate choice of applied voltage. This followed from the linearised Ericksen-Leslie model considered by Da Costa *et al.* [30], who examined kickback in nematic liquid crystals due to a large magnetic field analytically. The avoidance of kickback can have practical implications for switching in devices since any increase in the director angle when the field is switched off can lead to an increase in the cell switch-off time. The realignment of active agents in a liquid crystal subject to a uniform magnetic field has recently been considered experimentally by Guillamat *et al.* [64, 65] and theoretically by Doostmohammadi *et al.* [37], which showed similar reorientations to those observed in inactive nematic liquid crystals. The motion of active colloids in liquid crystals subject to an electric field

was considered by Lavrentovich [78]. This was extended by Conklin *et al.* [27], who proposed an analogy between the active stresses which induce flow in active liquid crystals and the backflow induced in inactive liquid crystals due to electric fields. In this section we consider the transient behaviour of an active nematic liquid crystal confined in a shallow channel, subject to a uniform orienting field, where a transient flow will be created by director rotation due to the uniform orienting field. A similar approach to that in [104] will be adopted here, where we assume zero pressure gradient and decouple the Ericksen-Leslie equations in order to examine the dynamics of the director orientation of an active nematic liquid crystal when the field is applied, and then switched off. We consider director configurations which are symmetric and anti-symmetric with respect to the channel centre.

A uniform orienting field \mathbf{F} is applied perpendicular to the boundaries of the channel such that $\mathbf{F} = (0, 0, F)$, where $F = |\mathbf{F}|$. Note that, if we were to interpret this orienting field as a classic electric/magnetic field applied to an inactive nematic, then the applied field would need to also satisfy the appropriate Maxwell equations (see Chapter 2). In order to ensure that the director switches after the field is turned on, a small pretilt of the director is imposed on the plates such that $\theta(0, t) = \Phi_0$ and $\theta(d, t) = \Phi_d$. In the absence of pretilt, the initial director tilt angle is zero at both plates, which leads to a discontinuity when the field is switched on. Initially, the liquid crystal is at rest and the director orientation changes linearly across the channel,

$$\theta(z, 0) = \Phi_0 + \frac{z(\Phi_d - \Phi_0)}{d}. \quad (4.6.1)$$

We include a classic magnetic/electric energy density in the bulk energy density of the form

$$w_{\text{field}} = -\frac{1}{2}\chi_f(\mathbf{n} \cdot \mathbf{F})^2, \quad (4.6.2)$$

where χ_f is the anisotropic susceptibility of the active nematic to the aligning field, which we assume is positive so that for a sufficiently strong orienting field, the director will align with the field in the bulk of the channel in the same way as it would due to an electric/magnetic field. In comparison with a classic magnetic

field energy density, χ_f is analogous to the coefficient $\mu_0\Delta\chi$ in a magnetic-field induced Fredericksz transition, where $\mu_0 = 4\pi \times 10^{-7} \text{ Hm}^{-1}$ is the permeability of free space and $\Delta\chi$ is the magnetic anisotropy of the liquid crystal (see Chapter 2). Minimisation of (4.6.2) with respect to the director angle θ generates the same term in the angular momentum equation due to a magnetic field when modelling one-dimensional splay-bend Fredericksz cells [104, 129]. In the absence of fluid inertia and assuming that the hydrostatic pressure is constant across the channel in the x -direction, the Ericksen-Leslie equations with the external orienting field and activity terms are

$$\begin{aligned} \gamma_1\theta_t &= (K_1 \cos^2 \theta + K_3 \sin^2 \theta)\theta_{zz} + (K_3 - K_1) \sin \theta \cos \theta(\theta_z)^2 + \chi_f F^2 \sin \theta \cos \theta \\ &\quad - m(\theta)v_z, \end{aligned} \tag{4.6.3}$$

$$0 = (g(\theta)v_z + m(\theta)\theta_t + \zeta \sin \theta \cos \theta)_z. \tag{4.6.4}$$

with boundary conditions

$$\theta(0, t) = \Phi_0, \quad v(0, t) = 0, \tag{4.6.5}$$

$$\theta(d, t) = \Phi_d, \quad v(d, t) = 0. \tag{4.6.6}$$

The individual dimensions of χ_f and F are unknown. However, in order to match with the dimensions of the rest of the terms in equation (4.6.3), it follows that the product $\chi_f F^2$ must have dimensions of pressure, which means that the external orienting field can be thought of as a pressure-like driving field. Employing the calculations outlined in Appendix C, the decoupled dynamic equation for the director angle is

$$\begin{aligned} \left(\gamma_1 - \frac{m^2(\theta)}{g(\theta)} \right) \theta_t &= (K_1 \cos^2 \theta + K_3 \sin^2 \theta)\theta_{zz} + (K_3 - K_1) \sin \theta \cos \theta(\theta_z)^2 \\ &\quad + \chi_f F^2 \sin \theta \cos \theta - \frac{m(\theta)\bar{\mathcal{H}}}{g(\theta)\bar{\mathcal{B}}} \\ &\quad + \frac{\zeta m(\theta)}{g(\theta)} \left(\sin \theta \cos \theta - \bar{\mathcal{C}} - \frac{\bar{\mathcal{D}}}{\bar{\mathcal{B}}} \right), \end{aligned} \tag{4.6.7}$$

where the definitions of the integrals $\bar{\mathcal{B}}$, $\bar{\mathcal{C}}$ and $\bar{\mathcal{D}}$ are the same as those given

previously in equations (4.3.4)–(4.3.5), and

$$\bar{\mathcal{H}} = \int_0^d \frac{m(\theta)}{\gamma_1 g(\theta) - m^2(\theta)} \left[(K_1 \cos^2 \theta + K_3 \sin^2 \theta) \theta_{zz} + (K_3 - K_1) \sin \theta \cos \theta (\theta_z)^2 + \chi_f F^2 \sin \theta \cos \theta \right] dz. \quad (4.6.8)$$

We will solve equation (4.6.7) numerically in COMSOL for both a contractile and extensile active nematic liquid crystal. We assume that the magnitude of the two pretilt angles Φ_0 and Φ_d are the same, where the relative signs of the pretilt angles determine whether we have a director angle solution which is symmetric or anti-symmetric with respect to the centre of the channel. If we choose our boundary conditions such that the signs of the pretilts on both boundaries are the same, then this will induce a director profile which is symmetric with respect to the centre of the channel. This technique is known as anti-parallel rubbing [104]. The alternative scenario is when the pretilts at the two boundaries are equal in magnitude but opposite in sign - this is known as parallel rubbing. In the calculations that follow, we impose small pretilts $\Phi_0 = \pm 0.01$ radians and $\Phi_d = 0.01$ radians. For future reference, we define the director profile obtained from anti-parallel rubbing as Mode I, and the director structure derived from parallel rubbing as Mode II.

4.6.1 Reorientation of Contractile Active Nematic Liquid Crystals

We first consider the reorientation of a contractile active nematic liquid crystal subject to anti-parallel rubbed anchoring. An external pressure driving field with coefficient $\chi_f F^2 = 100$ Pa is applied to the liquid crystal, which proves to be sufficiently large enough to reorient the director such that it aligns with the orienting field in the bulk of the channel during switch-on. Figure 4.15(a) shows the initial stages of the dynamics of the director angle when the orienting field is switched on for an active nematic liquid crystal with activity $\zeta = 50$ Pa. This value of activity is chosen on the basis that it exceeds the critical value of activity for this mode when we had zero pretilt and orienting field. During switch-

on, the orienting field forces the director angle to increase from an initial state of $\theta = 0.01$ rad for all z to a distorted director structure with $\theta \approx \pi/2$ in most of the channel, which is also what occurs in the early stages of the dynamics of a Fredericksz transition for a strong electric/magnetic field [104], so the influence of the activity during switch-on appears to be minimal.

Figure 4.15(b) shows the dynamics of the director angle configuration after the applied field is removed at switch-off time $t_{\text{off}} = 0.05$ seconds, where we find that the director angle structure has relaxed into an equilibrium state which resembles the bulk symmetric director angle structure we found previously. We have plotted each of the director structures in Figure 4.15(b) labelling time as a difference of the times after switch-off and the switch-off time t_{off} so that $\theta(z, t_{\text{off}}) = \theta_{\text{eq}}(z)$, (i.e., the system is “initially” at equilibrium after the field is switched off). We find that due to the strength of the activity of the liquid crystal, there is no evidence of kickback upon removal of the applied field. An investigation into kickback in contractile and extensile active nematic liquid crystals will be discussed in Subsection 4.6.3.

When we consider the boundary conditions for parallel rubbing, this will generate a solution for θ which is odd in z . In this case, the integrals $\bar{\mathcal{C}}$, $\bar{\mathcal{D}}$ and $\bar{\mathcal{H}}$ are all equal to zero so that equation (4.6.7) simplifies to

$$\begin{aligned} \left(\gamma_1 - \frac{m^2(\theta)}{g(\theta)} \right) \theta_t &= (K_1 \cos^2 \theta + K_3 \sin^2 \theta) \theta_{zz} + (K_3 - K_1) \sin \theta \cos \theta (\theta_z)^2 \\ &+ \left(\chi_f F^2 + \frac{\zeta m(\theta)}{g(\theta)} \right) \sin \theta \cos \theta. \end{aligned} \quad (4.6.9)$$

Therefore, when we have a solution for the director angle which is anti-symmetric with respect to the centre of the channel, the only terms which are associated with the flow when the field is switched off are the reduced rotational viscosity and the simplified activity term. For this symmetry, the flow is always aiding director relaxation and leads to faster switching. We use the same values of the applied field and activity as used for Mode I where like Mode I, the chosen activity exceeds the numerically calculated critical activity value for Mode II with zero pretilt and orienting field. The strength of the orienting field forces the director to adjust its orientation such that it aligns with the field in most of the channel

during switch-on, as shown in Figure 4.15(c). Figure 4.15(d) shows the dynamics of the director angle profile once the field is switched off, where the director angle relaxes towards the anti-symmetric structure we found before in the bulk of the channel. Even though we found that this director configuration was unstable in Section 4.4, we have shown here that the symmetry of the system means that we can at least access this unstable solution transiently through an external orienting field. We find that for times larger than the final time shown in Figure 4.15(d) ($t - t_{\text{off}} = 10$ seconds), the director structure does not change appreciably and we remain on the solution branch. Unlike Mode I, we find that for a value of activity which is less than the critical value, there is no evidence of kickback and the Mode II director configuration relaxes towards its alignment prior to the field being switched on. Anti-symmetric director structures of inactive nematic liquid crystals also do not appear to exhibit any kickback upon removal of an applied field [104].

4.6.2 Reorientation of Extensile Active Nematic Liquid Crystals

We now consider the reorientation of extensile active nematics subject to a driving field. First, we examine the scenario of anti-parallel rubbing. In our previous investigation with zero pressure gradient and orienting field, we found four possible director angle configurations which were symmetric with respect to the centre of the channel, with two of them the mirror images of each other. One of these solutions was stable to both symmetric and anti-symmetric perturbations in θ , where the director angle aligned at $\pi - \theta_L$ in the bulk of the channel. The other solution we found was unstable to anti-symmetric perturbations in θ and the director angle aligned at θ_L in most of the channel. In the calculations that follow, we fix the activity strength parameter at $\zeta = -250$ Pa. Unlike the contractile active nematic liquid crystal, we consider two values of the coefficient of the orienting field, one of which is the same value considered for the contractile active nematic liquid crystal, with the other significantly smaller. As we will see,

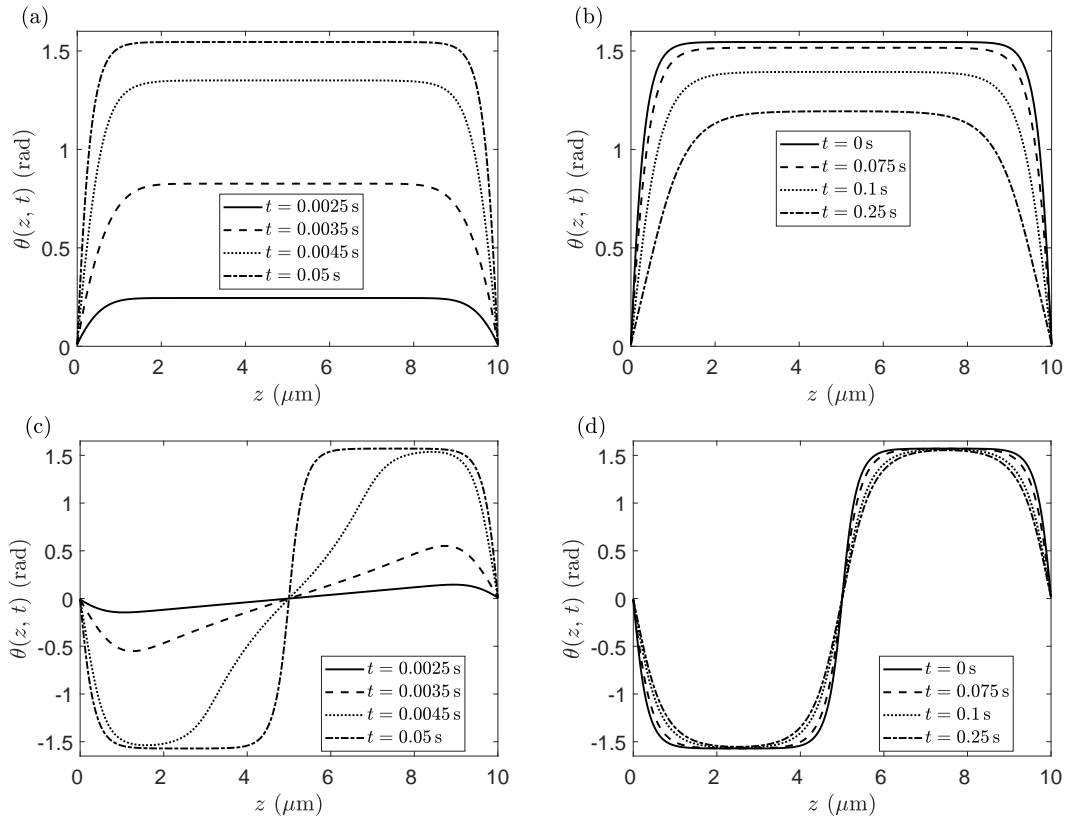


Figure 4.15: The evolution of the director angle $\theta(z, t)$ throughout the channel during (a, c) switch-on and (b, d) switch-off for a contractile active nematic with activity strength $\zeta = 50$ Pa. The orienting field coefficient during switch-on is $\chi_f F^2 = 100$ Pa.

changing the size of the field strength allows for both of the symmetric director structures to be obtained for a fixed value of activity strength. We also find that a smaller orienting field proves necessary in order to access the anti-symmetric director configuration for an extensile active nematic.

Figure 4.16(a) shows the evolution of the director angle during switch-on with field strength $\chi_f F^2 = 100$ Pa, where we find that a combination of the backflow caused by the activity and the orienting field have forced the director to evolve to an angle $\theta \approx \pi - \theta_L$ in most of the channel. The response of the director angle during switch-off is shown in Figure 4.16(b) where we find that the removal of the field leads to more pronounced kickback. For a symmetric director angle profile of an inactive nematic liquid crystal, application of a sufficiently strong

external orienting field will always lead to kickback when the field is switched off [30]. Combining the initial increase in the director angle in the middle of the channel that occurs after the field is switched off due to kickback with the realignment of the director induced by activity forces the director angle to evolve closer to $\theta \approx \pi - \theta_L$ in most of the channel. Whenever we consider a large orienting field, our dynamic solver always equilibrates at the solution branch shown in Figure 4.16(b) when the field is switched off. Therefore, in order to access the remaining two director configurations found previously for an extensile active nematic, where the director aligns with the flow at the Leslie angle in most of the channel for large magnitudes of extensile activity, we need to use a smaller orienting field.

When we consider a much smaller value of a driving field, we find that the dynamics of the director orientation of Mode I change significantly. The evolution of the director angle during switch-on with field coefficient $\chi_f F^2 = 10$ Pa is shown in Figure 4.16(c). At switch-off time $t = 0.05$ seconds, we find that the magnitude of the director orientation in most of the channel has slightly increased beyond the Leslie angle $\theta_L = 0.2$ rad. This means that upon removal of the field, there is less of an energy cost for the liquid crystal to relax towards the unstable symmetric mode than there is for the liquid crystal to evolve towards the high elastic energy stable mode we discussed above. This is exactly what we can see happens in Figure 4.16(d), where we find that the director structure does not change appreciably for larger times ($t - t_{\text{off}} = 10$ seconds). Therefore, one way in which the symmetric director structure which aligns at the Leslie angle in most of the channel can be accessed transiently is through a reduced orienting field for a large magnitude of activity strength. Even though this configuration was shown to be unstable, we have again shown how we can access unstable solutions transiently. In the analysis considered earlier in this chapter with zero pretilt and orienting field, we found a non-trivial anti-symmetric director structure for an extensile active nematic in which the director aligned with the flow in most of the channel. This mode was shown to be stable to both symmetric and anti-symmetric perturbations in θ . In order to achieve an anti-symmetric director

configuration, we find that a much smaller orienting field coefficient is needed as a large field leads to the equilibrium director configuration in Figure 4.16(b). From Figure 4.16(e), we observe that when a field with coefficient $\chi_f F^2 = 10$ Pa is applied to the liquid crystal, the director orientation in most of the channel is close to the Leslie angles. The evolution of the director angle profile for Mode II when the field is switched off is shown in Figure 4.16(f), which demonstrates that the director angle relaxes towards the anti-symmetric flow-aligning structure we found from our previous analysis in the bulk of the channel. In summary, we have shown how stable and unstable active nematic liquid crystal director configurations can be accessed transiently through an external orienting field.

4.6.3 Kickback in Active Nematic Liquid Crystals

To conclude this section, we now examine kickback in active nematic liquid crystals. We do so for a range of positive and negative activity strengths. Our attention is focussed on the symmetric director configurations in Figures 4.15(a, b) for a contractile active nematic, and Figures 4.16(a, b) for an extensile active nematic. As mentioned previously, we find that anti-symmetric director configurations do not exhibit any kickback once the external orienting field is switched off, similar to the findings in [104].

We first consider the dynamics of contractile active nematic liquid crystals subject to an external orienting field of strength $\chi_f F^2 = 100$ Pa. Figure 4.17(a) shows the variation of the director angle in the centre of the channel $\theta(d/2, t)$ with time for positive activity strengths. For each of the activity strength values, we can see that as time progresses, the director at the centre of the channel evolves towards a switch-on equilibrium value of $\theta_{\text{on}}(d/2) \lesssim \pi/2$. We include a zoomed-in plot of $\theta(d/2, t)$ in order to distinguish the equilibrium values of the director orientation at the channel centre for each activity strength. Once the director in the centre of the channel has achieved its equilibrium switch-on value, the orienting field is switched off at time $t = t_{\text{off}}$ and we solve the evolution equation (4.6.7) for the switch-off equilibrium director orientation. The

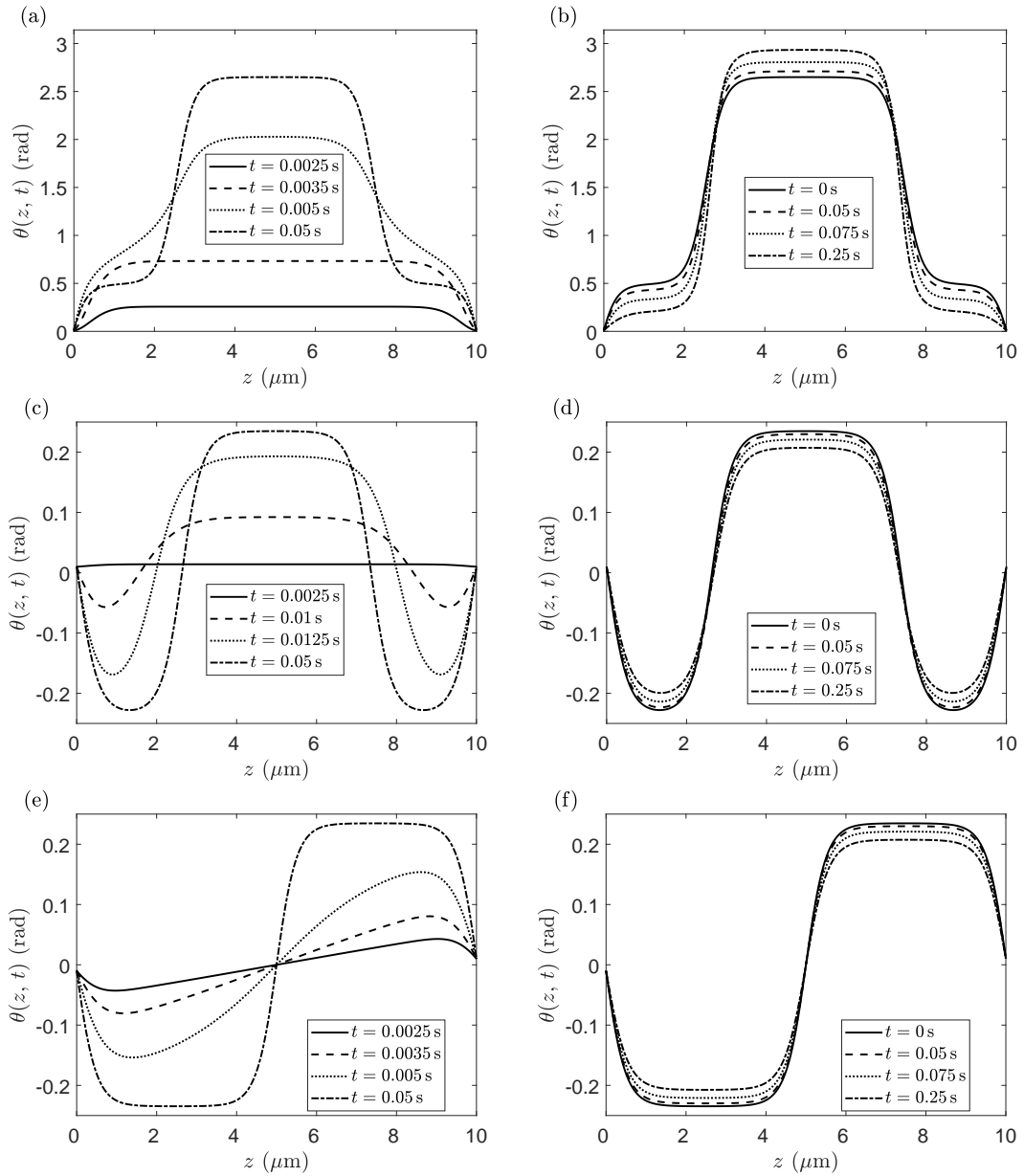


Figure 4.16: The evolution of the director angle $\theta(z, t)$ throughout the channel during (a, c) switch-on and (b, d) switch-off for an extensile active nematic with activity strength $\zeta = -250$ Pa. The orienting field coefficients during switch-on are (a) $\chi_f F^2 = 100$ Pa, and (c, e) $\chi_f F^2 = 10$ Pa.

dynamics of the director in the centre of the channel when the field is switched off are shown in Figure 4.17(b). Our calculations show that for the activity strengths $\zeta = 0.5$ and 1 Pa, the director angle at the centre of the channel does not simply decrease towards its pre-switched state value, $\theta(d/2, 0) = 0.01$ rad. Instead, the

director angle in the centre of the channel increases during a short interval before decreasing to an equilibrium value of $\theta_{\text{off}}(d/2) = 0.01$ rad. This initial increase in the director orientation at the centre of the channel is the kickback effect, where we highlight the increase in the director orientation in the centre of the channel by zooming in at times close to when the field is switched off. At activity strength $\zeta = 2.5$ Pa, we find that there is no kickback, and the director decays back to its pre-switched configuration $\theta = 0.01$ rad for all $z \in [0, d]$ upon removal of the field. For larger values of positive activity strengths (e.g., $\zeta = 5$ Pa), the director structure decays towards a non-trivial configuration without kickback, similar to that in Figure 4.15(b). For large positive activity strengths, the director in the centre of the channel approaches a switch-off equilibrium value of $\theta_{\text{off}}(d/2) \approx \theta^*$.

We now concentrate on the director orientation of an extensile active nematic liquid crystal subject to an external orienting field. Figure 4.18(a) shows the variation of the director angle in the centre of the channel with time for various negative activity strengths. We find that the combination of the reorientation of the director due to the external orienting field and the spontaneous director rotation induced by the activity leads to switch-on equilibrium values $\theta_{\text{on}}(d/2) \gtrsim \pi/2$. This is in contrast to both inactive nematics and contractile active nematics which, as mentioned previously, have switch-on equilibrium values $\theta_{\text{on}}(d/2) \lesssim \pi/2$. In order to distinguish the director orientations for each activity strength, we include a zoomed-in caption in Figure 4.18(a) of the director orientation at the channel centre for values of times close to when the system starts to equilibrate once the field is switched on. Figure 4.18(b) shows how the director orientation in the centre of the channel adapts once the field is switched off. For each of the activity strengths, we find that the extensile active nematic liquid crystal exhibits kickback. Our numerical calculations show that for negative activity strengths which are large in magnitude, the director in the centre of the channel equilibrates at a switch-off value of $\theta_{\text{off}}(d/2) \approx \pi - \theta_L$. By contrast, when the extensile activity strength is smaller in size, the liquid crystal director structure decays to its configuration prior to switch-on.

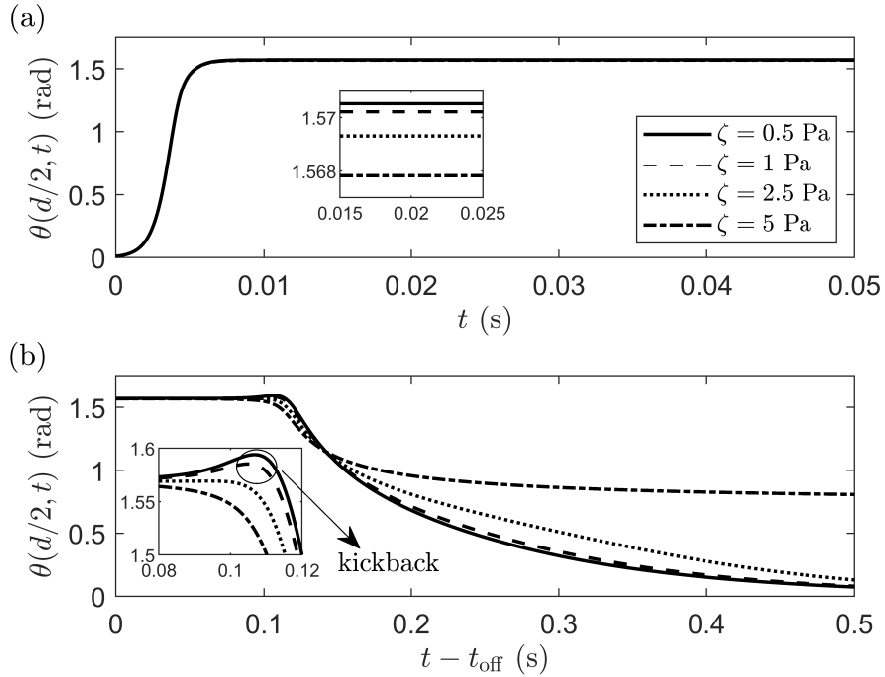


Figure 4.17: Variation of the director angle in the centre of the channel with time for a contractile active nematic liquid crystal when an external orienting field $\chi_f F^2 = 100$ Pa is (a) switched-on and then (b) switched-off. At activity strengths $\zeta = 0.5$ and 1 Pa, the liquid crystal exhibits kickback, whereas there is no kickback at activity strengths $\zeta = 2.5$ and 5 Pa. As the activity strength increases, the active nematic liquid crystal director structure decays to a non-trivial configuration. For large positive activity strengths, the director in the centre of the channel approaches a switch-off equilibrium value of $\theta_{\text{off}}(d/2) \approx \theta^*$.

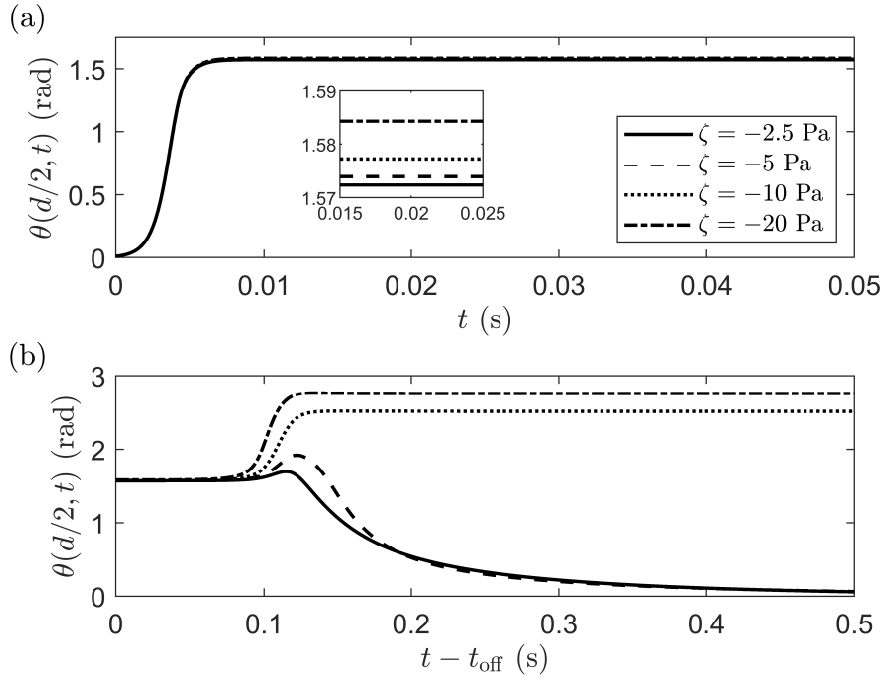


Figure 4.18: Variation of the director angle in the centre of the channel with time for an extensile active nematic liquid crystal when an external orienting field $\chi_f F^2 = 100$ Pa is (a) switched-on and then (b) switched-off. At activity strengths $\zeta = -2.5$ and -5 Pa, the liquid crystal director structure exhibits kickback, before decaying to $\theta = 0.01$ rad for all $z \in [0, d]$. By contrast, at activity strengths $\zeta = -10$ and -20 Pa, the director in the centre of the channel does not decrease with time. For large magnitudes of extensile activity strength, the director in the centre of the channel approaches a switch-off equilibrium value of $\theta_{\text{off}}(d/2) \approx \pi - \theta_L$.

4.7 Conclusions

In this chapter we have modelled spontaneous and pressure-driven flows in a channel containing an active nematic liquid crystal with infinite planar anchoring and no-slip conditions on the boundaries of the channel. We employed a model based on an adapted form of the Ericksen-Leslie equations, where the stress tensor comprises the usual nematic viscous stress and an additional active term which accounts for the activity of the fluid. A constant pressure gradient was applied across the channel to drive an external flow which competed with the flow caused internally by the motion of the active agents.

As expected, in the limit of large pressure gradients, the non-linear equation for the director angle had equilibrium solutions that demonstrate flow-alignment with the Leslie angle, $\theta = \pm\theta_L$, with an associated classic Poiseuille parabolic flow. However, less intuitively, in the limit of large activity, we found that there were five possible director orientations in the bulk of the channel. These were $\theta = \pm\theta_L$, 0 , $\pi/2$ or $\theta^* \approx 1.1656$ rad.

By linearising the decoupled director angle equation about the trivial solution, and assuming zero pressure gradient, we found that two symmetry breaking modes for the director angle, one of which is anti-symmetric with the respect to the centre of the channel and the other symmetric, bifurcate from the trivial state $\theta = 0$ at the same critical value of activity. These are two subcritical pitchfork bifurcations where four solution branches appear, since mirror images of the two symmetry breaking modes are also possible solutions when there is no pressure gradient.

We then considered steady state solutions of the full non-linear system both with and without an applied pressure gradient. For an extensile active nematic with zero pressure gradient, we found that as the magnitude of the activity increased, the symmetric and anti-symmetric non-trivial director structures align at the positive and negative Leslie angles in the bulk of the channel. By calculating the eigenvalues of the Jacobian of the discretised numerical system of equations,

we were able to determine the stability of each of the non-trivial solutions. Applying a pressure gradient then leads to a perturbed pitchfork bifurcation diagram in which the pressure introduced elements of directional bias in the system. We observed that the anti-symmetric director structure with zero pressure gradient remained anti-symmetric when a pressure gradient is applied. However, the zero pressure gradient symmetric director structure became asymmetric as a result of the applied pressure gradient. For a contractile active nematic, we found nine possible solution branches, including the trivial state. Two of these branches contain stable solutions and the remaining six non-trivial solutions are unstable. The pressure gradient had the same effect on the symmetry of the solutions as it did in the extensile case and either enhanced or delayed the spontaneous flow transition. Finally, we investigated how it could be possible to manufacture various non-trivial extensile and contractile active nematic liquid crystal director structures through pretilt and an external orienting field. The competition between the backflow caused by activity and an external orienting field could be examined to a similar level of detail as has been done with a pressure gradient.

We have discovered a rich bifurcation structure in this model of flow of an active nematic within a channel. However, there may still be more solution branches at higher activity parameter values, where the high levels of activity induced flow could stabilise regions of high elastic energy. For instance, as well as solutions in which the director aligns with an angle $\pi - \pm\theta_L$, as in Figure 4.7(a), there may be solutions where the bulk director orientation is $n\pi - \pm\theta_L$ for integer values of $n > 1$. Such areas of high distortion may lead to a reduction in scalar order parameter, and indeed phase “melting” and topological change, and thus a model based on a \mathbf{Q} -tensor would then be more suitable. We will consider a \mathbf{Q} -tensor model of active nematics in the next chapter which will allow for an investigation into the effects of changes of the system temperature and ordering.

Chapter 5

Active Nematic Liquid Crystals with Variable Degree of Orientation

5.1 Introduction

As discussed in Chapters 2 and 4, it is possible to model active nematic liquid crystals in terms of an alignment tensor (i.e., the \mathbf{Q} -tensor) instead of a nematic director. Such tensor models have an advantage over director-based approaches in that they can be used for modelling active nematic liquid crystals which contain defects without generating unphysical free energies, as well as the effects due to changes in the temperature of the system. The latter of these effects will be one of our key focusses in this chapter. A recent theoretical investigation of active nematics based on a \mathbf{Q} -tensor theory was considered by Kitavtsev *et al.* [72], who examined a free-boundary problem for an active liquid crystal containing defects in the bulk. Their thin-film model of an active gel suggested that an active nematic liquid crystal can exhibit non-zero flow that can be spontaneously initiated from a homogeneous state by increasing the thickness of the film. Such behaviour had also been observed in the studies of Voituriez *et al.* [143, 144]. Hybrid lattice Boltzmann simulations were used by Coelho *et al.* [24] in order to

model channel flows of active fluids between nematic and isotropic phases. The nematic phase was set in the centre of the channel with isotropic fluid either side of the interface. Their numerical simulations showed that at large activity strengths, the interface disappeared and the system became nematic. At the boundaries of the channel, the director was subject to homeotropic anchoring and the velocity satisfied the classical no-slip and no-penetration conditions. Chandragiri *et al.* [19] demonstrated that at temperatures below and above the passive isotropic-nematic phase transition, nematic ordering in active fluids confined in shallow channels is predominantly induced by thermodynamic forces and self-generating motion due to activity, respectively. Each of the theoretical investigations [19, 24, 72] were based on a continuum description of an active nematic liquid crystal in terms of the Beris-Edwards equations [11], which are another example of dynamic equations of liquid crystal hydrodynamics written in terms of an alignment tensor.

In this chapter, we continue our investigation into spontaneous flow transitions in active nematic liquid crystals confined in a shallow one-dimensional channel, but now in terms of the \mathbf{Q} -tensor model of active nematics introduced in Chapter 2. Employing a simplified approach similar to that used in Chapter 4, we show that an analytic expression for the critical activities at which the active nematic liquid crystal undergoes a spontaneous flow transition can be derived in terms of nematic parameters which now include the scalar order parameter. We then consider numerical calculations of the full non-linear problem for a range of temperatures for which the nematic phase exists. The main aim of this chapter is to examine how the results of a tensor-based model of active nematic liquid crystals may differ from those obtained from the director-based approach considered in Chapter 4.

5.2 Mathematical Model

We consider a uniaxial, active nematic liquid crystal, confined between two parallel plates at $z = 0$ and $z = d$ (see Figure 5.1). The forms of the director and velocity are the same as those in Chapter 4. We also include a scalar or-

der parameter $S(z, t)$ in this model, which we assume is homogenous in the x and y -directions. In contrast to the model considered in Chapter 4, we assume throughout this chapter that there is no pressure gradient applied across the channel. The director and velocity profiles are subject to the same infinite planar anchoring and no-slip conditions as in Chapter 4. The scalar order parameter is assumed to be fixed at both boundaries at constant values $S(0, t) = S_0$ and $S(d, t) = S_d$. The total bulk energy density, w , is the sum of the elastic energy density (2.3.10) and thermotropic energy density (2.3.20),

$$w = w_1(S, \theta)\theta_z^2 + w_2(S, \theta)\theta_z S_z + w_3(S, \theta)S_z^2 + \frac{2}{3}\alpha\Delta T S^2 + \frac{4}{27}bS^3 + \frac{2}{9}cS^4, \quad (5.2.1)$$

where

$$w_1(S, \theta) = \frac{1}{2} \left((2L_1 + L_2 + L_3)S^2 - \frac{2}{3}L_4S^3 \right) \cos^2 \theta + \frac{1}{2} \left((2L_1 + L_2 + L_3)S^2 + \frac{4}{3}L_4S^3 \right) \sin^2 \theta, \quad (5.2.2)$$

$$w_2(S, \theta) = \frac{1}{3}(L_2 + L_3)S \sin \theta \cos \theta, \quad (5.2.3)$$

$$w_3(S, \theta) = \left(\frac{1}{3}L_1 + \frac{1}{18}(L_2 + L_3) - \frac{1}{9}L_4S \right) \cos^2 \theta + \left(\frac{1}{3}L_1 + \frac{2}{9}(L_2 + L_3) + \frac{2}{9}L_4S \right) \sin^2 \theta. \quad (5.2.4)$$

As mentioned in Chapter 2, the coefficients α , b and c are constants which do not depend on temperature, and $\Delta T = T - T^*$ is the temperature difference between the system temperature, T , and the critical temperature at which the isotropic phase becomes unstable, T^* . The coefficients L_i are the elastic constants which are homogeneous in space and defined by (2.3.16)–(2.3.19). The dissipation function (2.3.22) is given by

$$\mathcal{D} = \frac{1}{2}g(S, \theta)v_z^2 + m(S, \theta)\theta_t v_z + \xi_1 S^2 \theta_t^2 + \xi_2 S_t \sin \theta \cos \theta v_z + \frac{1}{3}\xi_1 S_t^2, \quad (5.2.5)$$

where the S and θ -dependent viscosity terms are

$$g(S, \theta) = \frac{1}{2}\xi_1 S^2 + \xi_2 S \cos(2\theta) + \frac{1}{12}\xi_4 S + \xi_6 S^2 \sin^2 \theta \cos^2 \theta + \frac{1}{2}\xi_8, \quad (5.2.6)$$

$$m(S, \theta) = \xi_2 S \cos(2\theta) + \xi_1 S^2. \quad (5.2.7)$$

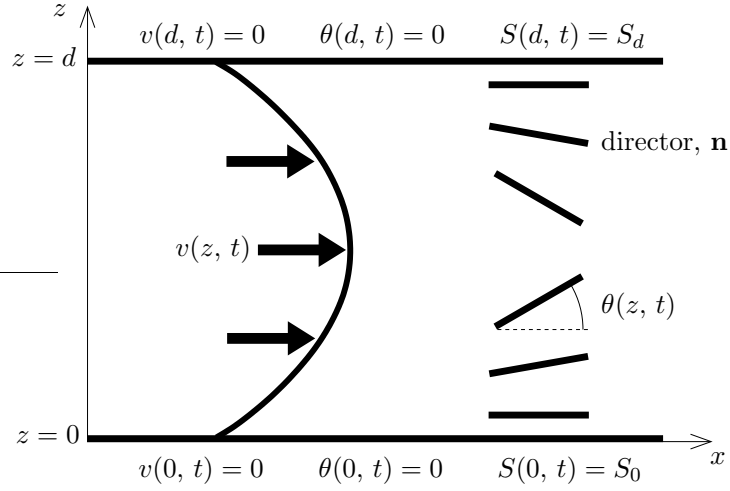


Figure 5.1: A uniaxial, active nematic liquid crystal in a channel between two plates at $z = 0$ and $z = d$, with flow parallel to the x -direction. The director is constrained to lie in the (x, z) plane and is fixed in the x -direction on the plates. The velocity satisfies the no-slip condition on both plates, while the scalar order parameter satisfies a Dirichlet condition at each boundary.

The coefficients ξ_i are the spatially independent nematic viscosities defined by (2.3.30)–(2.3.34). The activity of the liquid crystal is governed by the active stress term (2.3.47), with homogenous activity strength μ .

If we assume that fluid inertia is negligible, as we did in Chapter 4, then the dynamics of the director angle, velocity and scalar order parameter are governed by the three non-linear coupled partial differential equations (2.3.6)–(2.3.8),

$$2\xi_1 S^2 \theta_t = (2w_1(S, \theta) \theta_z + w_2(S, \theta) S_z)_z - \frac{\partial w_1}{\partial \theta} \theta_z^2 - \frac{\partial w_2}{\partial \theta} \theta_z S_z - \frac{\partial w_3}{\partial \theta} S_z^2 - m(S, \theta) v_z, \quad (5.2.8)$$

$$0 = (g(S, \theta) v_z + m(S, \theta) \theta_t + (\xi_2 S_t + \mu S) \sin \theta \cos \theta)_z, \quad (5.2.9)$$

$$\frac{2}{3} \xi_1 S_t = (2w_3(S, \theta) S_z + w_2(S, \theta) \theta_z)_z - \frac{\partial w_1}{\partial S} \theta_z^2 - \frac{\partial w_2}{\partial S} \theta_z S_z - \frac{\partial w_3}{\partial S} S_z^2 - \frac{4\alpha \Delta T}{3} S - \frac{4b}{9} S^2 - \frac{8c}{9} S^3 - \xi_2 \sin \theta \cos \theta v_z, \quad (5.2.10)$$

with boundary conditions

$$\theta(0, t) = 0, \quad v(0, t) = 0, \quad S(0, t) = S_0, \quad (5.2.11)$$

$$\theta(d, t) = 0, \quad v(d, t) = 0, \quad S(d, t) = S_d. \quad (5.2.12)$$

We will examine these equations using a mixture of linear stability analysis and numerical calculations.

5.3 The Effect of Temperature Changes on the Bifurcation of Non-Trivial States

5.3.1 Linear Stability Analysis

Equations (5.2.8) and (5.2.9) are satisfied when $\theta(z, t) = 0$, $v(z, t) = 0$ and S is constant. In this case, equation (5.2.10) provides a polynomial equation for equilibrium values of the nematic scalar order parameter S_{eq} , namely,

$$3\alpha\Delta T S_{\text{eq}} + bS_{\text{eq}}^2 + 2cS_{\text{eq}}^3 = 0, \quad (5.3.1)$$

which has solutions

$$S_{\text{eq}} = 0, \quad S_{\text{eq}} = \frac{-b \pm \sqrt{b^2 - 24\alpha\Delta T c}}{4c}. \quad (5.3.2)$$

The solutions (5.3.2)₂ depend on temperature due to the ΔT contribution to the thermotropic energy density. As mentioned in Chapter 1, the equilibrium scalar order parameter for the nematic liquid crystal phase is usually positive and so we will only consider the positive value for S_{eq} in (5.3.2). It can be shown analytically that the nematic phase disappears at the critical temperature difference $\Delta T = b^2/(24\alpha c)$ [103]. In order for the boundary conditions to be compatible with (5.2.10) when $\theta(z, t) = 0$, $v(z, t) = 0$ and S is constant, we must restrict our attention in this subsection to the special case $S_0 = S_d = S_{\text{eq}}$.

We now consider the linear stability of the state $\theta(z, t) = 0$, $v(z, t) = 0$ and $S(z, t) = S_{\text{eq}}$. Linearisation of equations (5.2.8), (5.2.9) and (5.2.10) around

this state leads to, at leading order,

$$2\xi_1 S_{\text{eq}}^2 \theta_t = \left((2L_1 + L_2 + L_3) S_{\text{eq}}^2 - \frac{2}{3} L_4 S_{\text{eq}}^3 \right) \theta_{zz} - (\xi_1 S_{\text{eq}}^2 + \xi_2 S_{\text{eq}}) v_z, \quad (5.3.3)$$

$$0 = \left(\frac{1}{2} \xi_1 S_{\text{eq}}^2 + \xi_2 S_{\text{eq}} + \frac{1}{12} \xi_4 S_{\text{eq}} + \frac{1}{2} \xi_8 \right) v_{zz} + (\xi_1 S_{\text{eq}}^2 + \xi_2 S_{\text{eq}}) \theta_{tz} + \mu S_{\text{eq}} \theta_z, \quad (5.3.4)$$

where the equation for S is satisfied by $S = S_{\text{eq}}$ at leading order. We can re-write equations (5.3.3) and (5.3.4) in the same form as those in the Ericksen-Leslie theory,

$$\gamma_1 \theta_t = K_1 \theta_{zz} - \frac{1}{2} (\gamma_1 + \gamma_2) v_z, \quad (5.3.5)$$

$$0 = \eta_1 v_{zz} + \frac{1}{2} (\gamma_1 + \gamma_2) \theta_{tz} + \zeta \theta_z, \quad (5.3.6)$$

where $\gamma_1 \equiv \gamma_1(S_{\text{eq}})$, $K_1 \equiv K_1(S_{\text{eq}})$, etc. It is possible to decouple equations (5.3.5) and (5.3.6) using the calculations outlined in Appendix C, which leads to the linearised dynamic equation for the director angle

$$\eta_{\text{splay}} \theta_t = K_1 \theta_{zz} - \frac{K_1 (\gamma_1 + \gamma_2)^2}{4\gamma_1 \eta_1 d} \int_0^d \theta_{zz} dz + \frac{\zeta (\gamma_1 + \gamma_2)}{2\eta_1} \left[\theta - \frac{1}{d} \int_0^d \theta dz \right], \quad (5.3.7)$$

where $\eta_{\text{splay}} = \gamma_1 - (\gamma_1 + \gamma_2)^2 / (4\eta_1) > 0$. We consider the same two sets of potential instability modes (4.3.19) and (4.3.22) considered in Chapter 4, both of which lead to an instability at $\bar{\zeta} = \bar{S} n^2 \zeta_c / S_{\text{eq}}$ for $n = 1, 2, \dots$, where \bar{S} is the experimentally measured scalar order parameter we introduced in Chapter 2, and the critical activity for the $n = 1$ mode ζ_c is

$$\zeta_c = \frac{8\pi^2 K_1 \eta_1}{(\gamma_1 + \gamma_2) d^2}, \quad (5.3.8)$$

or equivalently, an instability occurs at $\mu = n^2 \mu_c$, where the critical activity for the $n = 1$ mode μ_c is

$$\mu_c = \frac{\pi^2 (6L_1 + 3L_2 + 3L_3 - 2L_4 S_{\text{eq}}) (6\xi_1 S_{\text{eq}}^2 + 12\xi_2 S_{\text{eq}} + \xi_4 S_{\text{eq}} + 6\xi_8)}{9(\xi_1 S_{\text{eq}} + \xi_2) d^2}. \quad (5.3.9)$$

Since the equilibrium scalar order parameter value S_{eq} is temperature dependent, it follows that the critical activity strength will also change with temperature. We assume that in the special case of $\Delta T = 0$ K, the scalar order parameter values

S_{eq} and \bar{S} are equal at this particular value of temperature difference, where $\bar{S} = 0.6$ is a typical value of the experimentally measured scalar order parameter [103]. We can now rearrange (5.3.1) in order to specify b in terms of c ,

$$b = -\frac{6c}{5}. \quad (5.3.10)$$

An increase in the value of ΔT will mean that $S_{\text{eq}} < \bar{S}$, that is, there will be a reduction in the ordering of the liquid crystal in the bulk of the channel at higher temperature differences.

5.3.2 Numerical Calculations I: Extensile Active Nematic Liquid Crystals

We now consider numerical solutions of the full non-linear system (5.2.8)–(5.2.10), with boundary conditions (5.2.11) and (5.2.12). In contrast to the numerics considered in Chapter 4, where the corresponding non-linear system was solved using both COMSOL and MATCONT, all of the numerical calculations in this chapter are undertaken only in COMSOL. Since we have an additional equation to solve for as part of this model, using MATCONT could potentially lead to a significant increase in the computational times compared to those in Chapter 4, and so we use COMSOL.

In order to generate a scalar order parameter structure which is no longer uniform throughout the channel, we now set $S_0 = S_d = \bar{S}$. We use the same liquid crystal parameters as in Chapter 4 and only consider solutions with mode number $n = 1$. Furthermore, we use the same values for the coefficients α and c in the thermotropic energy density used in [103], with the value of b calculated via (5.3.10),

$$\alpha = 0.042 \times 10^6 \text{ Nm}^{-2}\text{K}^{-1}, \quad b = -0.42 \times 10^6 \text{ Nm}^{-2}, \quad c = 0.35 \times 10^6 \text{ Nm}^{-2}. \quad (5.3.11)$$

For our choice of liquid crystal parameter values, the nematic phase disappears at temperature difference $\Delta T = b^2/(24\alpha c) = 0.5 \text{ K}$. We first examine the variation of the critical threshold activity with the temperature difference ΔT for both

symmetry breaking modes. Figure 5.2 shows the critical values calculated from both the linear stability analysis and the numerical scheme in COMSOL as ΔT increases. We have indicated the disappearance of the nematic phase in Figure 5.2 with a dashed vertical line at $\Delta T = 0.5$ K, where the nematic phase only exists for temperature difference values to the left of this line. Since both of the symmetry breaking modes have exactly the same analytic value for the critical activity, we can only see one curve in Figure 5.2. The numerical critical activities are indicated by the markers, where the crosses and circles are the critical activities for the symmetric and anti-symmetric director angle modes, respectively. For all temperature differences for which the nematic phase exists, i.e., $0 \leq \Delta T < 0.5$ K, we can see that an increase in ΔT increases the critical activity. In other words, the spontaneous flow transition of extensile active nematics occurs at a smaller magnitude of activity for higher values of ΔT . When $\Delta T = 0$ K, the scalar order parameter is uniform throughout the channel and, as we would expect, we recover the same critical activity values derived in Chapter 4 for both symmetry breaking modes. The results from the linear stability analysis of equations (5.2.8), (5.2.9) and (5.2.10) show very good agreement with the corresponding numerical calculations based on the full non-linear system. For each value of ΔT used to calculate the numerical critical activities, we find that the difference between the analytic and numerical critical activities for both modes is less than 1%. Furthermore, this agreement supports our assumption of $S_0 = S_d = S_{\text{eq}}$ for the linear stability calculations in Subsection 5.3.1.

The equilibrium director structures for both symmetry breaking modes at activity strength $\bar{\zeta} = -250$ Pa and temperature differences $\Delta T = 0, 0.14, 0.28$ and 0.49 K are shown in Figure 5.3, along with the corresponding steady state solutions for the velocity and scalar order parameter structures. We saw in Chapter 4 that, for a negative activity of large magnitude, the director aligns in the bulk of the channel close to the positive and negative Leslie angles $\pm\theta_L$. This is also what we observe from the \mathbf{Q} -tensor model in Figures 5.3(a) and (b), where the maximum director angles for each ΔT are very close to the corresponding value of θ_L . Since the nematic viscosities are affected by changes in the scalar order

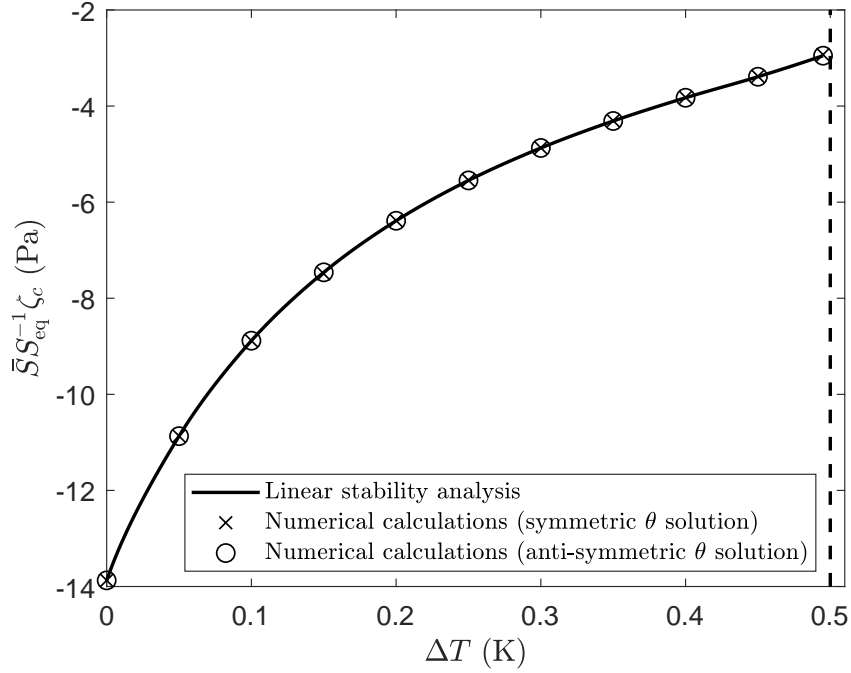


Figure 5.2: Variation of the critical activity calculated from the linear stability analysis (solid curve) and numerically (markers) with the temperature difference ΔT . The nematic phase disappears at $\Delta T = 0.5$ K.

parameter, it follows that θ_L will also vary with the scalar order parameter via

$$\theta_L = \tan^{-1} \left(\sqrt{\frac{\gamma_2(S) + \gamma_1(S)}{\gamma_2(S) - \gamma_1(S)}} \right), \quad \text{provided} \quad \frac{\gamma_2(S) + \gamma_1(S)}{\gamma_2(S) - \gamma_1(S)} \geq 0. \quad (5.3.12)$$

The variation of the Leslie angle (5.3.12) with the temperature difference ΔT is indicated by the solid curve in Figure 5.4, which shows that the Leslie angle increases as ΔT increases. The maximum director angles obtained from the numerical solutions at various values of ΔT for both symmetry breaking modes are shown by the markers in Figure 5.4. These maximum angles have been calculated using the same activity strength used in Figure 5.3 and are all within 1% of the Leslie angle (5.3.12) for each value of ΔT . We can see from the profiles in Figures 5.3(c) and (d) that the speed increases in most of the channel for the first three temperature differences ($\Delta T = 0, 0.14$ and 0.28 K), before decreasing for $\Delta T = 0.49$ K. We explore this further in Figure 5.5, which shows the maximum speed, $|v|_{\text{max}}$, for an extensile active nematic. The reduction in the maximum

speed at large temperature for both symmetry breaking modes may be explained in terms of the changes in the director orientation and scalar order parameter that occur when ΔT increases. Both the Leslie angle and the gradients in the director angle increase as the temperature difference increases. These increases coincide with a reduction in the scalar order parameter as the liquid crystal starts melting, which leads to a decrease in the stress due to activity and less flow. In the case of Figure 5.5(a), numerical calculations show that after initially increasing with ΔT , $|v|_{\max}$ starts to decrease at $\Delta T = 0.25$ K, while the reduction of $|v|_{\max}$ in Figure 5.5(b) begins at $\Delta T = 0.23$ K.

As can be seen in Figures 5.3(e) and (f), the competition between the preferred ordering in the bulk, $S = S_{\text{eq}}$, and the Dirichlet condition, $S = \bar{S}$, at the boundaries leads to the creation of boundary layers in S as ΔT increases. This increase in ΔT also leads to small reductions in S at the centre of the channel for scalar order parameter structure in Figure 5.3(e) and approximately at $z = d/4$ and $z = 3d/4$ for the scalar order parameter structure in Figure 5.3(f), i.e., wherever $|\theta_z|$ is large. In order to minimise the free energy, regions of increased director distortion must coincide with regions of lower ordering. Both of the scalar order parameter structures in Figures 5.3(e) and (f) are symmetric with respect to the channel centre. Similar scalar order parameter structures have been found in the kinetic model considered by Ezhilan and Saintillan [49] for a suspension of Brownian active particles confined in a shallow channel with the fluid flow driven internally by activity and externally by a pressure gradient. The configuration of the active suspension is governed by a conservation equation for the probability distribution function of active particle positions and orientations throughout the channel.

We now examine the bifurcation of the non-trivial states from the trivial state $\theta(z, t) = 0$ as ΔT increases. Figure 5.6 shows the measure ϕ_e , defined by (4.4.1), as the activity strength changes for director angle solutions which are symmetric with respect to the channel centre using the same values of ΔT as Figure 5.3. The bifurcation diagrams for anti-symmetric director angle solutions are shown in Figure 5.7, where we use ϕ_o , defined by (4.4.1), as the choice of

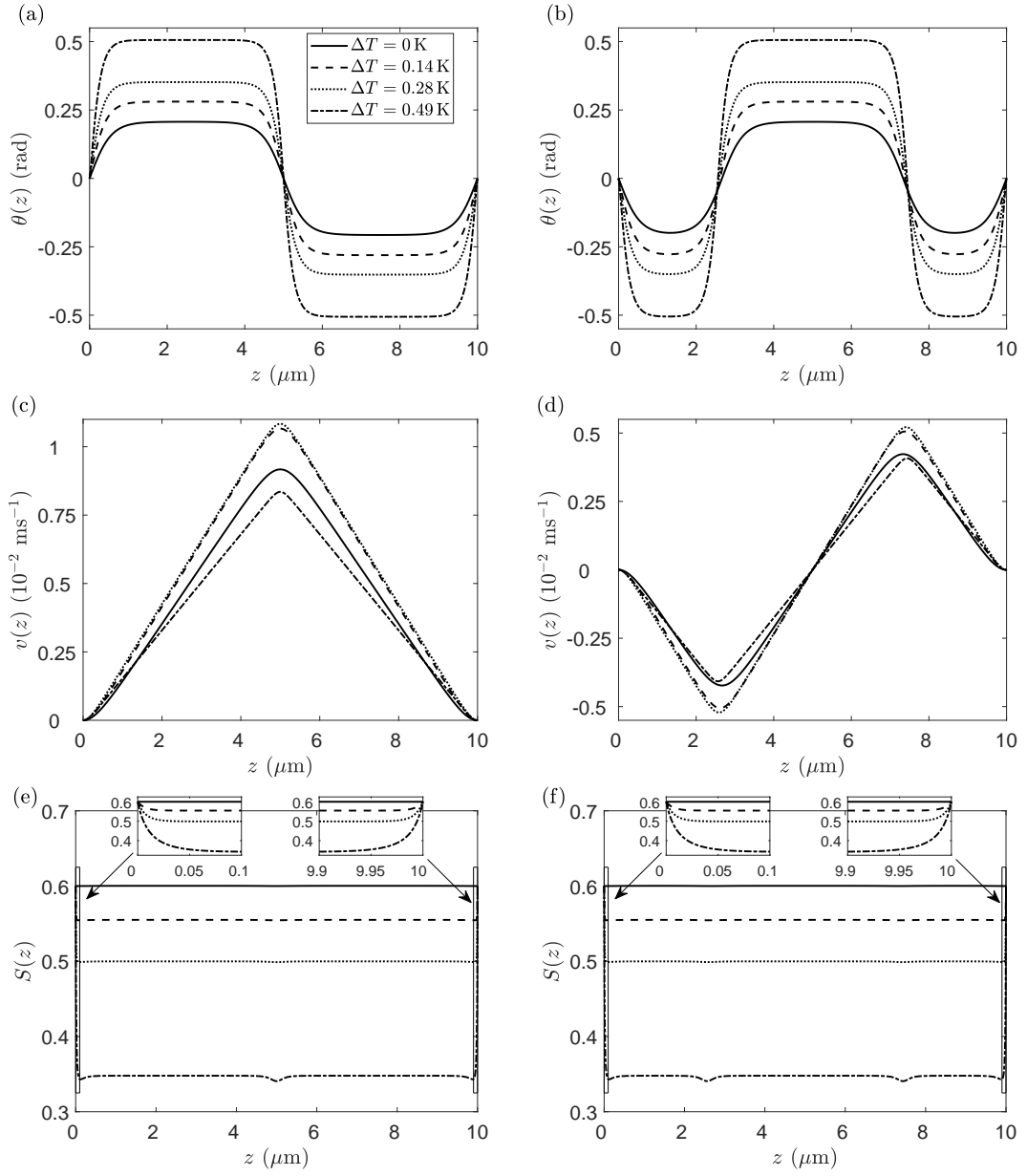


Figure 5.3: ((a), (b)) The equilibrium director angle, ((c), (d)) velocity and ((e), (f)) scalar order parameter structures at various temperature differences for an extensile active nematic with activity $\bar{\zeta} = -250\text{ Pa}$. At the boundaries of the channel, $S = \bar{S} = 0.6$.

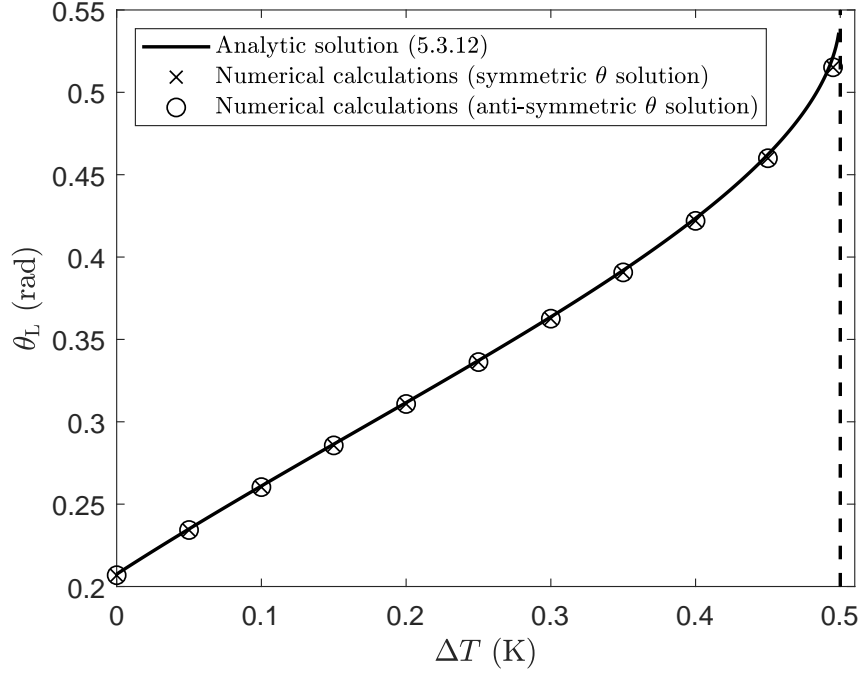


Figure 5.4: Variation of the Leslie angle (5.3.12) with the temperature difference ΔT (solid curve). The markers show the maximum director angles calculated numerically for both symmetry breaking modes.

measure. Since the negatives of the director solution profiles in Figure 5.3 are also possible solutions, two solution branches appear in Figures 5.6 and 5.7, where each of the bifurcations from the trivial state are subcritical pitchforks. As was suggested from the linear stability calculations in Subsection 5.3.1, an increase in ΔT leads to an increase in the critical activity value.

Our numerical calculations reveal that the stability of each equilibrium director angle solution is consistent with the results in Chapter 4. That is, the trivial state is stable when $\bar{S}\zeta_c/S_{\text{eq}} < \bar{\zeta} < 0$ and unstable when $\bar{\zeta} < \bar{S}\zeta_c/S_{\text{eq}}$. The solution branches of the anti-symmetric director structures in Figure 5.3(a) are stable, whereas those in Figure 5.3(b) are unstable.

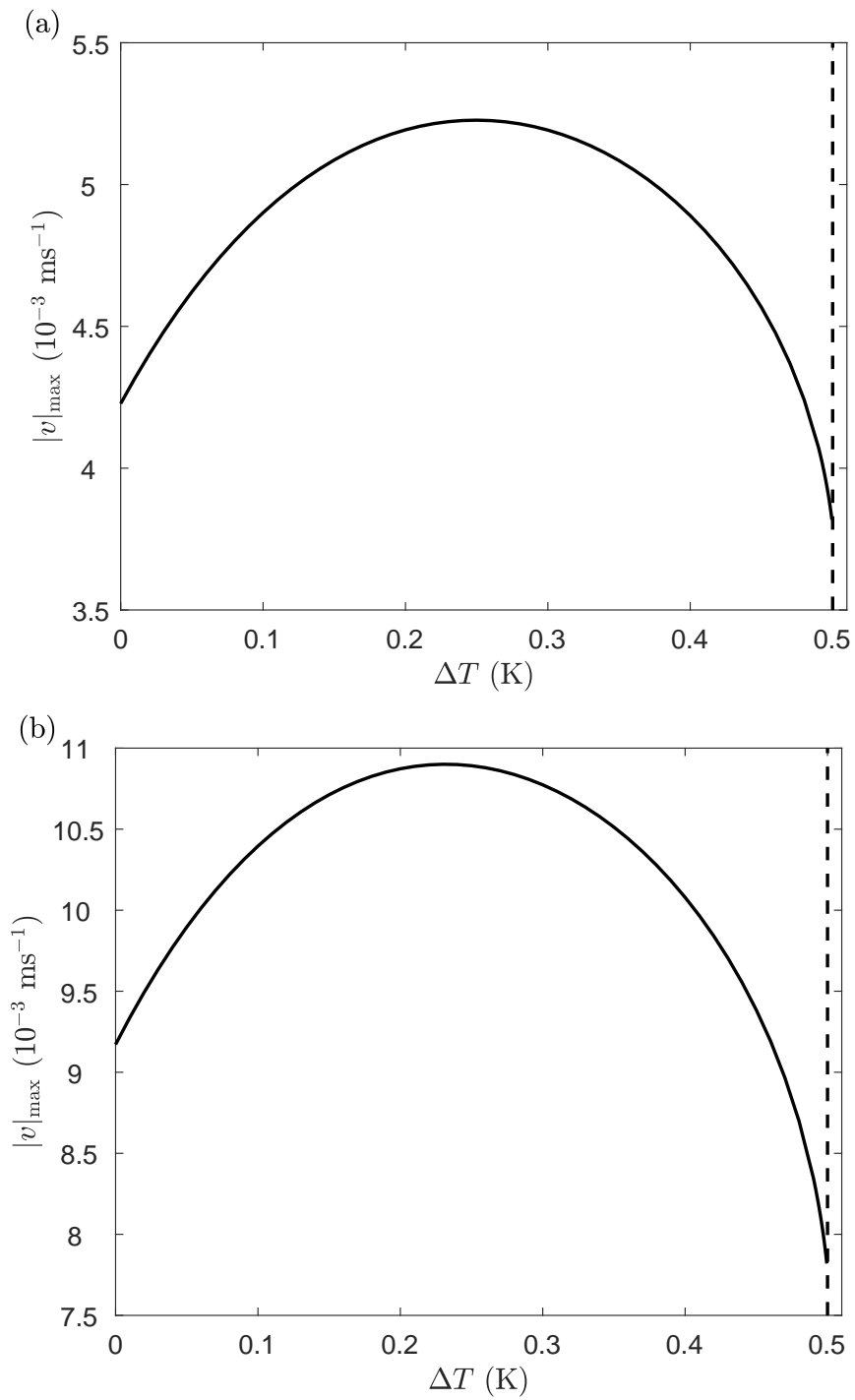


Figure 5.5: Variation of the maximum speed with temperature difference when the velocity structure is (a) anti-symmetric and (b) symmetric for activity strength $\bar{\zeta} = -250 \text{ Pa}$.

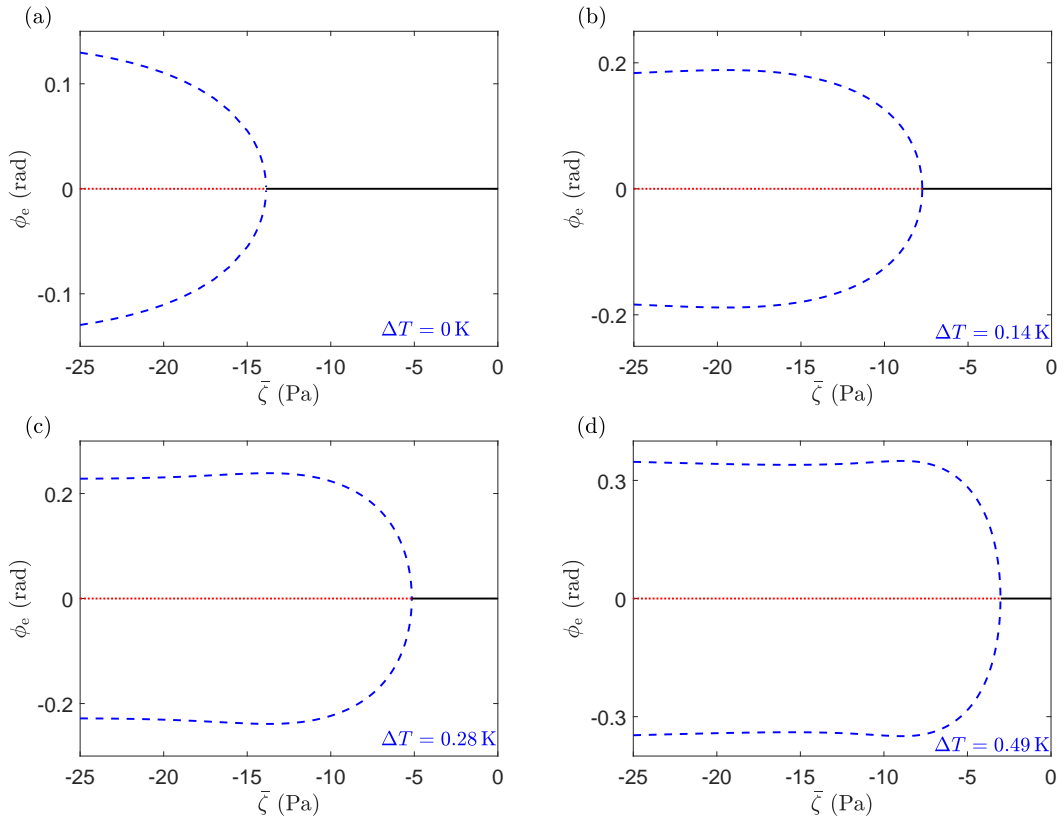


Figure 5.6: Bifurcation diagrams for negative activity parameter values, using the measure of even $\theta(z)$ solutions at various temperature differences. The stable equilibria solution branch is indicated by a solid curve and unstable equilibria solution branches are indicated by either dashed or dotted curves.

5.3.3 Numerical Calculations II: Contractile Active Nematic Liquid Crystals

In Chapter 4 we found that, while there are no bifurcations from the trivial state branch $\theta(z, t) = 0$, there are non-trivial solutions on branches that terminated at fold bifurcations. For all positive values of the activity strength, the trivial state $\theta(z, t) = 0$ was shown to be always stable. The director-based model considered in Chapter 4 generated non-trivial solutions in which the director structures were characterised by regions of large distortion. The associated velocity profiles exhibited either boundary or central jets of fluid which were increasingly sharp for larger activity strengths. These jets of fluid coincide with the regions of high

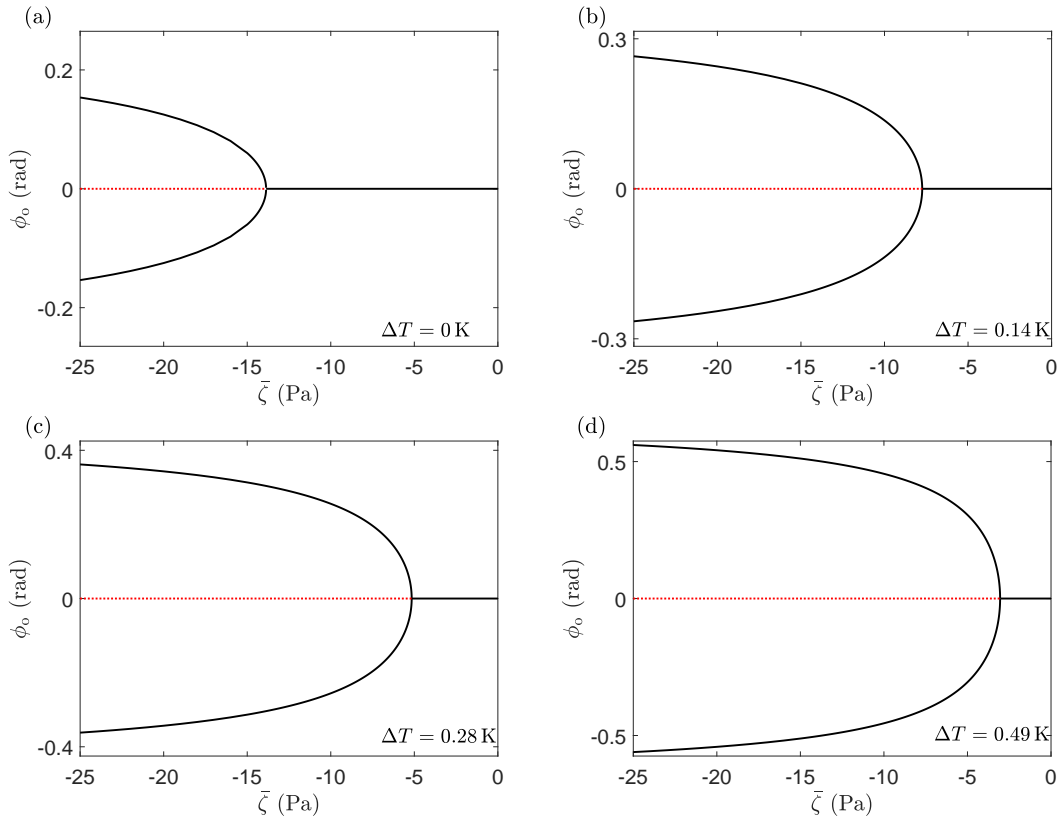


Figure 5.7: Bifurcation diagrams for negative activity parameter values, using the measure of odd $\theta(z)$ solutions at various temperature differences. Stable equilibria solution branches are indicated by solid curves and the solution branch which is unstable to any non-zero initial guess is indicated by a dotted line.

gradients in the director structure. We now examine the existence of similar solutions using a \mathbf{Q} -tensor approach.

The steady state director structures at activity strength $\bar{\zeta} = 100$ Pa and temperature difference values $\Delta T = 0, 0.28, 0.42$ and 0.49 K are shown in Figure 5.8, along with the steady state velocity solutions and scalar order parameter profiles. As we would expect, the director and velocity profiles derived from the Ericksen-Leslie and \mathbf{Q} -tensor approaches are the same at $\Delta T = 0$ K. For both the symmetric and anti-symmetric director structures, we show an expanded view of regions in the channel where the director orientation shows significant change with ΔT . In the remaining regions of the channel, we do not observe any major variations in the director orientation. Figure 5.9 shows how the maximum of the

absolute value of the director angle, $|\theta|_{\max}$, changes as ΔT increases. It is not clear how the value of $|\theta|_{\max}$ for the symmetric director structure depends on the nematic viscosities and so we cannot explain why $|\theta|_{\max}$ is non-monotonic with ΔT . We find that as ΔT increases for the anti-symmetric director structure, $|\theta|_{\max}$ increases towards $\pi/2$, which was one of the equilibrium director orientations we predicted analytically in Chapter 4. We can see the effect of an increase in ΔT for the symmetric velocity structure close to the boundaries and for the anti-symmetric velocity structure in the bulk of the channel. These velocity structures contain jets of fluid which exist due to the activity of the liquid crystal and reduce in magnitude for a fixed value of activity as ΔT increases. Other than close to the boundaries of the channel, the symmetric velocity structures in Figure 5.8(c) are very similar for all values of ΔT considered, whereas the anti-symmetric velocity structure in Figure 5.8(d) shows a reduction in the bulk velocity as ΔT increases. Figure 5.10 shows the variation of the maximum speed, $|v|_{\max}$, as ΔT increases. In each case, we can see that an increase in ΔT leads to a reduction in the maximum speed. The decrease in the flow occurs due to the decrease in the scalar order parameter as the liquid crystal starts to melt. The scalar order parameter structures in Figures 5.8(e) and (f) are again symmetric with respect to the channel centre and are characterised by boundary layers which increase with ΔT , but also by regions of large distortion which are caused by melting, and coincide with the regions where the boundary and central jets of fluid flow exist.

As was also the case in Chapter 4, we find that the non-trivial solutions in Figure 5.8 do not bifurcate from the trivial state. This means that the trivial state is always stable for positive activity strengths. Furthermore, we find that the solution branches of the director structures in Figure 5.8(a) are stable, whereas the solution branches of the director structures in Figure 5.8(b) are unstable, which is again consistent with our findings in Chapter 4. As mentioned previously, we derive numerical solutions of the non-linear system (5.2.8)–(5.2.10) in this chapter using COMSOL. One disadvantage of using COMSOL to find solutions of a system of partial differential equations is that it is not always able to find unstable equilibrium solutions. The solution branches which connect to

the branches of the non-trivial director angle solutions in Figure 5.8(a, b) are not accessible in COMSOL, presumably because they are unstable. The inability of COMSOL to find these unstable solution branches means that we have not been able to complete the bifurcation diagrams for a contractile active nematic liquid crystal in the same way as we did in Chapter 4. Therefore, in order to be able to find disconnected unstable branches, we would need to make use of MATCONT in a similar manner as done for Chapter 4, albeit we would have an additional variable to solve for, namely the scalar order parameter S .

Despite not being able to find the solution branches which connect to those for the director structures in Figures 5.8(a) and (b), we are able to calculate numerically the fold bifurcation points at which these solutions no longer exist. Figure 5.11 shows how the critical activities of the symmetric and anti-symmetric director structures in Figure 5.8 vary as a function of ΔT . The critical activities for each value of ΔT are indicated by the markers. As was also the case in Chapter 4, the fold bifurcations for the symmetric and anti-symmetric director angles do not occur at the same critical activities. We find that the critical activities for the symmetric director structures always appears to be less than those for the anti-symmetric director structure at the same value of ΔT . Our calculations show that for temperature differences $0 \leq \Delta T < 0.5$ K, an increase in ΔT leads to an increase in the critical activity at which a spontaneous flow transition occurs for both the symmetric and anti-symmetric director structures. This increase in the critical activity for contractile active nematic liquid crystals corresponds to a delay in the spontaneous flow transition.

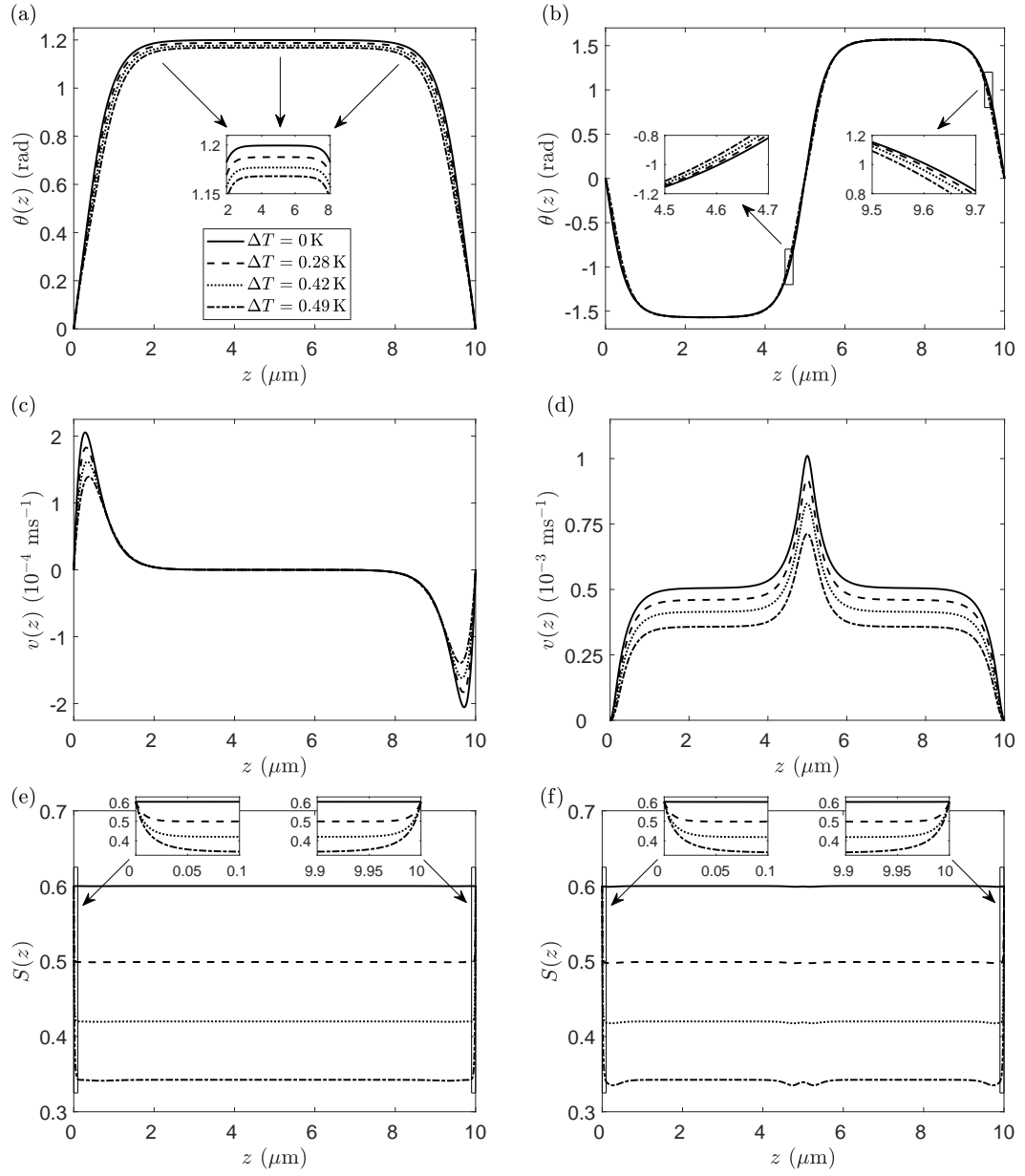


Figure 5.8: ((a), (b)) The equilibrium director angle, ((c), (d)) velocity and ((e), (f)) scalar order parameter structures at various temperature differences for a contractile active nematic with activity $\bar{\zeta} = 100 \text{ Pa}$. At the boundaries of the channel, $S = \bar{S} = 0.6$.

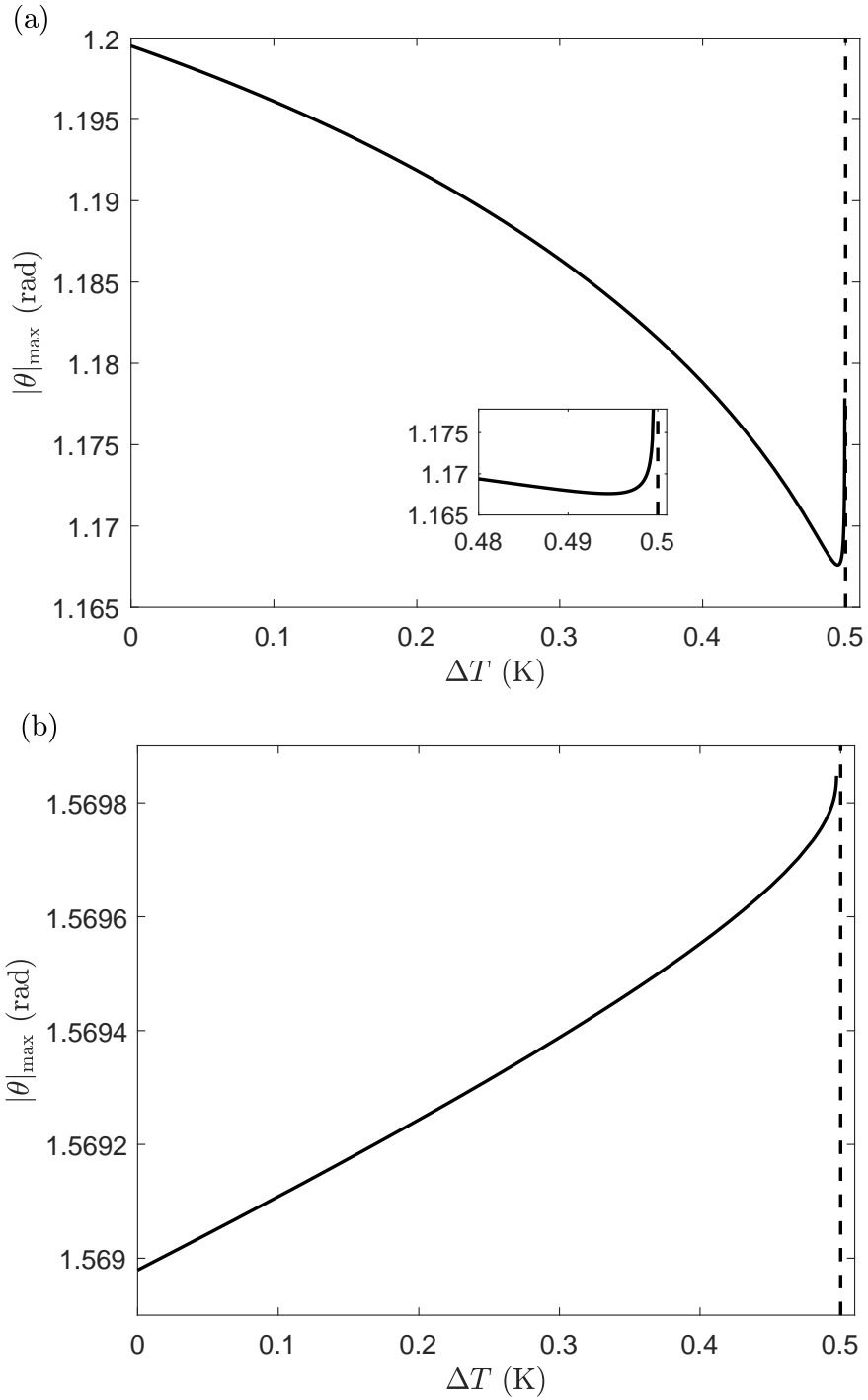


Figure 5.9: Variation of the maximum of the absolute value of the director angle with ΔT for the (a) symmetric and (b) anti-symmetric director structure of a contractile active nematic. The activity strength used to calculate these values is $\bar{\zeta} = 100$ Pa.

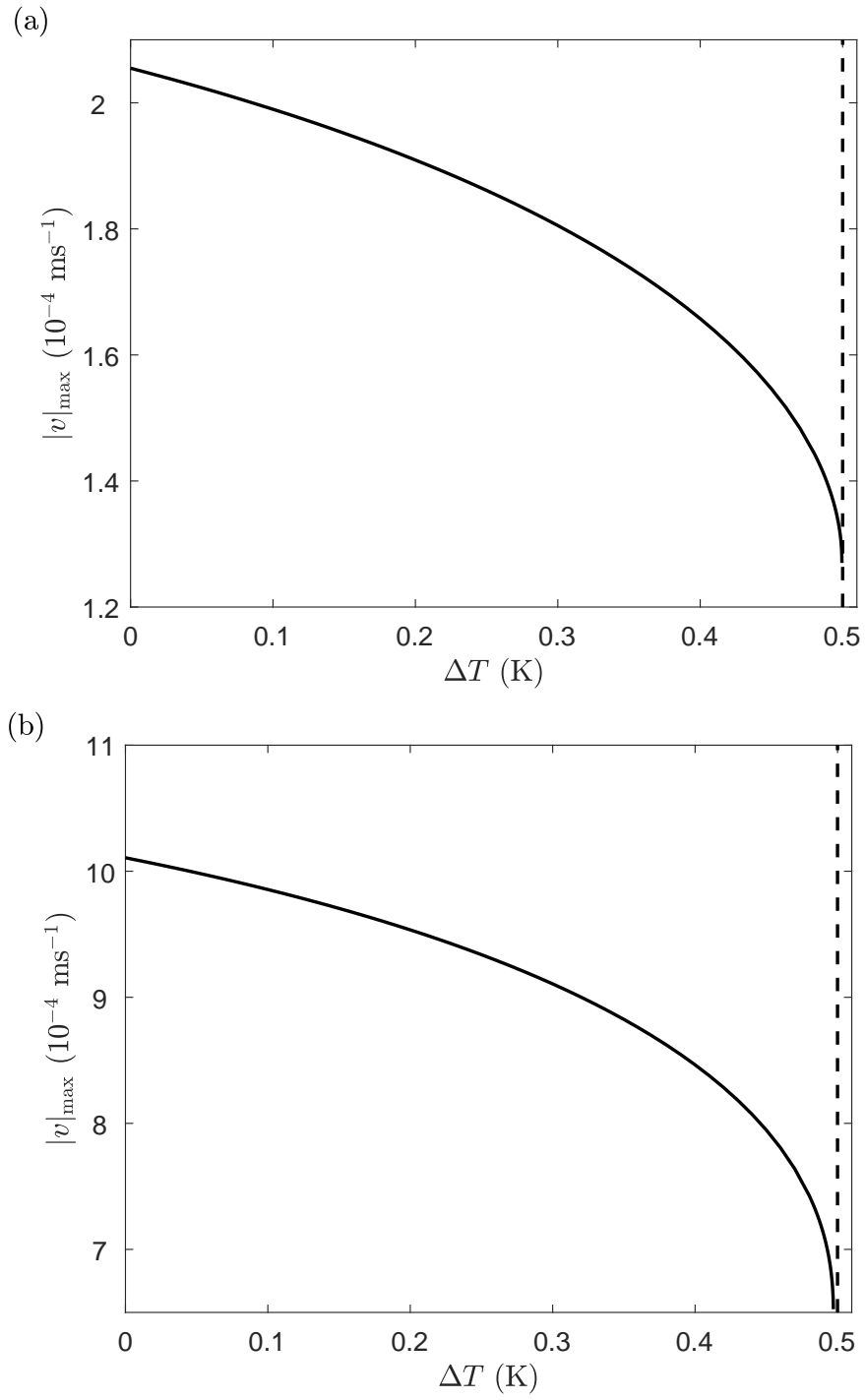


Figure 5.10: Variation of the maximum speed with ΔT for the (a) anti-symmetric and (b) symmetric velocity structure of a contractile active nematic for activity strength $\bar{\zeta} = 100$ Pa.

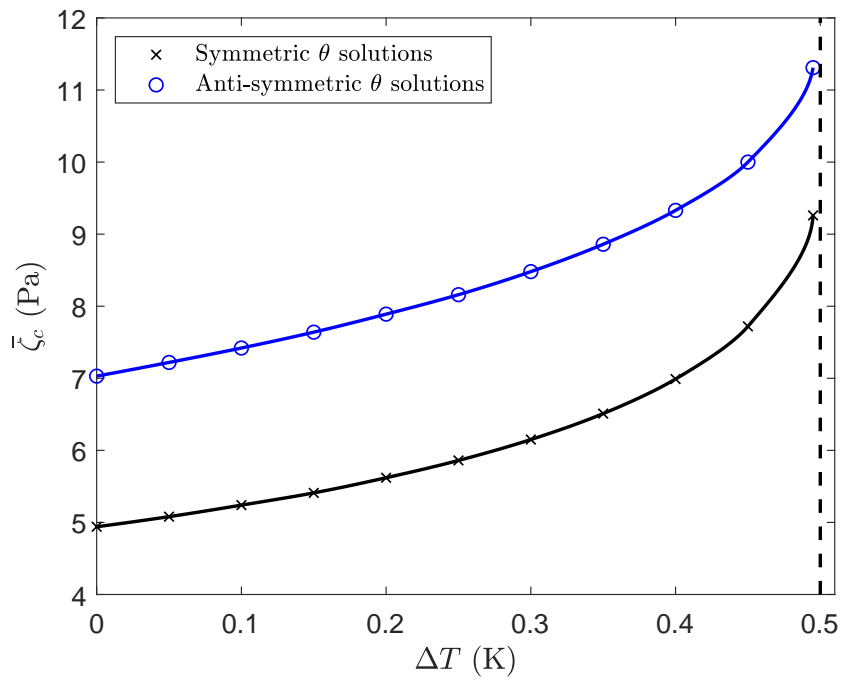


Figure 5.11: Variation of the critical activities $\bar{\zeta}_c$ for the symmetric and anti-symmetric director structures of a contractile active nematic liquid crystal with the temperature difference ΔT .

5.4 Conclusions

In this chapter we have considered a \mathbf{Q} -tensor model of uniaxial active nematic liquid crystals confined in a shallow channel. We have examined the same geometry as that considered in Chapter 4, with the key aim of examining how the results for the director and \mathbf{Q} -tensor approaches may differ. We first considered a linear stability analysis of the non-linear system in which the scalar order parameter was assumed to be constant throughout the channel. By decoupling the linearised dynamic equations, we were able to derive an analytic critical activity in terms of mode numbers and nematic parameters at which spontaneous flow transitions occur. By assuming that the experimental and equilibrium scalar order parameters were the same at temperature difference $\Delta T = 0$ K, we showed that the analytic results in this chapter matched with those in Chapter 4.

The full non-linear system was then solved numerically at different temperature differences ΔT . For all values of ΔT , we fixed the scalar order parameter on the boundaries as the value at which we fix the constant parameters. Comparing the results of the linear stability analysis with the numerical calculations, we showed that there was very good agreement between the critical threshold activities for an extensile active nematic, which justified our assumption of a constant scalar order parameter for the linear stability analysis. We observed that when the magnitude of the activity strength for an extensile active nematic is large, the flow induced by activity lead to flow-aligning director structures, where the Leslie angle increased as a result of the reduction in the ordering caused by melting. Similar to the results in Chapter 4 for a contractile active nematic, our \mathbf{Q} -tensor model of active nematics generated director structures which exhibit large gradients either close to the boundaries or the centre of the channel. The associated velocity solutions were characterised by either central or boundary jets of fluid flow, where the magnitude of the jets of velocity for both the symmetric and anti-symmetric profiles decreased in the bulk of the channel as a result of the reduced ordering due to melting. The competition between the order at the boundaries and bulk of the channel led to the formation of boundary layers in

the scalar order parameter structures for both extensile and contractile active nematics at higher temperature differences. For each value of ΔT , the numerical values of the order in the bulk of the channel were close to the equilibrium scalar order parameter values calculated analytically by minimising the thermotropic energy density with respect to S . We observed that a reduction in S leads to an increase in the critical activities at which non-trivial director structures for extensile and contractile active nematic liquid crystals exist. Therefore, an increase in the temperature difference means that the extensile active system will exhibit a spontaneous flow transition at a lower magnitude of activity strength. The increase in the critical activity for contractile active nematic liquid crystals as a result of higher temperature differences corresponds to a delay in the spontaneous flow transition.

This chapter and the results in Chapter 4 have a number of similarities. That being said, there are still some areas that need further examination with the \mathbf{Q} -tensor approach. For the extensile active nematic liquid crystal, we only considered non-trivial solutions which emerge from the trivial state at subcritical pitchfork bifurcations in this chapter. A solution branch which is not connected to the trivial state was found in Chapter 4, and an examination of how a similar solution derived from the \mathbf{Q} -tensor model is affected by changes in the temperature would be of some interest. Completed bifurcation diagrams for a contractile active nematic liquid crystal which include the unstable solution branches also need to be constructed.

Chapter 6

Active Fluids Confined in Two-Dimensional Geometries

6.1 Introduction

In biological systems, one of the key factors that determine the organisation of active agents in a fluid environment is confinement, where the interaction of self-propelling agents with the walls of a region can lead to structures that compete with those formed in the bulk. For example, Dammone *et al.* [33] used Lattice Boltzmann simulations to model a colloidal liquid crystalline virus (the *fd*-virus) confined within a wedge. An experimental investigation of this system was undertaken using laser scanning confocal microscopy. By increasing the wedge angle between the two boundaries, the director underwent a splay to bend transition. This experimental approach provided an estimation of the ratio of splay-to-bend elasticity ratios, namely, K_3/K_1 of the virus as the wedge angle changes. Lattice Boltzmann simulations were also used by Cates *et al.* [18] and Marenduzzo *et al.* [93] for an active liquid crystal confined in two-dimensional geometries. These simulations were based on \mathbf{Q} -tensor theory and showed that spontaneous flows of an active fluid formed a pair of localised high speed jets of flow in the bulk of the geometry. Confinement of active nematic fluids in rectangular regions was considered experimentally and theoretically by Lewis *et al.* [86], where they used

confocal scanning laser microscopy on the *fd* and Y21M viruses. Their experiments showed that the viruses aligned into various ordered steady state director configurations which were similar to the D and U_1 states found using a theoretical director-based model of liquid crystals. A continuum model based on the Beris–Edwards equations of nematic liquid crystals was recently used by Mondal *et al.* [100] to simulate colloidal particles confined in a microfluidic channel, with a particular focus on the mechanisms of particle migration, self-reorganisation and separation in liquid crystals.

Defects in active nematics occur spontaneously and can be generated due to continuous production and expenditure of internal energy [59, 131]. Experimental studies by Sanchez *et al.* [120] identified disclinations in active nematic gels which were assembled from microtubules and kinesins. These defects demonstrated the ability to drive shear flows internally. Subsequent theoretical investigations into the dynamics of defects in active systems using a \mathbf{Q} -tensor model were considered by Giomi *et al.* [58, 59] and Thampi *et al.* [134], each of which showed very good agreement with the experimental observations in [120]. The theoretical models considered in [58, 59] showed how defects of strengths $\pm 1/2$ behave as self-propelled particles. The direction of motion is determined by the extensile or contractile nature of the active stress exerted by the agents on the surrounding fluid. The mechanisms which lead to the formation of defects in active nematics were examined in [134] via numerical simulations of a model based on \mathbf{Q} -tensor theory. Defects have also been investigated theoretically in polar active fluids. For example, Elgeti *et al.* [42] used Lattice Boltzmann simulations to study the hydrodynamic interaction between defects close to each other in a polar active fluid. Their simulations showed that due to the activity of the fluid, tumbling active liquid crystals can exhibit stable steady states, which of course does not happen in inactive liquid crystal for any amount of shear. Furthermore, it is shown that when two nearby defects in an active fluid interact, they can continuously rotate, oscillate around each other, and spontaneously form a distorted and rotating droplet of active fluid.

In this chapter, we examine the flow of active nematic fluids confined in

two-dimensional geometries. We first use an adapted Ericksen-Leslie model with significant simplifications in order to model the flow of an active fluid in a wedge geometry close to a defect. We show how the modelling assumptions allow analytic solutions of the simplified Ericksen-Leslie equations. We then investigate numerically the full Ericksen-Leslie model for an active fluid in the rectangular regions first examined in Chapter 3. We obtain director and velocity profiles for each of the nematic equilibria when the Ericksen number is zero, showing that there are similarities with the analytic results derived for the wedge geometry. Finally, we examine how a non-zero Ericksen number can influence the director and velocity structures for the D, U_1 and U_2 states described in Chapter 3.

6.2 A Simplified Ericksen-Leslie Model of Active Fluids

The non-linearity of the Ericksen-Leslie equations (2.2.31)–(2.2.33) makes them impossible to solve analytically unless significant simplifications are made. We will therefore use a simplified system to model the flow of an active fluid close to the corner of a wedge. First, we assume the one-constant approximation for the Frank elastic coefficients (i.e., $K_1 = K_2 = K_3 \equiv K$, $K_4 = 0$). When elasticity dominates flow effects (i.e., small Ericksen number), the angular momentum equation (2.2.32) simplifies to an Euler-Lagrange equation which, due to the one constant approximation, reduces to Laplace’s equation for the director,

$$\nabla^2 \mathbf{n} = \mathbf{0}, \tag{6.2.1}$$

where $\nabla^2 \mathbf{n} = (\nabla^2 n_1, \nabla^2 n_2, \nabla^2 n_3)$. We also introduce simplifications for the nematic viscosities. As the temperature approaches the critical temperature at which a nematic-isotropic phase transition occurs, i.e., T_{NI} , the Miesowicz viscosities η_1, η_2 and η_3 converge to the same viscosity, η [40] which, from (2.2.59) and (2.2.60), means that the active nematic fluid is tumbling. Experimental evidence also shows that the viscosity η_{12} is small in comparison to the other viscosities, and so we neglect it from the viscous stress tensor. This means that

the only nematic viscosities in the viscous stress tensor are γ_1 and η . Finally, we include activity in the model by adopting the same active term that was also used in Chapter 4. When fluid inertia is ignored, along with the above assumptions on the elastic and viscous coefficients, the flow equations (2.2.31) and (2.2.33) in vectorised form simplify to [128]

$$0 = \nabla \cdot \mathbf{v}, \quad (6.2.2)$$

$$\mathbf{0} = \nabla \cdot \left(2\eta \mathbf{A} + \zeta (\mathbf{n} \otimes \mathbf{n}) + \frac{\gamma_1}{2} (\mathbf{n} \otimes \mathbf{N} - \mathbf{N} \otimes \mathbf{n} - \mathbf{A}\mathbf{n} \otimes \mathbf{n} - \mathbf{n} \otimes \mathbf{A}\mathbf{n}) - \tilde{p}\mathbf{I} \right). \quad (6.2.3)$$

This system of equations is identical to those considered by Tang and Selinger [131] in their study of defect motion in 2D inactive and active nematic liquid crystals. In making the modelling assumptions on the elastic and viscous parameters, we can see that the director angle is no longer coupled to the fluid velocity and can be solved for independently via (6.2.1). The velocity is then a function of the director orientation through (6.2.3).

6.3 Flow of Active Fluids in a Wedge Geometry

In this section, we employ the simplified Ericksen-Leslie system (6.2.1)–(6.2.3) to model the flow of an active nematic fluid confined in a wedge geometry which contains a defect at the corner (see Figure 6.1). We model this system in cylindrical polar coordinates (r, ϕ, z) , where r is the radial distance, ϕ is the polar angle and z is the out-of-plane Cartesian z -coordinate. We assume that both the director orientation and velocity are uniform in the z -direction, thereby simplifying the model to two dimensions. The director \mathbf{n} makes an angle θ with the Cartesian x -axis. The corner of the wedge is assumed to be at the origin, with wedge boundaries at $\phi = -\Theta$ and $\phi = \Theta$, so that the wedge angle separating the two boundaries is 2Θ . We introduce a defect into our model by assuming that the nematic director is subject to infinite planar anchoring at the two boundaries, $\theta = -\Theta$ on $\phi = -\Theta$ and $\theta = \Theta + m\pi$ on $\phi = \Theta$, where $m \in \mathbb{Z}$ is introduced

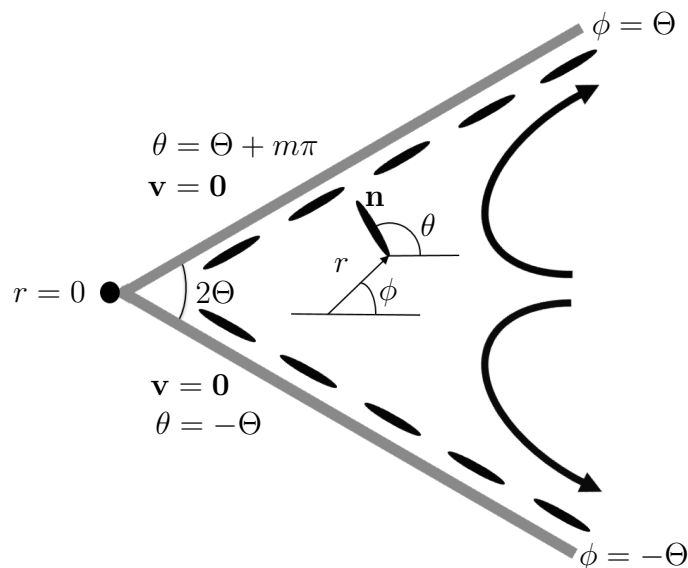


Figure 6.1: A wedge geometry of angle 2Θ containing active fluid in the bulk with a defect pinned at the origin. The velocity (indicated by the curved arrows) is subject to no-slip conditions and the director orientation (indicated by the ellipsoids) is subject to infinite planar anchoring. The polar coordinates (r, ϕ) used to specify the director orientation around a defect are also shown, with the corner corresponding to $r = 0$.

to ensure that the director aligns parallel to the boundary $\phi = \Theta$ after possible multiple rotations in the bulk of the wedge. Since the director undergoes m half-turn rotations as we proceed in the polar direction from one boundary to the other for a fixed value of $r > 0$, the director orientation is undefined at $r = 0$, the corner of the wedge. In other words, a defect exists at the corner of the wedge, which we model as a line defect that lies along the z -axis with the director lying perpendicular to the z -axis. Such defects are commonly referred to as axial line disclinations since the director needs to rotate about an axis parallel to the disclination in order for these line defects to form [129]. With this setup, the director takes the form

$$\mathbf{n} = \cos(\theta - \phi)\mathbf{e}_r + \sin(\theta - \phi)\mathbf{e}_\phi, \quad (6.3.1)$$

where \mathbf{e}_r and \mathbf{e}_ϕ are the basis vectors for polar coordinates, which are related to the basis vectors in Cartesian coordinates \mathbf{e}_x and \mathbf{e}_y via

$$\mathbf{e}_r = \cos \phi \mathbf{e}_x + \sin \phi \mathbf{e}_y, \quad (6.3.2)$$

$$\mathbf{e}_\phi = -\sin \phi \mathbf{e}_x + \cos \phi \mathbf{e}_y. \quad (6.3.3)$$

We obtain the governing equation for the director angle θ by substituting (6.3.1) into (6.2.1), which yields Laplace's equation in polar coordinates,

$$\theta_{rr} + \frac{1}{r}\theta_r + \frac{1}{r^2}\theta_{\phi\phi} = 0, \quad (6.3.4)$$

where we adopt the same subscript notation for partial derivatives in this chapter as used in Chapters 3 and 4. For axial disclinations, the director angle is expected to be independent of r [129], which means that (6.3.4) simplifies to the second order, ordinary differential equation

$$\theta_{\phi\phi} = 0. \quad (6.3.5)$$

The velocity of the active fluid is expressed in terms of a radial and a transverse component, which in turn can be expressed in terms of derivatives of a streamfunction $\psi(r, \phi)$,

$$\mathbf{v} = \frac{1}{r}\psi_\phi \mathbf{e}_r - \psi_r \mathbf{e}_\phi. \quad (6.3.6)$$

This form of the velocity means that the incompressibility condition (6.2.2) is automatically satisfied. In component form, the flow equations in polar coordinates with the additional active forcing term are then

$$0 = \eta \left(\frac{1}{r}\psi_{rr\phi} + \frac{1}{r^2}\psi_{r\phi} + \frac{1}{r^3}\psi_{\phi\phi\phi} \right) + \frac{\zeta}{r}\theta_\phi \cos(2(\phi - \theta)) - \tilde{p}_r + \gamma_1 F_1(r, \phi), \quad (6.3.7)$$

$$0 = \eta \left(\frac{2}{r^3}\psi_{\phi\phi} - \psi_{rrr} - \frac{1}{r}\psi_{rr} + \frac{1}{r^2}(\psi_r - \psi_{r\phi\phi}) \right) - \frac{\zeta}{r}\theta_\phi \sin(2(\phi - \theta)) - \frac{1}{r}\tilde{p}_\phi + \gamma_1 F_2(r, \phi), \quad (6.3.8)$$

where

$$F_1(r, \phi) = \frac{\partial}{\partial r} \left(\frac{2(\psi_\phi - r\psi_{r\phi}) \cos(\phi - \theta) - (r^2\psi_{rr} - r\psi_r - \psi_{\phi\phi}) \sin(\phi - \theta)}{2r^2} \right) \\ \times \cos(\phi - \theta) + \frac{\partial}{\partial \phi} \left(\frac{\psi_{rr} - \psi_r\theta_\phi}{2r^2} \right) + \frac{\psi_\phi - r\psi_{r\phi}}{r^3}, \quad (6.3.9)$$

$$F_2(r, \phi) = \frac{\partial}{\partial r} \left(\frac{r\psi_r - r\theta_\phi\psi_r - \psi_{\phi\phi}}{2r^2} \right) + \frac{r^2\psi_{rr} - r\psi_r - \psi_{\phi\phi}}{2r^3} - \sin(\phi - \theta) \\ \times \frac{\partial}{\partial \phi} \left(\frac{2(\psi_\phi - r\psi_{r\phi}) \sin(\phi - \theta) + (r^2\psi_{rr} - r\psi_r - \psi_{\phi\phi}) \cos(\phi - \theta)}{2r^3} \right). \quad (6.3.10)$$

The velocity of the active fluid is subject to no-slip and no penetration boundary conditions which, along with the boundary conditions for the director angle, are given by

$$\phi = -\Theta \ (r > 0) : \quad \theta = -\Theta, \quad \psi_\phi = 0, \quad \psi_r = 0, \quad (6.3.11)$$

$$\phi = \Theta \ (r > 0) : \quad \theta = \Theta + m\pi, \quad \psi_\phi = 0, \quad \psi_r = 0. \quad (6.3.12)$$

6.3.1 Calculating the Streamfunction

In order to derive the streamfunction, we first need to obtain the director field angle θ . Integrating (6.3.5) with respect to ϕ twice and using the boundary conditions (6.3.11) and (6.3.12), we arrive at the solution

$$\theta = \left(1 + \frac{m\pi}{2\Theta} \right) \phi + \frac{m\pi}{2} \quad (m \in \mathbb{Z}). \quad (6.3.13)$$

The coefficient of ϕ in (6.3.13) is commonly referred to as the strength, or winding number, of a defect and is denoted by s ,

$$s = 1 + \frac{m\pi}{2\Theta}. \quad (6.3.14)$$

As discussed in Chapter 1, for a defect in an unconfined system, this parameter represents the number of complete rotations of the director on a closed circuit containing the defect for $\Theta = \pi$. The strength of the defect now depends on the value of the wedge angle 2Θ and m , the number of half-turn rotations for a fixed r . For example, consider a wedge geometry with wedge angle $2\Theta = 3\pi/2$. For

such a wedge geometry, the relationship between s and m simplifies to

$$s = 1 + \frac{2m}{3}. \quad (6.3.15)$$

When $m = -1$, then the defect strength is $s = 1/3$, a value that would be impossible for a defect in an unconfined system, where s is restricted to $s = k/2$ for some integer k in order for \mathbf{n} to be continuous. Throughout this analysis, we consider examples such that the wedge angle is an integer multiple of $\pi/2$, that is, $2\Theta = n\pi/2$, $n \in \mathbb{Z}$. This means that the strength of the defect (6.3.14) can be expressed as

$$s = 1 + \frac{2m}{n}. \quad (6.3.16)$$

The two specific cases we will examine in this chapter are a sharp corner with perpendicular boundaries and a flat plate, which correspond to the integer values $n = 1$ and 2 , respectively. Since m is necessarily an integer value in order for the director to align parallel to the boundary $\phi = \Theta$, it follows that when $n = 1$, then the only admissible values of s are the odd integers. When the wedge geometry is a flat plate, so that $n = 2$, then the defect strength can be any integer value. The strength of the defect is then related to m via (6.3.16).

Having derived the solution for the director angle, we substitute (6.3.13) into equations (6.3.7) and (6.3.8), which are then combined to generate a single equation for the streamfunction $\psi(r, \phi)$, independent of the modified pressure gradient terms. The single governing equation for the streamfunction is

$$\nabla^4 \psi = \frac{2(-1)^m \zeta s(s-1) \sin(2(s-1)\phi)}{\eta r^2} - \frac{\gamma_1 s (r^3 \psi_{rrr} - r^2 \psi_{rr} + r \psi_{r\phi\phi} + r \psi_r)}{2\eta r^4}. \quad (6.3.17)$$

From equation (6.3.17), it is clear that no flow will be induced in this system unless the activity strength parameter $\zeta \neq 0$. It is not obvious how this equation can be solved analytically unless we consider some simplifications, where analytic solutions for active fluid flows are our primary focus in this section. In order to derive analytic solutions for the streamfunction, we consider the special case of when the activity term is dominant compared to the terms pre-multiplied by γ_1 , that is, the special case of when $\gamma_1 = 0$ Pa s in equation (6.3.17), thereby

reducing the flow equation to a forced biharmonic equation. A similar system of equations were solved by Giomi *et al.* [59] for an isolated defect in an active fluid confined in a circle. We will re-introduce all of the nematic viscosities and elastic constants in Section 6.4, where we implement a numerical scheme in COMSOL to solve the fully coupled Ericksen-Leslie equations for an active nematic liquid crystal confined in a rectangular region. Our main focus in this section is to get qualitative pictures for director and flow structures of active fluids close to regions of high director distortion using an analytic approach. While setting $\gamma_1 = 0$ Pa s is a significant modelling simplification, we will see over the course of the chapter that there are some similarities in the analytic and numerical flow structures close to regions of high director distortion. Furthermore, when we consider the streamfunction solution for an active fluid close to a flat plate with a defect of strength $s = -1$ and compute the ratio of γ_1 and ζ terms in equation (6.3.17), we find that neglecting γ_1 from (6.3.17) is a very good approximation except for when $\phi = \pm\pi/4, \pm3\pi/4$. It is only at these points where we may need to consider the role of the γ_1 terms in equation (6.3.17). We therefore consider the effects due to the advection term $(\mathbf{v} \cdot \nabla)\theta$ negligible.

For the remainder of this section, the governing equation for the streamfunction is

$$\nabla^4 \psi = \frac{2(-1)^m \zeta s(s-1)}{\eta r^2} \sin(2(s-1)\phi). \quad (6.3.18)$$

Similar to the solution for the velocity in [111], we find that the magnitude of flow is proportional to the ratio of active and viscous forces, ζ/η . We seek a separable solution for (6.3.18) of the form $\psi(r, \phi) = r^j g(\phi)$, where $g(\phi)$ is a function to be determined, and j is an exponent which will be a positive integer to ensure there is no singularity in the flow at $r = 0$ [99]. Substituting this expression for ψ into (6.3.18), we obtain the fourth order, ordinary differential equation

$$\begin{aligned} \left(\frac{d^4 g}{d\phi^4} + 2(j^2 - 2j + 2) \frac{d^2 g}{d\phi^2} + (j(j-2))^2 g \right) r^{j-4} \\ = \frac{2(-1)^m \zeta s(s-1)}{\eta r^2} \sin(2(s-1)\phi). \end{aligned} \quad (6.3.19)$$

By solving this differential equation for $g(\phi)$, we find that the streamfunction has

the general solution [2]

$$\begin{aligned} \psi(r, \phi) = & -\frac{r^2}{4} \left(A_2 \cos(2\phi) + B_2 \sin(2\phi) - 4(C_2\phi + D_2) \right. \\ & \left. - \frac{(-1)^m \zeta}{2\eta(s-1)(s-2)} \sin(2(s-1)\phi) \right) + \sum_{j \geq 3} r^j f_j(\phi) \quad (s \neq 1, 2), \end{aligned} \quad (6.3.20)$$

where A_2, B_2, C_2, D_2 are arbitrary constants associated with terms of $O(r^2)$, and

$$\begin{aligned} f_j(\phi) = & A_j \cos(j\phi) + B_j \sin(j\phi) + C_j \cos((j-2)\phi) \\ & + D_j \sin((j-2)\phi). \end{aligned} \quad (6.3.21)$$

In (6.3.21), A_j, B_j, C_j, D_j are arbitrary constants associated with terms of $O(r^j)$, with $j \geq 3$. We have not considered a contribution to the general solution (6.3.20) of $O(r)$ since it could lead to a velocity which is non-zero at the location of the defect, $r = 0$, where no-slip and no-penetration of the velocity must be satisfied.

As mentioned previously, we will only consider the special cases of a wedge with perpendicular boundaries and a flat plate (i.e., a wedge with angles $2\Theta = \pi/2$ and π , respectively). For these two special cases, the no-slip and no-penetration conditions can only determine the values of the constants A_2, B_2, C_2, D_2 . It is also clear from the solution (6.3.20) that in the limit as $r \rightarrow \infty$, we have infinite flow. We will consider only finite flows induced by activity close to the defect, and so only the contributions to (6.3.20) which are of the smallest order in the radial direction, (i.e., $O(r^2)$), will be considered. Although this is a significant simplification, and the higher order terms may be required if the flow far away from the corner necessitates it, we expect this $O(r^2)$ solution to contain the dominant terms close to the corner. All of the higher order terms in r tend to infinity faster and so we remove them from the solution (6.3.20). Furthermore, there will be zero flow generated when there is no activity, and so any terms in the general solution which do not contain the activity strength ζ will not contribute to the flow. The arbitrary constants A_2, B_2, C_2, D_2 are determined via the no-slip

and no-penetration conditions,

$$A_2 = 0, \quad (6.3.22)$$

$$B_2 = \frac{(-1)^m \zeta (2\Theta(s-1) \cos(2(s-1)\Theta) - \sin(2(s-1)\Theta))}{2\eta(s-1)(s-2)(2\Theta \cos(2\Theta) - \sin(2\Theta))}, \quad (6.3.23)$$

$$C_2 = \frac{(-1)^m \zeta ((s-2) \sin(2s\Theta) - s \sin(2(s-2)\Theta))}{8\eta(s-1)(s-2)(2\Theta \cos(2\Theta) - \sin(2\Theta))}, \quad (6.3.24)$$

$$D_2 = 0. \quad (6.3.25)$$

We can see from these constants, as well as the activity term in (6.3.20), that the streamfunction solution (6.3.20) is undefined when $s = 1$ and $s = 2$. These are two special cases which we will consider independently later in this chapter.

6.3.2 Active Fluid Flows Close to Sharp Corners

The director structures and velocity profiles of a contractile system (i.e., $\zeta > 0$) confined in a wedge with angle $2\Theta = \pi/2$ ($n = 1$) close to defects of strengths $s = -1$ and $s = 3$ ($m = -1$ and $m = 1$, respectively), are shown in Figures 6.2(a) and (c). The two director structures in Figures 6.2(a) and (c) are the same as those observed for inactive nematics, albeit restricted by the boundaries of the wedge. The streamfunction solutions in this case are

$$\psi = \begin{cases} \frac{\zeta r^2 (4\phi - \pi \sin(2\phi) + \sin(4\phi))}{48\eta} & \text{when } s = -1, \\ \frac{-\zeta r^2 (4\phi - \pi \sin(2\phi) + \sin(4\phi))}{16\eta} & \text{when } s = 3. \end{cases} \quad (6.3.26)$$

These streamfunction solutions exhibit the same dependence on the polar angle ϕ , and only differ due to the change in the sign and size of the ratio of active and viscous forces. This will simply lead to different velocity magnitudes for the same values of ζ and η . The curves in the flow profiles shown in Figures 6.2(b) and (d) represent the streamlines, with the arrows indicating the direction of flow. The colouring indicates the magnitude of the velocity, with red regions corresponding to areas of weakest flow and yellow regions corresponding to areas of strongest flow. Figure 6.2(b) shows that close to the boundaries of the wedge with an $s = -1$ defect, the active fluid is pulled towards the singularity before then being

expelled out into the bulk, leading to localised regions of high speed as r increases near the centre line $\phi = 0$. Figure 6.2(d) shows the flow near a sharp corner with a defect of strength $s = 3$, where the fluid is now pulled in from the bulk before being pushed parallel to the boundaries away from the singularity. When we consider an extensile active nematic, the directions of the flows are the opposite of those for the contractile active nematic because, for this particular model, the director structures of extensile and contractile active nematics are unaffected by the flow and so are exactly the same.

6.3.3 Active Fluid Flows Close to Flat Plates

We now consider the orientational ordering and flow of a contractile active fluid close to a flat plate, i.e., a corner of angle $2\Theta = \pi$. The director and flow profiles close to a flat plate containing defects of strengths $s = -1$ (with $m = -2$) and $s = 3$ (with $m = 2$) are shown in Figure 6.3. The solutions for the streamfunction in this case are

$$\psi = \begin{cases} \frac{-\zeta r^2 (2 \sin(2\phi) + \sin(4\phi))}{48\eta} & \text{when } s = -1, \\ \frac{\zeta r^2 (2 \sin(2\phi) + \sin(4\phi))}{16\eta} & \text{when } s = 3. \end{cases} \quad (6.3.27)$$

As was the case for the results near a sharp corner, we find that these streamfunction solutions have the exactly same dependence on the polar angle ϕ , and only differ due to the sign and size of the ratio of active to viscous forces. Comparing the flow profiles in Figures 6.2 and 6.3, we can see that the directions of flow, both close to and away from the boundaries, are different. This change in the direction of flow can be seen clearly by the change in the sign of the activity strength ζ in the solutions (6.3.26) and (6.3.27) for both defect strengths. In the case of the $s = -1$ defect, Figure 6.3(b) shows the flow close to the flat plate is being pulled in the direction of the singularity, before then being expelled away from the defect close to the boundaries. A similar conclusion can be drawn for the flow near a flat plate with an $s = 3$ defect, shown in Figure 6.3(d), although we do not investigate this change in the flow direction further.

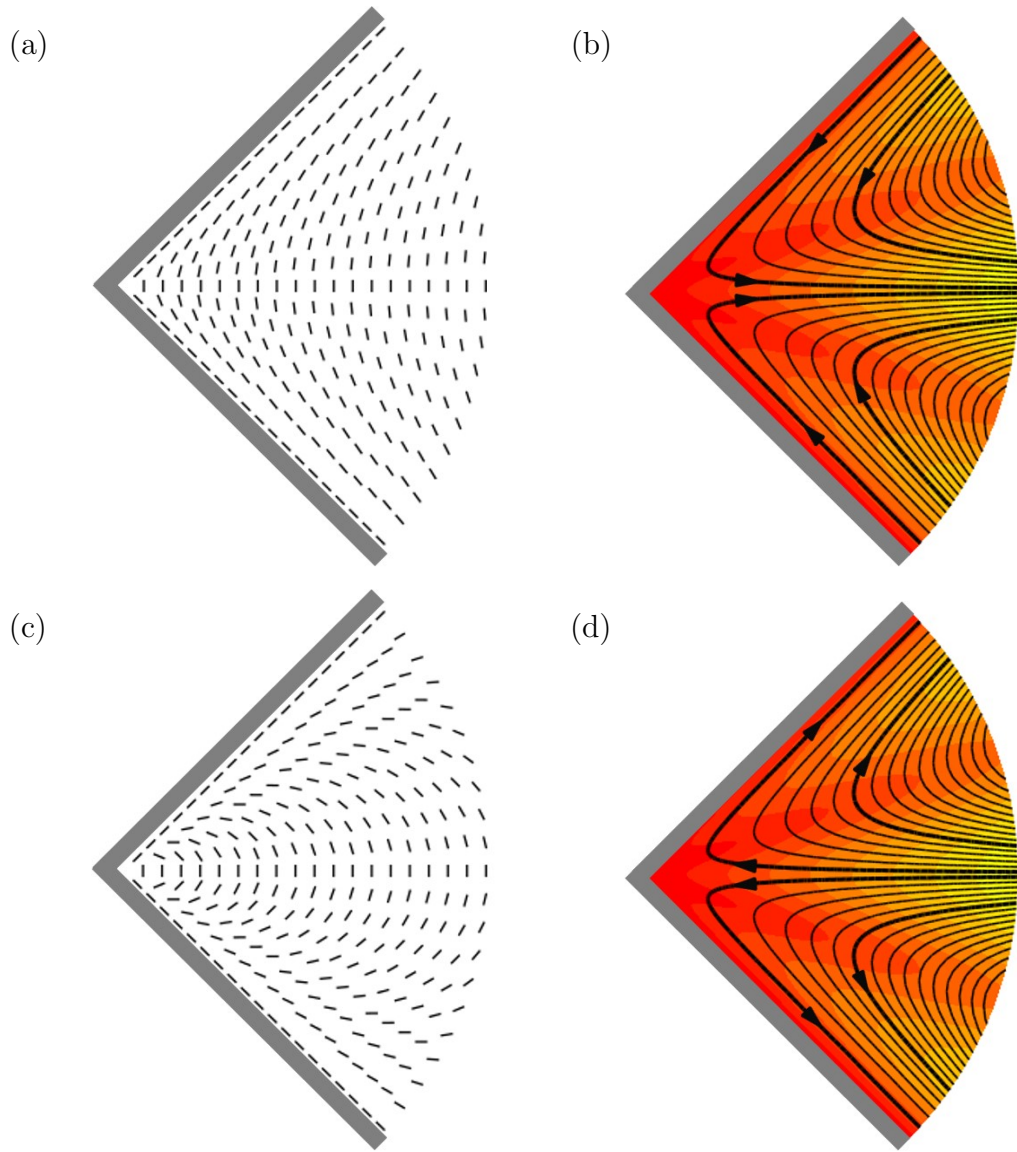


Figure 6.2: (a), (c) Director structures and (b), (d) associated flow profiles of a contractile active fluid close to a sharp corner containing defects of strengths (a), (b), $s = -1$ and (c), (d), $s = 3$, with wedge angle $2\Theta = \frac{\pi}{2}$.

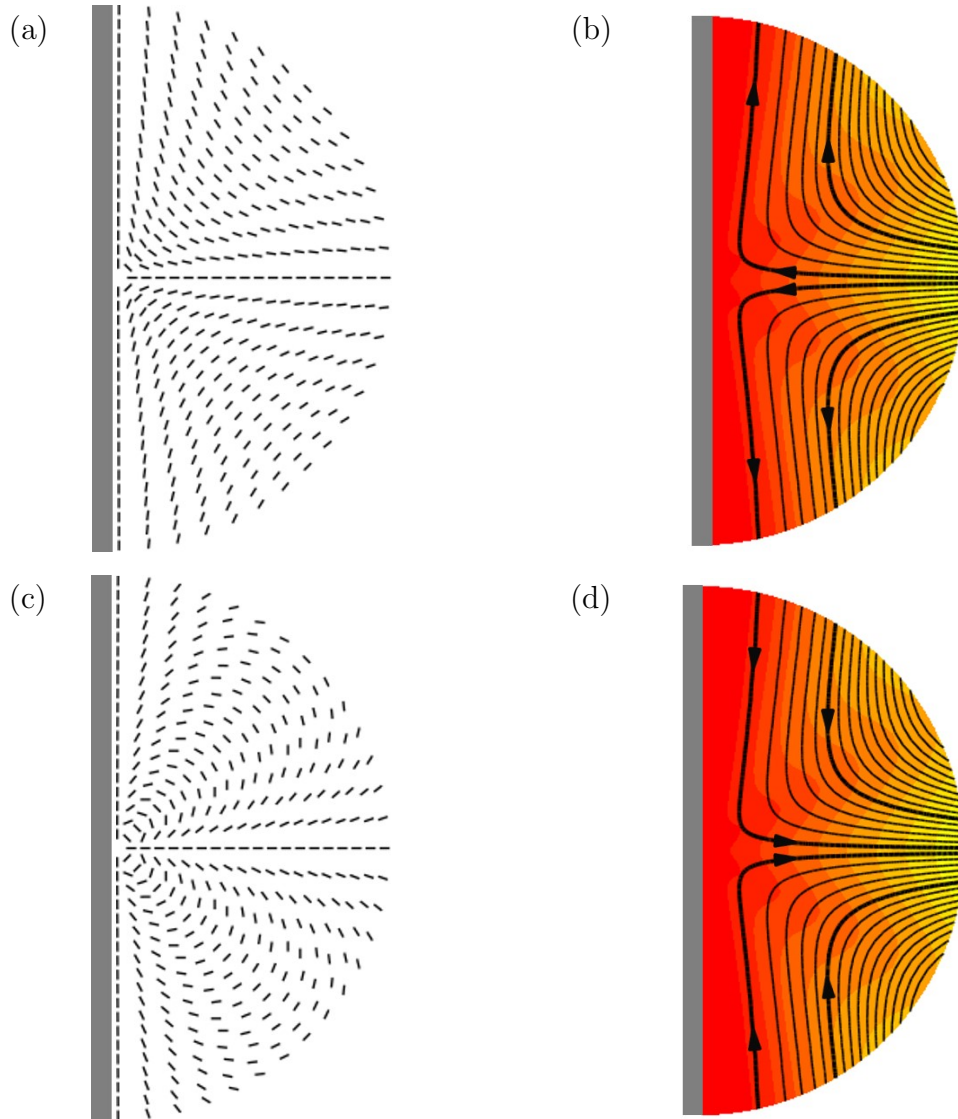


Figure 6.3: (a), (c) Director structures and (b), (d) associated flow profiles of a contractile active fluid close to a flat plate containing defects of strengths (a), (b), $s = -1$ and (c), (d), $s = 3$, with wedge angle $2\Theta = \pi$.

6.3.4 The Special Cases of $s = 1$ and $s = 2$ Defects

As mentioned previously, the solution (6.3.20) was not valid in the special cases $s = 1$ and $s = 2$. So we now return to (6.3.18) for these two special cases. For a defect of strength $s = 1$, the streamfunction satisfies the biharmonic equation $\nabla^4\psi = 0$, which has the general solution at $O(r^2)$

$$\psi(r, \phi) = r^2(A \cos(2\phi) + B \sin(2\phi) + C\phi + D), \quad (6.3.28)$$

where A, B, C, D are arbitrary constants. We have neglected terms in the general solution (6.3.28) which are of higher order in the radial distance r for the same reason as before. Using the no-slip and no-penetration boundary conditions, where we find that the constants A, B, C, D are all equal to zero and so the solution for the streamfunction is $\psi = 0$. This means that for all wedge angles, there is no flow generated within the wedge for a defect of strength $s = 1$.

For a defect of strength $s = 2$, there are only two compatible wedge geometries corresponding to $2\Theta = \pi$ or 2π . We consider the former, which corresponds to a flat plate geometry. In this case, $m = 1$ and the director angle solution (6.3.13) simplifies to

$$\theta = 2\phi + \frac{\pi}{2}, \quad (6.3.29)$$

and equation (6.3.18) becomes

$$\nabla^4\psi = -\frac{4\zeta \sin(2\phi)}{\eta r^2}. \quad (6.3.30)$$

The solution of (6.3.30) subject to the no-slip and no-penetration conditions is

$$\psi = -\frac{\zeta r^2 \phi \cos^2 \phi}{2\eta}. \quad (6.3.31)$$

The director structure of an $s = 2$ defect near a flat plate when $\zeta > 0$ is shown in Figure 6.4, along with the associated velocity profile. From the velocity profile, we see that, like the $s = -1$ defect, the fluid closest to the boundaries of the wedge initially flows towards the defect, before then travelling away from it. However, the behaviour is slightly different from the case $s = -1$ in Figure 6.3. In particular, the velocity profiles exhibit different behaviours close to the plates.

We explore this further by calculating the Cartesian x -component of the velocity, u , for $s = -1$ and $s = 2$ defects in the flat plate situation. From equations (6.3.2) and (6.3.3), we can obtain u in terms of the streamfunction,

$$u = \frac{1}{r}\psi_\phi \cos \phi + \psi_r \sin \phi. \quad (6.3.32)$$

For the $s = -1$ and $s = 2$ defects, equation (6.3.32) leads to an x -component of the velocity of

$$u = \begin{cases} -\frac{\zeta r \cos(2\phi) \cos^3 \phi}{6\eta} & \text{when } s = -1, \\ -\frac{\zeta r \cos^3 \phi}{2\eta} & \text{when } s = 2. \end{cases} \quad (6.3.33)$$

We can solve (6.3.33) in order to determine the first non-zero values of ϕ when $u = 0$. We find that the first non-zero solutions for the polar angle are $\phi = \pm\pi/4$ when $s = -1$ and $\phi = \pm\pi/2$ when $s = 2$. Figure 6.5 shows the velocities (6.3.33) as a function of the polar angle ϕ for a contractile active nematic. The solid curve shows that the x -component of velocity for the $s = -1$ defect is non-monotonic, with the flow initially moving away from the wall and increasing, before eventually decreasing towards it. By contrast, the dashed curve shows that away from the line $\phi = 0$, the x -component of velocity for the $s = 2$ defect continuous to increase towards the wall.

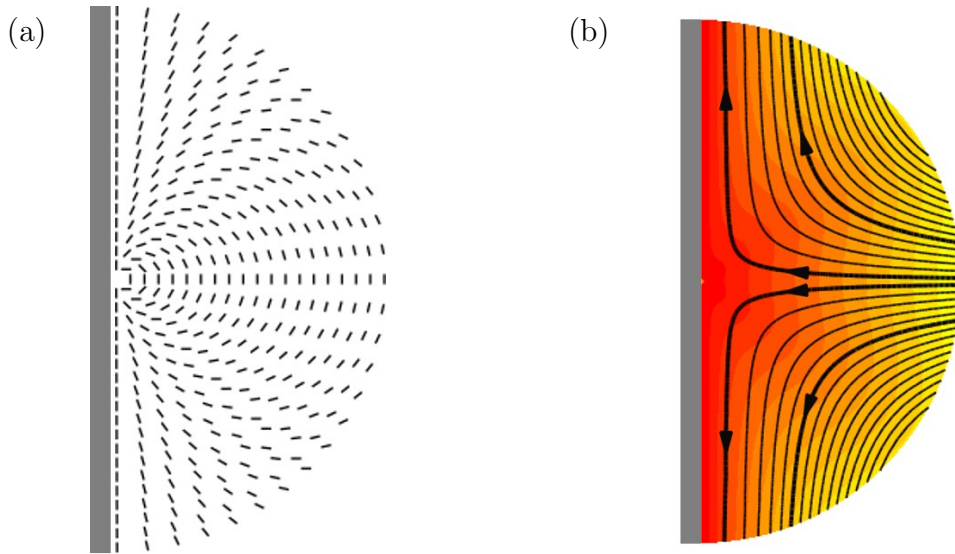


Figure 6.4: (a) Director angle and (b) velocity structures of a contractile active fluid close to a flat plate containing a defect of strength $s = 2$ with wedge angle $2\Theta = \pi$.

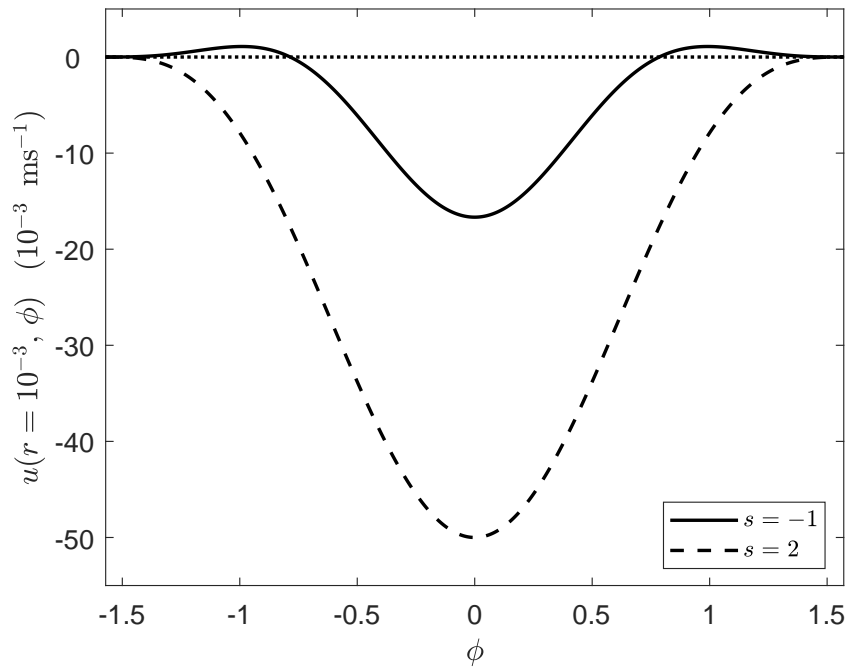


Figure 6.5: The velocities $u(r, \phi)$ defined in (6.3.33) as a function of the polar angle ϕ with radial distance $r = 10^{-3}$, activity strength $\zeta = 10 \text{ Pa}$ and viscosity $\eta = 0.1 \text{ Pa s}$.

6.4 Director and Flow Structures of Active Nematic Liquid Crystals in Rectangular Regions

The results of the previous section, as well as Chapters 4 and 5, have shown that close to regions of director distortion, an active fluid can spontaneously generate a flow for any magnitude of activity. In Chapter 3 we demonstrated various director distortions that occur in confined rectangular regions. In this section, we bring all of this work together and examine the flow spontaneously generated by a flow aligning active nematic liquid crystal in the rectangular regions considered in Chapter 3. As in Chapter 4, we use an adapted Ericksen-Leslie model, where the velocity and director angle are governed by equations (2.2.31), (2.2.32) and (2.2.33). Unlike in the wedge geometry, we will now retain each of the elastic and viscous coefficients in the elastic energy density and dissipation function, respectively. As in Chapter 3, the liquid crystal is subject to a Rapini-Papoular surface anchoring condition at each boundary, thus avoiding the presence of defects at the corners of the region that arise when infinite planar anchoring is considered. The nematic director is assumed to be of the form

$$\mathbf{n} = (\cos \theta(x, y), \sin \theta(x, y), 0), \quad (6.4.1)$$

and the velocity of the active nematic is

$$\mathbf{v} = (u(x, y), v(x, y), 0). \quad (6.4.2)$$

The elastic energy density (2.2.40) can now be written as

$$w_F = \frac{1}{4} \left((K_3 - K_1) ((\theta_x^2 - \theta_y^2) \cos(2\theta) + 2\theta_x \theta_y \sin(2\theta)) + (K_1 + K_3) (\theta_x^2 + \theta_y^2) \right), \quad (6.4.3)$$

while the dissipation function from (2.2.29) becomes

$$\begin{aligned}
\mathcal{D} = & \frac{\eta_{12}}{8} \left((u_y + v_x) \sin(2\theta) + (u_x - v_y) \cos(2\theta) + u_x + v_y \right)^2 \\
& + \frac{\gamma_2}{4} (2\dot{\theta} + u_y - v_x) \left((u_y + v_x) \cos(2\theta) - (u_x - v_y) \sin(2\theta) \right) \\
& + \frac{\eta_3}{2} \left(2u_x^2 + u_y^2 + 2u_y v_x + v_x^2 + 2v_y^2 \right) + \frac{\gamma_1}{8} \left(2\dot{\theta} + u_y - v_x \right)^2 \\
& + \frac{1}{2} (2\eta_1 + 2\eta_2 - 4\eta_3 - \gamma_1) \left(\left(u_x \cos \theta + \frac{1}{2} (u_y + v_x) \sin \theta \right)^2 \right. \\
& \left. + \left(\frac{1}{2} (u_y + v_x) \cos \theta + v_y \sin \theta \right)^2 \right). \tag{6.4.4}
\end{aligned}$$

We use a superposed dot to represent the material time derivative which, as we are seeking steady solutions of a two-dimensional system in Cartesian coordinates, is $\dot{\theta} \equiv D\theta/Dt = u\theta_x + v\theta_y$. The Ericksen-Leslie equations (2.2.31), (2.2.32) and (2.2.33), for which we will seek steady solutions, are now

$$0 = u_x + v_y, \tag{6.4.5}$$

$$\rho \dot{u} = \frac{\partial}{\partial x} \left(\frac{\partial \mathcal{D}}{\partial u_x} + \zeta \cos^2 \theta \right) + \frac{\partial}{\partial y} \left(\frac{\partial \mathcal{D}}{\partial u_y} + \zeta \sin \theta \cos \theta \right) - \frac{\partial \mathcal{D}}{\partial \dot{\theta}} \theta_x - \tilde{p}_x, \tag{6.4.6}$$

$$\rho \dot{v} = \frac{\partial}{\partial x} \left(\frac{\partial \mathcal{D}}{\partial v_x} + \zeta \sin \theta \cos \theta \right) + \frac{\partial}{\partial y} \left(\frac{\partial \mathcal{D}}{\partial v_y} + \zeta \sin^2 \theta \right) - \frac{\partial \mathcal{D}}{\partial \dot{\theta}} \theta_y - \tilde{p}_y, \tag{6.4.7}$$

$$0 = -\tilde{p}_z, \tag{6.4.8}$$

$$0 = \frac{\partial}{\partial x} \left(\frac{\partial w_F}{\partial \theta_x} \right) + \frac{\partial}{\partial y} \left(\frac{\partial w_F}{\partial \theta_y} \right) - \frac{\partial w_F}{\partial \theta} - \frac{\partial \mathcal{D}}{\partial \dot{\theta}}. \tag{6.4.9}$$

6.4.1 Non-Dimensionalisation

We introduce dimensionless quantities (indicated by a bar) as follows:

$$x = d\bar{x}, \quad y = d\bar{y}, \quad u = V\bar{u}, \quad v = V\bar{v}, \quad \tilde{p} = P\bar{p}, \tag{6.4.10}$$

where V and P are velocity and pressure scales, respectively, and d is the length of the channel. Given that we are interested in activity driven flow, by considering equations (6.4.6)–(6.4.9), we can define both V and P in terms of the activity magnitude $|\zeta|$,

$$V = \frac{|\zeta|d}{\eta_3} \quad \text{and} \quad P = |\zeta|. \tag{6.4.11}$$

The non-dimensionalisation results in a set of dimensionless constants: a measure of the deviation from isotropic elasticity, $k = K_3/K_1$; dimensionless nematic viscosities η_i/η_3 and γ_i/η_3 ; the aspect ratio λ ; and the Reynolds and Ericksen numbers,

$$\text{Re} = \frac{\rho V d}{\eta_3} = \frac{\rho |\zeta| d^2}{\eta_3^2}, \quad (6.4.12)$$

$$\text{Er} = \frac{\eta_3 V d}{K_1} = \frac{|\zeta| d^2}{K_1}. \quad (6.4.13)$$

The Reynolds number is a ratio of inertial to viscous forces, while the Ericksen number measures the ratio of viscous to elastic forces. Using typical values for the Miesowicz viscosities, channel length, fluid density and elastic constants (for example, 5CB at 26°C [129] with $d = 10^{-5}$ m), we obtain $\text{Re} \simeq 10^{-3}|\zeta|$ and $\text{Er} \simeq 10^2|\zeta|$ and therefore, we assume that $\text{Re} \ll 1$ and neglect terms of $O(\text{Re})$.

The dimensionless system under consideration is then

$$0 = \bar{u}_x + \bar{v}_y, \quad (6.4.14)$$

$$0 = \frac{\partial}{\partial \bar{x}} \left(\frac{\partial \bar{\mathcal{D}}}{\partial \bar{u}_x} + \text{sgn}(\zeta) \cos^2 \bar{\theta} \right) + \frac{\partial}{\partial \bar{y}} \left(\frac{\partial \bar{\mathcal{D}}}{\partial \bar{u}_y} + \text{sgn}(\zeta) \sin \bar{\theta} \cos \bar{\theta} \right) - \frac{\partial \bar{\mathcal{D}}}{\partial \dot{\bar{\theta}}} \bar{\theta}_x - \tilde{p}_x, \quad (6.4.15)$$

$$0 = \frac{\partial}{\partial \bar{x}} \left(\frac{\partial \bar{\mathcal{D}}}{\partial \bar{v}_x} + \text{sgn}(\zeta) \sin \bar{\theta} \cos \bar{\theta} \right) + \frac{\partial}{\partial \bar{y}} \left(\frac{\partial \bar{\mathcal{D}}}{\partial \bar{v}_y} + \text{sgn}(\zeta) \sin^2 \bar{\theta} \right) - \frac{\partial \bar{\mathcal{D}}}{\partial \dot{\bar{\theta}}} \bar{\theta}_y - \tilde{p}_y, \quad (6.4.16)$$

$$0 = -\tilde{p}_z, \quad (6.4.17)$$

$$0 = \frac{\partial}{\partial \bar{x}} \left(\frac{\partial \bar{w}_F}{\partial \bar{\theta}_x} \right) + \frac{\partial}{\partial \bar{y}} \left(\frac{\partial \bar{w}_F}{\partial \bar{\theta}_y} \right) - \frac{\partial \bar{w}_F}{\partial \bar{\theta}} - \text{Er} \frac{\partial \bar{\mathcal{D}}}{\partial \dot{\bar{\theta}}}, \quad (6.4.18)$$

where $\text{sgn}(\zeta)$ denotes the sign (or signum) function. We swap between contractile and extensile active nematics by setting $\text{sgn}(\zeta) = 1$ in equations (6.4.15) and (6.4.16) for contractile active nematics, and $\text{sgn}(\zeta) = -1$ for extensile active nematics. For convenience, we will now remove the $\bar{\cdot}$ from each of the quantities in equations (6.4.14)–(6.4.18) with the understanding that, henceforth, all quantities in this chapter are dimensionless. The derivatives of the dimensionless free energy density and dissipation function are

$$\frac{\partial w_F}{\partial \theta_x} = \frac{1}{2}(k-1)(\theta_x \cos(2\theta) + \theta_y \sin(2\theta)) + \frac{1}{2}(1+k)\theta_x, \quad (6.4.19)$$

$$\frac{\partial w_F}{\partial \theta_y} = \frac{1}{2}(k-1)(\theta_x \sin(2\theta) - \theta_y \cos(2\theta)) + \frac{1}{2}(1+k)\theta_y, \quad (6.4.20)$$

$$\frac{\partial w_F}{\partial \theta} = \frac{1}{2}(k-1)(2\theta_x \theta_y \cos(2\theta) - (\theta_x - \theta_y)(\theta_x + \theta_y) \sin(2\theta)), \quad (6.4.21)$$

$$\frac{\partial \mathcal{D}}{\partial \dot{\theta}} = \frac{1}{2} \left(\gamma_1(2\dot{\theta} + u_y - v_x) - \gamma_2 \left((u_x - v_y) \sin(2\theta) - (u_y + v_x) \cos(2\theta) \right) \right), \quad (6.4.22)$$

$$\begin{aligned} \frac{\partial \mathcal{D}}{\partial u_x} &= \frac{\eta_{12}}{4} \left((u_y + v_x) \sin(2\theta) + (u_x - v_y) \cos(2\theta) + u_x + v_y \right) (1 + \cos(2\theta)) \\ &\quad - \frac{\gamma_2}{4} (2\dot{\theta} + u_y - v_x) \sin(2\theta) + 2u_x \\ &\quad + (2\eta_1 + 2\eta_2 - 4 - \gamma_1) \left(u_x \cos \theta + \frac{1}{2}(u_y + v_x) \sin \theta \right) \cos \theta, \end{aligned} \quad (6.4.23)$$

$$\begin{aligned} \frac{\partial \mathcal{D}}{\partial u_y} &= \frac{\eta_{12}}{4} \left((u_y + v_x) \sin(2\theta) + (u_x - v_y) \cos(2\theta) + u_x + v_y \right) \sin(2\theta) \\ &\quad + \frac{\gamma_2}{4} \left(2(\dot{\theta} + u_y) \cos(2\theta) + (v_y - u_x) \sin(2\theta) \right) \\ &\quad + \frac{1}{4} (2\eta_1 + 2\eta_2 - 4 - \gamma_1) \left((u_x + v_y) \sin(2\theta) + u_y + v_x \right) \\ &\quad + u_y + v_x + \frac{\gamma_1}{4} (2\dot{\theta} + u_y - v_x), \end{aligned} \quad (6.4.24)$$

$$\begin{aligned} \frac{\partial \mathcal{D}}{\partial u_y} &= \frac{\eta_{12}}{4} \left((u_y + v_x) \sin(2\theta) + (u_x - v_y) \cos(2\theta) + u_x + v_y \right) \sin(2\theta) \\ &\quad + \frac{\gamma_2}{4} \left(2(\dot{\theta} - v_x) \cos(2\theta) - (v_y - u_x) \sin(2\theta) \right) \\ &\quad + \frac{1}{4} (2\eta_1 + 2\eta_2 - 4 - \gamma_1) \left((u_x + v_y) \sin(2\theta) + u_y + v_x \right) \\ &\quad + u_y + v_x - \frac{\gamma_1}{4} (2\dot{\theta} + u_y - v_x), \end{aligned} \quad (6.4.25)$$

$$\begin{aligned} \frac{\partial \mathcal{D}}{\partial v_y} &= \frac{\eta_{12}}{4} \left((u_y + v_x) \sin(2\theta) + (u_x - v_y) \cos(2\theta) + u_x + v_y \right) (1 - \cos(2\theta)) \\ &\quad + \frac{\gamma_2}{4} (2\dot{\theta} + u_y - v_x) \sin(2\theta) + 2v_y \\ &\quad + (2\eta_1 + 2\eta_2 - 4 - \gamma_1) \left(v_y \sin \theta + \frac{1}{2}(u_y + v_x) \cos \theta \right) \sin \theta. \end{aligned} \quad (6.4.26)$$

Finally, the dimensionless boundary conditions for the director angle due to weak surface anchoring are

$$\begin{aligned}
\sigma_1 : \quad & (1+k)\theta_x + \tau \sin(2\theta) + (k-1)(\theta_x \cos(2\theta) + \theta_y \sin(2\theta)) = 0, \\
\sigma_2 : \quad & (1+k)\theta_x - \tau \sin(2\theta) + (k-1)(\theta_x \cos(2\theta) + \theta_y \sin(2\theta)) = 0, \\
\sigma_3 : \quad & (1+k)\theta_y - \tau \sin(2\theta) - (k-1)(\theta_y \cos(2\theta) - \theta_x \sin(2\theta)) = 0, \\
\sigma_4 : \quad & (1+k)\theta_y + \tau \sin(2\theta) - (k-1)(\theta_y \cos(2\theta) - \theta_x \sin(2\theta)) = 0,
\end{aligned} \tag{6.4.27}$$

where τ is the dimensionless anchoring strength. The boundary conditions for the velocity are the classic no-slip and no-penetration boundary conditions, $u = 0$ and $v = 0$. In the calculations that follow, we have assumed the liquid crystal has the physical parameters of 5CB given in Appendix D of Stewart [129] as in the investigations considered in Chapters 4 and 5.

6.4.2 Flow Induced with Zero Ericksen Number

We first consider the flow of active nematic liquid crystals in a rectangle for zero Ericksen number, $Er = 0$. In this case, the equation for the director angle (6.4.18) no longer contains terms due to gradients in the velocity and, therefore, the director orientation is the same for both extensile and contractile agents. We solve the non-linear system (6.4.14)–(6.4.18) numerically in COMSOL. The governing equation for the director angle solved here is similar to the equation solved in Chapter 3, where we assumed that the inactive nematic liquid crystal was elastically isotropic. For the active nematic liquid crystal, we use the experimentally measured values for the splay and bend elastic constants for the liquid crystal 5CB given in Appendix D in Stewart [129]. so that the liquid crystal is elastically anisotropic. We would not expect any significant changes visually in the director structures of elastically isotropic and anisotropic liquid crystals for large anchoring strength, although a quantitative difference between the two will exist due to the presence of extra non-linear terms in the director angle equation when $k \neq 1$. Director profiles for the U_1 and DD states when the active system is contractile are given in Figures 6.6, along with the associated velocity profiles. Director and flow structures for the D and U_2 states are given in Figure 6.7. The direction of

fluid flow in Figures 6.6 and 6.7 is indicated by the arrowheads, with the colour bar used to indicate the velocity magnitude (i.e., speed) in the rectangular region. The regions of strong flow are indicated by the bright regions, whereas regions of weak flow are dark. An increase in the size of the arrows coincides with a higher speed. Similar to the velocity profiles found by Marenduzzo *et al.* [93], we find that our adapted Ericksen-Leslie model shows the spontaneous flow of the active nematic liquid crystal appearing as a pair of circulating jets in the bulk in Figures 6.6 and 6.7. The \mathbf{Q} -tensor model of active nematics considered in [93] was based on the Beris-Edwards equations, and generated flow profiles for which the velocity was subject to periodic boundary conditions, with the director orientation subject to infinite planar anchoring along the boundaries.

We will now examine the flows generated close to sharp corners and flat plates in the rectangular region, with a particular focus on the similarities between the numerically calculated flows for the rectangular region and those calculated analytically for the wedge geometry. If we consider, for example, the D state, the director structures close to the corners $(0, 0)$ and $(1, \lambda)$ are similar to the director structure close to a defect of strength $s = 1$ (see Figure 6.8(a)). By contrast, the director structures close to the corners $(1, 0)$ and $(0, \lambda)$ are similar to the director structure close to a defect of strength $s = -1$ (see Figure 6.8(b)). Figure 6.9(a) shows the velocity structure for the D state close to the corner $(1, \lambda)$, while Figure 6.9(b) shows the D state velocity structure near the corner $(0, \lambda)$. Comparing these two plots, we see that the velocity magnitude close to the corner $(0, \lambda)$ is much stronger than that near $(1, \lambda)$. Furthermore, close to the corner $(0, \lambda)$, we find that there is flow near the boundaries which travels in towards the corner, i.e., inflow. This inflow is then expelled out in the bulk of the region, i.e., outflow. This flow structure is similar to that in Figure 6.2(b), which shows inflow close to the boundaries of the wedge, with an outflow close to the centre line of the wedge. The wedge model suggested zero flow near $s = 1$ defects. However, we recognise that since we are examining a fully confined rectangular region, the distortion in the director close to each of the corners will lead to a non-zero flow close to each corner, including those with director structures which resemble those near $s = 1$

defect. These flows are however much weaker than those in the vicinity of director structures which are similar to those near $s = -1$ defects, as indicated by the increase in darker regions and the reduced arrows in Figure 6.9(a). The distortion in the director close to the corners $(1, 0)$ and $(0, \lambda)$ leads to swirls of fast fluid flow around the centre of the region, with very weak flow induced near the remaining two corners. We have therefore observed similar inflow and outflow behaviour for tumbling and flow-aligning active nematic liquid crystals close to sharp corners. Similar conclusions can be drawn for the two rotated states. The U_1 state velocity structure is given by Figure 6.6(c), where we find that the regions of strongest flow occur near the vertical walls and centre of the rectangular region. The flow is generated due to the distortion in the director close to the corners $(0, \lambda)$ and $(1, \lambda)$. Figure 6.7(d) shows the U_2 state velocity structure, where the regions of strongest flow occur near the horizontal boundaries, with the flow generated near the corners $(1, 0)$ and $(1, \lambda)$.

So far, we have discussed only the flows close to a sharp corner of a rectangular region. When we examined the wedge geometry in Subsection 6.3.3, we also considered the flow induced by activity close to the special case of a flat plate. In order to compare these two geometries, we now consider the DD state which contained regions of strong director distortion close to the midpoints of the vertical boundaries. We find that close to the points $(0, \lambda/2)$ for the velocity structure in Figure 6.6(d), there appears to be generation of a central jet of fluid, with the inflow of the active agents towards the vertical boundary on the left, followed by outflow away from the boundaries. By contrast, there is very weak flow close to the point $(1, \lambda/2)$. As can be seen in Figure 6.10, the director structures close to the points $(0, \lambda/2)$ and $(1, \lambda/2)$ are similar to those near defects of strengths $s = -1$ and $s = 1$, respectively. Comparing the numerical flow structure in Figure 6.6(d) with the analytic flow structure near a flat plate shown in Figure 6.3(b), we again see similar inflow and outflow behaviour for tumbling and flow-aligning active nematic liquid crystals, despite the large number of modelling simplifications that were made for the analytic approach considered for a tumbling active nematic.

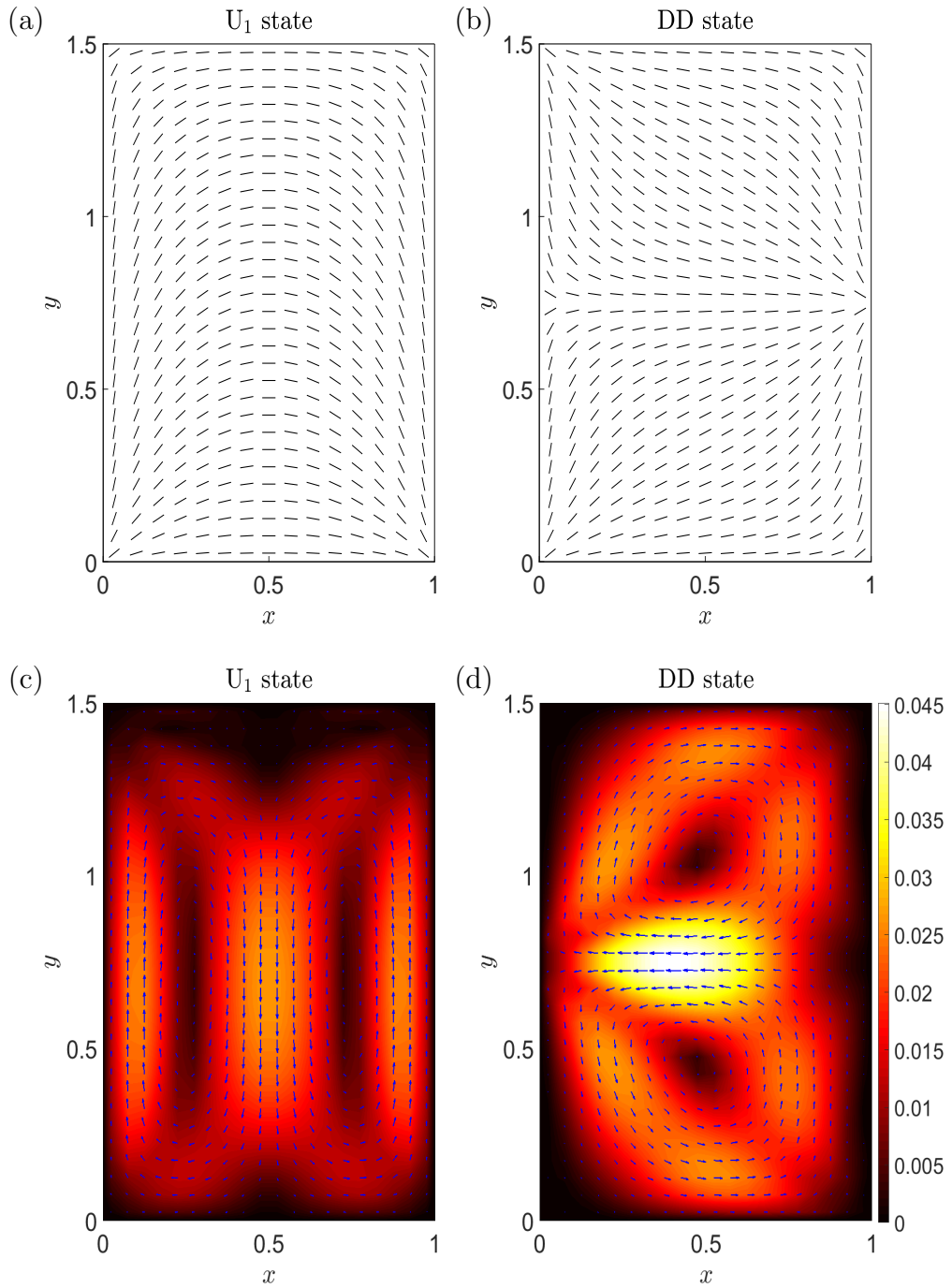


Figure 6.6: (a), (b) Director and (c), (d) flow structures of the U_1 and DD states for a contractile active nematic in a rectangle with aspect ratio $\lambda = 1.5$, elastic constant ratio $k \approx 1.31$, anchoring strength $\tau = 100$ and Ericksen number $Er = 0$. The colour bar indicates the magnitude of the velocity throughout the rectangular region.

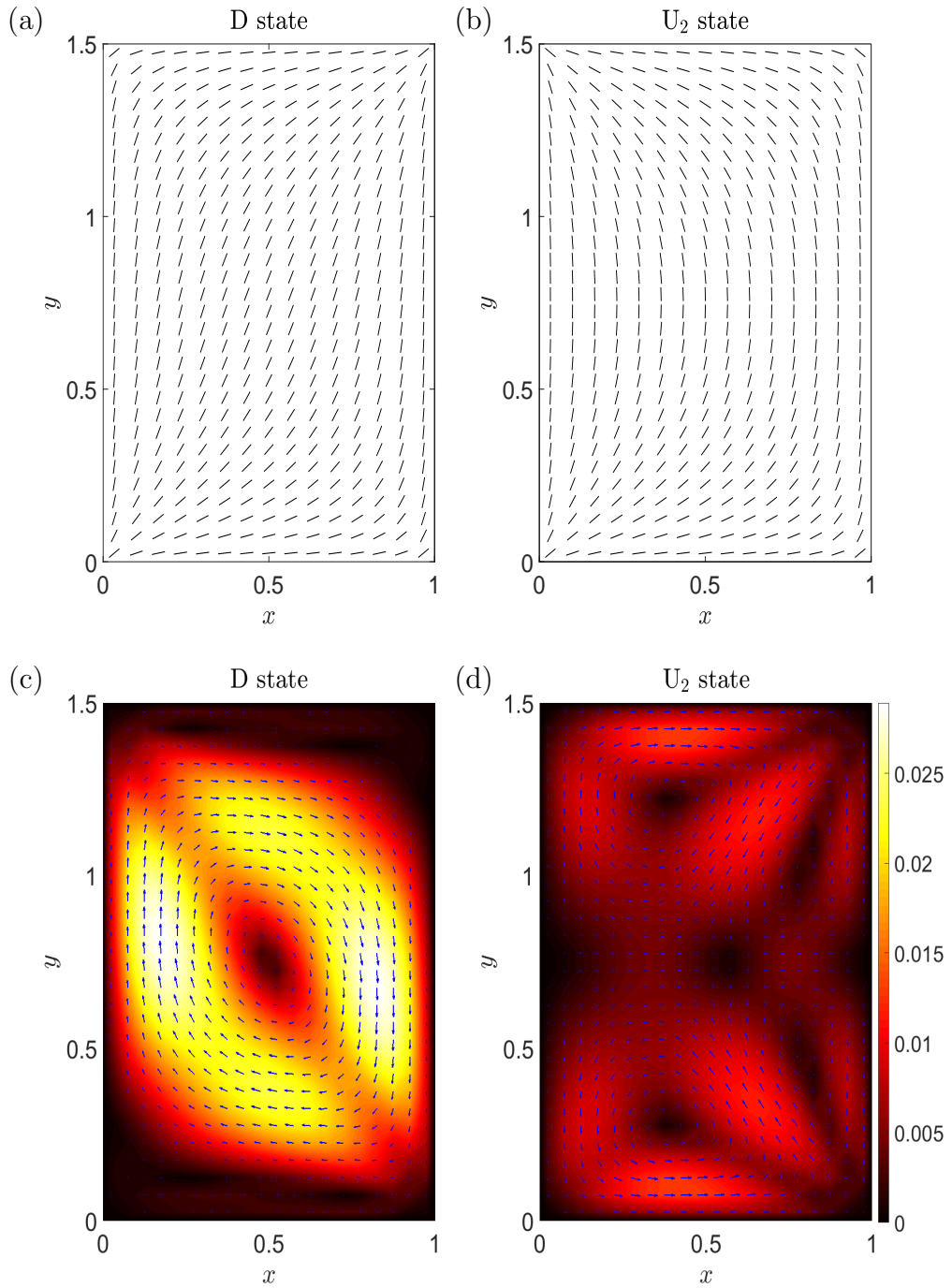


Figure 6.7: (a), (b) Director and (c), (d) flow structures of the D and U_2 states for a contractile active nematic in a rectangle with aspect ratio $\lambda = 1.5$, elastic constant ratio $k \approx 1.31$, anchoring strength $\tau = 100$ and Ericksen number $Er = 0$. The colour bar indicates the magnitude of the velocity throughout the rectangular region.

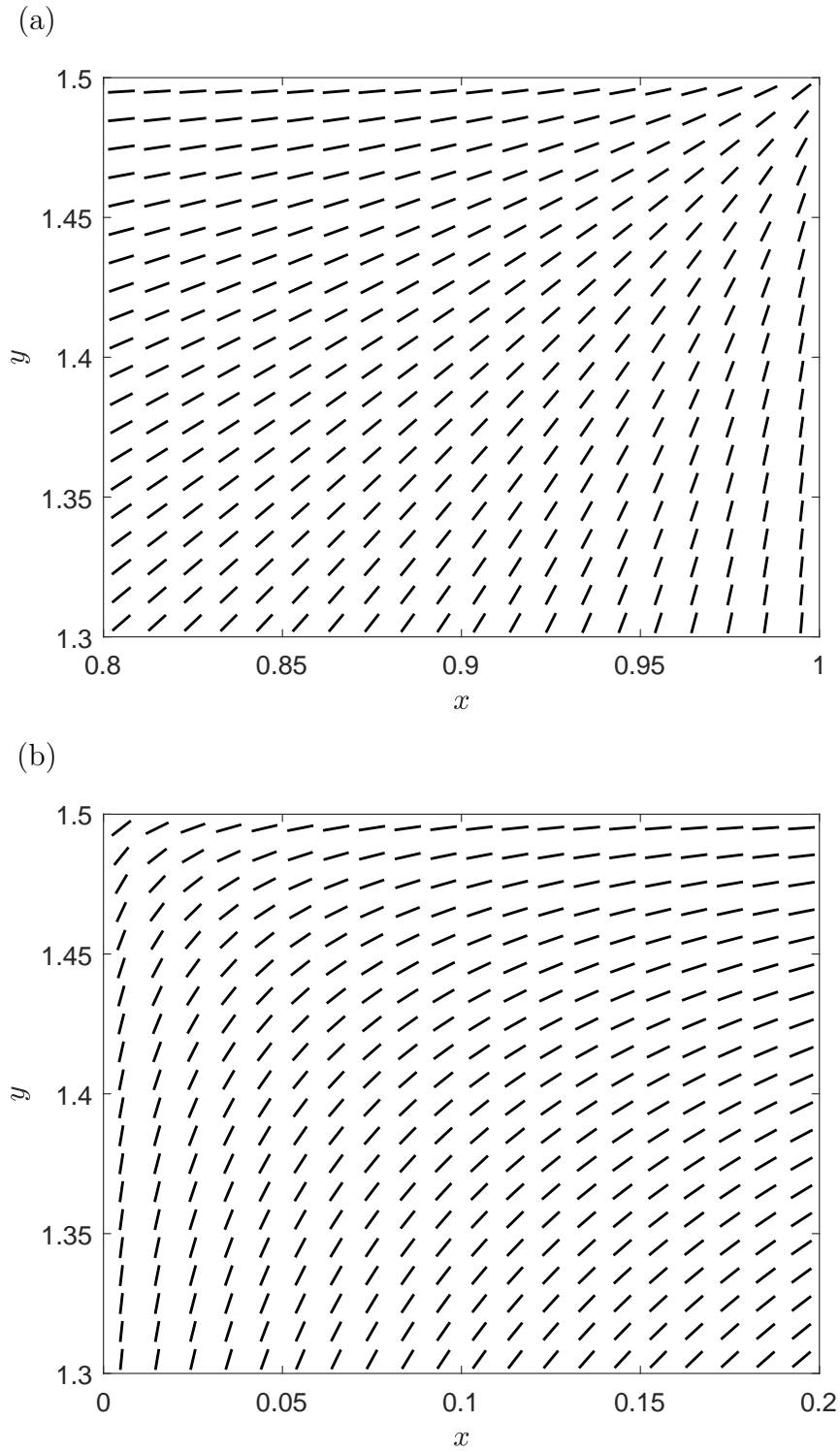


Figure 6.8: Director structures close to the corner (a) $(1, \lambda)$ and (b) $(0, \lambda)$ for the D state with aspect ratio $\lambda = 1.5$, elastic constant ratio $k \approx 1.31$, anchoring strength $\tau = 100$ and Ericksen number $\text{Er} = 0$.

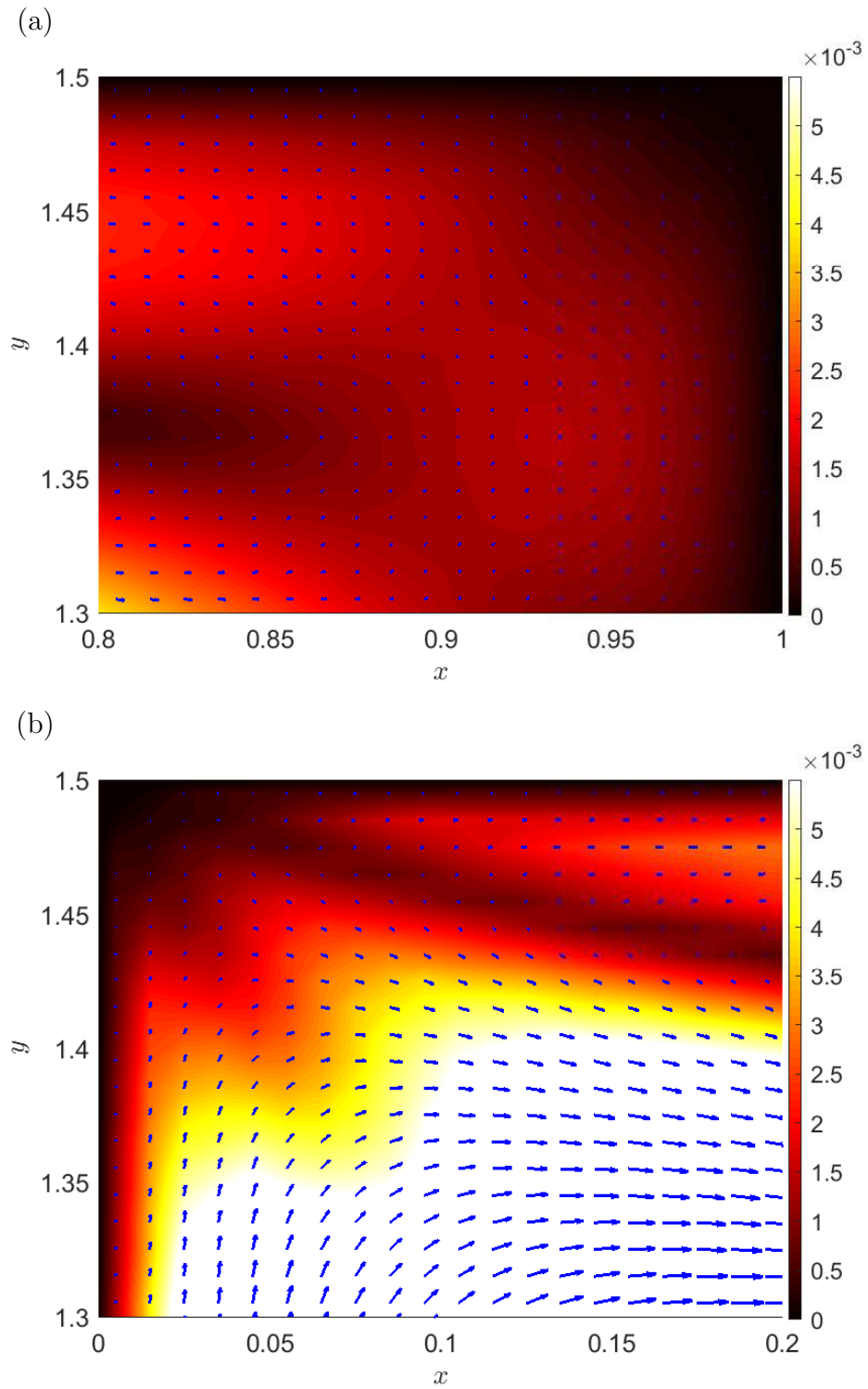


Figure 6.9: Flow structures close to the corner (a) $(1, \lambda)$ and (b) $(0, \lambda)$ for the contractile D state with aspect ratio $\lambda = 1.5$, elastic constant ratio $k \approx 1.31$, anchoring strength $\tau = 100$ and Ericksen number $Er = 0$. The colour bar indicates the magnitude of the velocity close to the corners.

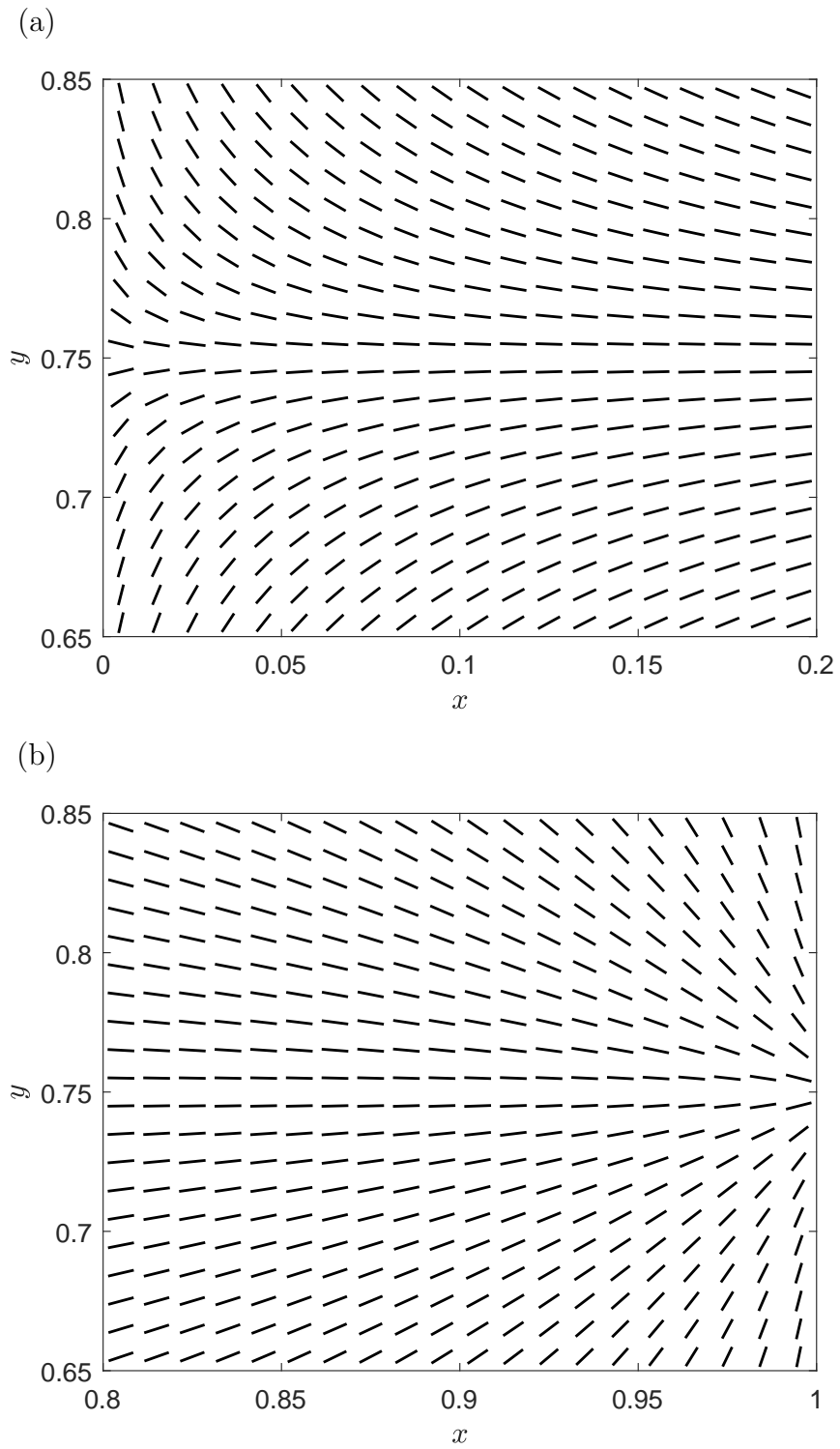


Figure 6.10: Director structures close to the point (a) $(0, \lambda/2)$ and (b) $(1, \lambda/2)$ for the DD state with aspect ratio $\lambda = 1.5$, elastic constant ratio $k \approx 1.31$, anchoring strength $\tau = 100$ and Ericksen number $Er = 0$.

6.4.3 Flow Induced with Non-Zero Ericksen Numbers

In Chapters 4 and 5, we saw that the flows of extensile and contractile active nematic systems were very different due to the differences in director structures for the two types of active agents. When we considered the flow induced in the rectangular region in the last subsection when $Er = 0$, the director structure was the same for extensile and contractile agents and, therefore, a change in the sign of ζ simply leads to a flow moving in the opposite direction. In this subsection, we examine the system (6.4.14)–(6.4.18) for a non-zero Ericksen number, so that the director structure may be affected by the flow. An increase in the Ericksen number can be thought of as increasing the magnitude of the activity parameter.

The director structures for a contractile D state (i.e., $\text{sgn}(\zeta) = 1$) with Ericksen numbers $Er = 250$ and 500 are shown in Figures 6.11, along with the associated flow profiles. We have chosen these values for the Ericksen number in order to highlight clearly the influence of activity on the system when compared to the zero Ericksen number state in Figure 6.7. From Figures 6.11(a) and (b), we can see that the director adopts a uniform diagonal structure in the bulk of the region as the Ericksen number increases, which coincides with regions of weaker flow, as shown by the velocity profiles in Figures 6.11(c) and (d). The strongest regions of flow are found close to the vertical walls where the active agents flow parallel to the vertical walls. Comparing the velocity profiles in Figures 6.11 with the velocity profile in Figure 6.7(c), we can see that an increase in the Ericksen number has led to a reduction in the maximum speed.

Figure 6.12 shows the director and velocity profiles for an extensile D state (i.e., $\text{sgn}(\zeta) = -1$) at Ericksen numbers $Er = 75$ and 100 . The director structures for contractile active nematics at Ericksen numbers $Er = 75$ and 100 are not significantly different from those when $Er = 0$, and so we have not shown them here. In order to see any significant change in the contractile director structures, larger Ericksen numbers are used than those for the extensile case. Even with the choice of smaller Ericksen number, the director structure in Figure 6.12(a), the extensile active nematic exhibits larger regions of director distortion compared to

the contractile agents. The increased director distortion appears as a wave-like pattern in the director structure and looks like a region of high fluid velocity will be formed from the boundary as the activity magnitude further increases. We indicate this by the markers and arrows in Figure 6.12(b). This change then leads to a complicated flow structure in which the regions of strongest flow occur where there is greater distortion in the director. Comparing the velocity profiles in Figures 6.12 with Figure 6.7(c), we can see that, unlike the contractile case, an increase in the Ericksen number has led to faster spontaneous flow and, similar to the zero Ericksen number case, the strongest flow occurs as a swirl-like structure around the centre of the region.

The structures for a contractile and extensile U_1 state at the same Ericksen numbers used for the D state, are shown in Figures 6.13 and 6.14, respectively. We can see that, like the D state, increasing the Ericksen number of contractile and extensile active nematics leads to completely different director and velocity structures. Similar to the zero Ericksen number case, the regions of strongest flow for the contractile U_1 state are observed near the vertical boundaries, with an increase in activity causing a reduction in the maximum speed. By contrast, there is faster spontaneous flow in the extensile active nematic close to the centre of the region as the Ericksen number increases. The director and velocity profiles for the U_2 state are shown in Figures 6.15 and 6.16. Once again, we find that increasing the magnitude of activity for a contractile active nematic leads to a reduction in the velocity magnitude, with the strongest regions of flow for this state now observed close to the horizontal boundaries, as it also did when $Er = 0$. As was also the case for the extensile D and U_1 states, we find that the extensile U_2 state exhibits faster flow as the magnitude of activity increases, with the active agents closer to the centre of the region swimming faster than those elsewhere. Similar to the extensile D state, both the extensile U_1 and U_2 states exhibit a wave-like pattern in the director structure. Our numerical scheme in COMSOL has not been able to find solutions for the DD state at non-zero Ericksen numbers, possibly due to the activity inducing a flow that causes a break in the symmetry of the DD state director structure, leading to an unstable configuration.

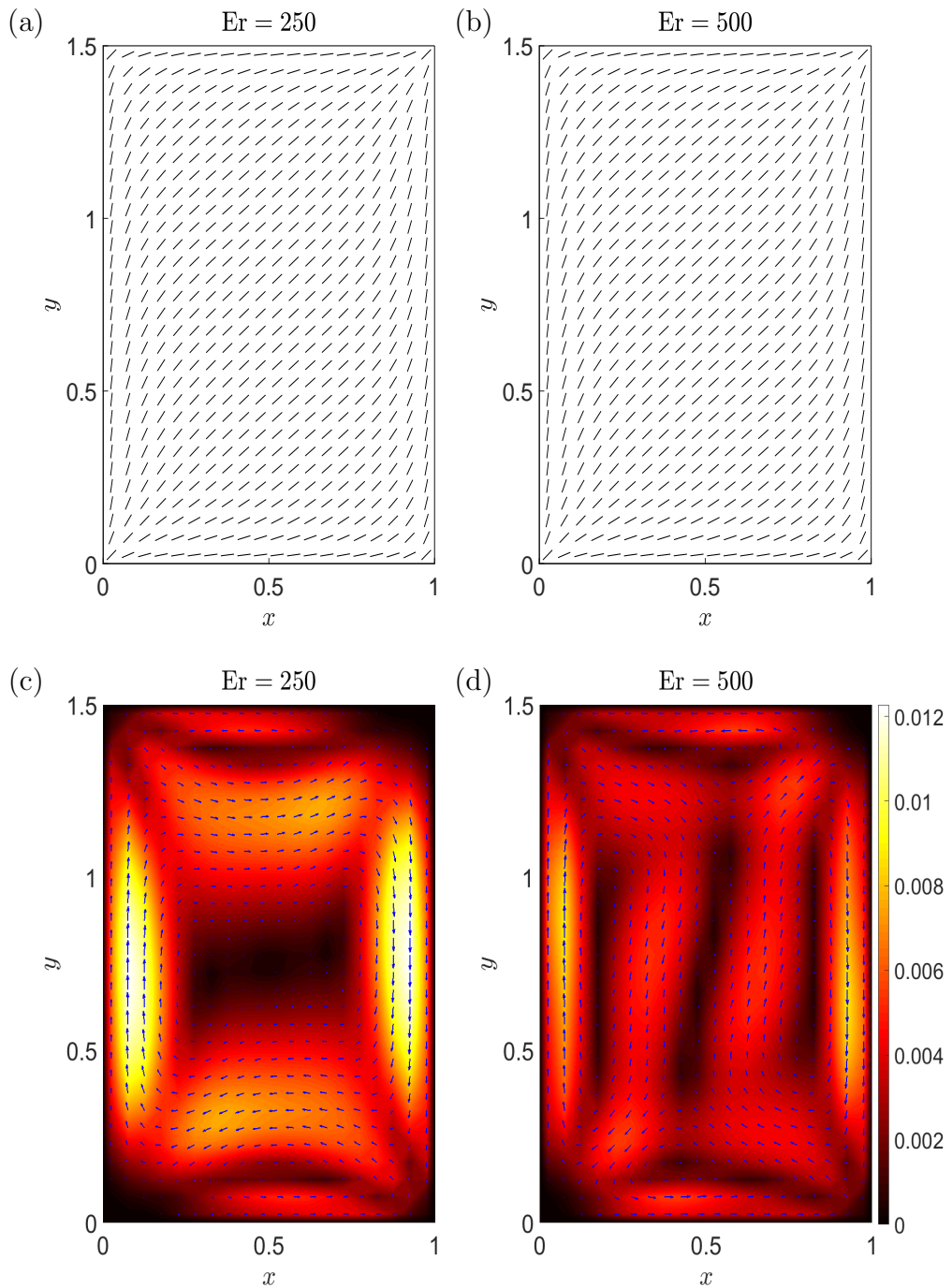


Figure 6.11: (a), (b) Director and (c), (d) flow structures of the D state for a contractile active nematic in a rectangle with aspect ratio $\lambda = 1.5$, elastic constant ratio $k \approx 1.31$, anchoring strength $\tau = 100$ and Ericksen numbers $Er = 250$ and $Er = 500$. The colour bar indicates the magnitude of the velocity throughout the rectangular region.

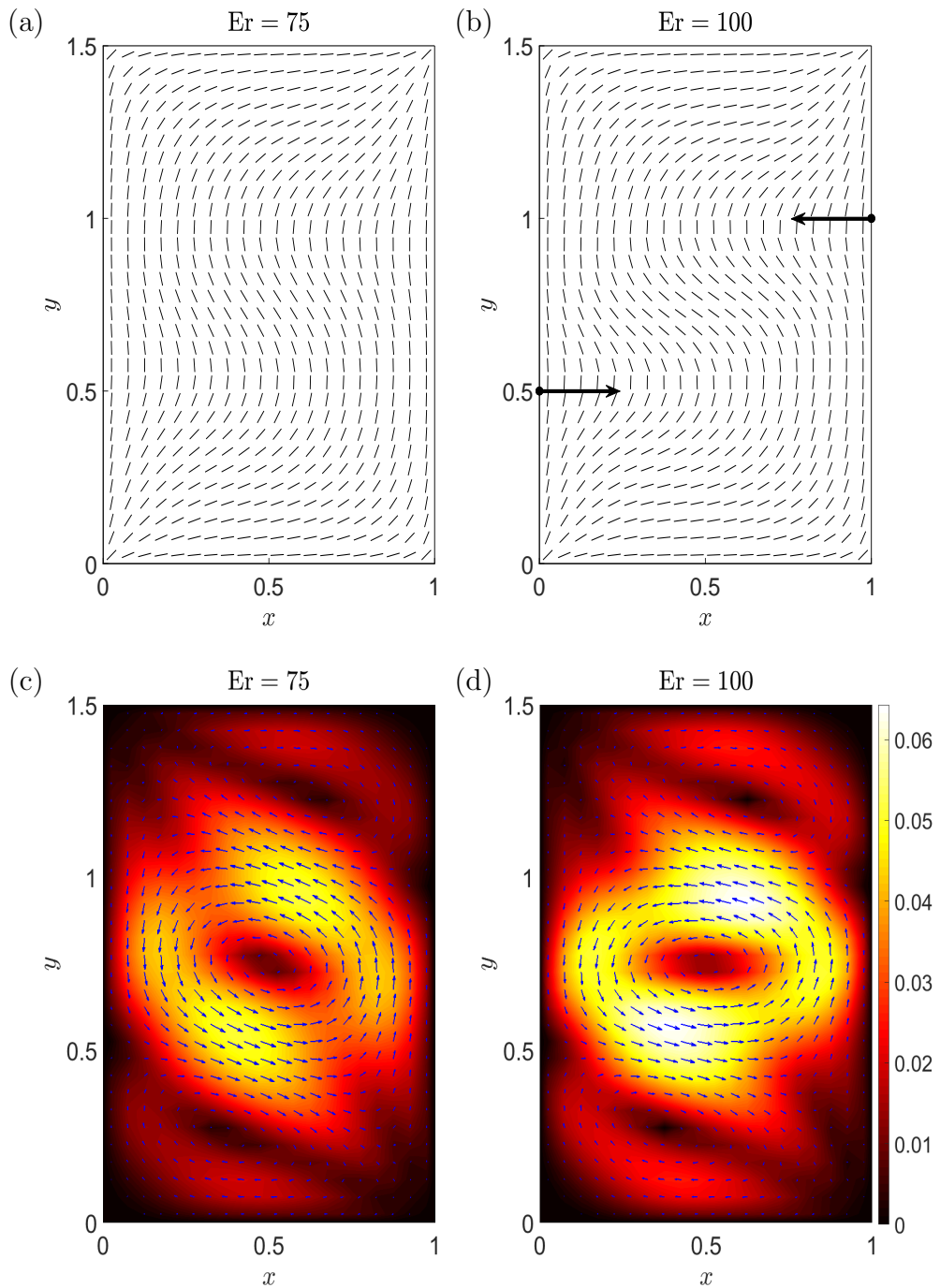


Figure 6.12: (a), (b) Director and (c), (d) flow structures of the D state for an extensile active nematic in a rectangle with aspect ratio $\lambda = 1.5$, elastic constant ratio $k \approx 1.31$, anchoring strength $\tau = 100$ and Ericksen numbers $Er = 75$ and $Er = 100$. The colour bar indicates the magnitude of the velocity throughout the rectangular region.

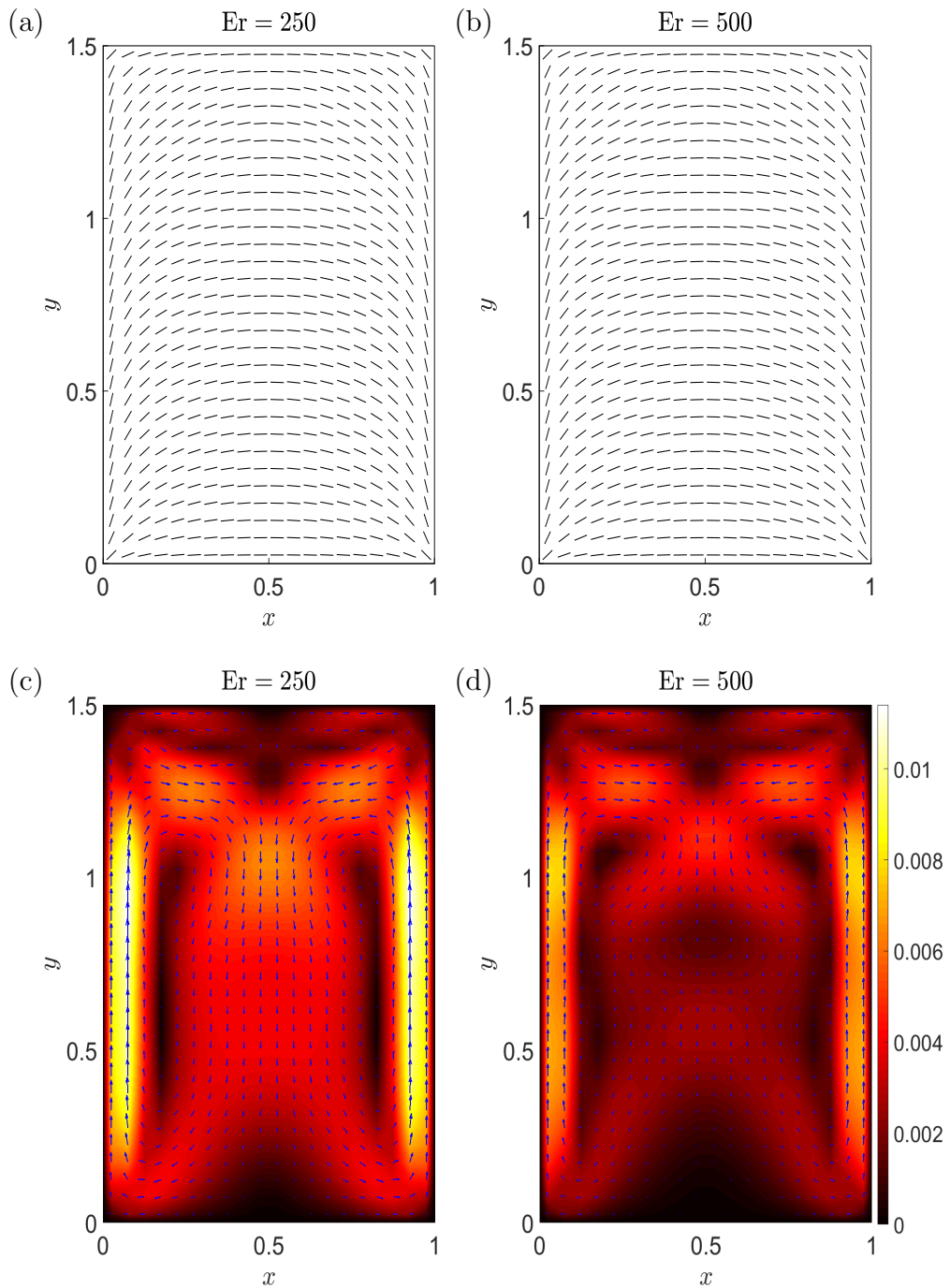


Figure 6.13: (a), (b) Director and (c), (d) flow structures of the U_1 state for a contractile active nematic in a rectangle with aspect ratio $\lambda = 1.5$, elastic constant ratio $k \approx 1.31$, anchoring strength $\tau = 100$ Ericksen numbers $Er = 250$ and $Er = 500$. The colour bar indicates the magnitude of the velocity throughout the rectangular region.

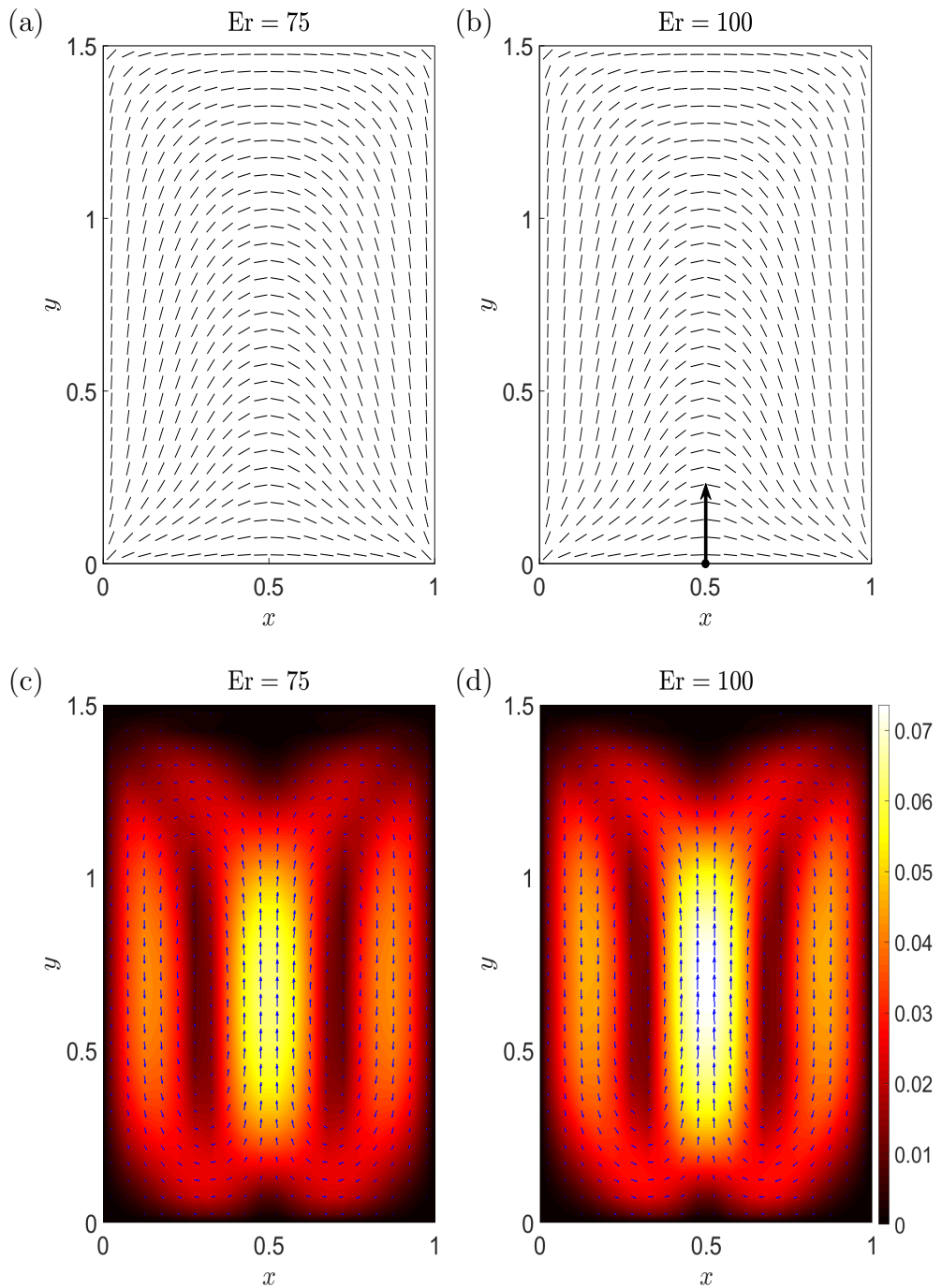


Figure 6.14: (a), (b) Director and (c), (d) flow structures of the U_1 state for an extensile active nematic in a rectangle with aspect ratio $\lambda = 1.5$, elastic constant ratio $k \approx 1.31$, anchoring strength $\tau = 100$ and Ericksen numbers $Er = 75$ and $Er = 100$. The colour bar indicates the magnitude of the velocity throughout the rectangular region.

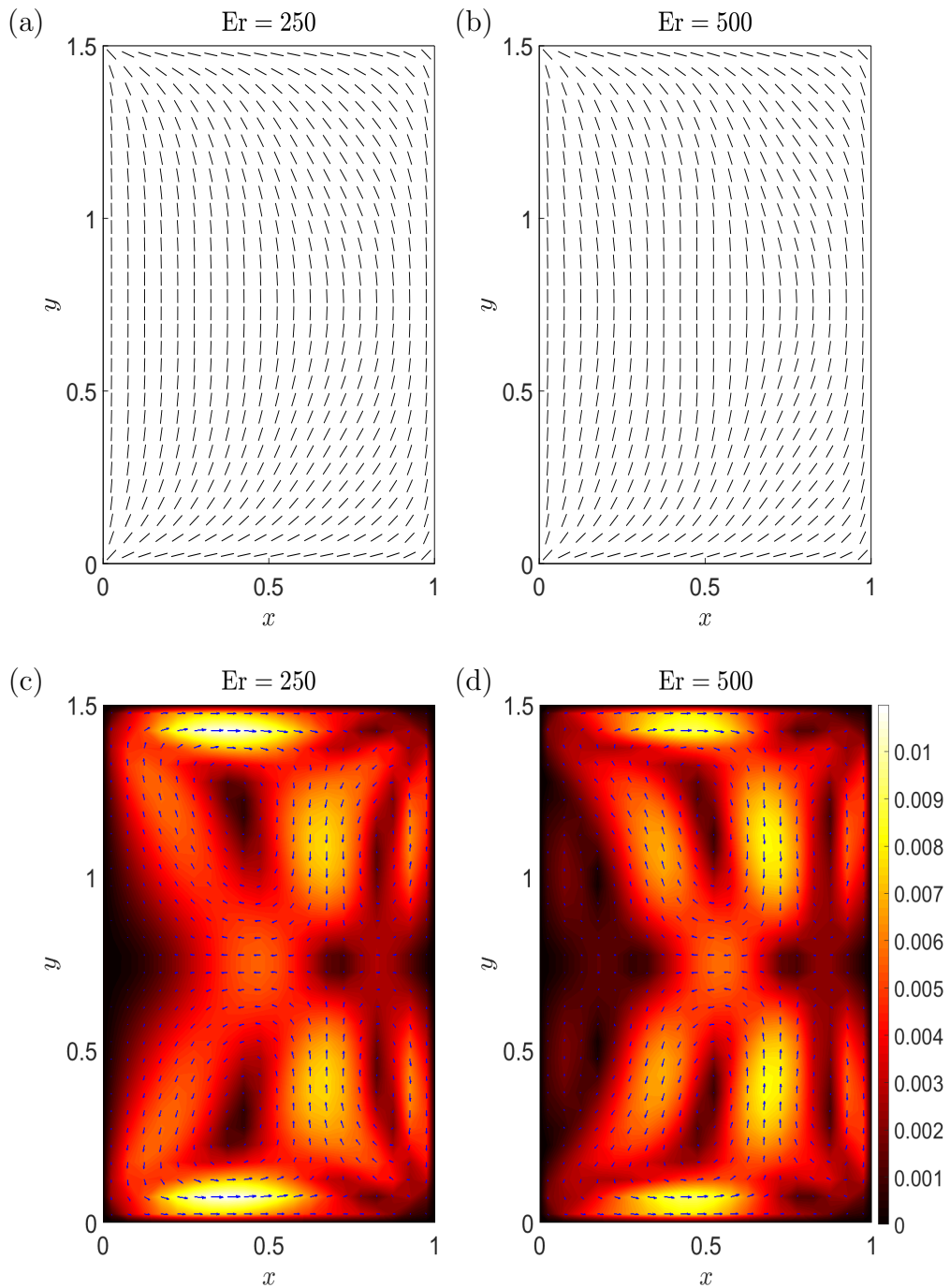


Figure 6.15: (a), (b) Director and (c), (d) flow structures of the U_2 state for a contractile active nematic in a rectangle with aspect ratio $\lambda = 1.5$, elastic constant ratio $k \approx 1.31$, anchoring strength $\tau = 100$ and Ericksen numbers $Er = 250$ and $Er = 500$. The colour bar indicates the magnitude of the velocity throughout the rectangular region.

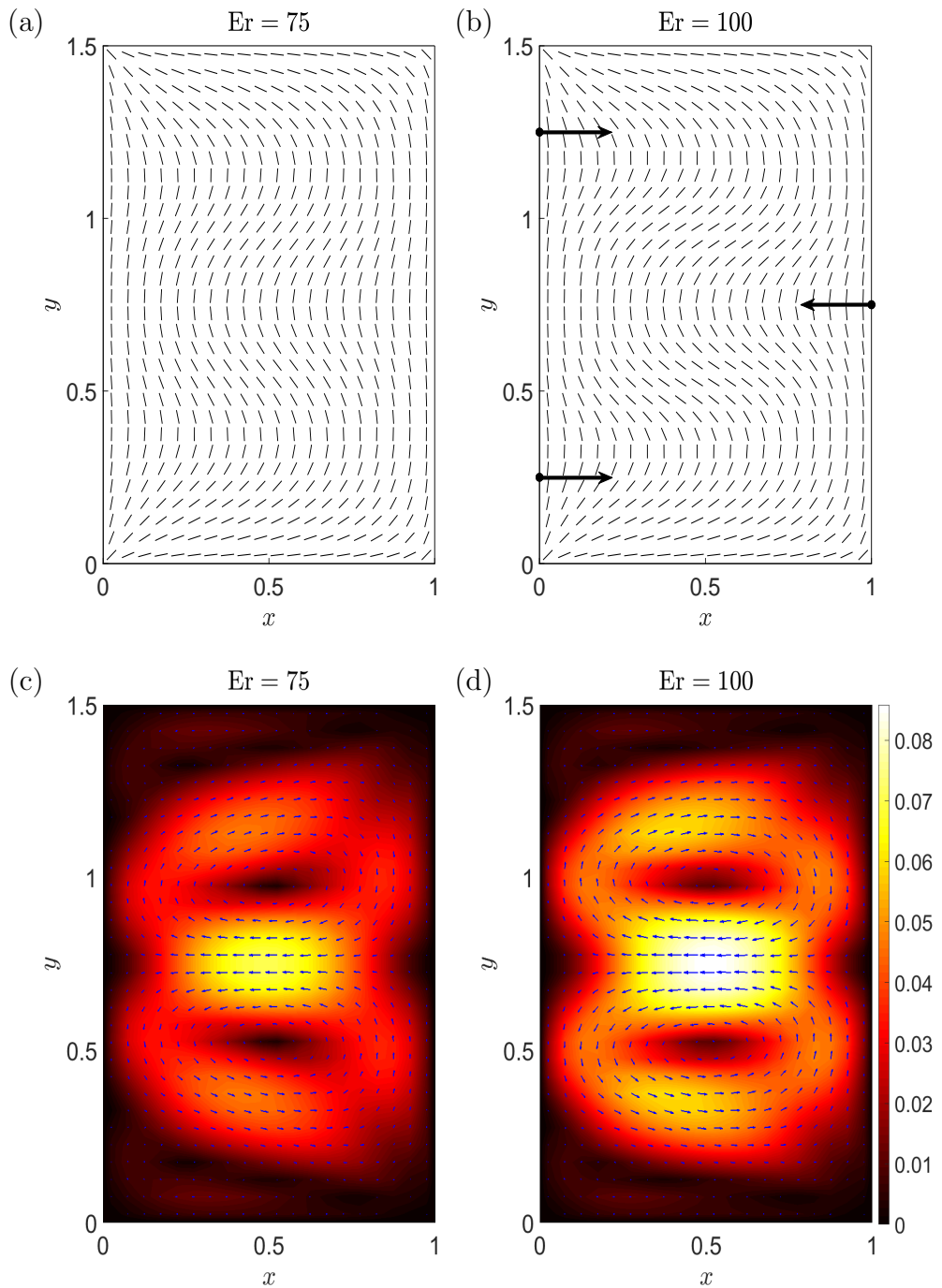


Figure 6.16: (a), (b) Director and (c), (d) flow structures of the U_2 state for an extensile active nematic in a rectangle with aspect ratio $\lambda = 1.5$, elastic constant ratio $k \approx 1.31$, anchoring strength $\tau = 100$ and Ericksen numbers $Er = 75$ and $Er = 100$. The colour bar indicates the magnitude of the velocity throughout the rectangular region.

6.5 Conclusions

In this chapter, we have examined the flow of active fluids confined in two-dimensional geometries using an adapted Ericksen-Leslie theory. First, we considered a simplified adapted Ericksen-Leslie model to solve for the director orientation and flow of a tumbling active nematic fluid in a wedge geometry, close to a singularity in the director structure. By examining the limit of large elasticity, we decoupled the director orientation from the flow. The director angle could then be solved for independently, with the velocity determined subsequently from the director orientation. This meant that extensile and contractile director structures were indistinguishable, with the only difference being that the direction of flow is reversed. By changing the wedge angle of the geometry, we found that different director and flow structures were possible. Our analysis led to two special cases in the velocity solution for defects of strengths $s = 1$ and $s = 2$, where we were able to find analytic solutions for the flow. Our two-dimensional model has therefore demonstrated that tumbling active fluids can exhibit steady director and flow structures, which we also observed in Chapter 4 for a contractile active nematic liquid crystal confined in a shallow one-dimensional channel.

We then re-examined the rectangular region considered in Chapter 3, extending the analysis to introduce a flow-aligning active nematic liquid crystal. We first considered zero Ericksen number, so that the governing equation for the director angle contained no terms due to flow. As was the case for the wedge geometry, our numerical calculations for the rectangular region showed that when the director orientation decoupled from the velocity, extensile and contractile director structures are identical. By increasing the Ericksen number, thereby allowing for the flow to affect the director orientation, we showed that extensile and contractile active nematics have different director and flow structures. In the case of the extensile active nematic, we found increased regions of director distortion as the Ericksen number was increased, which lead to faster spontaneous flow close to the centre of the region. The increased distortion in the director structure for the extensile active nematic led to what seems a wave-like pattern in the director

structure and looks like a defect will be formed from the boundary as the activity magnitude further increases. This is outwith the scope of an Ericksen-Leslie model, but will be an interesting area of future research in which a \mathbf{Q} -tensor model could be used to model the formation of defects. By contrast, increasing the Ericksen number for a contractile active nematics led to a reduction in the maximum speed, with the director adopting a uniform orientation in the bulk of the region. The regions of strongest flow for the contractile active nematic were close to either the horizontal or vertical boundaries of the region.

Chapter 7

Conclusions and Future Work

7.1 Summary of Work Undertaken

This thesis details a series of theoretical investigations into inactive nematic and active nematic liquid crystals confined in different geometries. The research considered here is based on adapted forms of the Ericksen-Leslie and \mathbf{Q} -tensor theories of nematic liquid crystals in which extra terms were included in the governing equations to generate an out-of-equilibrium system. A summary of the key findings in each chapter is provided below.

In Chapter 3, we considered the director configuration of a static inactive nematic liquid crystal confined in a shallow rectangular well subject to weak anchoring on the sides. For relatively weak anchoring, we derived expressions for the critical anchoring strengths at which uniform and distorted director structures exchanged stabilities. In the limit of infinite anchoring, we showed that linearisation of the non-linear system allowed for the derivation of asymptotic approximations for the energy which agreed very well with numerical calculations of the full non-linear model.

In Chapter 4, we used an adapted Ericksen-Leslie model of active nematic liquid crystals to examine the phenomena of spontaneous flow transitions that occur in active nematic liquid crystals confined in a shallow channel. Decoupling of the Ericksen-Leslie equations into a single dynamic equation for the director

angle meant we were able to find asymptotic solutions for the director orientation in the bulk of the channel in the limits of large pressure gradients and activity strengths. By linearising the decoupled dynamic equation for the director angle, we showed that when there is no pressure gradient, the critical activities for an active nematic at which non-trivial director structures exist can be calculated analytically. By solving the steady state equations numerically, we found non-trivial solutions for an extensile active nematic which bifurcate from the trivial state as subcritical pitchforks, but also solution branches which were not connected to the trivial state. When the active nematic was contractile, we found disconnected solution branches. The competition between internally driven flows due to activity and externally driven pressure gradient flows was then examined, which introduced elements of directional bias in the system. Finally, we explored the possibility of manufacturing the various active nematic director structures with an external orienting field applied to the channel and pretilt of the director at the boundaries.

In Chapter 5, we explored the same shallow channel as in Chapter 4 except in terms of \mathbf{Q} -tensor theory. Unlike Chapter 4, we did not consider effects due to pressure gradients or external orienting fields. We first considered a linear stability of the system. This showed very good agreement with the corresponding numerical calculations in predicting the activity at which non-trivial solutions exist. Our numerical calculations showed how increasing the temperature also increases the critical activity strength at which a spontaneous flow transition occurs. The effect of larger temperatures on the director, flow and order parameter structures was also considered.

Finally, Chapter 6 combined the phenomena observed in Chapters 3, 4 and 5 in order to examine active nematic liquid crystals confined in two-dimensional geometries. First, we considered an active fluid confined in a wedge geometry, showing that by simplifying the Ericksen-Leslie equations to a decoupled system of equations. Non-trivial analytic solutions for the director angle and velocity were possible. By changing the angle between the two boundaries, we showed that only certain director and velocity structures are possible for certain wedge

angles. We then returned to the rectangular regions considered in Chapter 3, showing that by putting an active nematic liquid crystal in the rectangle, extensile and contractile active nematics exhibit different director and flow profiles for sufficiently large Ericksen numbers.

7.2 Future Work

We now outline some possible general directions for future research following on from the work presented in this thesis. Throughout this thesis, we have only considered active liquid crystals in which the molecules exhibit nematic symmetry. As we discussed in Chapter 2, active polar liquid crystals allow for the inclusion of additional activity terms in the governing equations which lead to a break in symmetry. It would be interesting to consider the effect of terms unique to polar active liquid crystals individually before building a thorough model of active liquid crystals which combines apolar and polar active terms. We have also not considered the effects that changes in the concentration can have on the system. This is governed by an additional partial differential equation which is coupled to those for the orientation and flow [28, 60, 62, 63]. For such models of active liquid crystals, the free energy and stress tensor include additional terms due to changes in the concentration and lead to a system of partial differential equations which will be more complicated to solve than those considered in this thesis. This is something which can be done for both apolar and polar active liquid crystals. Another effect which has not been considered in this thesis is the occurrence of friction due to the transfer of momentum between active liquid crystals and the surrounding environment. One way in which friction can be accounted for is to add a term of the form $-\gamma\mathbf{v}$ in the flow equations [37, 89, 132], where γ is the friction coefficient.

In Chapter 3, we considered a shallow rectangular well of nematic liquid crystal, subject to a Rapini-Papoular surface energy in which each boundary surface preferred planar director alignment. It is possible for a nematic director to instead prefer a homeotropic alignment at the boundaries, that is, the director

is parallel to the unit outward normal at each boundary. It would, therefore, be worthwhile to investigate the possible non-trivial director structures and to derive asymptotic energies in the limit of strong anchoring. Our weak anchoring director model found an additional director structure composed of two diagonal states, as well as single diagonal and rotated states which have already been observed theoretically from both director and \mathbf{Q} -tensor models of nematic liquid crystals. It would be interesting to examine the behaviour of high elastic energy, rotated director structures both in the limit of weak and infinite anchoring. The application of an external orienting field to the liquid crystal in both limits is also something which could be examined, and how the alignment induced by the field would affect the bifurcation of non-trivial director structures due to surface anchoring. Finally, the director model could readily be made three-dimensional by relaxing the assumption of a two-dimensional director angle independent of the z -coordinate, by which we may hope to describe more complicated director structures. This will inevitably lead to a more complicated system of equations to solve which might only be possible to achieve numerically, thereby removing the possibility of any form of analysis which could be used to derive forms of the director angle solutions and energies.

In Chapter 4, we showed how pretilt and an external orienting field can be used as a technique to manufacture the director structures we found when the only source of flow was the activity. One could investigate the influence of an external orienting field on the orientation of an active nematic liquid crystal to a similar level of detail with which we investigated the role of a pressure gradient. A deeper understanding of effects due to externally applied field on active liquid crystals would then allow for the possibility of combining the effects due to pressure gradients and external orienting fields. This has been done recently, experimentally and theoretically, by Mottram *et al.* [102] for an inactive nematic liquid crystal layer in a rectangular cross-section manometer, which showed that a pressure gradient causes a delay to the classical electric-field-induced Fredericksz transition. All of the results derived in Chapter 4 were in terms of Dirichlet boundary conditions for the director angle and velocity. A mixture of Dirichlet

and Neumann boundary conditions have been considered in previous theoretical studies of active liquid crystals [41, 144], although not in terms of the complete Ericksen-Leslie theory. These boundary conditions could be examined further, with the potential of generating bifurcation diagrams which contain different possible director and velocity structures using the full Ericksen-Leslie theory. This may lead to similar disconnected solution branches to those found in Chapter 4. Finally, the analysis undertaken in Chapters 4 and 5 was based around the trivial state $\theta = 0$. Another constant director structure which leads to zero flow is $\theta = \pi/2$. Therefore, it may be possible to find steady state solutions in which the director exhibits a homeotropic alignment at the boundaries.

In Chapter 6, we first used a simplified Ericksen-Leslie theory to model an active nematic fluid confined in a wedge geometry which contained a defect at the corner. We made various modelling assumptions on the elastic and viscous coefficients in order to simplify the governing equations to a system which could be solved analytically. A comparison between the analytic results with potential numerical solutions of both the simplified and full system of equations would be useful. In order to avoid unphysical energies at the corners of the wedge, a \mathbf{Q} -tensor model would need to be considered. We also examined the full Ericksen-Leslie model for an active nematic confined in the rectangular regions considered in Chapter 3. Our numerical scheme was unable to find solutions when the activity was more prominent. In particular, we found that a defect could form near the boundary of a rectangle containing an extensile active nematic. An alternative \mathbf{Q} -tensor theory approach could allow us to obtain results for larger Ericksen numbers and the possible formation of defects. Finally, the two dimensional geometry considered in Chapter 6 could be extended to three dimensions.

Appendix A

Derivation of the Active Stress Tensor

In Chapter 1, we introduced the active stress tensor (1.2.4) as one possible term which can be used in the theory of active nematic liquid crystals. We made use of this active stress tensor in Chapters 4 and 6, whereas a scalar order parameter version of (1.2.4) was considered in Chapter 5. In this appendix, we outline one possible way of deriving the active stress tensor (1.2.4). The derivation presented here follows the approach considered by Simha and Ramaswamy [123].

We consider an active fluid system consisting of apolar self-propelling particles (SPPs) in which the activity of these particles will drive the system out of equilibrium. In order to derive the stress $\boldsymbol{\sigma}^\zeta$ associated from the dynamics of individual SPPs, we make use of Newton's Third Law, which states that the forces exerted by an SPP on the fluid and by the fluid on an SPP are equal and opposite. First, we consider the force density $\mathbf{f}(\mathbf{r})$ acting on the fluid solvent due to a single force dipole of magnitude F (see Figure A.1). This force density is related to the stress tensor via

$$\mathbf{f}(\mathbf{r}) = -\nabla \cdot \boldsymbol{\sigma}^\zeta. \quad (\text{A.1})$$

and can be written as

$$\mathbf{f}(\mathbf{r}) = F\mathbf{n}_\alpha\delta\left(\mathbf{r} - \mathbf{r}_\alpha - \frac{L}{2}\right) - F\mathbf{n}_\alpha\delta\left(\mathbf{r} - \mathbf{r}_\alpha + \frac{L}{2}\right), \quad (\text{A.2})$$

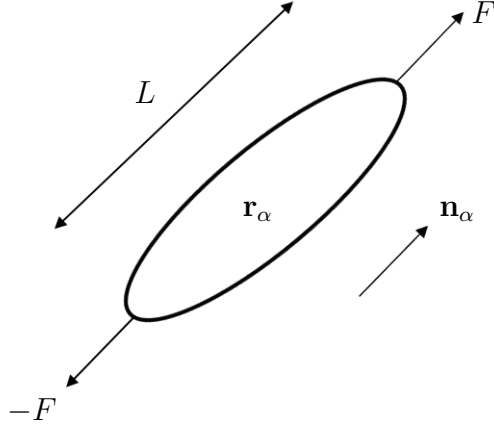


Figure A.1: Geometry of the force dipole considered in the derivation of the active stress tensor.

where \mathbf{r} is the position vector, \mathbf{n}_α is the director orientation, \mathbf{r}_α is the centre of mass and L is the length of the SPP. We have assumed that \mathbf{r}_α is equidistant from the two point forces and that the shape of the SPP is symmetric about the midpoint. For a collection of permanent force dipoles, we can write the force density as

$$\mathbf{f}(\mathbf{r}) = F \sum_{\alpha} \mathbf{n}_{\alpha} \left[\delta \left(\mathbf{r} - \mathbf{r}_{\alpha} - \frac{L}{2} \right) - \delta \left(\mathbf{r} - \mathbf{r}_{\alpha} + \frac{L}{2} \right) \right]. \quad (\text{A.3})$$

To proceed further, we now consider a Taylor series expansion of the delta functions in (A.3) about \mathbf{r}_α , which leads to

$$\delta \left(\mathbf{r} - \mathbf{r}_{\alpha} \pm \frac{L}{2} \right) = \delta(\mathbf{r} - \mathbf{r}_{\alpha}) \pm \frac{L}{2} \nabla \cdot \mathbf{n}_{\alpha} \delta(\mathbf{r} - \mathbf{r}_{\alpha}) + O(L^2 \nabla^2). \quad (\text{A.4})$$

Terms of $O(L\nabla)$ are considered as small in the above Taylor series expansions [136]. Substituting (A.4) into (A.3) leads to a force density which, in component form, can be written at leading order as

$$f_i(\mathbf{r}) \approx -FL \nabla_j \sum_{\alpha} n_{\alpha i} n_{\alpha j} \delta(\mathbf{r} - \mathbf{r}_{\alpha}). \quad (\text{A.5})$$

In equation (A.5), the delta function corresponds to the concentration of the SPPs $C(\mathbf{r})$ [136]. Throughout this thesis, we assume that the concentration of SPPs is constant. Therefore, we can write the force density in component form as

$$f_i = -FLC \nabla_j n_i n_j = -\zeta \nabla_j n_i n_j, \quad (\text{A.6})$$

where $\zeta = FLC$ is an activity parameter proportional to the strength of the force dipoles. This parameter has the dimensions of pressure. Using equation (A.1), we can define the stress due to the activity of the fluid as

$$\sigma_{ij}^{\zeta} = \zeta n_i n_j. \quad (\text{A.7})$$

In vectorised form, equation (A.7) is given by

$$\boldsymbol{\sigma}^{\zeta} = \zeta(\mathbf{n} \otimes \mathbf{n}). \quad (\text{A.8})$$

In Chapters 4 and 6, the activity strength parameter is treated as a constant. By contrast, it is considered as a function of the scalar order parameter in Chapter 5.

Appendix B

Energies Close to the Critical Anchoring Strengths

In Subsection 3.3.2 we derive polynomial approximations of the energies for four non-trivial elastically isotropic nematic equilibria. The approximations are expressed in terms of critical values of the wavenumbers p/q and anchoring strengths τ_c and contain coefficients in terms of the anchoring strength τ .

The polynomial approximations for the energy given by equations (3.3.16) and (3.3.17), restated, are

$$W \approx 2\lambda\tau - \frac{a_2^2(\tau)}{4a_4(\tau)}, \quad (\text{B.1})$$

$$W \approx 2\tau - \frac{b_2^2(\tau)}{4b_4(\tau)}. \quad (\text{B.2})$$

The expressions $a_{2,4}(\tau)$ in (B.1) and $b_{2,4}(\tau)$ in (B.2) are the coefficients of $A_{\theta,1}^2/B_{\theta,1}^2$ and $A_{\theta,1}^4/B_{\theta,1}^4$ (where $\theta = 0, \pi/2$) in the energies (3.3.13) and (3.3.14), respectively and are given by

$$\begin{aligned}
a_2(\tau) = & \left(\sinh(2p) \left(\tau(p^4 - 4p^2\tau_c^2 - \tau_c^4) \cos(2p\lambda) + 4p^3\tau\tau_c \sin(2p\lambda) + 2p^6\lambda \right. \right. \\
& + (4\lambda\tau\tau_c + 4\lambda\tau_c^2 + 3\tau)p^4 + (4\lambda\tau\tau_c^3 + 2\lambda\tau_c^4 + 8\tau\tau_c^2)p^2 + \tau_c^4\tau \left. \right) \\
& + \cosh(2p) \left(-\tau(p^4 + 4p^2\tau_c^2 - \tau_c^4) \sin(2p\lambda) - 2p(-2\tau\tau_c^3 \cos(2p\lambda) \right. \\
& + \lambda(2\tau_c + \tau)p^4 + 2\tau_c(\lambda\tau\tau_c + \lambda\tau_c^2 + 2\tau)p^2 + \tau\tau_c^3(\lambda\tau_c + 2)) \left. \right) \\
& + 4((2\tau_c + \tau)p^4 - 2\tau_c(\tau\tau_c + \tau_c^2 - 2\tau)p^2 + \tau\tau_c^3(\tau_c - 2))p(\cos(p\lambda))^2 \\
& - 4(p^6 + (-2\tau\tau_c - 2\tau_c^2 + 3/2\tau)p^4 + (2\tau\tau_c^3 + \tau_c^4 - 4\tau\tau_c^2)p^2 \\
& + \tau_c^4\tau/2) \sin(p\lambda) \cos(p\lambda) - 6(((-2\lambda/3 + 4/3)\tau_c + \tau(\lambda - 2/3))p^4 \\
& + 2((- \lambda - 2)\tau_c^2 + \tau\tau_c\lambda + 2\tau)\tau_cp^2/3 - \tau(4 + (\lambda - 2)\tau_c)\tau_c^3)p/3 \left. \right) \\
& \times \left(\frac{1}{8p^5} \right), \tag{B.3}
\end{aligned}$$

$$\begin{aligned}
b_2(\tau) = & \left(\sinh(2q\lambda) \left(\tau(q^4 - 4q^2\tau_c^2 - \tau_c^4) \cos(2q) + 4\tau\tau_cq^3 \sin(2q) + 2q^6 \right. \right. \\
& + (4\tau\tau_c + 4\tau_c^2 + 3\tau)q^4 + (4\tau\tau_c^3 + 2\tau_c^4 + 8\tau\tau_c^2)q^2 + \tau_c^4\tau \left. \right) \\
& + \cosh(2q\lambda) \left(-\tau(q^4 + 4q^2\tau_c^2 - \tau_c^4) \sin(2q) - 2(-2\tau\tau_c^3 \cos(2q) \right. \\
& + (2\tau_c + \tau)q^4 + 2\tau_c(\tau\tau_c + \tau_c^2 + 2\tau)q^2 + \tau\tau_c^3(\tau_c + 2))q \left. \right) \\
& + 4(\lambda(2\tau_c + \tau)q^4 - 2\tau_c(\tau\tau_c\lambda + \tau_c^2\lambda - 2\tau)q^2 + \tau\tau_c^3(\lambda\tau_c - 2))q \\
& \times (\cos(q))^2 - 4(q^6\lambda + (-2\tau\tau_c\lambda - 2\tau_c^2\lambda + 3\tau/2)q^4 + (2\lambda\tau\tau_c^3 + \lambda\tau_c^4 \\
& - 4\tau\tau_c^2)q^2 + \tau_c^4\tau/2) \sin(q) \cos(q) + 4(((-2\lambda + 1)\tau_c + \tau(\lambda - 3/2))q^4 \\
& - \tau_c((-2\lambda - 1)\tau_c^2 + \tau\tau_c + 2\tau)q^2 - (-2 + (\lambda - 1/2)\tau_c)\tau_c^3\tau) \left. \right) \\
& \times \left(\frac{1}{8q^5} \right), \tag{B.4}
\end{aligned}$$

$$\begin{aligned}
a_4(\tau) = & \left(16\tau \sinh(2p) \left((5p^5\tau_c - 6p^3\tau_c^3 - 3p\tau_c^5) \sin(2p\lambda) \cos(2p\lambda) + (p^6 - 9p^4\tau_c^2 \right. \right. \\
& - p^2\tau_c^4 + \tau_c^6)(\cos(2p\lambda))^2 + 6p^6\tau_c\lambda + 12p^4\tau_c^3\lambda + 6\lambda p^2\tau_c^5 + (8p^5\tau_c \\
& + 8p^3\tau_c^3) \sin(2p\lambda) + (2p^6 - 6p^4\tau_c^2 - 10p^2\tau_c^4 - 2\tau_c^6) \cos(2p\lambda) + 5p^6 \\
& + 23p^4\tau_c^2 + 11p^2\tau_c^4 + \tau_c^6)(p^2 - \tau_c^2) \left. \right) - 48 \cosh(2p)(p + \tau_c)\tau(p - \tau_c) \\
& \times \left(((-4p^3\tau_c^3 + 4p\tau_c^5/3)(\cos(2p\lambda))^2 + ((p^6/6 + 11p^4\tau_c^2/6 - 7p^2\tau_c^4/2 \right. \\
& + \tau_c^6/6) \sin(2p\lambda) - 8p\tau_c^3(p^2 + \tau_c^2)/3) \cos(2p\lambda) + ((2p^4/3 + 8\tau_c^2p^2/3 \\
& - 2\tau_c^4/3) \sin(2p\lambda) + p(p^4\lambda + (2\tau_c^2\lambda + 16\tau_c/3)p^2 + \tau_c^4\lambda + 4\tau_c^3/3)) \\
& \times (p^2 + \tau_c^2) \left. \right) + 48 \sinh(4p)\tau \left((-2\tau_c^2p^6/3 - 17\tau_c^4p^4/12 + 2\tau_c^6p^2/3 \right. \\
& + (p^8 + \tau_c^8)/24)(\cos(2p\lambda))^2 + (p^3\tau_c(p^4 - 5\tau_c^4) \sin(2p\lambda)/3 + (p^2 \\
& + \tau_c^2)(p^6 - 11p^4\tau_c^2 - 21p^2\tau_c^4 - \tau_c^6)/12) \cos(2p\lambda) + ((5p^5\tau_c/6 + (p\tau_c)^3 \\
& - p\tau_c^5/2) \sin(2p\lambda) + (\tau_c\lambda + 5/24)p^6 + (2\tau_c^3\lambda + 79\tau_c^2/24)p^4 + (\tau_c^5\lambda \\
& + 9\tau_c^4/8)p^2 + \tau_c^6/24)(p^2 + \tau_c^2) \left. \right) - 12 \cosh(4p)\tau \left((-20\tau_c^3p^5/3 \right. \\
& + 4\tau_c^7p/3)(\cos(2p\lambda))^2 + ((p^8/6 + 8\tau_c^2p^6/3 - 17\tau_c^4p^4/3 - 8\tau_c^6p^2/3 \\
& + \tau_c^8/6) \sin(2p\lambda) - 8\tau_c^3p^5 - 32\tau_c^5p^3/3 - 8\tau_c^7p/3) \cos(2p\lambda) + 2/3 \\
& \times (p^2 + \tau_c^2)(p^6 + 9p^4\tau_c^2 - p^2\tau_c^4 - \tau_c^6) \sin(2p\lambda) + p(p^8\lambda + (16\tau_c/3 \\
& + 8\tau_c^2\lambda)p^6 + (14\lambda\tau_c^4 + 20\tau_c^3)p^4 + (32\tau_c^5/3 + 8\tau_c^6\lambda)p^2 + \tau_c^8\lambda \\
& + 4\tau_c^7/3) \left. \right) + \tau \left((-96p^8\tau_c + 96p^6\tau_c^3 + 96p^4\tau_c^5 - 96p^2\tau_c^7 + 88p^8 \right. \\
& - 208p^6\tau_c^2 - 128p^4\tau_c^4 + 144p^2\tau_c^6 - 24\tau_c^8) \sin(2p\lambda) + (-48p^8\tau_c \\
& + 144p^6\tau_c^3 - 144p^4\tau_c^5 + 48p^2\tau_c^7 + 11p^8 - 152p^6\tau_c^2 + 178p^4\tau_c^4 \\
& - 72p^2\tau_c^6 + 3\tau_c^8) \sin(4p\lambda) + (-48p^9 + 96p^7\tau_c^2 - 96p^3\tau_c^6 + 48p\tau_c^8 \\
& - 256p^7\tau_c - 32p^5\tau_c^3 + 128p^3\tau_c^5 - 96p\tau_c^7) \cos(2p\lambda) + (96p^7\tau_c^2 - 12p^9 \\
& - 168p^5\tau_c^4 + 96p^3\tau_c^6 - 12p\tau_c^8 - 64p^7\tau_c + 200p^5\tau_c^3 - 128p^3\tau_c^5 \\
& + 24p\tau_c^7) \cos(4p\lambda) + 132\lambda p^9 + 192\lambda p^7\tau_c^2 + 24\lambda p^5\tau_c^4 + 36\lambda p\tau_c^8 \\
& \left. - 132p^9 + 192p^7\tau_c^2 - 24p^5\tau_c^4 - 36p\tau_c^8 + 24p^5\tau_c^3 + 72p\tau_c^7) \right) \\
& \times \left(-\frac{1}{768p^9} \right), \tag{B.5}
\end{aligned}$$

$$\begin{aligned}
b_4(\tau) = & \left(16\tau \sinh(2q\lambda) \left((5q^5\tau_c - 6q^3\tau_c^3 - 3q\tau_c^5) \sin(2q) \cos(2q) + (q^6 - 9q^4\tau_c^2 \right. \right. \\
& - q^2\tau_c^4 + \tau_c^6) (\cos(2q))^2 + (8q^5\tau_c + 8q^3\tau_c^3) \sin(2q) + (2q^6 - 6q^4\tau_c^2 \\
& - 10q^2\tau_c^4 - 2\tau_c^6) \cos(2q) + 6q^6\tau_c + 12q^4\tau_c^3 + 6q^2\tau_c^5 + 5q^6 + 23q^4\tau_c^2 \\
& \left. \left. + 11q^2\tau_c^4 + \tau_c^6) (q^2 - \tau_c^2) \right) - 48 \cosh(2q\lambda) (q + \tau_c) \tau (q - \tau_c) \left((-4q^3\tau_c^3 \right. \right. \\
& + 4q\tau_c^5/3) (\cos(2q))^2 + ((q^6 + 11q^4\tau_c^2 - 21q^2\tau_c^4 + \tau_c^6) \sin(2q) - 8q\tau_c^3 \\
& \times (q^2 + \tau_c^2)/3) \cos(2q)/6 + (q^2 + \tau_c^2) ((2q^4/3 + 8\tau_c^2q^2/3 - 2\tau_c^4/3) \\
& \times \sin(2q) + (q^4 + (2\tau_c^2 + 16\tau_c/3)q^2 + \tau_c^3(\tau_c + 4/3))q) \left. \right) + 48 \sinh(4q\lambda) \\
& \times \tau \left((q^8/24 + \tau_c^8/24 - 2\tau_c^2q^6/3 - 17\tau_c^4q^4/12 + 2\tau_c^6q^2/3) (\cos(2q))^2 \right. \\
& + (q^3\tau_c(q^4 - 5\tau_c^4) \sin(2q)/3 + (q^2 + \tau_c^2)(q^6 - 11q^4\tau_c^2 - 21q^2\tau_c^4 \\
& - \tau_c^6)/12) \cos(2q) + (q^2 + \tau_c^2) ((5q^5\tau_c/6 + q^3\tau_c^3 - q\tau_c^5/2) \sin(2q) \\
& + (5/24 + \tau_c)q^6 + (2\tau_c^3 + 79\tau_c^2/24)q^4 + \tau_c^4(\tau_c + 9/8)q^2 + \tau_c^6/24) \left. \right) \\
& - 12 \cosh(4q\lambda) \tau \left((-20q^5\tau_c^3/3 + 4q\tau_c^7/3) (\cos(2q))^2 + ((q^8/6 \right. \\
& + 8\tau_c^2q^6/3 - 17\tau_c^4q^4/3 - 8\tau_c^6q^2/3 + \tau_c^8/6) \sin(2q) - 8q^5\tau_c^3 \\
& - 32q^3\tau_c^5/3 - 8q\tau_c^7/3) \cos(2q) + 2(q^2 + \tau_c^2)(q^6 + 9q^4\tau_c^2 - q^2\tau_c^4 \\
& - \tau_c^6) \sin(2q)/3 + (q^8 + (8\tau_c^2 + 16\tau_c/3)q^6 + (14\tau_c^4 + 20\tau_c^3)q^4 + (8\tau_c^6 \\
& + 32\tau_c^5/3)q^2 + \tau_c^7(\tau_c + 4/3))q) \left. \right) + \tau \left((-12\lambda q^9 + 96\lambda q^7\tau_c^2 - 168\lambda q^5\tau_c^4 \right. \\
& + 96\lambda q^3\tau_c^6 - 12\lambda q\tau_c^8 - 64q^7\tau_c + 200q^5\tau_c^3 - 128q^3\tau_c^5 + 24q\tau_c^7) \cos(4q) \\
& + (-48\lambda q^8\tau_c + 144\lambda q^6\tau_c^3 - 144\lambda q^4\tau_c^5 + 48\lambda q^2\tau_c^7 + 11q^8 - 152q^6\tau_c^2 \\
& + 178q^4\tau_c^4 - 72q^2\tau_c^6 + 3\tau_c^8) \sin(4q) + (-48\lambda q^9 + 96\lambda q^7\tau_c^2 - 96\lambda q^5\tau_c^4 \\
& + 48\lambda q\tau_c^8 - 256q^7\tau_c - 32q^5\tau_c^3 + 128q^3\tau_c^5 - 96q\tau_c^7) \cos(2q) + (88q^8 \\
& - 96\lambda q^8\tau_c + 96\lambda q^6\tau_c^3 + 96\lambda q^4\tau_c^5 - 96\lambda q^2\tau_c^7 - 208q^6\tau_c^2 - 128q^4\tau_c^4 \\
& + 144q^2\tau_c^6 - 24\tau_c^8) \sin(2q) - 132\lambda q^9 + 192\lambda q^7\tau_c^2 - 24\lambda q^5\tau_c^4 \\
& - 36\lambda q\tau_c^8 + 132q^9 + 192q^7\tau_c^2 + 24q^5\tau_c^4 + 36q\tau_c^8 + 24q^5\tau_c^3 \\
& \left. \left. + 72q\tau_c^7) \right) \times \left(-\frac{1}{768q^9} \right), \tag{B.6}
\end{aligned}$$

Appendix C

Decoupling of the Ericksen-Leslie Equations

In Subsection 4.3.1 we decouple the Ericksen-Leslie equations using the same approach considered by Mottram *et al.* [104]. The Ericksen-Leslie equations (4.2.15) and (4.2.16), restated, are

$$\gamma_1 \theta_t = (K_1 \cos^2 \theta + K_3 \sin^2 \theta) \theta_{zz} + (K_3 - K_1) \sin \theta \cos \theta (\theta_z)^2 - m(\theta) v_z, \quad (\text{C.1})$$

$$0 = (g(\theta) v_z + m(\theta) \theta_t + \zeta \sin \theta \cos \theta)_z - p_x, \quad (\text{C.2})$$

with boundary conditions for the director angle and velocity

$$\theta(0, t) = \theta(d, t) = 0, \quad (\text{C.3})$$

$$v(0, t) = v(d, t) = 0. \quad (\text{C.4})$$

We decouple the Ericksen-Leslie equations by first integrating (C.2) with respect to z from 0 to z ,

$$0 = g(\theta) v_z + m(\theta) \theta_t + \zeta \cos \theta \sin \theta - z p_x - g(0) v_z(0, t) - m(0) \theta_t(0, t), \quad (\text{C.5})$$

where infinite planar anchoring of the director at $z = 0$ implies that $\theta_t(0, t) = 0$, so (C.5) can be rearranged in terms of the velocity gradient to give

$$v_z = \frac{1}{g(\theta)} \left[g(0) v_z(0, t) - m(\theta) \theta_t - \zeta \sin \theta \cos \theta + z p_x \right]. \quad (\text{C.6})$$

Integrating (C.6) from $z = 0$ to $z = d$ and employing the no-slip boundary conditions leads to the following expression for $v_z(0, t)$:

$$v_z(0, t) = \frac{1}{g(0)} \left[\bar{\mathcal{E}} + \zeta \bar{\mathcal{C}} - p_x \bar{\mathcal{F}} \right], \quad (\text{C.7})$$

where

$$\bar{\mathcal{E}} = \int_0^d \frac{m(\theta)}{g(\theta)} \theta_t \, dz \Big/ \int_0^d \frac{1}{g(\theta)} \, dz, \quad (\text{C.8})$$

$$\bar{\mathcal{C}} = \int_0^d \frac{\sin \theta \cos \theta}{g(\theta)} \, dz \Big/ \int_0^d \frac{1}{g(\theta)} \, dz, \quad (\text{C.9})$$

$$\bar{\mathcal{F}} = \int_0^d \frac{z}{g(\theta)} \, dz \Big/ \int_0^d \frac{1}{g(\theta)} \, dz. \quad (\text{C.10})$$

We substitute (C.7) into (C.6) in order to yield an expression for the velocity gradient in terms of only θ , namely,

$$v_z = \frac{1}{g(\theta)} \left[\bar{\mathcal{E}} - m(\theta) \theta_t - \zeta (\sin \theta \cos \theta - \bar{\mathcal{C}}) + p_x (z - \bar{\mathcal{F}}) \right]. \quad (\text{C.11})$$

Integrating (C.11) from 0 to z and employing the no-slip boundary condition at $z = 0$ generates the flow velocity

$$v(z, t) = \int_0^z \frac{1}{g(\theta)} \left[\bar{\mathcal{E}} - m(\theta) \theta_t - \zeta (\sin \theta \cos \theta - \bar{\mathcal{C}}) + p_x (z - \bar{\mathcal{F}}) \right] \, dz. \quad (\text{C.12})$$

It is clear from (C.12) that the velocity is “slaved” to the director orientation. Substituting (C.11) into (C.1) generates a dynamic equation for the director orientation without any explicit velocity gradients, namely,

$$\left(\gamma_1 - \frac{m^2(\theta)}{g(\theta)} \right) \theta_t = (K_1 \cos^2 \theta + K_3 \sin^2 \theta) \theta_{zz} + (K_3 - K_1) \sin \theta \cos \theta (\theta_z)^2 - \frac{m(\theta)}{g(\theta)} \left[\bar{\mathcal{E}} - \zeta (\sin \theta \cos \theta - \bar{\mathcal{C}}) + p_x (z - \bar{\mathcal{F}}) \right]. \quad (\text{C.13})$$

By rearranging (C.13) and integrating between $z = 0$ and $z = d$, we can obtain an expression for the integral involving θ_t in (C.8),

$$\bar{\mathcal{E}} = \frac{\bar{\mathcal{A}}}{\bar{\mathcal{B}}} + \frac{\zeta \bar{\mathcal{D}}}{\bar{\mathcal{B}}} - \frac{p_x \bar{\mathcal{G}}}{\bar{\mathcal{B}}}, \quad (\text{C.14})$$

where

$$\bar{\mathcal{A}} = \int_0^d \frac{m(\theta)[(K_1 \cos^2 \theta + K_3 \sin^2 \theta)\theta_{zz} + (K_3 - K_1) \sin \theta \cos \theta (\theta_z)^2]}{\gamma_1 g(\theta) - m^2(\theta)} dz, \quad (\text{C.15})$$

$$\bar{\mathcal{B}} = \int_0^d \frac{\gamma_1}{\gamma_1 g(\theta) - m^2(\theta)} dz, \quad (\text{C.16})$$

$$\bar{\mathcal{D}} = \int_0^d \frac{m^2(\theta)(\sin \theta \cos \theta - \bar{\mathcal{C}})}{g(\theta)(\gamma_1 g(\theta) - m^2(\theta))} dz, \quad (\text{C.17})$$

$$\bar{\mathcal{G}} = \int_0^d \frac{m^2(\theta)(z - \bar{\mathcal{F}})}{g(\theta)(\gamma_1 g(\theta) - m^2(\theta))} dz. \quad (\text{C.18})$$

Consequently, the decoupled dynamic equation for the director angle is

$$\begin{aligned} \left(\gamma_1 - \frac{m^2(\theta)}{g(\theta)} \right) \theta_t &= (K_1 \cos^2 \theta + K_3 \sin^2 \theta)\theta_{zz} + (K_3 - K_1) \sin \theta \cos \theta (\theta_z)^2 \\ &\quad - \frac{m(\theta)}{g(\theta)} \left[\frac{\bar{\mathcal{A}}}{\bar{\mathcal{B}}} - \zeta \left(\sin \theta \cos \theta - \bar{\mathcal{C}} - \frac{\bar{\mathcal{D}}}{\bar{\mathcal{B}}} \right) + p_x \left(z - \bar{\mathcal{F}} - \frac{\bar{\mathcal{G}}}{\bar{\mathcal{B}}} \right) \right]. \end{aligned} \quad (\text{C.19})$$

From the definition (C.14), the solution for the flow velocity (C.12) can alternatively be expressed as

$$\begin{aligned} v(z, t) &= \int_0^z \frac{1}{g(\theta)} \left[\frac{\bar{\mathcal{A}}}{\bar{\mathcal{B}}} - m(\theta)\theta_t - \zeta \left(\sin \theta \cos \theta - \bar{\mathcal{C}} - \frac{\bar{\mathcal{D}}}{\bar{\mathcal{B}}} \right) \right. \\ &\quad \left. + p_x \left(z - \bar{\mathcal{F}} - \frac{\bar{\mathcal{G}}}{\bar{\mathcal{B}}} \right) \right] dz. \end{aligned} \quad (\text{C.20})$$

Bibliography

- [1] M. Abramowitz and I.A. Stegun. *Handbook of Mathematical Functions with Formulas, Graphs, and Mathematical Tables, 10th Edition*. (Dover, New York), pp. 258–259, 1972.
- [2] D.M. Anderson and S.H. Davis. Two-fluid viscous flow in a corner. *J. Fluid Mech.*, **257**, pp. 1–31, (1993).
- [3] A. Anzelius. Über die Bewegung der anisotropen Flüssigkeiten. *Uppsala Univ. Arsskr., Mat. och Naturvet*, **1**, pp. 1–84, (1931).
- [4] R. Aris. *Vectors, Tensors and the Basic Equations of Fluid Mechanics*. (Dover, New York), 1989.
- [5] R.J. Atkin. Poiseuille flow of liquid crystals of the nematic type. *Arch. Rat. Mech. Anal.*, **38**, pp. 224–240, (1970).
- [6] J.M. Ball. Mathematics and Liquid Crystals. *Mol. Cryst. Liq. Cryst.*, **647**, pp. 1–27, (2017).
- [7] D. Banerjee, A. Souslov, A.G. Abanov, and V. Vitelli. Odd viscosity in chiral active fluids. *Nat. Commun.*, **8**, art. no. 1573, (2017).
- [8] R. Barberi, J.J. Bonvent, M. Giocondo, M. Iovane, and A.L. Alexe-Ionescu. Bistable nematic azimuthal alignment induced by anchoring competition. *J. Appl. Phys.*, **84**, pp. 1321–1324, (1998).
- [9] D. Bárdfalvy, H. Nordanger, C. Nardini, A. Morozov, and J. Stenhammar. Particle-resolved lattice Boltzmann simulations of 3-dimensional active turbulence. *Soft Matter*, **15**, pp. 7747–7756, (2019).

- [10] C.M. Bender and S.A. Orszag. *Advanced Mathematical Methods for Scientists and Engineers I: Asymptotic Methods and Perturbation Theory*. (Springer-Verlag, New York), 1999.
- [11] A.N. Beris and B.J. Edwards. *Thermodynamics of Flowing Systems: with Internal Microstructure*. (Oxford University Press, U.K.), 1994.
- [12] F. Bonelli, G. Gonnella, A. Tiribocchi, and D. Marenduzzo. Spontaneous flow in polar active fluids: the effect of a phenomenological self propulsion-like term. *Eur. Phys. J. E*, **39**, art. no. 1, (2016).
- [13] H.R. Brand, H. Pleiner, and D. Sventšek. Dissipative versus reversible contributions to macroscopic dynamics: the role of time-reversal symmetry and entropy production. *Rheol. Acta*, **57**, pp. 773–791, (2018).
- [14] H.R. Brand, H. Pleiner, and D. Sventšek. Reversible and dissipative macroscopic contributions to the stress tensor: Active or passive?. *Eur. Phys. J. E*, **37**, art. no. 83, (2014).
- [15] P.S. Bruckman. On the evaluation of certain infinite series by elliptic functions. *Fibonacci Quart.*, **15**, pp. 293–310, (1977).
- [16] A. Buka and L. Kramer. *Pattern Formation of Liquid Crystals*. (Springer Verlag, New York), 1996.
- [17] G. Canevari, A. Majumdar, and A. Spicer. Order reconstruction for nematics on squares and hexagons: a Landau-de Gennes study. *SIAM J. Appl. Math.*, **77**, pp. 267–293, (2017).
- [18] M.E. Cates, O. Henrich, D. Marenduzzo, and K. Stratford. Lattice Boltzmann simulations of liquid crystalline fluids: active gels and blue phases. *Soft Matter*. **5**, pp. 3791–3800, (2009).
- [19] S. Chandragiri, A. Doostmohammadi, J.M. Yeomans, and S.P. Thampi. Active transport in a channel: stabilisation by flow or thermodynamics. *Soft Matter*, **15**, pp. 1597–1604, (2019).

- [20] S. Chandrasekhar. *Liquid Crystals, 2nd Edition*. (Cambridge University Press, Cambridge), 1992.
- [21] J.Z.Y. Chen. Structure of two-dimensional rods confined by a line boundary. *Soft Matter*, **9**, pp. 10921–10930, (2013).
- [22] L. Chen, C.F. Lee, and J. Toner. Squeezed in three dimensions, moving in two: Hydrodynamic theory of three-dimensional incompressible easy-plane polar active fluids. *Phys. Rev. E*, **98**, art. no. 040602, (2018).
- [23] M.G. Clark. Algebraic derivation of the free-energy of a distorted nematic liquid crystal. *Molecular Physics*, **31**, pp. 1287–1289, (1976).
- [24] R.C.V. Coelho, N.A.M. Araújo, and M.M. Telo da Gama. Active nematic–isotropic interfaces in channels. *Soft Matter*, **15**, pp. 6819–6829, (2019).
- [25] P.J. Collings and M. Hird. *Introduction to Liquid Crystals: Chemistry and Physics*. (Taylor and Francis, London), 1997.
- [26] COMSOL Multiphysics Version 5.3a. COMSOL, Inc., Burlington MA, USA, <http://www.comsol.com>, 2018.
- [27] C. Conklin, J. Viñals, and O.T. Valls. A connection between living liquid crystals and electrokinetic phenomena in nematic fluids. *Soft Matter*, **14**, pp. 4641–4648, (2018).
- [28] D. Cortese, J. Eggers, and T.B. Liverpool. Nonlinear spontaneous symmetry breaking in active polar films. *EPL (Europhysics Letters)*, **115**, art. no. 28002, (2016).
- [29] D. Cortese, J. Eggers, and T.B. Liverpool. Pair creation, motion, and annihilation of topological defects in two-dimensional nematic liquid crystals. *Phys. Rev. E*, **97**, art. no. 022704, (2018).

- [30] F.P. Da Costa, M. Grinfeld, M. Langer, N.J. Mottram, and J.T. Pinto. Kickback in nematic liquid crystals. *Quart. Appl. Math.*, **70**, pp. 99–110, (2012).
- [31] M. Crespo, A. Majumdar, A.M. Ramos, and I.M. Griffiths. Solution landscapes in nematic microfluidics. *Physica D: Nonlinear Phenomena*, **351**, pp. 1–13, (2017).
- [32] P.K. Currie. Approximate solutions for Poiseuille flow of liquid crystals. *Rheol. Acta*, **14**, pp. 688–692, (1975).
- [33] O.J. Dammone, I. Zacharoudiou, R.P.A. Dullens, J.M. Yeomans, M.P. Lettinga, and D.G.A.L. Aarts. Confinement induced splay-to-bend transition of colloidal rods. *Phys. Rev. Lett.*, **109**, art. no. 108303, (2012).
- [34] A.J. Davidson and N.J. Mottram. Conformal mapping techniques for the modelling of liquid crystal devices. *Eur. J. Appl. Math.*, **23**, pp. 99–119, (2012).
- [35] A. Dhooge, W. Govaerts, and Yu. A. Kuznetsov. MATCONT: a MATLAB package for numerical bifurcation analysis of ODEs. *ACM Transactions on Mathematical Software*, **29**, pp. 141–164, (2003).
- [36] A. Doostmohammadi, M.F. Adamer, S.P. Thampi, and J.M. Yeomans. Stabilization of active matter by flow-vortex lattices and defect ordering. *Nat. Commun.*, **7**, art. no. 10557, (2016).
- [37] A. Doostmohammadi, J. Ignés-Mullol, J.M. Yeomans, and F. Sagués. Active nematics. *Nat. Commun.*, **9**, art. no. 3246, (2018).
- [38] A. Doostmohammadi, T.N. Shendruk, K. Thijssen, and J.M. Yeomans. Onset of meso-scale turbulence in active nematics. *Nat. Commun.*, **8**, art. no. 15326, (2017).
- [39] A. Doostmohammadi and J.M. Yeomans. Coherent motion of dense active matter. *Eur. Phys. J. Spec. Top.*, **227**, pp. 2401–2411, (2019).

- [40] D.A. Dunmur, A. Fukuda, and G.R. Luckhurst (Eds.). *Physical Properties of Liquid Crystals: Nematics*. (EMIS Data Review Series No. 25, The Institution of Electrical Engineers (INSPEC), London), 2001.
- [41] S.A. Edwards and J.M. Yeomans. Spontaneous flow states in active nematics: a unified picture. *EPL (Europhysics Letters)*, **85**, art. no. 18008, (2009).
- [42] J. Elgeti, M.E. Cates, and D. Marenduzzo. Defect hydrodynamics in 2D polar active fluids. *Soft Matter*. **7**, pp. 3177–3185, (2011).
- [43] J.L. Ericksen. Anisotropic fluids. *Arch. Rat. Mech. Anal.*, **4**, pp. 231–237, (1960).
- [44] J.L. Ericksen. Conservation laws for liquid crystals. *Trans. Soc. Rheol.*, **5**, pp. 23–34, (1961).
- [45] J.L. Ericksen. Hydrostatic theory of liquid crystals. *Arch. Rat. Mech. Anal.*, **9**, pp. 371–378, (1962).
- [46] J.L. Ericksen. Inequalities in liquid crystal theory. *The Physics of Fluids*, **9**, pp. 1205–1207, (1966).
- [47] J.L. Ericksen. On equations of motion for liquid crystals. *Q. J. Mech. Appl. Math.*, **29**, pp. 203–208, (1976).
- [48] J.L. Ericksen. Liquid crystals with variable degree of orientation. *Arch. Rat. Mech. Anal.*, **113**, pp. 97–120, (1991).
- [49] B. Ezhilan and D. Saintillan. Transport of a dilute active suspension in pressure-driven channel flow. *J. Fluid Mech.*, **777**, pp. 482–522, (2015).
- [50] C. Ferreiro-Córdova, J. Toner, H. Löwen, and H.H. Wensink. Long-time anomalous swimmer diffusion in smectic liquid crystals. *Phys. Rev. E*, **97**, art. no. 062606, (2018).
- [51] F.C. Frank. On the theory of liquid crystals. *Discuss. Faraday Soc.*, **25**, pp. 19–28, (1958).

- [52] V. Freedericksz and V. Zolina. Forces causing the orientation of an anisotropic liquid. *Trans. Faraday Soc.*, **29**, pp. 919–930, (1933).
- [53] G. Friedel. Les états mésomorphes de la matière. *Ann. Phys. (Paris)*, **18**, pp. 273–474, (1922).
- [54] B.J. Frisken and P. Palffy-Muhoray. Freedericksz transitions in nematic liquid crystals: The effect of an in-plane electric field. *Phys. Rev. A*, **40**, pp. 6099–6102, (1989).
- [55] I.C. Gârlea and B.M. Mulder. Defect structures mediate the isotropic-nematic transition in strongly confined liquid crystals. *Soft Matter*, **11**, pp. 608–614, (2015).
- [56] P.G. de Gennes and J. Prost. *The Physics of Liquid Crystals, 2nd Edition*. (Clarendon Press, Oxford), 1993.
- [57] L. Giomi. Geometry and topology of turbulence in active nematics. *Phys. Rev. X*, **5**, art. no. 031003, (2015).
- [58] L. Giomi, M.J. Bowick, X. Ma, and M.C. Marchetti. Defect annihilation and proliferation in active nematics. *Phys. Rev. Lett.*, **110**, art. no. 228101, (2013).
- [59] L. Giomi, M.J. Bowick, P. Mishra, R. Sknepnek, and M.C. Marchetti. Defect dynamics in active nematics. *Phil. Trans. R. Soc. A*, **372**, art. ID. 20130365, (2014).
- [60] L. Giomi, T.B. Liverpool, and M.C. Marchetti. Sheared active fluids: thickening, thinning and vanishing viscosity. *Phys. Rev. E*, **81**, art. no. 051908, (2010).
- [61] L. Giomi, L. Mahadevan, B. Chakraborty, and M.F. Hagan. Excitable patterns in active nematics. *Phys. Rev. Lett.*, **106**, art. no. 218101, (2011).
- [62] L. Giomi and M.C. Marchetti. Polar patterns in active fluids. *Soft Matter*, **8**, pp. 129–139, (2012).

- [63] L. Giomi, M.C. Marchetti, and T.B. Liverpool. Complex spontaneous flows and concentration banding in active polar films. *Phys. Rev. Lett.*, **101**, art. no. 198101, (2008).
- [64] P. Guillamat, J. Ignés-Mullol, and F. Sagués. Control of active liquid crystals with a magnetic field. *Proc. Natl. Acad. Sci. U.S.A.*, **113**, pp. 5498–5502, (2016).
- [65] P. Guillamat, J. Ignés-Mullol, and F. Sagués. Control of active nematics with passive liquid crystals. *Mol. Cryst. Liq. Cryst.*, **646**, pp. 226–234, (2017).
- [66] Y. Hatwalne, S. Ramaswamy, M. Rao, and R.A. Simha. Rheology of active-particle suspensions, *Phys. Rev. Lett.*, **92**, art. no. 118101, (2004).
- [67] B.L. Van Horn and H.H. Winter. Dynamics of shear aligning of nematic liquid crystal monodomains. *Rheol. Acta*, **39**, pp. 294–300, (2000).
- [68] J.T. Jenkins and P.J. Barratt. Interfacial effects in the static theory of nematic liquid crystals. *Q. J. Mech. Appl. Math.*, **27**, pp. 111–127, (1974).
- [69] P.J. Kedney and F.M. Leslie. Switching in a simple bistable nematic cell. *Liq. Cryst.*, **24**, pp. 613–618, (1998).
- [70] H. Kelker. History of Liquid Crystals. *Mol. Cryst. Liq. Cryst.*, **21**, pp. 1–48, (1973).
- [71] T.R. Kirkpatrick and J.K. Bhattacharjee. Driven active matter: Fluctuations and a hydrodynamic instability. *Phys. Rev. Fluids*, **4**, art. no. 024306, (2019).
- [72] G. Kitavtsev, A. Münch, and B. Wagner. Thin-film models for an active gel. *Proc. R. Soc. A*, **474**, art. ID. 20170828, (2018).
- [73] M. Kléman. Defects in liquid crystals. *Rep. Prog. Phys.*, **52**, pp. 555–654, (1989).

- [74] S. Kralj and A. Majumdar. Order reconstruction patterns in nematic liquid crystal wells. *Proc. R. Soc. A*, **470**, art. ID. 20140276, (2014).
- [75] K. Kruse, J.F. Joanny, F. Jülicher, J. Prost, and K. Sekimoto. Asters, vortices, and rotating spirals in active gels of polar filaments. *Phys. Rev. Lett.*, **92**, art. no. 078101, (2004).
- [76] K. Kruse, J.F. Joanny, F. Jülicher, J. Prost, and K. Sekimoto. Generic theory of active polar gels: a paradigm for cytoskeletal dynamics. *Eur. Phys. J. E*, **16**, pp. 5–16, (2005).
- [77] H. Kusumaatmaja and A. Majumdar. Free energy pathways of a multistable liquid crystal device. *Soft Matter*, **11**, pp. 4809–4817, (2015).
- [78] O.D. Lavrentovich. Active colloids in liquid crystals. *Curr. Opin. Colloid Interface Sci.*, **21**, pp. 97–109, (2016).
- [79] O. Lehmann. Über fließende Krystalle. *Zeitschrift für Physikalische Chemie*, **4**, pp. 462–472, (1889).
- [80] F.M. Leslie. Some constitutive equations for anisotropic fluids. *Q. J. Mech. Appl. Math.*, **19**, pp. 357–370, (1966).
- [81] F.M. Leslie. Some constitutive equations for liquid crystals. *Arch. Rat. Mech. Anal.*, **28**, pp. 265–283, (1968).
- [82] F.M. Leslie. Continuum theory for nematic liquid crystals. *Continuum Mech. Thermodyn.*, **4**, pp. 167–175, (1992).
- [83] F.M. Leslie. *Liquid Crystal Devices*. Institut Wiskundige Dienstverlening, Technische Universiteit Eindhoven, 1992.
- [84] F.M. Leslie, J.S. Laverly, and T. Carlsson. Continuum theory for biaxial nematic liquid crystals, *Q. J. Mech. Appl. Math.*, **45**, pp. 595–606, (1992).
- [85] A.H. Lewis. D.Phil. Thesis, University of Oxford (2015).

- [86] A.H. Lewis, I. Garlea, J. Alvarado, O.J. Dammone, P.D. Howell, A. Majumdar, B.M. Mulder, M.P. Lettinga, G.H. Koenderink, and D.G.A.L. Aarts. Colloidal liquid crystals in rectangular confinement: theory and experiment. *Soft Matter*, **10**, pp. 7865–7873, (2014).
- [87] C. Luo, A. Majumdar, and R. Erben. Multistability in planar liquid crystal wells. *Phys. Rev. E*, **85**, art. no. 061702, (2012).
- [88] A. Maitra and M. Lenz. Spontaneous rotation can stabilise ordered chiral active fluids. *Nat. Commun.*, **10**, art. no. 920, (2019).
- [89] A. Maitra, P. Srivastava, M.C. Marchetti, J.S. Lintuvuori, S. Ramaswamy, and M. Lenz. A nonequilibrium force can stabilize 2D active nematics. *Proc. Natl. Acad. Sci. U.S.A.*, **115**, pp. 6934–6939, (2018).
- [90] A. Majumdar. Equilibrium order parameters of nematic liquid crystals in the Landau de-Gennes theory. *Eur. J. of Appl. Math.*, **21**, pp. 181–203, (2010).
- [91] A. Majumdar, M.C. Marchetti, and E.G. Virga. Perspectives in active liquid crystals. *Philos. Trans. R. Soc. A*, **372**, art. ID. 201330373, (2014).
- [92] M.C. Marchetti, J.F. Joanny, S. Ramaswamy, T.B. Liverpool, J. Prost, M. Rao, and R.A. Simha. Hydrodynamics of soft active matter. *Rev. Mod. Phys.*, **85**, pp. 1143–1189, (2013).
- [93] D. Marenduzzo, E. Orlandini, M.E. Cates, and J.M. Yeomans. Steady-state hydrodynamic instabilities of active liquid crystals: Hybrid lattice Boltzmann simulations. *Phys. Rev. E*, **76**, art. no. 031921, (2007).
- [94] MATLAB. Version 9.4 (R2018a), The MathWorks Inc, Natick, Massachusetts, 2018.
- [95] L. Metselaar, A. Doostmohammadi, and J.M. Yeomans. Topological states in chiral active matter: Dynamic blue phases and active half-skyrmions. *J. Chem. Phys.*, **150**, art. no. 064909, (2019).

- [96] M. Miesowicz. Der Einfluß des magnetischen Feldes auf die Viskosität der Flüssigkeiten in der nematischen Phase. *Bull. Acad. Pol. A (Poland)*, pp. 228–247, (1936).
- [97] M. Miesowicz. The three coefficients of viscosity of anisotropic liquids. *Nature*, **158**, pp. 27, (1946).
- [98] P. Mishra. D.Phil. Thesis, University of Syracuse (2017).
- [99] H.K. Moffatt. Viscous and resistive eddies near a sharp corner. *J. Fluid Mech.*, **18**, pp. 1–18, (1964).
- [100] S. Mondal, A. Majumdar, and I.M. Griffiths. Nematohydrodynamics for colloidal self-assembly and transport phenomena. *J. Colloid Interface Sci.* **528**, pp. 431–442, (2018).
- [101] J.K. Moscicki. Measurements of viscosities in nematics. Section 8.2 in Reference [40].
- [102] N.J. Mottram, G. McKay, C.V. Brown, C.T. Russell, I.C. Sage, and C. Tsakonas. Flow-induced delayed Freedericksz transition. *Phys. Rev. E*, **93**, art. no. 030701, (2016).
- [103] N.J. Mottram and C.J.P. Newton. Introduction to Q-tensor theory. University of Strathclyde, Department of Mathematics and Statistics, Research Report 10, (2004).
- [104] N.J. Mottram, J.T. Pinto, and G. McKay. Decoupling of the Ericksen–Leslie equations. *Liq. Cryst.*, **40**, pp. 787–798, (2013).
- [105] D. Mucci and L. Nicolodi. On the elastic energy density of constrained Q-tensor models for biaxial nematics. *Arch. Rat. Mech. Anal.*, **206**, pp. 853–884, (2012).
- [106] A.H. Nayfeh. *Introduction to Perturbation Techniques*. (John Wiley & Sons, New York), 1981.

- [107] K. Okano, K. Kitahara, and E. Ushizawa. Surface disclinations on modified substrate. *Jpn. J. Appl. Phys.*, **33**, pp. 6262–6267, (1994).
- [108] C.W. Oseen. The theory of liquid crystals. *Trans. Faraday Soc.*, **29**, pp. 883–899, (1933).
- [109] P. Oswald and P. Pieranski. *Nematic and Cholesteric Liquid Crystals: Concepts and Physical Properties Illustrated by Experiments*. (Taylor and Francis, London and New York), 2005.
- [110] O. Parodi. Stress tensor for a nematic liquid crystal. *J. Phys. (Paris)*, **31**, pp. 581–584, (1970).
- [111] C. Peng, T. Turiv, Y. Guo, Q.-H. Wei, and O.D. Lavrentovich. Command of active matter by topological defects and patterns. *Science*, **354**, pp. 882–885, (2016).
- [112] P. Pieranski, F. Brochard, and E. Guyon. Static and dynamic behavior of a nematic liquid crystal in a magnetic field. Part II: dynamics. *J. Phys. (Paris)*, **34**, pp. 35–48, (1973).
- [113] H. Pleiner, D. Sventšek, and H.R. Brand. Active polar two-fluid macroscopic dynamics. *Eur. Phys. J. E*, **36**, art. no. 135, (2013).
- [114] H. Pleiner, D. Sventšek, and H.R. Brand. Hydrodynamics of active polar systems in a (visco)elastic background. *Rheol. Acta*, **55**, pp. 857–870, (2016).
- [115] E. Putzig, G.S. Redner, A. Baskaran, and A. Baskaran. Instabilities, defects, and defect ordering in an overdamped active nematic. *Soft Matter*, **12**, pp. 3854–3859, (2016).
- [116] A. Rapini and M. Papoular. Distortion d’une lamelle nématique sous champ magnétique. Conditions d’ancrage aux parois. *J. Phys. Colloq.*, **C 30**, pp. 54–56, (1969).

- [117] F. Reinitzer. Beiträge zur Kenntnis des Cholesterins. *Monatsh. Chem.*, **9**, pp. 421–441, (1888).
- [118] F. Reinitzer. Contributions to the knowledge of cholesterol. *Liq. Cryst.*, **5**, pp. 7–18, (1989). English translation of [117].
- [119] P. Romanczuk, H. Chaté, L. Chen, S. Ngo, and J. Toner. Emergent smectic order in simple active particle models. *New J. Phys.*, **18**, art. no. 063015, (2016).
- [120] T. Sanchez, D.T.N. Chen, S.J. DeCamp, M. Heymann, and Z. Dogic. Spontaneous motion in hierarchically assembled active matter. *Nature*, **491**, pp. 431–434, (2012).
- [121] R. Schaaf. *Global Solution Branches of Two-Point Boundary Value Problems*. (Springer-Verlag, Berlin), 1990.
- [122] T.N. Shendruk, K. Thijssen, J.M. Yeomans, and A. Doostmohammadi. Twist-induced crossover from two-dimensional to three-dimensional turbulence in active nematics. *Phys. Rev. E*, **98**, art. no. 010601, (2018).
- [123] R.A. Simha and S. Ramaswamy. Hydrodynamic fluctuations and instabilities in ordered suspensions of self-propelled particles. *Phys. Rev. Lett.*, **89**, art. no. 058101, (2002).
- [124] M. Slavinec, E. Klemenčič, M. Ambrožič, and M. Krašna. Impact of nanoparticles on nematic ordering in square wells. *Adv. Cond. Matter Phys.*, **2015**, art. ID. 532745, (2015).
- [125] T.J. Sluckin, D.A. Dunmur, and H. Stegemeyer. *Crystals That Flow: Collected Papers from the History of Liquid Crystals*. (Taylor and Francis, London), 2004.
- [126] A.M. Sonnet, P.L Maffettone, and E.G. Virga. Continuum theory for nematic liquid crystals with tensorial order. *J. Non-Newtonian Fluid Mech.*, **119**, pp. 51–59, (2004).

- [127] A.M. Sonnet and E.G. Virga. Dynamics of dissipative ordered fluids. *Phys. Rev. E*, **64**, art. no. 031705, (2001).
- [128] A.M. Sonnet and E.G. Virga. *Dissipative Ordered Fluids: Theories for Liquid Crystals*. (Springer, New York), 2012.
- [129] I.W. Stewart. *The Static and Dynamic Continuum Theory of Liquid Crystals*. (Taylor and Francis, London and New York), 2004.
- [130] W.A. Strauss. *Partial Differential Equations: An Introduction*. (John Wiley & Sons, New York), 1992.
- [131] X. Tang and J.V. Selinger. Theory of defect motion in 2D passive and active nematic liquid crystals. *Soft Matter*, **15**, pp. 587–601, (2019).
- [132] S.P. Thampi, R. Golestanian, and J.M. Yeomans. Active nematic materials with substrate friction. *Phys. Rev. E*, **90**, art. no. 062307, (2014).
- [133] S.P. Thampi, R. Golestanian, and J.M. Yeomans. Driven active and passive nematics. *Molecular Physics*, **113**, pp. 2656–2665, (2015).
- [134] S.P. Thampi, R. Golestanian, and J.M. Yeomans. Vorticity, defects and correlations in active turbulence. *Phil. Trans. R. Soc. A*, **372**, art. ID. 20130366, (2014).
- [135] S.P. Thampi and J.M. Yeomans. Active turbulence in active nematics. *Eur. Phys. J. Spec. Top.*, **225**, pp. 651–662, (2016).
- [136] E. Tjhung. D.Phil. Thesis, University of Edinburgh (2013).
- [137] E. Tjhung, M.E. Cates, and D. Marenduzzo. Nonequilibrium steady states in polar active fluids. *Soft Matter*, **7**, pp. 7453–7464, (2011).
- [138] J. Toner, Y. Tu, and S. Ramaswamy. Hydrodynamics and phases of flocks. *Ann. Phys.*, **318**, pp. 170–244, (2005).
- [139] C. Truesdell and W. Noll. *The Non-Linear Field Theories of Mechanics*. (In: S. Flügge (ed.) *Handbuch der Physik*, Springer-Verlag, Berlin), 1965.

- [140] C. Tsakonas, A.J. Davidson, C.V. Brown, and N.J. Mottram. Multistable alignment states in nematic liquid crystal filled wells. *Appl. Phys. Lett.*, **90**, art. no. 111913, (2007).
- [141] S.S. Turzi. Active nematic gels as active relaxing solids. *Phys. Rev. E*, **96**, art. no. 052603, (2017).
- [142] E.G. Virga. *Variational theories for liquid crystals*. (Chapman and Hall, London), 1994.
- [143] R. Voituriez, J.F. Joanny, and J. Prost. Generic phase diagram of active polar films. *Phys. Rev. Lett.*, **96**, art. no. 028102, (2006).
- [144] R. Voituriez, J.F. Joanny, and J. Prost. Spontaneous flow transition in active polar gels. *EPL (Europhysics Letters)*, **70**, pp. 404–410, (2005).
- [145] D. Vorländer. Einfluß der molekularen Gestalt auf den krystallinisch-flüssigen Zustand. *Ber. Deutsch. Chem. Ges.*, **40**, pp. 1970–1972, (1907). A translation into English can be found in Reference [125].
- [146] J. Walton, G. McKay, M. Grinfeld, and N.J. Mottram. Spontaneous and pressure-driven states in channel flow of active nematic liquid crystals. Submitted for publication to *Eur. Phys. J. E*, (2020).
- [147] J. Walton, N.J. Mottram, and G. McKay. Nematic liquid crystal director structures in rectangular regions. *Phys. Rev. E*, **97**, art. no. 022702, (2018).
- [148] C.A. Whitfield, T.C. Adhyapak, A. Tiribocchi, G.P. Alexander, D. Marenduzzo, and S. Ramaswamy. Hydrodynamic instabilities in active cholesteric liquid crystals. *Eur. Phys. J. E*, **40**, art. no. 50, (2017).
- [149] C.A. Whitfield and R.J. Hawkins. Instabilities, motion and deformation of active fluid droplets. *New J. Phys.*, **18**, art. no. 123016, (2016).
- [150] D.-K. Yang and S.-T. Wu. *Fundamentals of Liquid Crystal Devices*. (John Wiley & Sons, Chichester), 2006.

- [151] X. Yang, M.G. Forest, and Q. Wang. Near equilibrium dynamics and one-dimensional spatial-temporal structures of polar active liquid crystals. *Chin. Phys. B*, **23**, art. no. 118701, (2014).
- [152] X. Yang and Q. Wang. A 2D numerical study of polar active liquid crystal flows in a cavity. *Computers & Fluids*, **155**, pp. 33–49, (2017).
- [153] X. Yang and Q. Wang. Role of the active viscosity and self-propelling speed in channel flows of active polar liquid crystals. *Soft Matter*, **12**, pp. 1262–1278, (2016).
- [154] J.M. Yeomans. The hydrodynamics of active systems. *Soft Matter Self-Assembly*, **193**, pp. 383–416, (2016).
- [155] Y. Yi, M. Nakata, A.R. Martin, and N.A. Clark. Alignment of liquid crystals by topographically patterned polymer films prepared by nanoimprint lithography. *Appl. Phys. Lett.*, **90**, art. no. 163510, (2007).
- [156] E.C. Zeeman. Catastrophe Theory. *Scientific American*, **234**, pp. 65–83, (1976).
- [157] W. Zheng and Y.-T. Hu. Alignment of liquid crystal confined in polydimethylsiloxane channels. *Mol. Cryst. Liq. Cryst.*, **615**, pp. 1–8, (2015).
- [158] W. Zheng and Y.-T. Hu. Orientation of liquid crystal molecules in polydimethylsiloxane micro-channels. *Liq. Cryst.*, **43**, pp. 327–335, (2016).
- [159] H. Zocher. The effect of a magnetic field on the nematic state. *Trans. Faraday Soc.*, **29**, pp. 945–957, (1933).
- [160] V. Zwetkoff. Bewegung anisotroper Flüssigkeiten im rotierenden Magnetfeld. *Acta Physiocochemica URSS*, **10**, pp. 558–578, (1939).